

Unified Spin Electrodynamics of Dirac and Maxwell Fields

by

**Farhad Khosravi**

A thesis submitted in partial fulfillment of the requirements for the degree of

Doctor of Philosophy

in

Photonics and Plasmas

Department of Electrical and Computer Engineering  
University of Alberta

©Farhad Khosravi, 2020

# Abstract

Control and manipulation of the angular momentum of optical, electronic, or light-matter interacting systems has given rise to a myriad of applications. Majority of these applications, however, deploy only global angular momentum properties of these fields by solely incorporating far-field interactions or the conservation of total angular momentum. Local properties of optical and electronic fields and their interactions in the near-field region have been gaining attention only recently and a thorough understanding of these dynamics is still essential.

Here we study the angular momentum dynamics of light-matter interacting systems from a fundamental relativistic point of view. By applying Noether's theorem to the quantum electrodynamics Lagrangian, we discover a local conservation of angular momentum equation applicable to far-field and near-field interactions. In contrast to the widely used duality symmetry approach towards the local conservation of helicity, our approach is quantum, relativistic, applies to light-matter interactions, does not introduce a new gauge field, and thus is experimentally testable. Our theory not only applies to the recent near-field and local light-matter experiments, but it also pushes the frontiers in light-matter interactions for the realization of next generations of experiments on the role of angular momentum.

We further investigate the light-matter interacting system of an atom or a quantum dot coupled to the evanescent fields of a spherical resonator. We show that, due to the local alignment of the optical spin of the resonant modes and the radiated field of the source, the modes of the resonator are excited asymmetrically depending on the Zeeman transitions of the source. These results show the importance of local and near-field photonic spin in realizing on-chip quantum routing of single photons in quantum optical networks. Our work presents a generalization of universal spin-momentum locking of light to 3D structures.

Moreover, we take the Dirac-Maxwell correspondence approach – the study of similarities between the Dirac and Maxwell's equations – by presenting the solutions of Dirac equation for a cylindrical geometry. Labeled as Dirac wire, this geometry is the electronic analogue of an optical fiber. We have presented a set of new solutions for three types of

Jackiw-Rebbi problems. We have studied the spatial distribution and global quantization of spin and orbital angular momentum in Dirac wire. We show that, as a result of the field confinement, a longitudinal angular momentum component emerges which is absent in previously known solutions of Dirac equation. Dirac wire can have important implications for spintronic applications.

In addition, we demonstrate angular momentum properties of acoustic waves by solving for the Rayleigh surface acoustic waves (SAWs) propagating on a slab of Lithium Niobate. While these solutions are known, we show the spin-momentum locking property in the displacement field as well as the gyrating electric field of SAW and connect it to the spin-momentum locking observed in Dirac and Maxwell solutions of surface waves – highlighting the universality of this phenomenon.

Finally, we study the implications of spin optomechanics for quantum vacuum radiation and quantum vacuum torque. By solving for a magnetic nanosphere spinning in the vicinity of a slab of a metallic or magnetic material, we find quantum vacuum radiation emerging from the magnetic sphere that is orders of magnitude larger than any other known material. We further show that the consequences of this large vacuum radiation or vacuum friction is experimentally observable for feasible and realistic setup parameters. These results are a breakthrough for the field of quantum vacuum fluctuations proposing the first experimental observation of quantum vacuum radiation and quantum vacuum friction.

Our results have important implications for the future of the fields of spin photonics and light-matter interactions. They provide insight for the understanding of the role of angular momentum in the local light-matter interactions and propose unique platforms for test and understanding of such interactions. Our work lays the foundation for future tabletop experiments for spin quantum electrodynamics.

# Preface

This thesis presents the original work by Farhad Khosravi. Main chapters of this thesis have been published or are under preparation for submission as scholarly articles in well-known journals. Professor Zubin Jacob was the supervisory author and was involved with content formation, analysis and also manuscript composition of these articles.

Chapter 2 of this thesis is under preparation for submission as: Farhad Khosravi, Li-Ping Yang, Zubin Jacob, "Universal conservation laws of angular momentum for Dirac-Maxwell fields".

Chapter 3 of this thesis has been published as: Farhad Khosravi, Cristian L. Cortes, and Zubin Jacob, "Spin photonics in 3D whispering gallery mode resonators," *Opt. Express* 27, 15846-15855 (2019).

Chapter 4 of this thesis has been published as: Khosravi, Farhad, Todd Van Mechelen, and Zubin Jacob. "Dirac wire: Fermionic waveguides with longitudinal spin." *Physical Review B* 100.15 (2019): 155105.

Chapter 5 of this thesis is a collaboration with the group of Professor Hubert Krenner from the University of Augsburg, Germany. The results will be published under the title "Ultrafast electron cycloid driven by the transverse spin of a surface acoustic wave". In this work, we have contributed to the theoretical simulation of surface acoustic waves propagating on the surface of a slab of lithium niobate.

Chapter 6 of this thesis is under preparation for submission as: Farhad Khosravi, Chinmay Khandekar, and Zubin Jacob, "Colossal quantum vacuum radiation from spinning YIG nanospheres".

*Dedicated to my love, Roya  
my mother, Zohreh  
and my beloved family*

# Acknowledgements

I owe many thanks to a lot of people for their support during the period of my graduate studies. While my Ph.D period is filled with many dreadful and joyful moments, when I look back, I will remember the faces of the amazing people who supported me with their hearts.

First and foremost, I extend my humble gratitude to my mother's soul, Zohreh, whom I lost in the first year of my Ph.D. I owe all of my achievements, desires, and knowledge to her and I hope I can continue her love for math, music, poetry, painting, and living in general.

I also would like to pay tribute to my Master's supervisor, Professor Pedram Mousavi, who was killed tragically together with his wife Professor Mojgan Daneshmand and their two daughters Darya and Dorina in the ill-fated passenger flight PS752. His family were always dear friends to me and their memory and works will always be remembered.

I wish to thank my supervisor and mentor, Professor Zubin Jacob, who was always supportive of my scientific and musical career and always kept me excited about my research despite our distances. He taught me how to be a critical thinker, an independent researcher, and a kind and supportive leader. I also would like to thank my co-supervisor, Professor Robert Fedosejevs, for all of his support and fruitful discussions throughout my Ph.D.

I also wish to thank my evaluation committee members: Professor Vien Van, Professor Joseph Maciejko, and Professor Sandipan Pramanik. In addition, I would like to thank Pinder Bains for organizing the thesis defence session.

I would also like to thank my friends here in Edmonton who were a family to me and kept my heart warm during the cold winters. I also thank my colleagues, Li-Ping Yang, Farid Kalhor, Todd van Mechelen, Chinmay Khandekar, Cristian Cortes, Sarang Pendharker, Vishal Choudhury, Zohreh Poursoti, Saman Jahani, Parijat Sengupta, Prashant Shekhar, and Sean Molesky at University of Alberta as well as Purdue university for their support, knowledge, and discussions.

Last but not least, I would like to thank my beautiful wife, Roya, for her continuous and

unconditional love, support, and encouragement. I am also greatly thankful to my father, my siblings, my father-in-law, my mother-in-law, and my sister-in-law. Without their support and love none of these could have been possible.

# Table of Contents

<b>1</b>	<b>Introduction to Spin Electrodynamics</b>	<b>1</b>
1.1	Applications and Challenges	1
1.2	Experimental Platforms	2
1.3	Fundamental Aspects	6
1.3.1	Relativistic vs. Non-relativistic	6
1.3.2	Gauge Invariance	7
1.3.3	Quantum vs. Classical	8
1.3.4	Spin Statistics	10
1.3.5	Near-Field, Far-field, and Evanescent	11
1.3.6	Duality Symmetry and its Limitations	11
1.4	Summary of Contributions	13
<b>2</b>	<b>Universal Angular Momentum Conservation Laws for Dirac-Maxwell Fields</b>	<b>16</b>
2.1	Introduction	16
2.2	Noether's theorem, QED Lagrangian, and Lorentz transformation	19
2.3	Local conservation law of angular momentum	20
2.3.1	Helicity current density tensor	23
2.3.2	Orbital angular momentum current density tensor	23
2.3.3	Spin-orbit torque	24
2.4	Source-free problems	26
2.4.1	dual-mode optical fiber	26
2.4.2	double plane wave interference	27
2.5	Conclusion	28
<b>3</b>	<b>Spin Photonics in 3D Whispering Gallery Mode Resonators</b>	<b>31</b>
3.1	Introduction	31
3.2	Photonic spin in spherical whispering gallery modes	34
3.3	Near-field spin interaction	37
3.4	Conclusion	42
<b>4</b>	<b>Dirac Wire: Fermionic Waveguides with Longitudinal Spin</b>	<b>43</b>
4.1	Introduction	43
4.2	Dirac Wire	45
4.2.1	Cylindrical Jackiw-Rebbi domain wall	46
4.2.2	Dispersive Jackiw-Rebbi (topological insulator)	48
4.3	Dispersion of Dirac waveguides	50
4.4	Conclusion	52
<b>5</b>	<b>Spin-Momentum Locking in Surface Acoustic Waves</b>	<b>54</b>
5.1	Introduction	54
5.2	Rayleigh Surface Acoustic Waves	55
5.3	Experimental Observation	58
5.4	Conclusion	59

<b>6</b>	<b>Colossal Vacuum Radiation from Spinning YIG Nanosphere</b>	<b>60</b>
6.1	Introduction . . . . .	60
6.2	Quantum Vacuum Radiation . . . . .	62
6.3	Quantum Vacuum Torque . . . . .	66
6.4	Experimental Considerations . . . . .	66
6.5	Conclusion . . . . .	69
<b>7</b>	<b>Conclusion and Future Work</b>	<b>70</b>
7.1	Conclusion and Summary . . . . .	70
7.2	Future work . . . . .	71
7.2.1	Study of Local Angular Momentum Electrodynamics . . . . .	71
7.2.2	Angular Momentum of Quantum Vacuum Radiation . . . . .	72
7.2.3	Two-body Dirac Equations . . . . .	73
7.2.4	Atomic Selection Rules in Near-Field Interactions . . . . .	73
	<b>Bibliography</b>	<b>75</b>
<b>A</b>	<b>Proofs for Chapter 2</b>	<b>88</b>
A.1	Conserved Angular Momentum Tensor . . . . .	88
A.2	Spin-Orbit Torque . . . . .	92
A.3	<i>Semi-Local</i> Conservation Law . . . . .	95
A.4	Symmetrized Angular Momentum Tensor . . . . .	96
A.5	Boost Conservation Relations . . . . .	98
A.6	Two Plane Wave Interference . . . . .	98
A.7	Meaning of the Notations . . . . .	99
<b>B</b>	<b>Proofs for Chapter 3</b>	<b>101</b>
B.1	Spherical Solutions of Scalar Helmholtz Equation . . . . .	101
B.2	Spherical Solutions of Vector Helmholtz Equation . . . . .	102
B.3	Whispering-Gallery Modes in a Spherical Resonator . . . . .	103
B.4	Spin of WGMs . . . . .	105
B.5	Electric Field Green's Function . . . . .	106
B.6	Magnetic Field Green Function . . . . .	112
B.7	Electric and Magnetic Dipoles . . . . .	116
B.8	Properties of Legendre Polynomials . . . . .	117
<b>C</b>	<b>Proofs for Chapter 4</b>	<b>118</b>
C.1	Cylindrical Dirac Equation . . . . .	118
C.2	Cylindrical Jackiw-Rebbi problem . . . . .	120
C.2.1	Solutions of $JR^+$ Dirac Wire problem . . . . .	120
C.2.2	Solutions of $JR^-$ Dirac Wire problem . . . . .	120
C.3	Dirac Equation with dispersive mass . . . . .	122
C.3.1	Modal Behaviour of Solutions . . . . .	124
C.3.2	Group Velocity . . . . .	125
<b>D</b>	<b>Proofs for Chapter 5</b>	<b>126</b>
D.1	Equations of Motion . . . . .	126
D.2	Rayleigh Surface Wave . . . . .	127
D.3	Lithium Niobate Crystal Properties . . . . .	128
D.4	Boundary Conditions . . . . .	129
D.5	Solving the Equations . . . . .	130
<b>E</b>	<b>Proofs for Chapter 6</b>	<b>132</b>
E.1	Radiated Power due to Magnetic Fluctuations . . . . .	132
E.2	Green's Function Near an Anisotropic Magnetic Material . . . . .	134
E.3	Local Density of States . . . . .	139
E.4	Magnetic Polarizability Tensor of YIG . . . . .	139
E.5	Non-Electrostatic Limit and Magnetic Polarizability due to Electric Fluctuations . . . . .	141

E.6	Barnett Effect . . . . .	144
E.7	Non-local Model for Aluminum . . . . .	144
E.8	Quantum Vacuum Torque . . . . .	145
	E.8.1 Other components of torque . . . . .	146
	E.8.2 Recoil torque . . . . .	149
	E.8.3 Plots of torque terms . . . . .	151
E.9	Experimental Analysis . . . . .	152
	E.9.1 Effect of drag torque due to imperfect vacuum . . . . .	152
	E.9.2 Effect of torque due to the trapping laser . . . . .	154
	E.9.3 Effect of heating due to the shot noise . . . . .	155
E.10	Solving for Fresnel Coefficients for an Arbitrarily Positioned YIG . . . . .	156

# List of Tables

3.1	Summary of the properties of the WGMs . . . . .	42
3.2	Physical parameters of the spin photonics in 3D WGM resonators . . . . .	42
4.1	Physical parameters of Dirac wire problem. . . . .	53
6.1	Physical parameters of the YIG nanosphere spinning in vicinity of the aluminum or YIG interface . . . . .	69

# List of Figures

1.1	Experimental platforms for the investigation of near-field and evanescent local interactions. (a) Cold caesium atoms interacting with the local field of an optical fiber (image taken from [16]). (b) Local interaction between a single Rb atom and a spherical resonator allows an all-optical routing with single photons used as switches (image taken from [17]) (c) Local interaction between a circularly-polarized dipole and the spin of the surface plasmon polaritons in a metal lead to unidirectional coupling to the SPPs (image taken from [18]) (d) Interaction between the transitions in a quantum dot (QD) and the local spin of the photonic modes lead to unidirectional propagation of modes along the photonic waveguide(image taken from [19]).	4
1.2	Overall structure of the thesis. Chapter 2 discusses our fundamental approach towards the spin electrodynamics by deriving a new conservation law of angular momentum. This general topic encompasses the next four chapters of the thesis where we have discussed the implications of spin electrodynamics in four particular problems. Chapter 3 discusses a nanophotonic structure where we have shown the role of angular momentum in on-chip quantum emitter routing. Chapter 4 discusses Dirac-Maxwell correspondence where we have studied the similarities between the solutions of Dirac equation in cylindrical geometry and optical fiber. Chapter 5 investigates the spin properties in the acoustic waves propagating on the surface of lithium niobate. In chapter 6 the implications of spin optomechanics for quantum vacuum radiation and quantum vacuum torque has been studied.	13
2.1	Conservation laws of angular momentum in light-matter interacting systems (a) conventional conservation of global total photonic and electronic angular momentum. This conservation law applies to closed systems and does not include angular momentum exchange due to near-field interactions. (b) Local conservation of angular momentum applicable to all regions of interaction. The conventional conservation of sum of angular momenta is replaced by the conservation Eq. (2.6). (c) Table of quantities defined in this chapter, representing the spatial and temporal densities of the scalar, vector, or tensor observables pertinent to angular momentum. Highlighted quantities are the new terms defined in this chapter. The local conservation of angular momentum equation (Eq. (2.6)) connects the well-known terms such as spin density, OAM density, helicity and chirality to these newly defined quantities.	18

2.2	Local conservation law for the spin [Eq. (2.12)] in a dual-mode optical fiber. The individual terms in Eq. (2.12) are plotted on the first three columns from left: The first column is the time-derivative of spin ( $\frac{\partial}{\partial t}(\mathbf{E}^\perp \times \mathbf{A}^\perp)$ ), the second column is the divergence of helicity current tensor ( $-\nabla_i(A_i^\perp \mathbf{B})/\mu_0$ ), and the third column is the gradient of the helicity density ( $\nabla(\mathbf{A}^\perp \cdot \mathbf{B})/\mu_0$ ). The fourth column is the EM spin-orbit torque given by Eq. (2.11) (in this case $\tau_{\text{em}} = (\mathbf{B} \cdot \nabla)\mathbf{A}^\perp/\mu_0$ ). The three rows show the local value of each vector along the three axes of optical fiber problem: $\hat{\rho}$ radial direction, $\hat{\phi}$ azimuthal direction, and $\hat{z}$ axis of the fiber. Note that adding the first three column on each row together gives the last column $\tau_{\text{em}}$ ; thus confirming Eq. (2.12). The results are for an optical fiber of radius $50 \mu\text{m}$ with the two modes at the wavelengths $4.3 \mu\text{m}$ and $4.29 \mu\text{m}$ . . . . .	25
2.3	Dynamics of the terms in Eq. (2.12) versus (a) $z$ and (b) time. The plots only show the $\hat{z}$ component of each term. These plots show that the spin-orbit torque ( $\tau_{\text{em}}$ ) is equal to the sum of the other terms. The inset in panel (a) shows the location where the terms are evaluated for both of the figures. . . . .	27
3.1	Schematic of the proposed experiment to study spin photonics in WGMs. The unique proposed effect due to the locked electromagnetic triplet consisting of spin, momentum, and decay. (a) A quantum source with circularly polarized emission ( $\sigma^\pm$ transitions) is placed in the vicinity of a spherical resonator. The near-field interaction between the source and TM WGMs of the sphere results in excitation of WGM with only spin polarized, positive OAM along $z$ direction. This unidirectional behaviour is a manifestation of spin-momentum locking in a 3D structure. Spin, linear momentum, and decay are along $\hat{\theta}$ , $\hat{\phi}$ , and $\hat{r}$ , respectively, and form a triplet for the TE and TM modes. (b) General form of Zeeman transitions in a cold atom [100] or quantum dot [101]. For $\sigma^\pm$ and $\pi$ transitions, $\Delta m_F = \pm 1$ and $\Delta m_F = 0$ , respectively, where $m_F$ is the quantum number pertinent to the total angular momentum of the source (nucleus and electrons). These transitions can be modeled by dipole sources with the electric dipole moment given by Eq. (3.7) [16]. . . . .	33
3.2	Proposed experimental setup for the spin photonics in WGMs. By exciting the resonator using a $\sigma^-$ transition of a quantum source, WGMs with positive orbital angular momentum are excited stronger. This can be observed by proximity coupling of a tapered optical fiber to the spherical resonator. As a result of coupling between the WGMs with positive OAM and the fiber, modes propagate only in one particular direction in the fiber [17, 92]. Switching to a $\sigma^+$ transition instead, would also reverse the propagation direction inside the fiber. The source can be Zeeman transitions in cold Caesium atom prepared in the excited state using a excitation signal [100]. . . . .	34
3.3	Electromagnetic spin in TE and TM whispering gallery modes. The color plot shows the field intensity of $H_r$ ( $E_r$ ) component of the TE (TM) mode for $l = 16$ and $m = 16$ on the surface of the resonator. The blue arrows show the direction of spin on the surface of the sphere. Modes with positive $m$ , orbit the $z$ axis counter-clockwise ( $+\hat{\phi}$ ) while those with negative $m$ orbit the $z$ axis clock-wise ( $-\hat{\phi}$ ). With linear momentum along $+\hat{\phi}$ , Momentum, decay, and spin form a triplet. Spin direction follows the spin-momentum locking property for both TE and TM modes. This means that by changing the direction of OAM (changing the sign of $m$ ), the direction of the spin (blue arrows) reverses for both TE and TM modes. This behaviour inspires unidirectional coupling of a circularly polarized dipole to the WGMs. . . . .	35

- 3.4 Plots of normalized scattered electromagnetic fields due to the right-handed circularly polarized dipole ( $\sigma^+$  transition). (a)  $E_r$ , (b)  $E_\phi$ , and (c)  $H_\theta$  in the  $x - y$  plane. All components of the fields orbit along  $-\phi$  direction as a result of the circularly polarized dipole located at  $x_d = a + 10\text{nm}$  and  $y_d = z_d = 0$  with the dipole moment  $\mathbf{d}_+ = \frac{d_0}{\sqrt{2}}(\hat{x} + i\hat{y}) = d_0\hat{e}_+$ . The circularly polarized dipole couples unidirectionally to the orbit of the fields in the spherical resonator as a result of spin-momentum locking. One important consequence of this is that the photonic spin of the source is opposite to the OAM of the WGMs. Additional videos are available online [22]. . . . . 38
- 3.5 Normalized Poynting vector along  $\phi$  direction,  $P_\phi$ , for the three cases of (a)  $\sigma^+$  transitions (RH circularly polarized dipole), (b)  $\sigma^-$  transitions (LH circularly polarized dipole), and (c)  $\pi$  transitions (linearly polarized dipole along  $x$ ), in the  $x - y$  plane for the source located at  $x_d = a + 10\text{nm}$  and  $y_d = z_d = 0$ , and with the dipole moments given by Eq. (3.7). The negative value of  $P_\phi$  in (a) and positive value of  $P_\phi$  in (b) indicate that, for the RH and LH circularly polarized dipoles as the source, the WGMs of the spherical resonator orbit clockwise (along  $-\hat{\phi}$ ) and counter-clockwise (along  $+\hat{\phi}$ ), respectively. For the linearly polarized dipole in (c), however, the WGMs inside the sphere are a mixture of clockwise and counter-clockwise fields which eventually cancel out each other to give a net-zero OAM. Therefore, coupling the WGMs to an optical fiber, for instance, on the other side from the source, would result in an equal wave propagation in both directions inside the fiber. However, for a circularly polarized source, the modes would only propagate along one direction inside the fiber, depending on the handedness of source. This figure clearly shows the unidirectional behaviour of spin interaction of the source and WGMs, as a result of the spin-momentum locking. . . . . 39
- 4.1 (a) Schematic of the Dirac wire. (b) The three Jackiw-Rebbi (JR) type domains considered here are  $\text{JR}^+$  with electron mass inside ( $m_1$ ) and outside ( $m_2$ ) the wire both positive,  $\text{JR}^-$  with positive mass inside and negative mass outside, and JR-D with a dispersive electronic mass inside [Eq. (4.5)] and an arbitrary mass outside. JR-D corresponds to the minimal topological insulator. Distribution of the probability density,  $\psi^\dagger\psi$ , for the three problems are shown in the three panels of (b). The fields are normalized such that  $\int \psi^\dagger\psi = 1$  when integrated over the entire cross section. Notice that the probability amplitude of the  $\text{JR}^-$  state is localized around the perimeter of the wire  $\rho = a$ . Also, in the case of the JR-D problem, the wave function is identically zero at the boundary and outside the wire  $\psi(\rho \geq a) = 0$ . . . . . 44
- 4.2 Spin and orbital angular momentum densities for the three Jackiw-Rebbi (JR) domains (Fig. 4.1). As an example,  $a = 20 \text{ \AA}$ ,  $\mu = \frac{1}{2}$ , and  $k_z = 0$ .  $|m_1|v_F^2$  and  $m_2v_F^2$  are 1 eV and 2 eV, respectively. For the JR-D problem,  $m_0v_F^2 = 1 \text{ eV}$  and  $B\hbar^2 = 50 \text{ eV\AA}^2$  [138]. In all three scenarios we have assumed a Fermi velocity of  $v_F \simeq 1.52 \times 10^5 \text{ m/s}$ , such that the Compton wavelength is  $\lambda_c \simeq 8 \text{ \AA}$ . The values at the bottom of each figure are the integrated quantities of the respective distribution over the entire cross-section of the problem. Note that the spin and OAM are not individually conserved but their summation ( $J_z = S_z + L_z$ ) is. Although not individually conserved, the difference in the distribution of spin and OAM makes them locally distinguishable. This means that one can, in principle, couple exclusively to spin or OAM locally. . . . . 47

4.3	(a) Dispersion and group velocities (inset) for the dominant modes of $JR^+$ (dashed blue), $JR^-$ (dotted red), and $JR-D$ (solid black). Group velocities are normalized to the Fermi velocity $v_F \simeq 1.52 \times 10^5$ m/s. Wire radius dependence of (b) bandgaps, (c) spin, and (d) OAM for the three problems at $k_z = 0$ . Here $\mu = \frac{1}{2}$ , $k_z = 0$ , $ m_1 v_F^2 = 1$ eV, $m_2v_F^2 = 2$ eV, and $\lambda_c \simeq 8$ Å. The insets show the zoomed in region of the corresponding figure for wire radius between 1nm and 5nm. For the topological insulator ( $JR-D$ ), $m_0v_F^2 = 1$ eV and $B\hbar^2 = 50$ eVÅ <sup>2</sup> . Due to confinement in the cylindrical geometry, the bandgap is opened for all three problems. For $JR-D$ , however, the bandgap closes and reopens for certain values of $a$ as seen in the inset of panel (b). Note that the summation $J_z = S_z + L_z$ produces the conserved value of $\frac{1}{2}$ in all three cases. In the limit $a \rightarrow \infty$ , OAM vanishes $L_z \rightarrow 0$ for $JR^+$ , while spin vanishes $S_z \rightarrow 0$ for $JR^-$ and $JR-D$ .	51
5.1	(a) Momentum, decay and spin of the gyrating electric field generated by a Rayleigh-type SAW form a right-handed triplet. The direction of spin for both electric field and displacement are locked to the propagation direction. (b) Calculated displacement and (c) electric field (main panels) of the Rayleigh SAW propagating along the Z-direction on a Y-cut LiNbO <sub>3</sub> crystal. The side panels show the normalized magnitude of the transverse spin normal to the surface ( $y = 0$ ). The mechanical spin shows a characteristic sign change at $\simeq \lambda_{SAWS}$ below the surface, i.e. from being counterclockwise to clockwise, while the electrical spin changes from counterclockwise to clockwise exactly at the surface.	56
5.2	Experimental setup for the observation of spin of a Rayleigh-type SAW propagating on the surface of Lithium Niobate (LiNbO <sub>3</sub> ). By probing PL from the two quantum wells inside the NW, we are able to track the time-evolution of the electric field generated by the SAW and thus confirm the spin of the acoustic wave.	59
6.1	(a) A YIG sphere trapped in the laser beam and spinning at 1 GHz rotation frequency in vacuum. The stopping time for the sphere is on the order of age of the universe. (b) YIG sphere spinning the vicinity of an Aluminum or YIG interface exhibits colossal quantum vacuum radiation. The stopping time, due to the presence of the interface, is reduced to about 8 hours. (c) Number of photons emitted per second per radiation frequency, defined as $\frac{1}{\hbar\omega}dP/d\omega = \Gamma(\omega) - \Gamma(-\omega)$ , for a YIG (blue solid curve) and Aluminum (dashed orange curve) nanosphere of radius 200 nm in the vicinity of an Aluminum slab, and (d) in the vicinity of a YIG slab. For the Al slab, non-local model has been used. The YIG slab in panel (d) is biased along y direction (panel (a)) with a magnetic field of $H_0 = 812$ Oe. The distance between the sphere and both interfaces is chosen to be $d = 0.5\mu\text{m}$ .	63
6.2	(a) Schematic for the $s$ and $p$ polarization. The $k^-$ vector shows the propagation direction for waves propagating along $-z$ direction. $s$ and $p^-$ polarization are defined with respect to this propagation direction. Similarly, $k^+$ and $p^+$ vectors can also be defined for waves propagating along $+z$ direction. (b) Plots of the electric ( $\rho_E$ ), magnetic ( $\rho_H$ ), and total ( $\rho_T$ ) LDOS for a distance of $d = 0.5\mu\text{m}$ from an Al interface. Note that non-local model has been used for the Al. As shown, the total LDOS is dominated by the magnetic LDOS since it is about 12 orders of magnitude larger than the electric LDOS.	64

6.3	The negative quantum vacuum torque experienced by a YIG and Aluminum nanosphere of radius 200 nm at room temperature. (a) Torque experienced by a YIG sphere in vicinity of YIG slab (solid blue curve) and in vacuum (dashed black curve). (b) Torque exerted on an Al sphere in vicinity of YIG slab (solid orange curve) and in vacuum (dashed black curve). (c), (d) the same as (a) and (b) with YIG slab replaced by an Al slab. The YIG slab is biased along $y$ direction with $H_0 = 812$ Oe (see Fig. 1(a)). A non-local model is used for the Al slabs. The distance between the spinning spheres and slabs is $d = 0.5\mu\text{m}$ for all cases. Placing the YIG or Al interface in vicinity of spinning sphere results in about 12 orders of magnitude increase in the exerted quantum vacuum torque. . . . .	67
6.4	Experimental considerations of the setup. (a) Proposed experimental setup with nanosphere trapped inside a ring. (b) Balance speed $\Omega_b$ for Al sphere (red curve) and YIG sphere in presence of Al (blue curve) and YIG (pink curve) interfaces, as a function of distance $d$ from the interface for a 200 nm radius sphere at $10^{-4}$ Torr vacuum pressure. The values are normalized to the vacuum balance speed $\Omega_0$ . (c) Characteristic stopping time as a function of distance from the interface at vacuum pressure of $10^{-6}$ Torr. (d) Balance temperature of the YIG sphere $T_s$ at $d = 500$ nm distance from Al (blue curve) and YIG (pink curve) interface as a function of lab temperature $T_0$ , at vacuum pressure $10^{-4}$ Torr. For Al interface there is no final temperature as the temperature keeps raising with time. . . . .	68
C.1	Spatial distribution of probability densities, $\psi^\dagger\psi$ , for the first six modes of the $\text{JR}^+$ problem. The radius of the wire is $a = 20 \text{ \AA}$ , $m_1v_F^2 = 1 \text{ eV}$ , and $m_2v_F^2 = 2 \text{ eV}$ . . . . .	121
C.2	Properties of the first six modes of the $\text{JR}^+$ problem for $a = 20 \text{ \AA}$ . (a) dispersion and (b) spin and OAM of the first six modes. . . . .	121
C.3	Spatial distribution of probability densities, $\psi^\dagger\psi$ , for $\mu = \frac{1}{2}$ and for the first six modes of the $\text{JR}^-$ problem. The radius of the wire is $a = 20\text{\AA}$ , $ m_1 v_F^2 = 1\text{eV}$ , and $m_2v_F^2 = 2\text{eV}$ . . . . .	122
C.4	Properties of the first six modes of the $\text{JR}^-$ problem for $a = 20\text{\AA}$ . (a) Dispersion and (b) spin and OAM of the first six modes. . . . .	122
C.5	Spatial distribution of probability densities, $\psi^\dagger\psi$ , for the first six modes of the $\text{JR-D}$ problem. The radius of the wire is $a = 20 \text{ \AA}$ , $m_1v_F^2 = 1 \text{ eV}$ , and $m_2v_F^2 = 2 \text{ eV}$ . . . . .	123
C.6	Properties of the first six modes of the $\text{JR-D}$ problem. (a) Dispersion of the first six modes and (b) spin and OAM of the first six modes. . . . .	124
E.1	Schematic of the problem for the two cases of when the interface is in (a) $x - y$ plane and (b) $x - z$ plane. . . . .	136
E.2	Schematics of different bias directions for the YIG interface for the two cases of the interface being the $x - y$ (top row) and $x - z$ planes (bottom row). The green arrow shows the direction of the bias magnetic field applied to the slab of YIG. . . . .	152
E.3	Plots of $M_x$ and $M_y$ (first two rows) and $M_z$ and $M_{\text{rec}}$ (second two rows) in the vicinity of the YIG slab when the slab is the $x - y$ plane (first and third rows), and when the slab is $x - z$ plane (second and fourth rows). The plots show the results for various magnetic field directions. The meanings of $x-$ , $y-$ , and $z-$ bias are demonstrated in Fig. E.2 for the two orientations of the interface. . . . .	153
E.4	Plots of $M_z$ and $M_{\text{rec}}$ in the vicinity of the YIG slab when the slab is the $x - y$ plane (first row), and when the slab is $x - z$ plane (second row). Note that due to isotropy of Al, the other components of torque including $M_x$ and $M_y$ vanish. . . . .	154

# List of Symbols

<b>Symbol</b>	<b>Definition . . . . .</b>	<b>First Use</b>
$\hbar$	Planck's constant . . . . .	1
$\epsilon_0$	Vacuum Permittivity . . . . .	8
$\mu_0$	Vacuum Permeability . . . . .	8
$\mathcal{L}$	Lagrangian . . . . .	19
$\gamma^\mu$	Gamma matrices . . . . .	19
$F_{\mu\nu}$	Electromagnetic tensor . . . . .	19
$\Lambda^\mu{}_\nu$	Lorentz transformation tensor . . . . .	19
$\mathbf{A}^\perp$	Transverse component of the electromagnetic vector potential .	20
$\mathbf{A}^\parallel$	Longitudinal component of the electromagnetic vector potential	20
$\epsilon_{ijk}$	Levi-civita symbol . . . . .	24
$\tau_D$	Dirac spin-orbit torque . . . . .	25
$\tau_{em}$	Maxwell spin-orbit torque . . . . .	25
$HE_{11}$	The first hybrid electric mode of an optical fiber . . . . .	32
$\sigma^\pm$ +1 or -1.	Zeeman transitions with the change in angular momentum of . . . . .	33
$\mathbf{L}$	Total Orbital Angular Momentum . . . . .	34
$L_z$	Orbital Angular Momentum along $z$ direction . . . . .	34
$\mathbf{E}$	Electric Field . . . . .	34
$\omega$	Angular frequency . . . . .	34
$\mathbf{H}$	Magnetic Field . . . . .	34
$\mathbf{S}(\mathbf{r}, \omega)$	Electromagnetic Spin Density . . . . .	35
$\lambda_{TE}$	Wavelength of the TE mode . . . . .	36

$\lambda_{TM}$	Wavelength of the TM mode . . . . .	36
$j_l(ka)$	Spherical Bessel function of the first kind and order $l$ with the argument $ka$ . . . . .	36
$M_{lm}$ and $N_{lm}$	The two transverse solutions of the source-free Maxwell's equations with the orbital quantum numbers of $l$ and $m$ . . . . .	37
$Y_{lm}(\theta, \phi)$	Spherical Harmonics of orders $l$ and $m$ . . . . .	40
$\alpha$	Alpha matrices of the Dirac equation . . . . .	45
$v_F$	Fermi velocity . . . . .	45
$Z_{n_{\pm}}(k_{\perp}\rho)$	Cylindrical Bessel functions of order $n_{\pm}$ and argument $k_{\perp}\rho$ . . . . .	46
$\sigma$	The $2 \times 2$ Pauli matrices . . . . .	46
$\text{LiNbO}_3$	Chemical formula of Lithium Niobate . . . . .	54
$c_{ijk}$	Stiffness tensor . . . . .	56
$e_{ijk}$	Piezoelectric tensor . . . . .	56
$\Gamma^H(\omega)$ YIG sphere	Spectral density for the radiated power due to the spinning . . . . .	62
$\rho_0$	Vacuum density of states . . . . .	62
$n_i(\omega)$	Planck's distribution for temperature $T_i$ . . . . .	62
$\Omega$	Rotation frequency of the nanoparticle . . . . .	65
$\gamma$	Gyromagnetic ratio of the electron . . . . .	65

# List of Abbreviations

<b>Abbreviation</b>	<b>Description . . . . .</b>	<b>First Use</b>
ODMR	Optically Detected Magnetic Resonance . . . . .	2
ESR	Electron Spin Resonance . . . . .	2
NMR	Nuclear Magnetic Resonance . . . . .	2
MRI	Magnetic Resonance Imaging . . . . .	2
MOKE	Magneto-Optic Kerr Effect . . . . .	2
OAM	Orbital Angular Momentum . . . . .	14
SAW	Surface Acoustic Wave . . . . .	15
WGM	Whispering Gallery Mode . . . . .	31
TE	Transverse Electric . . . . .	34
TM	Transverse Magnetic . . . . .	34
SOC	Spin-Orbit Coupling . . . . .	52
NW	Nanowire . . . . .	58
PL	Photoluminescence . . . . .	58
IDT	Interdigital Transducer . . . . .	58
LDOS	Local Density of States . . . . .	60
FDT	Fluctuation-Dissipation Theorem . . . . .	63
TBDE	Two-Body Dirac Equations . . . . .	73

# Chapter 1

## Introduction to Spin Electrodynamics

### 1.1 Applications and Challenges

Angular momentum is a fundamental property of fields and particles that is associated with rotational degree of freedom. This property and the conservation of angular momentum has been exploited in numerous applications and technologies. One of the first uses of the conservation of angular momentum principle is the invention of gyroscopes where a rotating object maintains its rotation axis due to the conservation of angular momentum [1]. Gyroscopes have found many applications in navigational systems and sensors and are more recently being replaced by ring lasers and fiber optics gyroscopes for higher accuracy [2].

Conservation of angular momentum, however, is not limited to the classical systems and moving objects. Manifestations of rotational symmetries and angular momenta is numerous in interacting optical and electronic quantum systems. Ferromagnetism, anti-ferromagnetism, paramagnetism, and diamagnetism are all manifestations of spin and orbital angular momentum of the electrons inside materials which can only be explained by a quantum-mechanical treatment [3]. Conservation of angular momentum, together with exchange interaction [4] and quantum-mechanical nature of the spin and orbital angular momentum of electrons, is sufficient to explain many of these phenomena.

In the case of electromagnetic fields, on the other hand, angular momentum can be explained both in classical or quantum-mechanical senses. In interactions with quantum systems, however, the quantum nature of the electromagnetic wave becomes apparent leading to selection rules in atomic transitions and effects such as the photo-electric effect [5]. These observations show that the angular momentum of light comes in quanta of  $\hbar$ , showing both its quantum and bosonic (integer spin) natures. Spin and orbital angular momentum

of light has been extensively measured [6, 7] and has found many applications in spinning nanoparticles at high velocities [8] and quantum information [9].

The role of angular momentum in light-matter interacting systems becomes especially important, giving rise to effects and applications such as optically detected magnetic resonance (ODMR) [10], electron spin resonance (ESR) [11], nuclear magnetic resonance (NMR) [12] and magnetic resonance imaging (MRI) [13]. In these phenomena, the degeneracy between the quantum states with opposite spins is broken by the application of a magnetic field, while the electron (or the nuclei in the case of NMR and MRI) transitions between these quantum states by absorbing or emitting a photon. In these phenomena, conservation of angular momentum is maintained due to the interaction of spin of electron or nuclei with the angular momentum of photon. With a wide range of frequencies from a few MHz in NMR, GHz range in ESR, to optical frequencies in ODMR, these techniques have found many applications in spectroscopy, medical imaging, and defect detection in crystals.

Angular momentum transfer between the optical fields and the spin of a collection of electrons in magnetic materials also occur in the magneto-optic Kerr effect (MOKE) [14]. In this effect, the magnetic properties of a given material is inferred by probing the polarization of the light reflected from the surface of the material. MOKE can also locally probe the surface of a material, giving a map of magnetization domains. Similar to the MOKE, Faraday effect is also the study of magnetic properties of a material or a medium through the investigation of the polarization of the light transmitted through the medium. This effect has also found a myriad of applications such as the detection and measurement of magnetic fields in interstellar mediums [15]. In both of these effects, the exchange of angular momentum between the electrons and the optical field is the key factor that makes these observations possible.

## 1.2 Experimental Platforms

To show the importance of the spin of electromagnetic fields in the near-field, we look at some of the recent works that have led to unique observations. These observations show that new phenomena emerge as a result of near-field local interaction which is not captured in the conventional treatment of angular momentum as global and time-independent quantities. In chapters 3 and 6 we theoretically study the importance of near-field interactions for experimentally feasible photonic systems and show the emergence of new phenomena that are otherwise absent in far-field interactions.

Figure 1.1 shows a number of important experimental setups that lead to the observation new phenomena due to the role played by the angular momentum in the near-field interactions. These setups exploit atomic  $\sigma^\pm$  transitions to achieve asymmetrical interactions between quantum sources and optical modes.

The  $\sigma^\pm$  transitions are identified by atomic transitions during which the electron changes its orbital angular momentum by one unit of  $\hbar$ . This is denoted by the change in the quantum number  $m$ , pertinent to the projection of electron OAM along the  $z$ -axis, where the  $z$  axis is usually determined by an externally applied magnetic field. The magnetic field breaks the degeneracy of the states with opposite OAM and thus, by appropriate tuning of the excitation laser, the states that lead to  $\Delta m = +1$  or  $\Delta m = -1$  can be selectively excited. Due to the conservation of angular momentum, the change in the angular momentum of the electron is compensated by the angular momentum of the excitation photon. Therefore, the transitions with  $\Delta m = \pm 1$ , labeled as  $\sigma^\pm$  transitions, give rise to photons with opposite polarization handedness. Hence, due to the dominance of the electric dipolar transitions compared to the higher multipolar transitions, the  $\sigma^\pm$  transitions can be modeled by circularly-polarized dipoles.

In cold atom experiments, it has been shown that the local interaction between quantum transitions in a cold caesium atom and the angular momentum of evanescent fields of an optical fiber leads to an asymmetrical propagation of radiation inside the optical fiber [16, 20]. As shown in Fig. 1.1(a), cold caesium atoms are trapped near a tapered optical fiber. The optical modes of the fiber decay evanescently into the surrounding environment. By trapping the atoms at sub-wavelength distance from the optical fiber, pronounced coupling between the fiber and atomic transitions occurs. This coupling, however, is governed by the local spin of the optical modes. A  $\sigma^+$  transition (a transition modeled by a right-handed circularly-polarized dipole) excites the optical modes that have parallel optical spin to the handedness of the dipole, leading to the unidirectional propagation of guided waves inside the optical fiber. By exciting the  $\sigma^+$  or  $\sigma^-$  transition in the atom, the optical modes can be unidirectionally excited such that only detector 1 or detector 2 detects photons.

This phenomenon is also observed in resonant structures such as the one shown in Fig. 1.1(b) for a single Rubidium (Rb) atom trapped near a spherical resonator. Similar to the cylindrical geometry of Fig. 1.1(a), the local interaction between the  $\sigma^\pm$  transitions in the Rb atom and the modes of the resonator leads to the unidirectional propagation of optical modes in the tapered fiber coupled to the resonator [17, 21]. Our theoretical work shows that the local alignment of the spin of the radiation from the quantum source with the

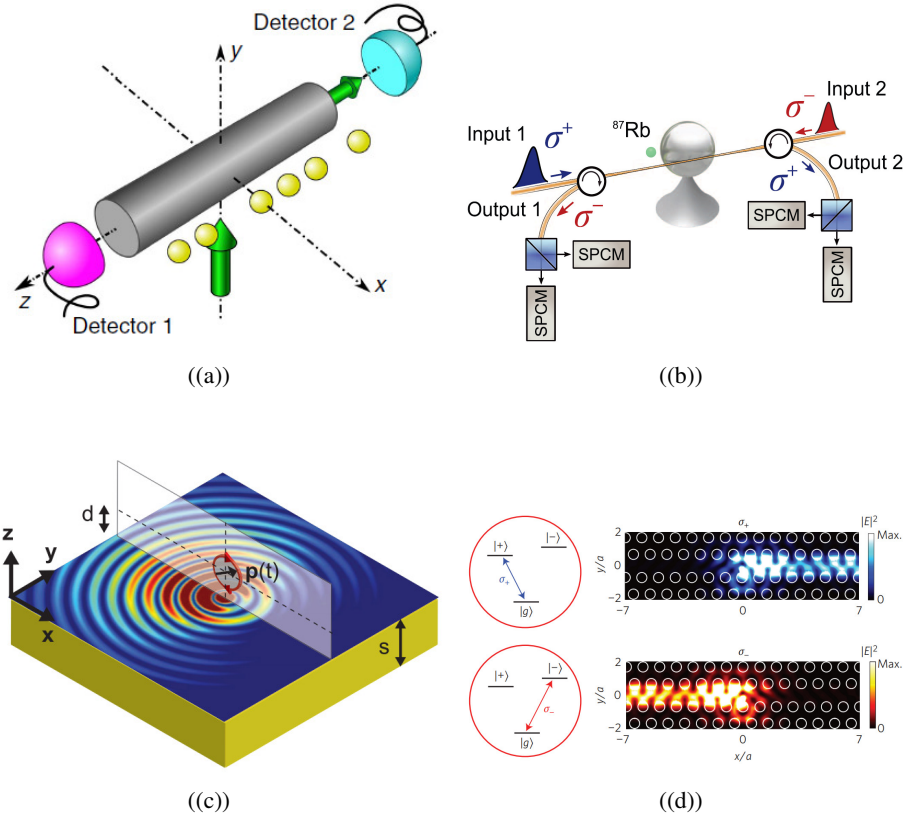


Figure 1.1: Experimental platforms for the investigation of near-field and evanescent local interactions. (a) Cold caesium atoms interacting with the local field of an optical fiber (image taken from [16]). (b) Local interaction between a single Rb atom and a spherical resonator allows an all-optical routing with single photons used as switches (image taken from [17]) (c) Local interaction between a circularly-polarized dipole and the spin of the surface plasmon polaritons in a metal lead to unidirectional coupling to the SPPs (image taken from [18]) (d) Interaction between the transitions in a quantum dot (QD) and the local spin of the photonic modes lead to unidirectional propagation of modes along the photonic waveguide (image taken from [19]).

modes of the resonator is responsible for this unidirectional behaviour [22]. In Ref. [17], authors have shown that this setup can be used as an optical routing mechanism where by triggering the Rb atom with single photons the photons propagating in the fiber can be directed controllably in the optical network.

Figures 1.1(c) and 1.1(d) demonstrate observation of these phenomena in 2D geometries. In Fig. 1.1(c) a circularly polarized dipole couples unidirectionally to the SPPs. Similar to the cylindrical and spherical structures discussed above, here also the local spin of the SPPs is the key factor in coupling to the spin of radiation from the source [18]. This is also clearly observed in the 2D photonic structure of Fig. 1.1(d) where a QD with  $\sigma^+$

and  $\sigma^-$  transitions is placed in vicinity of a photonic structure. By breaking the symmetry between the  $\sigma+$  and  $\sigma^-$  transitions with the use of an external magnetic field, these two oppositely-polarized transitions can be selectively coupled to the photonic structure. Again the local spin of the surface waveguide modes of the photonic structure determines whether the left-propagating or right-propagating modes are excited depending on the transition in the QD [19].

These studies show the importance of the local angular momentum properties in electrodynamics. These phenomena are only observed in near-field interactions where the resonator or the waveguide is placed in the near-field region of the source. These structures propose a variety of platforms for the study of local dynamics of angular momentum in light-matter interactions. This field of study is at its infancy where only the first evidences of local angular momentum interactions are manifested. Future developments can shed light on the details of the local interactions in terms of the dynamics of angular momentum.

The observations in the field of magnetometry with ODMR, ESR, and MOKE experiments, as well as the light-matter interaction experiments through evanescent and near-field couplings mentioned above, herald the progress of the field of spin photonics and its importance in building the next generation of experiments, instrumentation, and computational devices. These experiments show that near-field light-matter interactions can give rise to effects that are not observed in the cavity-based light-matter interactions where the quantum source interacts with the optical field only through the far-field free photons. As opposed to spintronics, which is the study and control of spin of electronic currents using magnetic fields, spin photonics provides more flexibility and speed through the manipulation of electronic spin using lasers and other optical fields. At the same time, the photonic and electronic components can be easily integrated into chips using current technologies.

Given these observations, we believe that the study of angular momentum in light-matter interacting systems, specialized to the near-field couplings, can shed light on the nature of these interactions and propose new possibilities for the field of spin photonics. From manipulation of decoherence time through interaction with evanescent electromagnetic fields [23] to manipulation of selection rules through evanescent interactions [24] (see section 7.2.4), study of near-field light-matter interaction provides new insight and proposes alternative solutions for spin photonic applications.

## 1.3 Fundamental Aspects

From a fundamental point of view, Emmy Noether showed that corresponding to any given symmetry of a system, there exists a conservation law and a conserved (time-independent) quantity [25]. Conservation of angular momentum corresponds to the rotational symmetry of a given system and is mathematically described as no change in the Lagrangian of the system as a result of an arbitrary rotation transformation. Lagrangian is a fundamental property of any theory, classically defined as kinetic energy minus the potential energy. The equations of motion for a given system are found by minimizing the integral of the Lagrangian density over the entire space (named action), over all possible distributions of solutions.

In the present work, we start our study by a fundamental treatment of angular momentum using the Noether's theorem and the quantum electrodynamics Lagrangian. Our major goal is to investigate the role of angular momentum in various optical, electronic, and light-matter interaction systems, with special attention to the evanescent and near-field properties of the fields. As we will see, other important features emerge as a result of this pursuit which show the universality of some of the effects related to near-field interactions.

Before presenting our contributions in this field, we find it necessary to address some fundamental aspect discussed so far. These clarifications are necessary for a true understanding of our results.

### 1.3.1 Relativistic vs. Non-relativistic

Quantum mechanical equations are traditionally derived from the classical equations of motion by the standard method of canonical quantization. In this method, observables are replaced by operators through which the Hamiltonian of the system is found. Hamiltonian is essentially the time-evolution operator of the system whose eigenvalues, when acted on the eigenvectors, give the energy of the system.

If the standard quantization is performed on the classical energy of the system,

$$E = \frac{\mathbf{p}^2}{2m} + V(\mathbf{r}, t), \quad (1.1)$$

where the first term is the kinetic energy with  $\mathbf{p}$  being the momentum and  $m$  mass of the particle and the second term potential energy, we find the Schrodinger's equation, written as

$$i\hbar \frac{\partial}{\partial t} \psi(\mathbf{r}, t) = \left[ -\frac{\hbar^2}{2m} \nabla^2 + V(\mathbf{r}, t) \right] \psi(\mathbf{r}, t). \quad (1.2)$$

In this equation, the wave function  $\psi(\mathbf{r}, t)$  is a scalar function and thus does not include the spin. Moreover, it does not correctly capture the motion of particles at relativistic energies. Due to these shortcomings, corrections are usually added to this equation to include relativistic and angular-momentum-related effects. These corrections are usually derived by approximating the relativistic quantum mechanical equation of motion.

Paul Dirac showed that, by quantizing the relativistic energy equation,

$$E = \sqrt{\mathbf{p}^2 c^2 + m^2 c^4}, \quad (1.3)$$

with  $c$  being the speed of light, relativistic quantum mechanical Hamiltonian can be found. Due to the presence of the square root in Eq. 1.3, Dirac showed that the linear Hamiltonian equation can be found by introducing the matrix equation,

$$i\hbar \frac{\partial}{\partial t} \psi(\mathbf{r}, t) = [-i\hbar c \boldsymbol{\alpha} \cdot \nabla + \beta m c^2] \psi(\mathbf{r}, t). \quad (1.4)$$

Here,  $\boldsymbol{\alpha}$  and  $\beta$  are  $4 \times 4$  matrices (see Appendix C) and, unlike Schrodinger's equation, the wave functions  $\psi(\mathbf{r}, t)$  is a 4-component vector called *bi-spinor*. Famously called 'Dirac equation', Eq. (1.4) naturally includes the spin property of the fields due to the bi-spinor nature of the wave function and correctly describes many of the higher energy phenomena in AMO and high energy physics. Moreover, it is important to note that the Dirac equation is Lorentz invariant; a property that is essential when discussing the rotational symmetries of the equations, as discussed in chapter 2.

Due to the fact that spin naturally emerges in the Dirac equation, and since it is Lorentz invariant, we incorporate the Dirac equation in our study since it is aligned with our goal of study of angular momentum dynamics in light-matter interactions.

### 1.3.2 Gauge Invariance

Gauge invariance expresses a mathematical freedom in choosing the fields that represent the same physical observables. This feature arises in many field theories and states that physical observables associated with the system should not change as a result of this freedom. For instance, in the electromagnetic theory, due to the fact that the magnetic field is divergenceless  $\nabla \cdot \mathbf{B} = 0$ , it can be written in terms another vector field, named electromagnetic vector potential  $\mathbf{A}$ , as,

$$\mathbf{B} = \nabla \times \mathbf{A}. \quad (1.5)$$

Also, using the Maxwell's equation  $\nabla \times \mathbf{E} = -\partial\mathbf{B}/\partial t$ , the electric field can be written in terms of the vector and scalar potentials,  $\mathbf{A}$  and  $\phi$ , as

$$\mathbf{E} = -\frac{\partial\mathbf{A}}{\partial t} - \nabla\phi. \quad (1.6)$$

While  $\mathbf{E}$  and  $\mathbf{B}$  are unique, observable, and physical quantities, the scalar and vector potentials  $\phi$  and  $\mathbf{A}$  clearly are not since under the transformation

$$\mathbf{A} \rightarrow \mathbf{A} + \nabla\Lambda, \quad \phi \rightarrow \phi - \frac{\partial\Lambda}{\partial t}, \quad (1.7)$$

for an arbitrary differentiable function  $\Lambda$ , the electric and magnetic fields in Eqs. (1.5) and (1.6) remain unchanged. The transformation in Eq. (1.7) is called a gauge transformation and corresponds to the mathematical freedom in choosing a gauge for the electromagnetic potentials by setting some restrictions on the potentials  $\mathbf{A}$  and  $\phi$ . These restrictions are usually chosen based on convenience in the underlying problem and do not have any physical significance. Examples of these fixing conditions (called gauges) in electromagnetic theory are Coulomb gauge which defines  $\nabla \cdot \mathbf{A} = 0$ , and Lorenz gauge which sets  $\nabla \cdot \mathbf{A} + \frac{1}{c^2} \frac{\partial\phi}{\partial t} = 0$ .

It should be pointed out that the mathematical description of physical observables of the system such as electric field, magnetic field, and charged currents cannot change as a result of this freedom. Since this is a mathematical freedom, quantities that change with the change of the chosen gauge are considered nonphysical. A quantity is said to be gauge-invariant or gauge-independent if the mathematical form of the quantity does not change as a result of a change in the chosen gauge. Since the quantum electrodynamic Lagrangian employed in chapter 2 is a theory with gauge freedom, in our discussion of conservation of angular momentum of light-matter interactions it is essential to define gauge-independent quantities in order to obtain physically meaningful observables.

### 1.3.3 Quantum vs. Classical

With regards to the electromagnetic radiation, classical fields are defined solely by the time- and space-dependent electric and magnetic fields defined through the Maxwell's equations,

$$\nabla \times \mathbf{E} = -\frac{\partial\mathbf{B}}{\partial t} \quad (1.8a)$$

$$\nabla \times \mathbf{B} = \frac{1}{c^2} \frac{\partial\mathbf{E}}{\partial t} + \mu_0\mathbf{J} \quad (1.8b)$$

$$\nabla \cdot \mathbf{B} = 0 \quad (1.8c)$$

$$\nabla \cdot \mathbf{E} = \frac{\rho}{\epsilon_0} \quad (1.8d)$$

where  $\epsilon_0$  and  $\mu_0$  are the vacuum permittivity and permeability, respectively, and  $\rho$  and  $\mathbf{J}$  are the free charges and free currents. The total electromagnetic energy density is defined through the sum of the squares of the electric and magnetic fields. The electromagnetic oscillations are considered quantized when each oscillation is modeled by a harmonic oscillator. Also considered as second quantization, in this case the energy comes in quanta of energy called photons where the energy of each photon is written famously as  $\hbar\omega$ , with  $\omega$  being the frequency of oscillation of the photon.

In the quantum electromagnetism, electric and magnetic fields become field operators and can be described as a quantum superposition of quantum states with  $n$  number of photons  $|n\rangle$ , also known as Fock states [26]. This quantization method, however, is well-developed to apply to the free electromagnetic radiations, implemented commonly by laser cavities. This method faces challenges when applied to the evanescent (decaying) electromagnetic field and near-fields. This is because these fields are represented by longitudinal and scalar photons, which are not physical since they are gauge-dependent, and a physical quantized number state for these photons cannot be written [27, 28]. Due to these challenges, in this study, we only focus on the 'classical' representation of electromagnetic fields in the sense that no second quantization is performed on the fields. However, in the study of light-matter interactions, the Dirac equation is used which is a quantum relativistic equation as explained below.

In studying the matter fields, the classical Newtonian or relativistic equations are quantized using the canonical quantization method where the momentum and energy quantities are replaced by operators that act on the wave function, as explained in section 1.3.1. These equations and wave functions specify the distribution of quantum state of the system. Even without performing the second quantization, quantum effects are still present due to the fact that canonical observables such as momentum and energy are non-commutative and thus follow the Heisenberg uncertainty principle which is a quantum mechanical phenomenon. Performing second quantization on these matter fields would give rise to the quanta of the fields called particles. In our study in chapters 2 and 4, no second quantization is performed on the quantum fields and only the relativistic quantum equation of the Dirac field is employed.

The study of angular momentum in second-quantized quantum electrodynamics requires a thorough and careful investigation of quantized electromagnetic fields, Dirac fields, and their interaction and is of great interest to high-energy physics. This research, however, is out of the scope of the current study and will be the focus of a future work.

### 1.3.4 Spin Statistics

Spin statistics studies the collective behaviour of fundamental particles. Depending on the type of behaviour, particles can be divided into two groups of fermions and bosons. Fermions follow the Pauli exclusion principle which states that no two identical fermions can occupy the same quantum state. On the other hand, bosons follow a different statistics which states that unlimited number of indistinguishable bosons can occupy the same quantum state. This is mathematically equivalent to stating that, under the exchange of particles, the fermionic wave function is antisymmetric while the bosonic one is symmetric, or,

$$\psi(k_1, k_2) \rightarrow \pm\psi(k_2, k_1) \quad (1.9)$$

where the first and second place in the argument of the wave function refer to the first and second particles, respectively, and  $k_1$  and  $k_2$  refer to two different quantum numbers. In Eq. (1.9), the plus sign refers to bosons since it is symmetric with respect to exchange, while the minus sign refers to fermions. It is evident that, by setting  $k_1 = k_2$ , the fermionic wave function (the one with negative sign) becomes zero, indicating that two identical fermions cannot occupy the same quantum state.

This collective behaviour of fermions and bosons is directly linked to the spin properties of these particles. Fermions are known to have half-integer spins while bosons are identified by integer spins. Since the symmetry of the wave function of fermions or bosons is directly linked to the spin of these particles, the collective behaviour of them is termed spin statistics.

The connection between the half-integer spin and the antisymmetric properties of the fermionic field can be naively explained by the fact that, for the second quantized Dirac solutions to be causal (Lorentz invariant) with positive-definite energies, the fields should be antisymmetric. Since Dirac fields manifestly describe half-integer particles only, the half-integer spin and antisymmetry of the fields are only satisfied simultaneously [29]. For bosonic fields of Maxwell's equations, on the other hand, a symmetric wave function is necessary for the second quantized fields in order to obtain positive energies. Since Maxwell's equations represent massless spin-1 particles [30], the symmetry of the wave function and spin-1 properties are satisfied simultaneously.

Obviously, these reasonings only apply to the fields of the Dirac equation and Maxwell's equations and do not fully prove the direct connection between the spin and symmetry properties of the wave function of fundamental particles. A general and robust proof has proven to be more challenging [31]. Note that the collective behaviour of bosons and fermions is not the focus of this thesis. However, an overall understanding of the fundamental differ-

ences between these two particle types is important in discerning between the fundamental spin properties and geometrical or structural field properties. In this work, we will study both the fermionic fields of the Dirac equation and the bosonic fields of Maxwell's equations separately and together. We show that, despite their fundamental differences, these fields can exhibit analogous angular momentum properties.

### **1.3.5 Near-Field, Far-field, and Evanescent**

Throughout this work, we will refer to these terms frequently in discussing different forms of electromagnetic interactions. While the terms near-field and far-field are specifically defined with respect to the distance from the current sources in electromagnetic theory, evanescent fields are the property of individual fields (apart from interactions) that can be manifested in all types of fields, including Maxwell and Dirac fields.

Near-field and far-field are defined according to the distance, with respect to the wavelengths, from the current sources. Although they have clear definitions [32], it is enough for the purpose of our study to know that far-field starts about a few wavelengths away from the source, while near-field is used for sub-wavelength distances.

Evanescent field, on the other hand, is the decaying property in the fields which can be created for purely optical or electronic fields. These fields are known by having an imaginary momentum number and are usually formed at the boundary between two media with different properties. For instance, in optical fibers, evanescent fields from outside of the fiber due to total internal reflection of light inside the fiber. To satisfy the boundary condition at the interface between the materials with different dielectric permittivities, the field outside of the core of the fiber (the region called cladding) is non-zero and can be shown to decay exponentially into the surroundings. SPPs have a similar signature which are created at the boundary of metals and vacuum. As discussed in section 1.2, these fields have found a myriad of applications in nanophotonics as well as condensed matter physics.

In the present work, these terms are frequently used since the focus is the local and near-field light-matter interactions.

### **1.3.6 Duality Symmetry and its Limitations**

Duality symmetry is a series of works by K. Bliokh [33], S. Barnett [34], M. Berry [35], and G. Molina-Terriza [36], where by writing the Maxwell's equations Lagrangian in a dual symmetric form and application of Noether's theorem, conservation equation for helicity of light is found. The duality symmetry refers to the symmetry property of the source-free

Maxwell's equation where upon the transformation,

$$\begin{aligned} \mathbf{E} &\rightarrow \mathbf{E} \cos \theta - \mathbf{H} \sin \theta \\ \mathbf{H} &\rightarrow \mathbf{E} \sin \theta + \mathbf{H} \cos \theta, \end{aligned} \tag{1.10}$$

Maxwell's equations remain unchanged for an arbitrary value of  $\theta$  [36]. Dual symmetric form of the electromagnetic Lagrangian is thus written such that this symmetry is evidently satisfied by adding to the free electromagnetic Lagrangian  $\frac{1}{4}F_{\mu\nu}F^{\mu\nu}$ , with  $F_{\mu\nu} = \partial_\mu A_\nu - \partial_\nu A_\mu$ , a secondary term,  $G_{\mu\nu}G^{\mu\nu}$  [33], where  $G_{\mu\nu} = \partial_\mu C_\nu - \partial_\nu C_\mu$  introduces a new vector potential  $C_\mu$  proportional to the curl of the electric field.

Application of Noether's theorem gives rise to the conservation of dual symmetric helicity of the free electromagnetic fields. Being defined as the projection of spin of a particular field along its momentum, helicity is a scalar quantity indicating the handedness of a particle as it propagates. It is written, in its dual symmetric form, for free electromagnetic fields as [33],

$$h = \mathbf{A} \cdot \mathbf{B} - \mathbf{C} \cdot \mathbf{E}. \tag{1.11}$$

While this quantity is conserved according to the Maxwell's equations, it introduces a new vector potential  $\mathbf{C}$  which does not have any physical significance. Since a new gauge field introduces fundamental problems into the masslessness of Maxwell's equations [37, 38], this new quantity cannot be an independent gauge field and is solely a mathematical choice.

Although conservation of the dual symmetric helicity defined in Eq. (1.11) is not mathematically incorrect, it is not a testable and physically significant conservation equation since it only applies to the source-free Maxwell's equations. In fact, as was shown by D. Lipkin [39], there are many of such conserved quantities for the source-free Maxwell's equations. Testing this conservation equation requires introduction of a localized matter-based probe which would convert the angular momentum of light into physical or electronic angular momentum for observation. Such a probe, however, would introduce an external or induced charged current into the system and would immediately break the source-free condition of Maxwell's equation and thus the dual symmetry condition of the Lagrangian would no longer hold.

In our approach towards the fundamental study of spin electrodynamics in light-matter interactions in chapter 2, however, we have employed the QED Lagrangian which gives the relativistic Dirac and Maxwell equations of motion. Unlike the duality symmetry discussed above, our study is quantum mechanical, relativistic, applies to light-matter interactions, and it does not introduce a new gauge field. In fact, as shown in section 2.3, the helicity

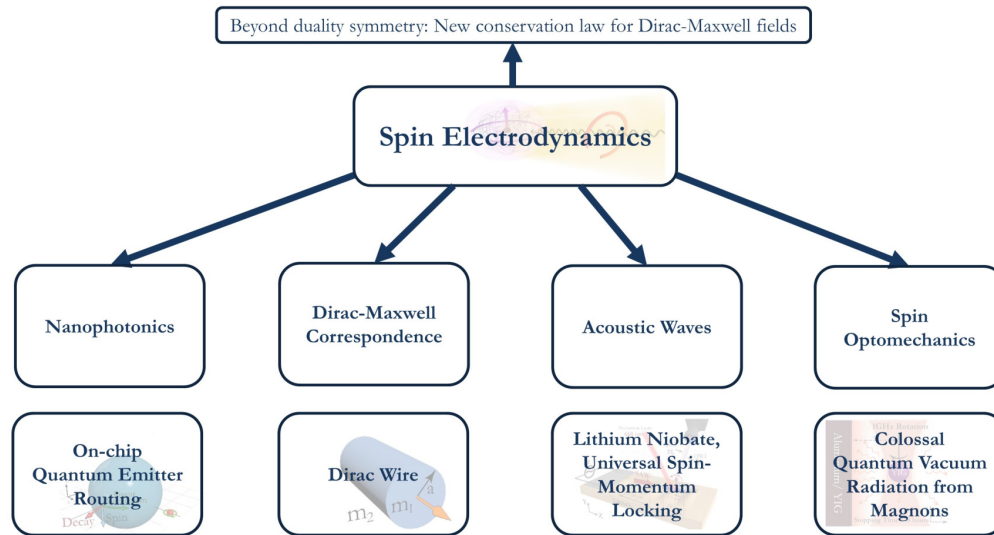


Figure 1.2: Overall structure of the thesis. Chapter 2 discusses our fundamental approach towards the spin electrodynamics by deriving a new conservation law of angular momentum. This general topic encompasses the next four chapters of the thesis where we have discussed the implications of spin electrodynamics in four particular problems. Chapter 3 discusses a nanophotonic structure where we have shown the role of angular momentum in on-chip quantum emitter routing. Chapter 4 discusses Dirac-Maxwell correspondence where we have studied the similarities between the solutions of Dirac equation in cylindrical geometry and optical fiber. Chapter 5 investigates the spin properties in the acoustic waves propagating on the surface of lithium niobate. In chapter 6 the implications of spin optomechanics for quantum vacuum radiation and quantum vacuum torque has been studied.

density appears in our conservation of angular momentum equations in its original form  $\mathbf{A} \cdot \mathbf{B}$ . As a result, our conservation equation has important physical significance since it is fundamentally testable. Moreover, our theory introduces new terms that become important in near-field light-matter interactions.

## 1.4 Summary of Contributions

Given these prominent observations regarding the angular momentum in optical and electronic fields, the importance of a deeper approach towards light-matter interacting systems, especially for fields interacting in near-fields, becomes essential. This approach is important in advancing the fields of quantum metrology, quantum computing, light-matter interacting systems, and spin photonics.

Figure 1.2 shows an overall picture of our contributions in this work. We present our

first contribution in chapter 2 related to the field of spin electrodynamics. This chapter takes a fundamental approach towards angular momentum through the application of Noether's theorem to the relativistic Dirac equation interacting with the electromagnetic field. In this approach, starting from the quantum electrodynamics Lagrangian, we derive a gauge-independent conservation equation which constitutes the contribution of Dirac and Maxwell's fields to the total angular momentum. More importantly, we derive a local (for every point in space) conservation equation and introduce new terms responsible for the transfer of angular momentum between different fields and different locations in space. This method defines rigorous, gauge-independent, and observable quantities for the angular momentum of the Dirac and Maxwell fields and connects them to other concepts encountered in spin electrodynamics such as chirality, helicity, spin current, and orbital angular momentum (OAM) current.

It is important to note that our work is beyond the duality symmetry discussed above. Being applicable to light-matter interaction, our conservation equation is fundamentally testable and does not introduce new non-physical gauge fields into the theory. It is also more fundamental since it puts well-known angular momentum related terms of optical and electronic fields such as spin, orbital angular momentum, helicity, and chirality, together with new terms such as angular momentum current tensor, into one master conservation equation for the angular momentum. Our results can be extended to gain insight into the role of angular momentum in high-energy physics, quantum photonics, as well as condensed matter physics.

Following a thorough understanding of the mathematical structure of angular momentum, we investigate the role of angular momentum in four different systems all falling under the larger scope of spin electrodynamics. In chapter 3, we study the role of angular momentum in nanophotonics systems by studying a quantum source interacting with the local spin of evanescent electromagnetic fields. In this system, a quantum source, modeled by a circularly-polarized dipole, is placed in vicinity of a spherical resonator. We show that, through the interaction between the spin of the radiation and the local optical spin of the resonator, resonant modes of the sphere are excited non-symmetrically giving rise to modes with only positive (or negative) OAM.

In chapter 4, we investigate the Dirac-Maxwell correspondence – the study of similarities between the Dirac and Maxwell's equations – by studying the local angular momentum in the Dirac equation. We particularly focus on the confined geometry of a cylindrical wire to study the evanescent nature of Dirac fields. This geometry, called Dirac Wire, is the

electronic analogue of an optical fiber where different properties of material inside and outside of the cylinder gives rise to confined solutions inside of the wire. We show that, as a result of confinement down to the Compton wavelength, a deterministic (not bound to the uncertainty principle) longitudinal spin component emerges which is exclusive to the confined geometry. We have taken this study a step further by looking at the case when the Dirac equation is topologically non-trivial by substituting for the mass term a quadratic momentum dependent mass, creating a simple topological insulator model. It is shown that, in addition to the presence of the longitudinal angular momentum component, topological insulators can manifest other interesting features that are not present in bulk structures.

Chapter 5 is a brief discussion of the local properties of angular momentum in surface acoustic waves (SAWs). Fundamentally mechanical oscillations, SAWs are generated on the surface of a crystal by the application of an RF signal to a transducer which converts the electrical energy into mechanical waves. By solving the equations of motion for a piezoelectric material, we show that SAWs also show angular momentum related phenomena observed in photonic and electronic systems such as spin-momentum locking.

In chapter 6 we investigate the implications of spin optomechanics for quantum vacuum radiation and quantum vacuum torque by studying a spinning magnetic nanoparticle in the vicinity of a metallic or magnetic material. We show that, due to the near-field coupling between the magnetic dipoles in the spinning nanoparticle and the evanescent surface modes of the metallic or magnetic interface, a large quantum vacuum radiation is observed. This system converts the mechanical rotational energy into the electromagnetic radiation, more efficiently compared to other non-magnetic nanoparticles, and magnifies the number of photons emitted due to quantum vacuum fluctuations. Our results show that this system leads to experimentally observable outcomes due to quantum vacuum radiation which is a breakthrough in the experimental detection of such radiations. Although the angular momentum properties of the radiated quantum vacuum radiation has not been investigated, this chapter signifies the importance of evanescent coupling in nanophotonic structures as well as the role of mechanical angular momentum in creating such effects.

Finally, we present our concluding remarks in chapter 7. Furthermore, we propose a few research topics with regards to the directions that this work can take in the future endeavors.

## Chapter 2

# Universal Angular Momentum Conservation Laws for Dirac-Maxwell Fields

Global conservation laws of angular momentum for light-matter interactions are well-known. However, local conservation laws, describing the conservation law of angular momentum at every point in space, remain unexplored. With recent advances in the cold atom and quantum dot communities, local interactions between atomic sources and optical fields are gaining more attention due to the emergent new phenomena. These experiments emphasize the need for a local conservation law describing the dynamics of angular momentum in light-matter interactions. Here, we use the quantum electrodynamics (QED) Lagrangian and Noether's theorem to derive a new local conservation law of angular momentum for Dirac-Maxwell fields. The explicit inclusion of Dirac field, unambiguously clarifies the interpretation of corresponding Maxwell field properties such as helicity, spin, and orbital angular momentum (OAM). In addition, with the definition of new terms such as *helicity current tensor* and *OAM current tensor*, we shed light on the local dynamics of angular momentum. We also present the vector *spin-orbit torque* as being the torque exerted on spin and OAM of the fields as a result of spin-orbit coupling. We evaluate the local conservation law for the EM spin for the interference of two plane waves as well as a dual-mode optical fiber and show that they hold locally. Our results can have important implications for phenomena related to the spin of gauge bosons.

### 2.1 Introduction

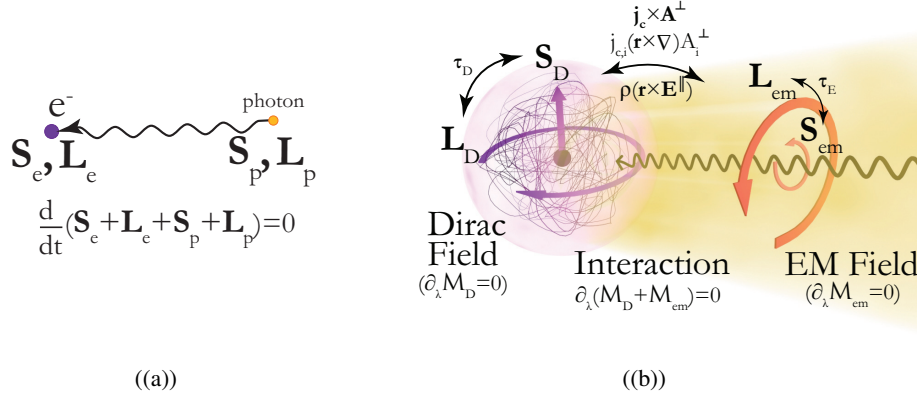
The interaction between the electronic spin and optical angular momentum has been widely used in devices such as optical circulators, insulators, electro-optic modulators, and Fara-

day rotators. In these devices, conservation of angular momentum combined with the field properties of the electromagnetic (EM) radiation gives rise to non-reciprocal effects that can be manipulated for a wide variety of applications. These devices incorporate the interaction between EM radiation and the magnetic materials in the far-field regions where a conservation law based on the total electronic and photonic angular momenta suffices to explain the underlying physical phenomena [40].

Due to the possibility of optical control of the quantum spin states, the dynamics of angular momentum between the electronic and optical fields has recently gained attention for the systems interacting in the near-field region. Coupling to the local spin of EM field has been observed for cold atoms in the vicinity of an optical fiber [16], magnons interacting with spherical whispering gallery modes (WGMs) [41], quantum dots in photonic crystals [42], as well as quantum sources coupling to other waveguide systems [19, 43, 44]. In such systems, since the interaction between the source and the EM field occurs in the near-field rather than the far-field regions, a local approach to the governing dynamical equations of angular momentum becomes important. These studies reveal the new insight that the local interaction with classical electromagnetic field has to offer. Moreover, we can see that the conservation of total angular momentum (Fig. 2.1(a)) may not fully capture the physics of the interacting systems. Therefore, a more comprehensive, gauge-independent, locally applicable conservation equation becomes essential in understanding the microscopic dynamics of the angular momentum (Fig. 2.1(b)).

The local approach towards field quantities such as helicity, chirality, and angular momentum has proven useful in the study of conservation laws as well as geometrical properties of EM fields [33–35, 44–47]. However, the procedure employed in these derivations is based on the dual symmetry of the source-free EM Lagrangian. Since the dual symmetry is only maintained in source-free regions, this form of Lagrangian neglects any form of interaction with fermionic fields and cannot be employed to present a local conservation law for the angular momentum of electrodynamics. These properties are captured in the manifestly covariant construction of the Dirac equation [48].

Connections between the fermionic field of the Dirac equation and the bosonic fields of Maxwell's equations is the focus of Dirac-Maxwell correspondence where the relativistic parallels between photons and electrons are studied [49, 50]. These studies show that, although different in nature, electronic and electromagnetic fields can exhibit many analogous properties. This correspondence is evident in phenomena such as spin-momentum locking which emerges in the Dirac equation [51] as well as the Maxwell's equations [52, 53].



quantity type	scalar	vector			tensor	
quantity	chirality & helicity	spin angular momentum	orbital angular momentum	spin-orbit torque	helicity current	orbital angular momentum current
Dirac Field	$\frac{\hbar}{2} \psi^\dagger \boldsymbol{\gamma} \psi$	$\frac{\hbar}{2} \psi^\dagger \boldsymbol{\Sigma} \psi$	$\mathcal{R} \{ \psi^\dagger (\mathbf{r} \times \mathbf{p}_\parallel) \psi \}$	$-c \mathcal{R} \{ \psi (\boldsymbol{\gamma} \times \mathbf{p}_\parallel) \psi \}$	0	$\mathcal{R} \{ \psi \gamma_i (\mathbf{r} \times \mathbf{p}_\parallel)_j \psi \}$
Maxwell Field	$\frac{1}{\mu_0 c} (\mathbf{A}^\perp \cdot \mathbf{B})$	$\epsilon_0 (\mathbf{E}^\perp \times \mathbf{A}^\perp)$	$\epsilon_0 [E_i^\perp (\mathbf{r} \times \nabla)_i A_i^\perp]$	$\frac{1}{\mu_0} (\mathbf{B} \cdot \nabla) \mathbf{A}^\perp$ $-\epsilon_0 \left( \frac{\partial \mathbf{E}^\parallel}{\partial t} \times \mathbf{A}^\perp \right)$	$-\frac{1}{\mu_0} (A_i^\perp B_j)$	$-\frac{1}{\mu_0} [\epsilon_{ikl} B_k (\mathbf{r} \times \nabla)_j A_l^\perp]$ $-\epsilon_0 A_i^\perp \left( \mathbf{r} \times \frac{\partial \mathbf{E}^\parallel}{\partial t} \right)_j$

(c)

Figure 2.1: Conservation laws of angular momentum in light-matter interacting systems (a) conventional conservation of global total photonic and electronic angular momentum. This conservation law applies to closed systems and does not include angular momentum exchange due to near-field interactions. (b) Local conservation of angular momentum applicable to all regions of interaction. The conventional conservation of sum of angular momenta is replaced by the conservation Eq. (2.6). (c) Table of quantities defined in this chapter, representing the spatial and temporal densities of the scalar, vector, or tensor observables pertinent to angular momentum. Highlighted quantities are the new terms defined in this chapter. The local conservation of angular momentum equation (Eq. (2.6)) connects the well-known terms such as spin density, OAM density, helicity and chirality to these newly defined quantities.

In this chapter, we study the Lorentz symmetry of the Dirac Lagrangian with the  $U(1)$  gauge symmetry [54]. With the application of Noether's theorem [25], we find the local conservation laws pertinent to the angular momentum of the interacting fields. We show that, in the near-field, the electronic angular momentum can be transferred not only to the optical angular momentum, but also to other field quantities that represent angular momentum current [55]. These extra terms include electromagnetic helicity density [56], fermionic chirality density [48], electromagnetic *helicity current tensor*, as well as the electromagnetic and electronic *orbital angular momentum (OAM) current tensors*. We further study these conservation laws and angular-momentum-carrying terms for the fully electromagnetic solutions of a dual-mode optical fiber.

The application of Noether's theorem to the Dirac Lagrangian has been used in the Quantum Chromodynamics (QCD) and Quantum Electrodynamics (QED) communities to

derive the expressions for the angular momentum of the nuclei and the gauge fields [57, 58]. In QCD and QED interactions, conservation of the total integrated angular momentum suffices to describe the angular momentum transfer in scattering processes. In nanophotonic and condensed matter systems, however, atoms can interact locally with an external EM field. Therefore, for such systems, a local conservation equation for the angular momentum density is necessary in the realization of naonscale applications.

This work, furthermore, can be extended to the quantized electromagnetic and Dirac fields. Long-standing challenges with regard to the spin of the quantized massless gauge fields has prevented the community from reaching a consensus over a physical definition of the spin operator of photons and gluons in QED and QCD [57–59]. These challenges arise in the search for a quantum spin operator of the gauge fields such that they are simultaneously physically observable (gauge-invariant) and satisfy the canonical commutation relations of rotation operators [60]. In Ref. [28], we have shown that the application of Noether’s theorem, together with a careful gauge-treatment of the QED Lagrangian, sheds light on the nature of these controversies and alleviates the challenges regarding the quantum spin operator of photons.

## 2.2 Noether’s theorem, QED Lagrangian, and Lorentz transformation

We start with the real (also called symmetrized) Lagrangian density of a Dirac field coupled to EM field [61],

$$\mathcal{L} = \bar{\psi} \left[ c\gamma^\mu \left( \frac{1}{2} i\hbar \overleftrightarrow{\partial}_\mu - eA_\mu \right) - mc^2 \right] \psi - \frac{1}{4\mu_0} F_{\mu\nu} F^{\mu\nu}, \quad (2.1)$$

where  $\bar{\psi} = \psi^\dagger \gamma^0$  and  $\gamma^\mu$  are the gamma matrices,  $F_{\mu\nu}$  the electromagnetic tensor,  $A_\mu = (\phi/c, -\mathbf{A})$  the electromagnetic four-potential,  $\psi$  Dirac fields,  $\hbar$  Planck’s constant, and  $\mu_0$  the vacuum permeability. Note that summation over repeated indices is assumed throughout this chapter. By applying Noether’s theorem [25], we obtain the conserved current for the given Lagrangian of Eq. (2.1) by finding,

$$\mathcal{M}^\lambda = \frac{\partial \mathcal{L}}{\partial(\partial_\lambda \psi)} \delta \psi + \delta \bar{\psi} \frac{\partial \mathcal{L}}{\partial(\partial_\lambda \bar{\psi})} + \frac{\partial \mathcal{L}}{\partial(\partial_\lambda A^\mu)} \delta A^\mu + \mathcal{L} \delta x^\lambda. \quad (2.2)$$

Lorentz transformations are defined as the coordinate transformations such that the coordinates transform as  $x^\mu \rightarrow \Lambda^\mu{}_\nu x^\nu$ , with

$$\Lambda^\mu{}_\nu = e^{-\frac{i}{2} \omega_{\kappa\sigma} (\hat{S}^{\kappa\sigma})^\mu{}_\nu}, \quad (2.3)$$

where  $(\hat{S}^{\kappa\sigma})^\mu{}_\nu = i(\eta^{\kappa\mu}\eta^\sigma{}_\nu - \eta^{\sigma\mu}\eta^\kappa{}_\nu)$  are the generators of rotation and boost in the four-dimensional real space [62] and  $\omega_{\kappa\sigma}$  are the rotation and boost parameters. It can be shown that, under the Lorentz transformation of Eq. (2.3), the Maxwell and Dirac fields change as,

$$\delta A^\mu(x) = -\frac{i}{2}\omega_{\kappa\sigma}(\hat{M}_{\text{em}}^{\kappa\sigma})^\mu{}_\nu, \quad \delta\psi(x) = -\frac{i}{2}\omega_{\mu\nu}\hat{M}_{\text{D}}^{\mu\nu}\psi(x) \quad (2.4)$$

where  $\hat{M}_{\text{em}}$  and  $\hat{M}_{\text{D}}$  are the angular momentum operators of the Dirac and Maxwell's fields, respectively. These operators are defined in Appendix A.1. Specializing to the rotations ( $\mu, \nu = i, j = 1, 2, 3$ ), we obtain the general continuity equation associated with rotational symmetry of the QED Lagrangian [62],

$$\partial_\lambda \mathcal{M}^{ij,\lambda} = \partial_\lambda \left( \mathcal{S}_{\text{D}}^{ij,\lambda} + \mathcal{L}_{\text{D}}^{ij,\lambda} + \mathcal{S}_{\text{em}}^{ij,\lambda} + \mathcal{L}_{\text{em}}^{ij,\lambda} \right) = 0, \quad (2.5)$$

where  $\mathcal{M}^{ij,\lambda}$  is the total angular current tensor. This tensor can be split into spin  $\mathcal{S}_{\text{D(em)}}^{ij,\lambda}$  (related to the rotation of the internal degrees of freedom) and OAM  $\mathcal{L}_{\text{D(em)}}^{ij,\lambda}$  (related to the coordinate dependence of the fields) parts of the Dirac and EM fields, respectively (Fig. 2.1). For non-interacting fields, we obtain separate continuity equations for the Dirac and EM fields. Note that the roman indices take the values  $i, j = 1, 2, 3$  while the Greek indices are  $\lambda = 0, 1, 2, 3$ .

The time-components ( $\lambda = 0$ ) of these four angular momentum tensors give the common spin and OAM densities for the Dirac and EM fields, which are generally gauge dependent. The electronic part of the spin and OAM respectively are  $\mathcal{S}_{\text{D}}^{ij,0} = \varepsilon_{ijk}\hbar\psi^\dagger\Sigma_k\psi/2$  ( $\varepsilon_{ijk}$  is the Levi-Civita symbol) and  $\mathcal{L}_{\text{D}}^{ij,0} = -i\varepsilon_{ijk}\hbar\mathcal{R}\{\psi^\dagger(\mathbf{r}\times\nabla)_k\psi\}$ , where  $\Sigma$  is the spin operator in Dirac equation and  $\mathcal{R}\{\dots\}$  takes the real part of its argument. The EM part of the spin and OAM, on the other hand, are  $\mathcal{S}_{\text{em}}^{ij,0} = \varepsilon_{ijk}(\epsilon_0\mathbf{E}\times\mathbf{A})_k$  and  $\mathcal{L}_{\text{em}}^{ij,0} = \varepsilon_{ijk}[\epsilon_0 E_l(\mathbf{r}\times\nabla)_k A_l]$ , respectively (see Appendix A), where  $\epsilon_0$  is vacuum permittivity. An important observation is that OAM densities of the Dirac fields as well as the spin and OAM of the EM field are gauge dependent and thus do not represent observable physical quantities in a local frame. In fact, one can see that most of the terms in the angular momentum tensors  $\mathcal{S}_{\text{D(E)}}^{ij,\lambda}$  and  $\mathcal{L}_{\text{D(E)}}^{ij,\lambda}$  are gauge dependent. Due to this problem, we rearrange the expressions in these four tensors to write the conservation law in Eq. (2.5) in terms of gauge-independent and physically observable quantities.

## 2.3 Local conservation law of angular momentum

By splitting the electromagnetic vector potential into transverse and longitudinal parts,  $\mathbf{A} = \mathbf{A}^\perp + \mathbf{A}^\parallel$ , defined as  $\nabla\cdot\mathbf{A}^\perp = 0$  and  $\nabla\times\mathbf{A}^\parallel = 0$  [27], X.-S. Chen *et al* de-

fined the gauge-independent angular momentum densities for both the Dirac field and EM field [58]. However, a gauge-independent form for the continuity equation has not been addressed. Here, following the same approach used in Ref. [58], we obtain a standard (vector) continuity equation for the angular momentum density of the combined system (see Appendix A for more details),

$$\frac{\partial M_j}{\partial t} + \nabla_i T_{ij} = 0 \quad (2.6)$$

where  $M_j$  are the components of the angular momentum density vector, written as

$$\begin{aligned} \mathbf{M} = & \frac{\hbar}{2}(\psi^\dagger \boldsymbol{\Sigma} \psi) + \mathcal{R} \left\{ \psi^\dagger (\mathbf{r} \times \mathbf{p}_{\parallel}) \psi \right\} \\ & + \epsilon_0(\mathbf{E}^\perp \times \mathbf{A}^\perp) + \epsilon_0 \left[ E_i^\perp (\mathbf{r} \times \nabla) A_i^\perp \right], \end{aligned} \quad (2.7)$$

with gauge-independent transverse vector potential  $\mathbf{A}^\perp$  and gauge-independent electron momentum operator  $\mathbf{p}_{\parallel} = (-i\hbar\nabla - e\mathbf{A}^{\parallel})$ . The first two terms in Eq. (2.7) are the spin and OAM densities of the electron, while the last two terms are the gauge-independent spin and OAM densities of the EM field [58, 59]. This shows that only the transverse part of the vector potential contributes to the physically observable spin and OAM of EM field.

The angular momentum current tensor,  $T_{ij}$ , is a second rank tensor, similar to the Maxwell stress tensor (EM momentum current) [51, 63]. The tensor  $T_{ij}$  is composed of three parts:  $\nabla_i T_{ij} = \nabla_i (\chi_{ij} + J_{ij} + N_{ij})$  with

$$\chi_{ij} = \left[ \overbrace{\frac{\hbar}{2}(\psi^\dagger \gamma^5 \psi)}^{\text{chirality}} + \overbrace{\frac{1}{\mu_0}(\mathbf{A}^\perp \cdot \mathbf{B})}^{\text{helicity}} \right] \delta_{ij} \equiv \chi \delta_{ij}, \quad (2.8a)$$

$$\begin{aligned} J_{ij} = & \overbrace{\mathcal{R} \left\{ \bar{\psi} \gamma_i (\mathbf{r} \times \mathbf{p}_{\parallel})_j \psi \right\}}^{\text{OAM current tensor (Dirac)}} - \overbrace{\frac{1}{\mu_0} (A_i^\perp B_j)}^{\text{helicity current tensor (Maxwell)}} \\ & - \underbrace{\frac{1}{\mu_0} \left[ \varepsilon_{ikl} B_k (\mathbf{r} \times \nabla)_j A_l^\perp \right]}_{\text{OAM current tensor (Maxwell)}} - \epsilon_0 A_i^\perp \left( \mathbf{r} \times \frac{\partial \mathbf{E}^{\parallel}}{\partial t} \right)_j, \end{aligned} \quad (2.8b)$$

$$\nabla_i N_{ij} = (\mathbf{r} \times \nabla) \mathfrak{N}_{\text{em}}, \quad \mathfrak{N}_{\text{em}} = \underbrace{\frac{\epsilon_0}{2} \mathbf{E}^\perp \cdot \mathbf{E}^\perp - \frac{1}{2\mu_0} \mathbf{B} \cdot \mathbf{B}}_{\text{free photon Lagrangian}} + \epsilon_0 \frac{\partial \mathbf{E}^{\parallel}}{\partial t} \cdot \mathbf{A}^\perp. \quad (2.8c)$$

where  $\gamma^5$  is the chirality operator in Dirac equation.

The term  $\chi$  in Eq. (2.8a) describes the chirality/helicity of the fields. The first term,  $\hbar(\psi^\dagger \gamma^5 \psi)/2$ , is the density of expectation value (in the classical sense of quantum mechanics) of the chirality operator of the Dirac field. The operator  $\gamma^5$  is widely used to

find the projections of fermionic fields into left-handed and right-handed chiral states [54]. Therefore, the expectation value  $\psi^\dagger \gamma^5 \psi$  represents the chirality of the Dirac field; a negative (positive) value means a left-handed (right-handed) chiral state. The second term in Eq. (2.8a), on the other hand, is widely known as the helicity of EM field [64–66]. Interestingly, Eq. (2.8a) shows that the chirality of the fermionic field is identified with the helicity of the electromagnetic field and the gradient of these quantities enter the continuity equation.

Note that the chirality of EM field defined in Ref. [39] does not appear in the continuity equation of angular momentum. This shows that the helicity is more fundamental for interacting systems. It is also important to note that helicity can be defined for the Dirac field. Being defined as the projection of spin onto the momentum, it fundamentally depends on the momentum of the field or particle. Since it is a momentum-dependent term for massive fields, helicity depends on the frame of reference and thus it signifies two different values in the proper frame (co-moving frame of reference) and the lab frame. For the massless fields of electromagnetic radiation, however, helicity becomes independent of the frame of reference since there cannot be any proper frame of reference defined for light. Interestingly, for the massless Dirac field, the definition of chirality and helicity become identical [67]. This points to a similar property in the massless electromagnetic fields of the Maxwell's equations.

Therefore the helicity of electromagnetic field and chirality of Dirac field defined here are both Lorentz invariant and are universal in every frame of reference. Although both chirality and helicity refer to the handedness of fields, chirality is independent of momentum and it is therefore an inherent and Lorentz invariant property of the particle. The term handedness might be confusing for chirality since for helicity it is defined as rotation around an axis which is chosen to be momentum. Due to Lorentz invariance, however, this cannot be the case for chirality. Thus it is more appropriate to define the "right-chiral" and "left-chiral" Dirac solutions simply as the eigenvalues of the chirality operator  $\gamma^5$ . They only obtain the meaning of handedness when an axis is imposed on the system in a given frame of reference such as momentum along a particular direction. Otherwise, these right- and left-chiral states are only eigenstates of the chirality operator.

In the next three sections we define the other new terms encountered in the conservation equation.

### 2.3.1 Helicity current density tensor

The second terms in Eq. (2.8b) is reminiscent of the EM helicity in Eq. (2.8a) with the difference that this quantity is a tensor, while helicity is a scalar. In fact, helicity density in Eq. (2.8a) is equal to the trace of  $\frac{1}{\mu_0} A_i^\perp B_j$ . We thus name this tensor quantity *helicity current density tensor* since it transforms as a helicity. Furthermore, the divergence of the helicity current tensor enters the conservation of angular momentum equation meaning that it serves as a current between different forms of Dirac or Maxwell angular momentum.

One important fact regarding this term is that it has no analog in the Dirac field representation, as one might expect. The equivalent expression for helicity current tensor, in the Dirac field, is normally considered to be spin current represented by a tensor involving  $\gamma$  matrices and spin operators. However, our derivation shows that this term vanishes due to the spinor nature of the Dirac fields (see Appendix A for more details). This, of course, does not put the numerous works on spin currents in condensed matter physics into question [68–71], since spin currents are generated by the collective motion of electrons through spatially separating electrons with opposite spins in a quantum cavity [72] or using ferromagnets with strong electron-electron interactions [73]. The relativistic treatment of the Dirac equation in this chapter, however, only incorporates the wave function of a single electron in vacuum and thus cannot account for the observed electronic spin currents. This shows that a single electron in vacuum does not exhibit spin current and that many-body Dirac equation should be considered for a relativistic account of electronic spin currents [74, 75].

### 2.3.2 Orbital angular momentum current density tensor

Equation (2.8b) specifies the angular momentum current tensors for the fields. This current tensor is specified by two directions: direction of angular momentum and direction of the current. For instance, in the first term of Eq. (2.8b), the direction of propagation of the current is specified by the gamma matrices  $\gamma^i$ , while the direction of the angular momentum is specified by the operator  $(\mathbf{r} \times \mathbf{p}_\parallel)$ . Thus we call this term *OAM current density tensor* of Dirac field. Similarly, the third term in Eq. (2.8b) is the OAM current tensor density of the EM field. The last term is the angular momentum current tensor due to longitudinal component of electric field and we incorporate that into the OAM current tensor of the EM field. Equation (2.8c) shows that the electromagnetic Lagrangian also contributes to the continuity Eq. (2.6).

S. Barnett introduced the angular momentum carrying terms in the source-free elec-

tromagnetism [55] as quantities that behave as the currents in the conservation equations written for angular momentum of light. The terms helicity and OAM current tensors introduced here for the electromagnetic field have a similar tensorial nature and extend to the QED interactions. These quantities are gauge-invariant and connect to similar terms coming from the Dirac fields.

Note that the expression for the angular momentum due to the electromagnetic field in Eq. (2.7) originally has contribution from the longitudinal electric field,  $\mathbf{E}^{\parallel}$ . This is the contribution due to the free charges ( $\nabla \cdot \mathbf{E}^{\parallel} = \rho/\epsilon_0$ ) which decays as a function of  $1/r^2$  outside of the region of charges [63]. We have shown in Appendix A that the contribution from this component, namely the term  $\mathbf{E}^{\parallel} \times \mathbf{A}^{\perp} + E_i^{\parallel}(\mathbf{r} \times \nabla)A_i^{\perp}$ , can be written as the divergence of some quantities involving  $\mathbf{E}^{\parallel}$ . Therefore, when integrated over the entire space, these terms vanish and thus the total global angular momentum of the interacting field does not involve longitudinal electric field components. Therefore, we have shown that the angular momentum density of the EM field only depends on the transverse component of the electric field  $\mathbf{E}^{\perp}$  since it is only these terms that give nonzero contribution to the total angular momentum.

It should be emphasized that, when working with global quantities (integrated over entire space), the contribution from the longitudinal electric field as well as the contribution from  $T_{ij}$  in Eq. (2.8) become surface terms and vanish assuming that the field quantities are zero on the surface of the integration volume. In such cases, the global angular momentum can be written in equivalent forms which are different only by the divergence of a function of the fields. In the local case, however, all of the terms in Eq. (2.8) are observable quantities and each have a different interpretation.

### 2.3.3 Spin-orbit torque

We now study the spin-orbital angular momentum exchange and the angular momentum transfer between the Dirac and EM fields. The continuity equation in Eqs. (2.5) and (2.6) only give the dynamics of the total angular momentum density. To obtain insight into the detailed interaction between spin and OAM of the Dirac and EM fields, we separately write the four-divergence of the gauge-independent spin and OAM tensors of the Dirac ( $S_D^{ij,\lambda}$  and  $L_D^{ij,\lambda}$ ) as well as the EM fields ( $S_{em}^{ij,\lambda}$  and  $L_{em}^{ij,\lambda}$ ). By incorporating the Dirac and Maxwell's equations into the gauge-invariant angular momentum densities in Eqs. (2.7) and (2.8), we obtain their detailed conservation equations (see Appendix A),

$$\partial_{\lambda} S_D^{ij,\lambda} = \varepsilon_{ijk} \left[ \tau_D + \mathbf{j}_c \times \mathbf{A}^{\perp} \right]_k, \quad (2.9a)$$

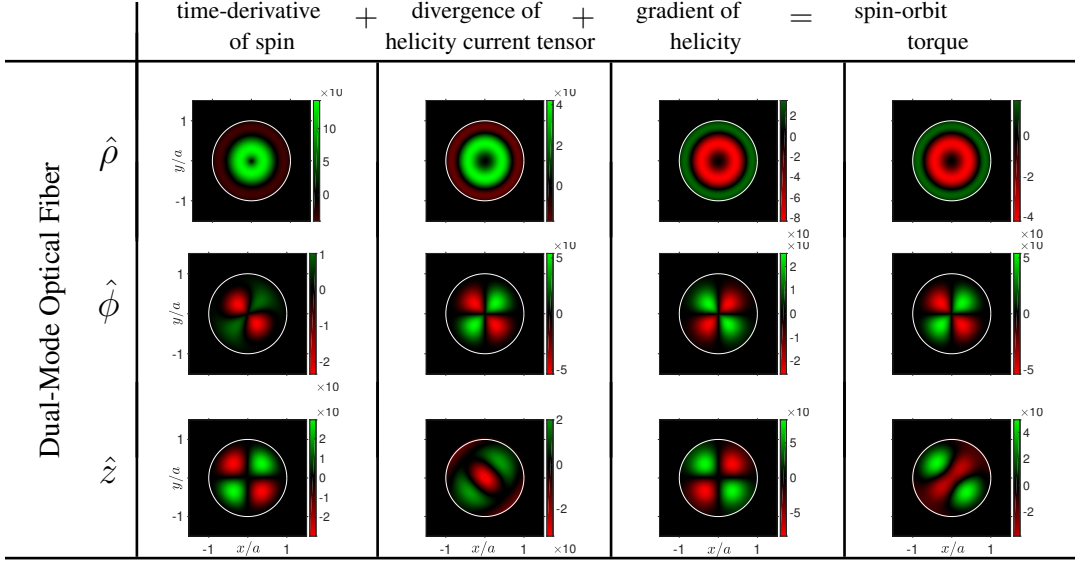


Figure 2.2: Local conservation law for the spin [Eq. (2.12)] in a dual-mode optical fiber. The individual terms in Eq. (2.12) are plotted on the first three columns from left: The first column is the time-derivative of spin ( $\frac{\partial}{\partial t}(\mathbf{E}^\perp \times \mathbf{A}^\perp)$ ), the second column is the divergence of helicity current tensor ( $-\nabla_i(A_i^\perp \mathbf{B})/\mu_0$ ), and the third column is the gradient of the helicity density ( $\nabla(\mathbf{A}^\perp \cdot \mathbf{B})/\mu_0$ ). The fourth column is the EM spin-orbit torque given by Eq. (2.11) (in this case  $\tau_{\text{em}} = (\mathbf{B} \cdot \nabla)\mathbf{A}^\perp/\mu_0$ ). The three rows show the local value of each vector along the three axes of optical fiber problem:  $\hat{\rho}$  radial direction,  $\hat{\phi}$  azimuthal direction, and  $\hat{z}$  axis of the fiber. Note that adding the first three column on each row together gives the last column  $\tau_{\text{em}}$ ; thus confirming Eq. (2.12). The results are for an optical fiber of radius  $50 \mu\text{m}$  with the two modes at the wavelengths  $4.3 \mu\text{m}$  and  $4.29 \mu\text{m}$ .

$$\partial_\lambda L_D^{ij,\lambda} = \varepsilon_{ijk} \left[ -\tau_D + \rho(\mathbf{r} \times \mathbf{E}^\parallel) + j_{c,l}(\mathbf{r} \times \nabla) A_l^\perp \right]_k, \quad (2.9b)$$

$$\partial_\lambda S_{\text{em}}^{ij,\lambda} = \varepsilon_{ijk} \left[ \tau_{\text{em}} - \mathbf{j}_c \times \mathbf{A}^\perp \right]_k, \quad (2.9c)$$

$$\partial_\lambda L_{\text{em}}^{ij,\lambda} = \varepsilon_{ijk} \left[ -\tau_{\text{em}} - \rho(\mathbf{r} \times \mathbf{E}^\parallel) - j_{c,l}(\mathbf{r} \times \nabla) A_l^\perp \right]_k, \quad (2.9d)$$

where we have defined

$$\tau_D = -c\mathcal{R} \{ \bar{\psi} (\boldsymbol{\gamma} \times \mathbf{p}_\parallel) \psi \} \quad (2.10)$$

and

$$\tau_{\text{em}} = \frac{1}{\mu_0} (\mathbf{B} \cdot \nabla) \mathbf{A}^\perp - \epsilon_0 \left( \frac{\partial \mathbf{E}^\parallel}{\partial t} \times \mathbf{A}^\perp \right) \quad (2.11)$$

as the *Dirac* and *Maxwell spin-orbit torque*, respectively, since it gives the amount of torque exerted on the spin from the OAM of the fields and vice versa. This nomenclature is further motivated by the resemblance of the Dirac spin-orbit torque (Eq. (2.10)) of the Rashba spin-orbit coupling Hamiltonian [76]. The direct connection between these terms, however, is out of scope of this article and is the focus of a future work. Note that  $\boldsymbol{\gamma} = \gamma^1 \hat{x} + \gamma^2 \hat{y} + \gamma^3 \hat{z}$  and  $\mathbf{j}_c = ec\bar{\psi} \boldsymbol{\gamma} \psi$  is the electric charge current density in Eqs. (2.9) and (2.10).

Equation (2.9) clearly shows that the spin-orbit torques contribute to the spin-OAM exchange in both Dirac and EM fields. Moreover, it is evident from Eqs. (2.9a), (2.9b), (2.9c), and (2.9d) that the charge-field coupling terms,  $\mathbf{j}_c \times \mathbf{A}^\perp$ ,  $j_{c,l}(\mathbf{r} \times \nabla)A_l^\perp$ , and  $\rho(\mathbf{r} \times \mathbf{E}^\parallel)$ , are responsible for the angular momentum transfer between the Dirac and EM fields [77]. In fact, the first terms gives rise to an optical torque exerted on dipoles due to a circularly polarized optical field [78]. Our results are significantly different from scalar continuity equations of EM helicity in Refs. [34] and [33], which derive a scalar conservation law for the dual-symmetric expressions of spin and helicity of EM field. The helicity continuity equation obtained from the free-space Maxwell equations can not characterize the spin-OAM exchange and specifically the angular momentum transfer between Dirac and EM fields.

## 2.4 Source-free problems

We now show the importance of these continuity equations by demonstrating the spin-OAM exchange via the spin-orbit torque for propagating EM fields. We evaluate the terms in  $\partial_\lambda S_{\text{em}}^{ij,\lambda}$  and the EM spin-orbit torque  $\tau_{\text{em}}$  (Eq. (2.11)) for two simple EM problems in source-free regions. Similar spin-orbit signature can also be observed in a cylindrical geometry for the Dirac fields [51]. However, a thorough study of each individual term in Eq. (2.8) for Dirac and EM fields is not the purpose of this chapter.

The general form of  $\partial_\lambda S_{\text{em}}^{ij,\lambda}$ , in a source-free regions, is

$$\epsilon \frac{\partial}{\partial t} (\mathbf{E}^\perp \times \mathbf{A}^\perp) - \frac{1}{\mu_0} \nabla_i (A_i^\perp \mathbf{B}) + \frac{1}{\mu_0} \nabla (\mathbf{A}^\perp \cdot \mathbf{B}) = \boldsymbol{\tau}_{\text{em}}. \quad (2.12)$$

Here, the extra term on the right hand side results from the coupling to OAM. The spin-orbit torque in the source-free case reduces to  $\boldsymbol{\tau}_{\text{em}} = (\mathbf{B} \cdot \nabla) \mathbf{A}^\perp / \mu_0$ . We emphasize that different from free-space case [33, 34], the near-field spin-OAM exchange can still exist in the presence of sources.

### 2.4.1 dual-mode optical fiber

We first consider a dual-mode optical fiber, which is placed along the  $z$  axis with radius  $a$ . The two modes have the same propagation constant,  $\beta$ , and different frequencies of  $\omega_1$  and  $\omega_2$ . Figure 2.2 shows the four terms in Eq. (2.12). The three rows show the components of these quantities along the radius  $\hat{\rho}$ , azimuthal  $\hat{\phi}$ , and  $z$  axis of the fiber. Note that for all three rows, the sum of the first three terms is equal to  $\boldsymbol{\tau}_{\text{em}}$ ; thus satisfying Eq. (2.12). These figures show that, for a dual-mode optical fiber, the helicity current current tensor,

helicity density, spin density, as well as the spin-orbit torque are all non-zero and can play a role in a local interaction between optical modes and atomic sources. Note that all three components become zero as the fiber radius  $a \rightarrow \infty$ , which confirms that the spin-orbit torque  $\tau_{em}$  becomes zero for plane wave solutions.

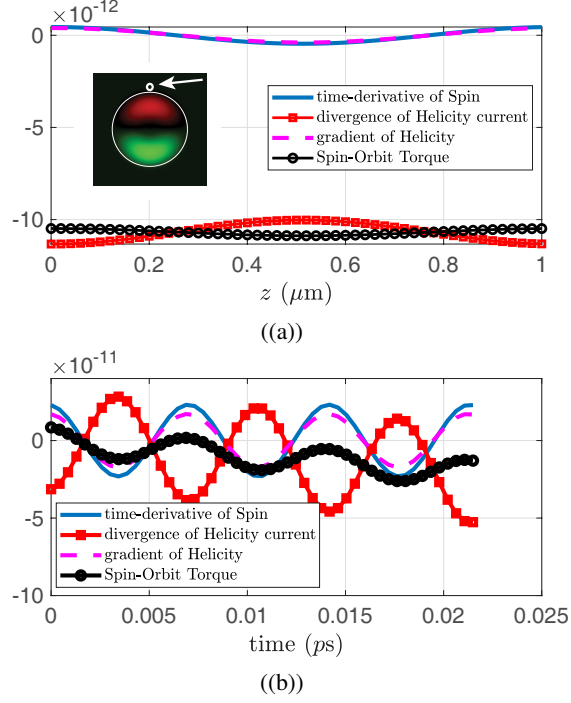


Figure 2.3: Dynamics of the terms in Eq. (2.12) versus (a)  $z$  and (b) time. The plots only show the  $\hat{z}$  component of each term. These plots show that the spin-orbit torque ( $\tau_{em}$ ) is equal to the sum of the other terms. The inset in panel (a) shows the location where the terms are evaluated for both of the figures.

Figure 2.3 shows the dynamics of the time-derivative of spin, divergence of helicity current density, and gradient of helicity (the terms in Eq. (2.12)) as a function of  $z$  (Fig. 2.3(a)) and time (Fig. 2.3(b)). The curves show the value of these terms at a point  $0.05 a$  from the fiber as shown in the insets. The black curve with the circle markers show the EM spin-orbit torque,  $\tau_{em}$ , which is essentially the torque that is transferred to the OAM of the fields. Note that the sum of other curves equals the black curve  $\tau_{em}$ ; satisfying the continuity Eq. (2.12).

## 2.4.2 double plane wave interference

The second example is the interference of two circularly polarized plane waves at two different frequencies. For the plane wave solutions, the current term  $\nabla_i(A_i^\perp \mathbf{B})$  and the spin-orbit torque  $\tau_{em}$  vanish. Therefore, we arrive at a simpler conservation law for the second

problem,

$$\frac{\partial}{\partial t} \left( \epsilon_0 \mathbf{E}^\perp \times \mathbf{A}^\perp \right) + c \nabla \left( \frac{1}{\mu_0 c} \mathbf{A}^\perp \cdot \mathbf{B} \right) = 0, \quad (2.13)$$

which shows the spin density propagating in space with light speed  $c$ . For circularly polarized plane waves propagating along  $z$  direction, the electric field is written as  $\mathbf{E} = \mathcal{R}\{\mathcal{E}_1 e^{-i(\omega_1 t - k_1 z)} + \mathcal{E}_2 e^{-i(\omega_2 t - k_2 z)}\}$ , where  $\mathcal{E}_i = \mathcal{E}_i(\hat{x} + i\hat{y})/\sqrt{2}$  are the complex electric field amplitudes of the two modes with frequencies  $\omega_i/c = k_i$ . For these fields, we find,

$$\begin{aligned} \frac{1}{\mu_0} \nabla (\mathbf{A}^\perp \cdot \mathbf{B}) &= -\epsilon_0 \frac{\partial}{\partial t} (\mathbf{E} \times \mathbf{A}^\perp) \\ &= \epsilon_0 \frac{\omega_1^2 - \omega_2^2}{2\omega_1 \omega_2} \mathcal{I} \left\{ \mathcal{E}_1 \mathcal{E}_2^* e^{-i[(\omega_1 - \omega_2)t - (k_1 - k_2)z]} \right\}, \end{aligned} \quad (2.14)$$

hence satisfying the conservation Eq. (2.13). This clearly shows that the change in time of the spin is compensated by the gradient of the helicity of the EM field.

## 2.5 Conclusion

We applied the Noether's theorem to the Dirac Lagrangian interacting with the EM field to find the local conservation laws of angular momentum for the most general electrodynamics problem. The results developed here can be applied to near-field as well as far-field to study the transformation of angular momentum between different fields in these regions. Our results show that, in consideration of local conservation laws, other quantities including helicity and OAM current tensors, EM helicity, and electronic chirality should also be considered in addition to the spin and OAM of the EM and Dirac fields.

Equation (2.6) holds everywhere in space and time. This shows that the total angular momentum density  $\mathbf{M}$  is not locally conserved. In other words,  $\frac{\partial \mathbf{M}}{\partial t} \neq 0$  and the conservation law can only be written after including all the other terms in Eqs. (2.6) and (2.8). Integrating Eq. (2.6) over some volume  $V$ , on the surface of which both Dirac and EM fields become zero,  $\psi \rightarrow 0$ ,  $\mathbf{E} \rightarrow 0$ , gives the usual global conservation law,  $\frac{\partial}{\partial t} \int_V \mathbf{M} d^3x = 0$ . This states that the integrated values of the spin and OAM densities of electron and EM field over the entire space is a conserved quantity (Fig. 2.1(a)).

We can also get a simpler continuity equation than Eq. (2.6) if we limit ourselves to regions outside the Dirac fields. To do so, we take the integral of Eq. (2.6) in the volume  $V'$  on which only the Dirac fields become zero  $\psi = 0$ . Doing so we get the *semi-local* conservation law,

$$\frac{\partial \tilde{\mathbf{M}}_D}{\partial t} = - \left[ \frac{\partial \tilde{\mathbf{M}}_{\text{em}}}{\partial t} + \tilde{\mathbf{J}} + \tilde{\mathbf{h}} + \int_{S'} \hat{\mathbf{n}} \times (\mathbf{r} \mathcal{N}_{\text{em}}) da \right] \quad (2.15)$$

which expresses the time-evolution of the angular momentum of electron  $\tilde{M}_D$  in terms of EM dependent quantities.  $\tilde{M}_{em}$  is the EM angular momentum in the region of the source, while  $\tilde{J}$  and  $\tilde{h}$  are the EM angular momentum current tensor (projected onto the normal of the surface) and helicity (multiplied by the normal of the surface), integrated on the surface of the volume surrounding the current charges. Also,  $\mathfrak{N}_{em}$  is given by Eq. (2.8c). Equation (2.15) can be used to find the conservation of angular momentum in the near-field of current sources and how is it transferred to the electromagnetic fields.

It is also important to note that the conservation of angular momentum derived here is based on the spatial components of Lorentz transformations (i.e. rotations). Time-space components of the Lorentz transformation can also give conservation equations related to the boost operators in the relativistic equations of motion. These equations provide a new conservation equation for the Dirac-Maxwell fields which can be of interest to applications investigating relativistic behaviour of the particles and their pertinent conserved quantities when interacting. A brief discussion about these conservation equations is given in Appendix A.

The method presented in this chapter can be further extended to find the dynamics of magnetization in different materials. The simplest system can be regarded as the interaction between an externally applied EM field and the electrons in a non-magnetic metal. A weak probe signal can then be used to study spin dynamics of the metal. Such a system can be closely modeled as a non-interacting electron gas whose dynamics can be described by the Dirac equation. Although the solutions of the Dirac equation interacting with an externally applied plane wave can be rigorously found [79, 80], these solutions are extremely complicated and only apply to the particular case of free electrons in a plane wave. Our method, circumvents the problem of solving the Dirac Hamiltonian to find the spin dynamics of the electrons, by using Noether's theorem and finding the conservation equation governing angular momentum dynamics of the electrons. By knowing the properties of the externally applied EM field, a simpler equation such as Eq. (2.15) can be used to find the dynamics of angular momentum without the need of electronic wavefunctions. Since in our derivations we make no simplifying assumption on the EM field, these equations can be easily used for interactions that take place in the near-field region and where EM fields cannot be regarded as plane waves.

The Dirac equation can be further extended to model ferromagnetic materials. Dirac-Kohn-Sham (DKS) equation is an extension to the Dirac equation which accounts for the Kohn-Sham potential as well as the spin-polarized part of the exchange correlation poten-

tial inside a magnetic material [81, 82]. Corrections from DKS equation can be added to the usual Pauli Hamiltonian to account for the terms in the Landau-Lifshitz-Gilbert (LLG) equation and to add corrections accounting for higher order terms dependent on external and internal parameters [83]. The method presented in this chapter can also be applied to the DKS Hamiltonian to derive the conservation equation for the angular momentum of electrons in magnetic materials.

## Chapter 3

# Spin Photonics in 3D Whispering Gallery Mode Resonators

Whispering gallery modes are known for possessing orbital angular momentum, however the interplay of local spin density, orbital angular momentum (OAM), and the near-field interaction with quantum emitters is far less explored. Here, we study the spin-orbit interaction of a circularly polarized dipole with the whispering gallery modes (WGMs) of a spherical resonator. Using an exact dyadic Green's function approach, we show that the near-field interaction between the photonic spin of a circularly polarized dipole and the local electromagnetic spin density of whispering gallery modes gives rise to unidirectional behaviour where modes with either positive or negative orbital angular momentum can be excited. We show that this is a manifestation of spin-momentum locking with the whispering gallery modes of the spherical resonator. We also discuss requirements for possible experimental demonstrations using Zeeman transitions in cold atoms or quantum dots, and outline potential applications of these previously overlooked properties. Our work firmly establishes local spin density, momentum and decay as a universal right-handed electromagnetic triplet for near-field light-matter interaction. This chapter presents the results presented in the paper "Spin Photonic in 3D Whispering Gallery Mode Resonators" published in *Optics express* 27.11 (2019): 15846-15855 [22].

### 3.1 Introduction

Spin-momentum locking explains the origin of unidirectional chiral phenomena in both electronic and photonic systems [18, 20, 84–89]. In topological insulators, spin-polarized edge modes have a spin direction that is dependent on the propagation direction of the modes [87, 90]. In photonics, the near-field interaction between a circularly polarized emit-

ter and a metal interface gives rise to the unidirectional propagation of surface plasmon polaritons (SPP) [18, 19, 42, 88, 91]. This unidirectional behavior has also been observed in the propagation of  $HE_{11}$  modes in optical fibers coupled to a trapped atom [20]. Alternative approaches for obtaining unidirectional chiral phenomena include the use of optical resonators with a broken symmetry; for example, using spatially deformed resonators [92], broken time-reversal symmetric resonators [21], or rotating resonators [93].

In this work, we present a manifestation of spin-momentum locking with the whispering gallery modes of a 3D spherical microresonator coupled to a circularly polarized emitter. Spin-momentum locking arises naturally in the description of evanescent electromagnetic fields through Maxwell's equations [94], resulting in a well-defined vector triplet for the electromagnetic spin, momentum, and decay vectors (shown in Fig. 3.1(a)). Although whispering gallery modes are not naturally described by propagating or evanescent plane waves, we show that whispering gallery modes also obey spin-momentum locking manifested by the strong field confinement of these modes. We should note that while the electromagnetic spin of guided modes can be probed by optical force measurements [95–98], probing the electromagnetic spin of an emitter faces complexities due to the interaction between the source and the probing system in the near-field limit. In fact, a universally accepted definition of photonic spin in the presence of sources remains an open question for this reason [99].

Here, we show that the whispering gallery modes of a spherical resonator form an excellent platform for studying the interaction of spin-polarized quantum radiation sources and the electromagnetic spin of confined modes. In particular, we show that the spin of an emitter effectively couples to the local spin density of whispering gallery modes and ultimately gives rise to the unidirectional propagation of orbital angular momentum modes inside the spherical resonator. The origin of the electromagnetic spin of a quantum emitter is the atomic  $\sigma^\pm$  transitions (shown in Fig. 3.1(b)) which can be modeled by a circularly polarized dipole.

Using a numerically exact 3D Dyadic Green function approach, we show it is possible to selectively excite particular TE and TM modes with specific radial ( $n_r$ ) and total orbital angular momentum ( $l$ ) numbers. Moreover, by coupling to the spin of TM modes, we show it is possible to induce unidirectional coupling between the Zeeman transitions of an atom [100] or a quantum dot [101] and the whispering gallery modes with either positive or negative orbital angular momentum. Similar observations have been made for 2D WGMs in microdisk resonators [21, 92] as well as 3D WGMs of spherical resonators [17]. There

is, however, to the best of our knowledge, a theoretical gap in the studies of spin properties of whispering gallery modes in a 3D spherical resonator due to the added complexity [102].

Our results should be experimentally observable by methods using spherical silica resonators and tapered fiber coupling (Fig. 3.2) [17,103]. Our proposed experiments will detect directional out-coupling of whispering gallery modes with positive (negative) orbital angular momentum which propagate only along the positive (negative) direction inside the fiber. In the setup proposed in Fig. 3.2, the Zeeman transitions of the quantum source are accessed in the excited state using an optical pump with the application of a magnetic field to split the degeneracy of  $\sigma^+$  and  $\sigma^-$  transitions. By tuning the resonator to the  $\sigma^-$  transition, for instance, WGMs with positive orbital angular momentum are preferentially excited. When coupled to a tapered fiber placed in the near-field of the resonator, the energy propagates in a unidirectional manner inside the fiber. Changing to a  $\sigma^+$  transition instead would reverse the propagation direction inside the fiber and serve as a clear signature of the spin photonic effect.

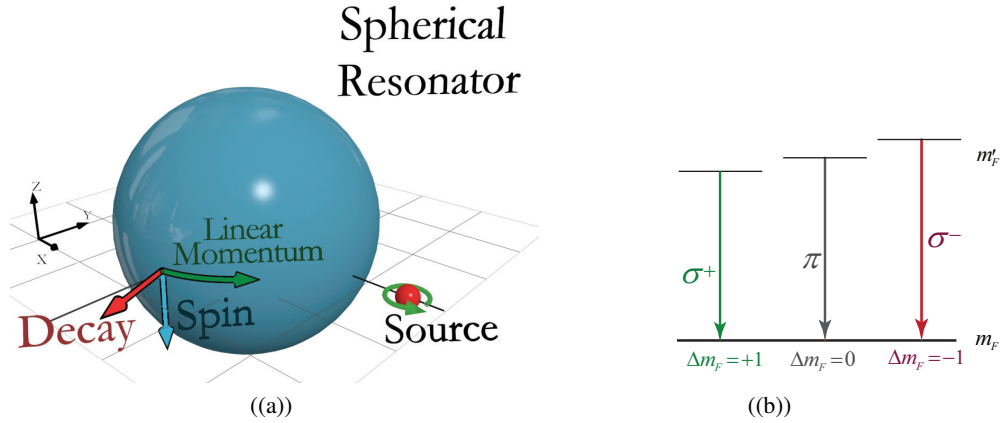


Figure 3.1: Schematic of the proposed experiment to study spin photonics in WGMs. The unique proposed effect due to the locked electromagnetic triplet consisting of spin, momentum, and decay. (a) A quantum source with circularly polarized emission ( $\sigma^\pm$  transitions) is placed in the vicinity of a spherical resonator. The near-field interaction between the source and TM WGMs of the sphere results in excitation of WGM with only spin polarized, positive OAM along  $z$  direction. This unidirectional behaviour is a manifestation of spin-momentum locking in a 3D structure. Spin, linear momentum, and decay are along  $\hat{\theta}$ ,  $\hat{\phi}$ , and  $\hat{r}$ , respectively, and form a triplet for the TE and TM modes. (b) General form of Zeeman transitions in a cold atom [100] or quantum dot [101]. For  $\sigma^\pm$  and  $\pi$  transitions,  $\Delta m_F = \pm 1$  and  $\Delta m_F = 0$ , respectively, where  $m_F$  is the quantum number pertinent to the total angular momentum of the source (nucleous and electrons). These transitions can be modeled by dipole sources with the electric dipole moment given by Eq. (3.7) [16].

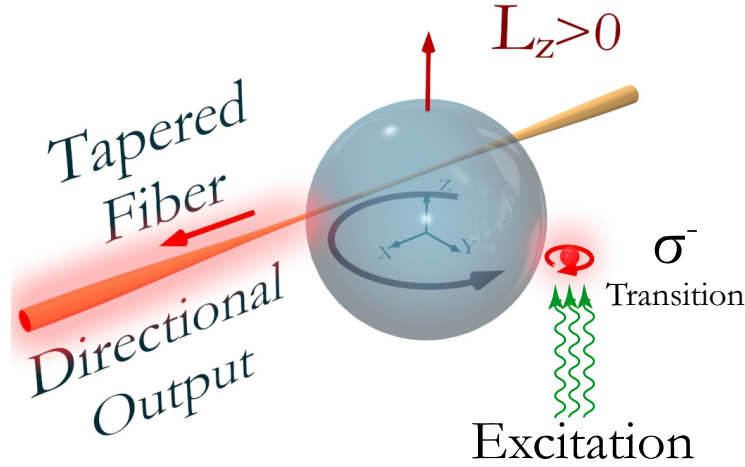


Figure 3.2: Proposed experimental setup for the spin photonics in WGMs. By exciting the resonator using a  $\sigma^-$  transition of a quantum source, WGMs with positive orbital angular momentum are excited stronger. This can be observed by proximity coupling of a tapered optical fiber to the spherical resonator. As a result of coupling between the WGMs with positive OAM and the fiber, modes propagate only in one particular direction in the fiber [17,92]. Switching to a  $\sigma^+$  transition instead, would also reverse the propagation direction inside the fiber. The source can be Zeeman transitions in cold Caesium atom prepared in the excited state using a excitation signal [100].

### 3.2 Photonic spin in spherical whispering gallery modes

The modes of a spherical resonator are found by solving Maxwell's equations using appropriate boundary conditions in the spherical coordinate representation [104,105]. Each mode is labeled by three eigennumbers:  $n_r, l$ , and  $m$  where  $n_r = 1, 2, 3, \dots$  is the radial eigennumber while  $l$  and  $m = -l, -l+1, \dots, +l-1, +l$  denote the orbital angular momentum eigennumbers through the eigenvalue relations  $\mathbf{L}^2\psi = l(l+1)\psi$  and  $L_z\psi = m\psi$ , where  $\psi$  is either the electric or magnetic field,  $\mathbf{L} = \mathbf{r} \times \nabla$ , and  $L_z = -i\frac{\partial}{\partial\phi}$ . These relations indicate that  $m$  is the projection of OAM along the  $z$  axis and modes with positive (negative)  $m$  are those that orbit the  $z$  axis counter-clockwise (clockwise). Note that  $+\hat{z}$  is defined in Fig. 3.1(a) where the  $+\hat{z}$  is parallel to the handedness of the source for  $\sigma^+$  transitions and  $-\hat{z}$  parallel to the handedness of the source for  $\sigma^-$  transitions. For a perfect spherical resonator, the eigenfrequency depends only on  $n_r$  and  $l$ , therefore an emitter with a fixed transition frequency can only selectively couple to  $l$  modes but not  $m$  modes. Whispering gallery modes are further distinguished by their polarization, denoted as transverse-electric (TE) modes ( $\mathbf{E}(\mathbf{r}, \omega) \cdot \mathbf{r} = 0$ ) or transverse-magnetic (TM) modes ( $\mathbf{H}(\mathbf{r}, \omega) \cdot \mathbf{r} = 0$ ). For the rest of the chapter, we will distinguish these two types of modes using the labels

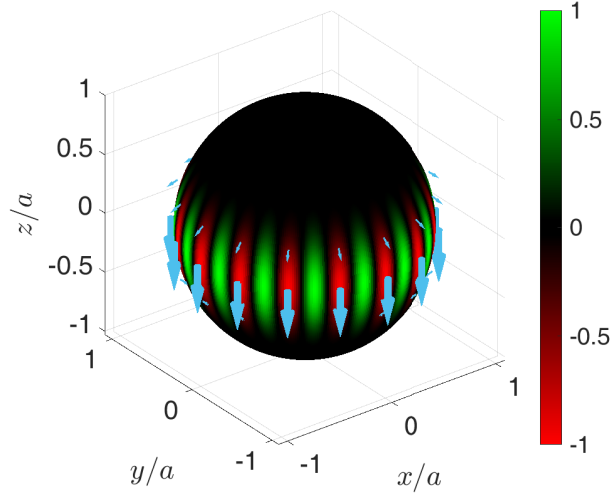


Figure 3.3: Electromagnetic spin in TE and TM whispering gallery modes. The color plot shows the field intensity of  $H_r$  ( $E_r$ ) component of the TE (TM) mode for  $l = 16$  and  $m = 16$  on the surface of the resonator. The blue arrows show the direction of spin on the surface of the sphere. Modes with positive  $m$ , orbit the  $z$  axis counter-clockwise ( $+\hat{\phi}$ ) while those with negative  $m$  orbit the  $z$  axis clock-wise ( $-\hat{\phi}$ ). With linear momentum along  $+\hat{\phi}$ , Momentum, decay, and spin form a triplet. Spin direction follows the spin-momentum locking property for both TE and TM modes. This means that by changing the direction of OAM (changing the sign of  $m$ ), the direction of the spin (blue arrows) reverses for both TE and TM modes. This behaviour inspires unidirectional coupling of a circularly polarized dipole to the WGMs.

TE $_{n_r, l, m}$  and TM $_{n_r, l, m}$ .

Orbital angular momentum (OAM) and spin are distinctly different properties of the fields. While orbital angular momentum is a global property, photonic spin is a local property related to the rotational symmetry of the spin-1 electromagnetic vector field [99]. This difference is revealed by observing how spin-polarized sources interact with the whispering gallery modes locally. As one might expect, placing the spin-polarized source in the vicinity of spherical resonator should generate modes with positive OAM. However, as shown in the next section, the exact opposite happens. Spin-polarized source excites WGMs with an OAM that is anti-parallel to the spin of source. This can only be explained by the interplay between the spin of the source and the local spin of the WGMs resulting in the generation of scattered fields that have their OAM anti-parallel to the spin of the source. This observation shows that the spin-polarized source couples to the local spin of the WGMs and not their OAM.

In a source-free region, the local spin density of the electromagnetic field is given by  $\mathbf{S}(\mathbf{r}, \omega) = \frac{1}{4\omega} \text{Im}\{\epsilon_0 \mathbf{E}^*(\mathbf{r}, \omega) \times \mathbf{E}(\mathbf{r}, \omega) + \mu_0 \mathbf{H}^*(\mathbf{r}, \omega) \times \mathbf{H}(\mathbf{r}, \omega)\}$  [106–109]. From this

expression, we see that a circularly polarized plane wave propagating along the  $z$ -direction in free-space,  $\mathbf{E}(\mathbf{r}, \omega) = E_0(\hat{x} + i\hat{y})e^{ikz}e^{-i\omega t}$ , has an electromagnetic spin pointing along the  $z$ -direction. For the rest of the chapter, we will drop the arguments  $(\mathbf{r}, \omega)$  for notational simplicity. Using this expression, we can calculate the spatial distribution of the photonic spin density for whispering gallery modes. Figure 3.3 shows the field distribution for the TE and TM modes (color plot) as well as their respective electromagnetic spin (blue arrows) on the surface of the sphere with radius  $a$ . The plots correspond to the  $TE_{1,16,16}$  and  $TM_{1,16,16}$  modes for which  $\lambda_{TE} = 0.54a$  and  $\lambda_{TM} = 0.52a$ . In particular, the spin can be written as:

$$\mathbf{s} = \mathbf{p} \times \boldsymbol{\gamma} \quad (3.1)$$

where  $\mathbf{s}$ ,  $\mathbf{p}$ , and  $\boldsymbol{\gamma}$  denote the unit vectors pointing along the spin, the linear momentum, and the decay directions respectively [94,95,110], thereby forming a right-hand rule triplet. Note that  $\mathbf{p}$  and  $\boldsymbol{\gamma}$  are defined as the real and imaginary part of the Poynting vector, respectively [108,111].

As shown in Fig. 3.3, the spin of both TE and TM modes (blue arrows) are dominated by the  $\hat{\theta}$  component. Explicitly, the dominant electromagnetic spin components  $S_{lm, \theta}^{TM}$  and  $S_{lm, \theta}^{TE}$  can be written as:

$$S_{lm, \theta}^{TM} = S_{lm, \theta}^{TE} = -m \frac{\mu_0}{2\omega} \frac{l(l+1)}{|k_1|^2 a^2} g(\theta) [\mathcal{R}\{k_1 a j_l^*(k_1 a) j_{l+1}(k_1 a)\} - (l+1)|j_l(k_1 a)|^2], \quad (3.2)$$

with  $k_1 = \frac{\omega\sqrt{\epsilon_r}}{c}$  being the propagation constant inside the sphere,  $\epsilon_r = 3$  is the dielectric permittivity of the sphere,  $\omega$  the angular eigenfrequency of the TE or TM mode,  $\mu_0$  the vacuum permeability,  $j_l(ka)$  the spherical Bessel function of the first kind and order  $l$ , and  $g(\theta)$  a real function of  $\theta$ .  $\mathcal{R}\{\}$  takes the real part of its argument. These expressions are derived for fields on the surface of the sphere. We emphasize that the electromagnetic spin,  $S$ , is linearly dependent on the azimuthal orbital angular momentum,  $m$ . This result indicates that the direction of the electromagnetic spin is locked to the direction of  $z$ -projected orbital angular momentum. In other words, changing the sign of  $m$  flips the sign of the spin for both TE and TM modes.

These solutions are found under the assumption that the solutions outside the sphere are decaying. Changing the outside solutions to growing solutions, instead, changes the sign of the expression inside the brackets in Eq. (3.2). This means that under the change of direction in the decay vector, the spin for both TE and TM modes flips sign. Together with the linear dependence on  $m$ , these observations show the spin-momentum locking property

as shown in [94], and also the fact that spin, momentum, and decay form a triplet. These properties are manifestations of spin-orbit coupling where the change in the OAM results in a change in the spin of WGMs. These previously overlooked properties of WGMs have important implications which we will discuss in the next section. Note that these properties are valid for arbitrary-sized spherical resonators.

### 3.3 Near-field spin interaction

We aim to investigate the near-field interaction of Zeeman transitions of a quantum source with the WGMs of a spherical resonator. For such interactions we focus on the  $\sigma^\pm$  transitions observed in a cold atom [100] or quantum dots [101]. Solutions of the Green function for a source outside of a sphere can be written in terms of WGMs with different  $l$  and  $m$  as [112, 113],

$$\overline{\mathbf{G}}_e(\mathbf{r}, \mathbf{r}') = \overline{\mathbf{G}}_{0e}(\mathbf{r}, \mathbf{r}') + \overline{\mathbf{G}}_{es}(\mathbf{r}, \mathbf{r}'), \quad (3.3)$$

$$\overline{\mathbf{G}}_{0e}(\mathbf{r}, \mathbf{r}') = \frac{\hat{r}\hat{r}'}{k_0^2} \delta(r-r') + \frac{ik_0}{4\pi} \sum_{l=0}^{\infty} \sum_{m=0}^l C_{lm} \begin{cases} \mathbf{M}_{lm}^{(1)}(k_0) \mathbf{M}'_{lm}(k_0) + \mathbf{N}_{lm}^{(1)}(k_0) \mathbf{N}'_{lm}(k_0) & r \geq r' \\ \mathbf{M}_{lm}(k_0) \mathbf{M}'_{lm}^{(1)}(k_0) + \mathbf{N}_{lm}(k_0) \mathbf{N}'_{lm}^{(1)}(k_0) & r \leq r' \end{cases}, \quad (3.4)$$

$$\overline{\mathbf{G}}_{es}^{(11)}(\mathbf{r}, \mathbf{r}') = \frac{ik_0}{4\pi} \sum_{l=0}^{\infty} \sum_{m=0}^l C_{lm} \left[ \mathcal{B}_M \mathbf{M}_{lm}^{(1)}(k_0) \mathbf{M}'_{lm}{}^{(1)}(k_0) + \mathcal{B}_N \mathbf{N}_{lm}^{(1)}(k_0) \mathbf{N}'_{lm}{}^{(1)}(k_0) \right], \quad (3.5)$$

$$\overline{\mathbf{G}}_{es}^{(21)}(\mathbf{r}, \mathbf{r}') = \frac{ik_0}{4\pi} \sum_{l=0}^{\infty} \sum_{m=0}^l C_{lm} \left[ \mathcal{D}_M \mathbf{M}_{lm}(k_1) \mathbf{M}'_{lm}{}^{(1)}(k_0) + \mathcal{D}_N \mathbf{N}_{lm}(k_1) \mathbf{N}'_{lm}{}^{(1)}(k_0) \right]. \quad (3.6)$$

where the subscript  $e$  indicates that these are the Green's functions for the electric field, while the subscripts 0 and  $s$  refer to the homogeneous and scattered solutions, respectively. The functions  $\mathbf{M}_{lm}$  and  $\mathbf{N}_{lm}$  are the two transverse solutions of Maxwell's equations [112, 113]. The superscript (1) in  $\mathbf{M}_{lm}^{(1)}$  and  $\mathbf{N}_{lm}^{(1)}$  refers to the solutions with the spherical Hankel functions of the first kind, while no superscript implies solutions with spherical Bessel functions of the first kind. Also, the unprimed and primed solutions show the dependence on the location of the observation point ( $\mathbf{r}$ ) and the location of the source ( $\mathbf{r}'$ ), respectively. The superscripts (11) and (21) in  $\overline{\mathbf{G}}_{es}^{(11)}$  and  $\overline{\mathbf{G}}_{es}^{(21)}$  indicate the scattered solutions outside and inside the sphere, respectively.  $C_{lm}$ 's are some constants,  $k_0$  and  $k_1$  propagation constants outside and inside the sphere, respectively, and  $\mathcal{B}_M, \mathcal{B}_N, \mathcal{D}_M,$  and  $\mathcal{D}_N$  are the coefficients found by applying the boundary conditions [112, 113]. Note that these solutions are the summation of the modes with different OAM quantum numbers  $l$  and  $m$ . Also, since  $\mathbf{M}$  and  $\mathbf{N}$  are the solutions without and with the radial field components [112], we can consider

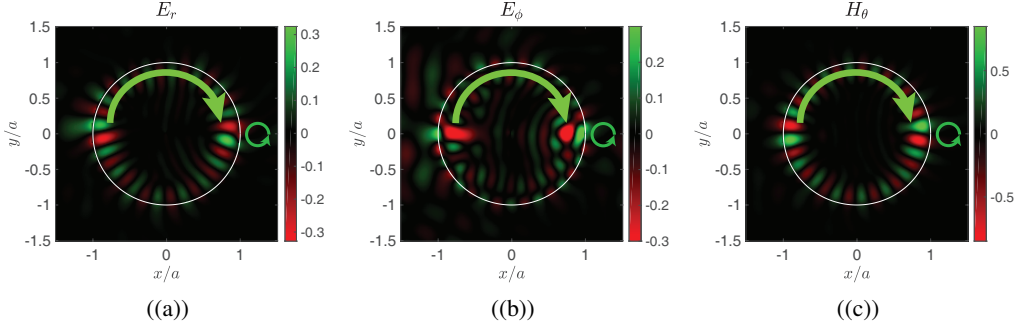


Figure 3.4: Plots of normalized scattered electromagnetic fields due to the right-handed circularly polarized dipole ( $\sigma^+$  transition). (a)  $E_r$ , (b)  $E_\phi$ , and (c)  $H_\theta$  in the  $x - y$  plane. All components of the fields orbit along  $-\phi$  direction as a result of the circularly polarized dipole located at  $x_d = a + 10\text{nm}$  and  $y_d = z_d = 0$  with the dipole moment  $\mathbf{d}_+ = \frac{d_0}{\sqrt{2}}(\hat{x} + i\hat{y}) = d_0\hat{e}_+$ . The circularly polarized dipole couples unidirectionally to the orbit of the fields in the spherical resonator as a result of spin-momentum locking. One important consequence of this is that the photonic spin of the source is opposite to the OAM of the WGMs. Additional videos are available online [22].

them as the TE and TM contributions to the WGMs, respectively. We have used these solutions to find the interaction of  $\sigma^\pm$  and  $\pi$  transitions with the dipole moments [16],

$$\mathbf{d}_\pm = d_0\hat{e}_\pm = \frac{d_0}{\sqrt{2}}(\hat{r} \pm i\hat{\phi}), \quad \mathbf{d}_\pi = d_0\hat{x} \quad (3.7)$$

located outside of a lossless spherical resonator with a relative permittivity of 3 at  $r_d = a + 10\text{nm}$ ,  $\theta_d = \pi/2$ , and  $\phi_d = 0$ . Here, we look at the WGMs with  $n_r = 1$  and  $l = 16$  by setting the wavelength of the source to that of the WGMs for the corresponding  $n_r$  and  $l$ . The radius of the sphere is therefore chosen to be  $a = 1177\text{nm}$  to have the resonance of the desired mode at  $\lambda_0 = 610\text{nm}$ . The sphere is thus located in the near-field region of the source.

Figure 3.4 shows the simulation results for the source with the dipole moment  $\mathbf{d}_+$  of a  $\sigma^+$  transition. Photonic spin of the source in Fig. 3.4 is parallel to the spin of the  $\text{TE}_{1,16,m>0}$  and  $\text{TM}_{1,16,m>0}$  modes (Fig. 3.3). As a result, the dipole excites a mixture of degenerate modes of positive orbital angular momentum along the  $z$  direction ( $m > 0$ ) and thus gives rise to the unidirectional orbit of the fields inside the sphere. Although spin of the source is parallel to that of both TE and TM modes, only TM modes are excited here. This is due to the fact that the spin of TE mode is primarily from magnetic field while the spin of the TM mode is primarily electric. Having a purely electric spin, the source therefore only couples to the TM mode. This can be equivalently explained by the fact that the TE modes do not have a radial electric field component and therefore they do not couple to the radial

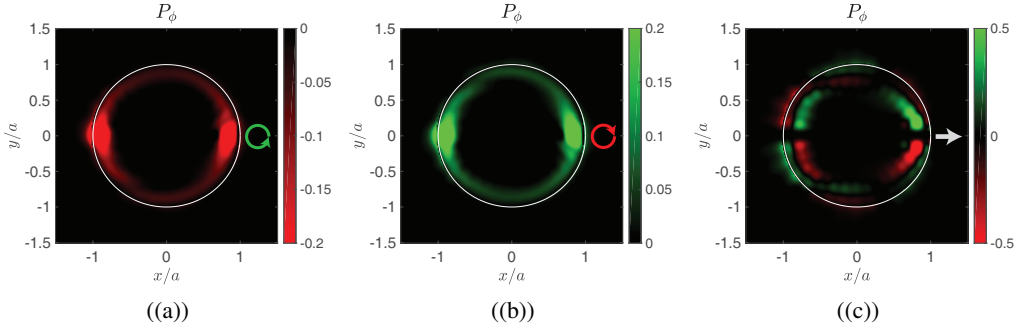


Figure 3.5: Normalized Poynting vector along  $\phi$  direction,  $P_\phi$ , for the three cases of (a)  $\sigma^+$  transitions (RH circularly polarized dipole), (b)  $\sigma^-$  transitions (LH circularly polarized dipole), and (c)  $\pi$  transitions (linearly polarized dipole along  $x$ ), in the  $x - y$  plane for the source located at  $x_d = a + 10\text{nm}$  and  $y_d = z_d = 0$ , and with the dipole moments given by Eq. (3.7). The negative value of  $P_\phi$  in (a) and positive value of  $P_\phi$  in (b) indicate that, for the RH and LH circularly polarized dipoles as the source, the WGMs of the spherical resonator orbit clockwise (along  $-\hat{\phi}$ ) and counter-clockwise (along  $+\hat{\phi}$ ), respectively. For the linearly polarized dipole in (c), however, the WGMs inside the sphere are a mixture of clockwise and counter-clockwise fields which eventually cancel out each other to give a net-zero OAM. Therefore, coupling the WGMs to an optical fiber, for instance, on the other side from the source, would result in an equal wave propagation in both directions inside the fiber. However, for a circularly polarized source, the modes would only propagate along one direction inside the fiber, depending on the handedness of source. This figure clearly shows the unidirectional behaviour of spin interaction of the source and WGMs, as a result of the spin-momentum locking.

component of the dipole moment of the source.

One important observation in Fig. 3.4 is that the photonic spin of the source (pointing out of the plane) is anti-parallel to the orbital angular momentum of the scattered modes inside the sphere (into the plane). This generation of an anti-parallel angular momentum, in the scattered fields, by using a spin-polarized source can only be explained by the fact that the spin of the source is parallel to the local spin of the WGMs (Fig. 3.3) which results in excitation of modes with anti-parallel OAM. This shows that using a spin-polarized source we can exclusively couple to the photonic spin of the WGMs [99].

Visualization 1 and Visualization 2 (see online animations) show the clockwise and counter-clockwise rotation of the scattered fields inside the sphere as a result of the circularly polarized dipole located outside of the sphere with the dipole moments of  $\mathbf{d}_+$  and  $\mathbf{d}_-$ , respectively. This result is an important generalization of spin-momentum locking observed in 1D [86] and 2D [20] problems. In the 3D problem, however, the linear momentum is a result of the orbital angular momentum of the fields.

Figure 3.5 shows the azimuthal Poynting vector,  $P_\phi$ , inside the sphere, for three cases of

right-handed (RH) circularly polarized (Fig. 3.5(a)), left-handed (LH) circularly polarized (Fig. 3.5(b)), and linearly polarized (Fig. 3.5(c)) dipoles, with the dipole moments given by Eq. (3.7). The dipoles are placed at the same location as that of Fig. 3.4 ( $x_d \simeq 1.01a$  and  $y_d = z_d = 0$ ). The unidirectional azimuthal propagation of WGMs inside the sphere is evident as a result of circularly polarized dipole. For the RH dipole (Fig. 3.5(a)) the Poynting vector is along negative  $\hat{\phi}$  (shown as purely red color inside the sphere) meaning that the fields orbit the sphere clockwise, while for the LH dipole (Fig. 3.5(b)) the Poynting vector is along positive  $\hat{\phi}$  (shown as purely green color inside the sphere) meaning that the fields orbit the sphere counter-clockwise. Changing the sense of polarization from RH to LH, changes the sign of azimuthal Poynting vector from negative to positive as seen in Figs. 3.5(a) and 3.5(b). For the linearly polarized dipole in Fig. 3.5(c), however, the fields are a mixture of positively and negatively spinning fields (clockwise and counter-clockwise) which gives a net zero OAM. This result shows that a linearly polarized dipole cannot selectively couple to positive or negative OAM modes, while a circularly polarized dipole can.

To understand this unidirectional behavior further we look at the energy dissipated in the TM WGMs written as [114],

$$\mathcal{W}_{lm}^{TM} = \frac{1}{2} \mathcal{R} \{ \mathbf{E}_{lm}^{TM} \cdot \mathbf{d}_{\pm}^* \}. \quad (3.8)$$

where  $\mathbf{E}_{lm}^{TM}$  is the electric field of the  $\text{TM}_{1,lm}$  WGM at the location of the source and  $\mathbf{d}_{\pm}$  is given by Eq. (3.7). The electric TM WGMs fields can be written as [104],

$$\mathbf{E}_{lm}^{TM} = E_{lm,+} \hat{\mathbf{e}}_+ + E_{lm,-} \hat{\mathbf{e}}_- + E_{lm,\theta} \hat{\theta} \quad (3.9)$$

with

$$E_{lm,\pm} = -\frac{1}{2} \sqrt{\frac{\mu_0}{\epsilon_0}} \left[ \frac{l+1}{k_0 r_d} f_l(k_0 r_d) (l \pm m) \mp f_{l+1}(k_0 r_d) \right] Y_{lm}(\theta_d, \phi_d) \quad (3.10a)$$

$$E_{lm,\theta} = -\sqrt{\frac{\mu_0}{\epsilon_0}} \left[ \frac{l+1}{k_0 r_d} f_l(k_0 r_d) - f_{l+1}(k_0 r_d) \right] \frac{\partial Y_{lm}(\theta_d, \phi_d)}{\partial \theta} \quad (3.10b)$$

where  $f_l(k_0 r_d)$  are the spherical Hankel functions of the first kind evaluated at the location of the dipole,  $Y_{lm}(\theta_d, \phi_d)$  spherical harmonics evaluated at the location of the dipole,  $k_0$  free space propagation constant,  $r_d = a + 10\text{nm}$ ,  $\theta_d = \pi/2$ ,  $\phi_d = 0$ , and  $\hat{\mathbf{e}}_{\pm}$  are given by Eq. (3.7). Note that  $E_{lm,+}$  and  $E_{lm,-}$  give spin components along  $-\hat{\theta}$  and  $+\hat{\theta}$ , respectively.

We get from Eq. (3.10),

$$\frac{E_{lm,+}}{E_{lm,-}} = \frac{l(l+1)f_l(k_0 r_d) - m[k_0 r_d f_{l+1}(k_0 r_d) - (l+1)f_l(k_0 r_d)]}{l(l+1)f_l(k_0 r_d) + m[k_0 r_d f_{l+1}(k_0 r_d) - (l+1)f_l(k_0 r_d)]}. \quad (3.11)$$

Note that the terms  $[k_0 r_d f_{l+1}(k_0 r_d) - (l+1)f_l(k_0 r_d)]$  and  $f_l(k_0 r_d)$  are always positive for  $r_d/a \sim 1$ . Therefore we get,

$$\begin{aligned} \frac{E_{lm,+}}{E_{lm,-}} &\leq 1, \quad m \geq 0 \\ \frac{E_{lm,+}}{E_{lm,-}} &> 1, \quad m < 0. \end{aligned} \tag{3.12}$$

This means that according to Eq. (3.8), more energy is dissipated into modes with  $m < 0$  (larger  $E_{lm,+}$ ) for  $\mathbf{d} = \mathbf{d}_+$ , while for  $\mathbf{d} = \mathbf{d}_-$ , more energy dissipates in modes with  $m > 0$  (larger  $E_{lm,-}$ ). Since modes with larger  $E_{lm,+}$  ( $E_{lm,-}$ ) have their spin along  $-\hat{\theta}$  ( $+\hat{\theta}$ ), we can say that the spin of  $m < 0$  ( $m > 0$ ) modes aligns with that of the dipole with  $\mathbf{d} = \mathbf{d}_+$  ( $\mathbf{d} = \mathbf{d}_-$ ). Note that although  $E_{lm,\theta}$  and  $E_{lm,\pm}$  have out-of-phase components, they do not contribute any spin component along  $\hat{r}$  at the location of the source. This means that the photonic spin of the TM WGMs are completely aligning with that of the source.

Using similar expressions and arguments we can show that the dissipated energy into the TE WGMs, as a result of the dipole moment in Eq. (3.7), does not depend on the sign of  $m$  because the radial component of the electric field of the TE WGM is zero. In other words, the TE mode does not show any unidirectional behaviour. Although the photonic spin of the TE mode is parallel to that of the source, the spin of the TE mode is primarily generated by the magnetic field. Since the spin of the source is completely from the electric field (being an electric dipole), a circularly polarized magnetic source should be used to couple to the spin of the TE modes.

Although we have only looked at a particular location of the source, we cannot couple the source to any arbitrary point of the WGMs. This is due to the symmetry of the problem where we essentially choose the  $z$  axis (quantization axis) by placing the source in the vicinity of the sphere. Because the total angular momentum of the problem should be conserved, the quantization axis of WGMs (direction of OAM) aligns with the photonic spin of the source. In other words, changing the orientation of the source would also change the quantization axis of the WGMs. For the case when the circularly polarized dipole has no radial component ( $\mathbf{d}_+ = \frac{d_0}{\sqrt{2}}(\hat{y} + i\hat{z})$  for instance), no spin-momentum locking related phenomenon is observed, as in this case, the spin of the dipole (pointed along  $\hat{x}$  direction) is perpendicular to the spin of the TE and TM WGMs.

This unidirectional behavior can be observed by methods such as tapered fiber coupling (Fig. 3.2) [103, 115] or evanescent coupling [17, 116] to the spherical resonator. By coupling the modes of a tapered optical fiber, for instance, to the WGMs of the sphere, unidirectionally orbiting WGMs of the sphere would couple to the optical fiber modes that

Table 3.1: Summary of the properties of the WGMs

Whispering Gallery Mode	TM <sub>lm</sub> Mode		TE <sub>lm</sub> Mode	
Orbital Angular Momentum	$m > 0$	$m < 0$	$m > 0$	$m < 0$
Spin	along $+\hat{\theta}$	along $-\hat{\theta}$	along $+\hat{\theta}$	along $-\hat{\theta}$
Spin-Momentum-Decay Triplet	Yes		Yes	
Spin-Momentum Locking	Yes		Yes	
Interaction with $\sigma^\pm$ Transitions	$\sigma^-$	$\sigma^+$	No Interaction	

propagate only in a particular direction. Similar methods to those used in [17, 20, 100] for a cylindrical problem can be used to trap the source at a particular distance from the sphere and to excite it at the same time. This structure can be an excellent platform to study different forms of spin-spin interaction between electromagnetic fields, atoms, or electrons. Interaction between sources with non-zero electronic spin and the photonic WGMs can be used to understand the near-field spin-spin interaction between the photons and fermions.

### 3.4 Conclusion

We have presented the theory of spin-momentum locking in 3D whispering gallery modes (WGMs). Our results show that the spin-orbit coupling in WGMs results in modes which form a spin-momentum-decay triplet. This spin-momentum locking property can be observed by coupling the WGMs to the near-fields of  $\sigma$  transitions in a cold atom or quantum dot. The results of this chapter show that  $\sigma^+$  transitions, for instance, only excite TM WGMs with positive OAM. Table 3.1 shows the summary of the results of the chapter. These results are observable through methods such as tapered fiber coupling or evanescent coupling to the WGMs of the sphere. This structure can be used to study more complex forms of interaction between photonic spin and electronic spin or the interaction of multiple sources with the WGMs.

Table 3.2 summarizes the physical parameters of the problem discussed here.

Parameter	radius of the sphere ( $a$ )	source distance from the sphere	dielectric constant of the sphere	resonance wavelength of the TE mode	resonance wavelength of the TM mode
Value	1177nm	10nm	3	$0.54a$	$0.52a$

Table 3.2: Physical parameters of the spin photonics in 3D WGM resonators

## Chapter 4

# Dirac Wire: Fermionic Waveguides with Longitudinal Spin

The interplay of photon spin and orbital angular momentum (OAM) in the optical fiber (one-dimensional waveguide) has recently risen to the forefront of quantum nanophotonics. Here, we introduce the fermionic dual of the optical fiber, the Dirac wire, which exhibits unique electronic spin and OAM properties arising from confined solutions of the Dirac equation. The Dirac wires analyzed here represent cylindrical generalizations of the Jackiw-Rebbi domain wall and the minimal topological insulator, which are of significant interest in spintronics. We show the unique longitudinal spin arising from electrons confined to propagation in a wire, an effect which is fundamentally prohibited in planar geometries. Our work sheds light on the universal spatial dynamics of electron spin in confined geometries and the duality between electronic and photonic spin.

### 4.1 Introduction

Confined solutions of Maxwell's equations exhibit unique phenomena such as transverse photon spin and universal spin-momentum locking [18–20, 94, 95, 100]. These effects do not occur in conventional circularly polarized propagating plane waves where the spin is always directed longitudinally along the momentum vector [107]. One striking example is an optical fiber where Zeeman transitions in a cold atom shows spin-dependent directional photon transport [20, 100]. The goal of this chapter is to introduce the concept of Dirac waveguides and understand the intriguing spin characteristics of confined electronic waves. Our work is motivated by the Dirac-Maxwell correspondence [49, 50, 107] which studies the relativistic parallels between photons and electrons.

Here, we introduce the Dirac wire [see Fig. 4.1(a)], the fermionic dual of the optical

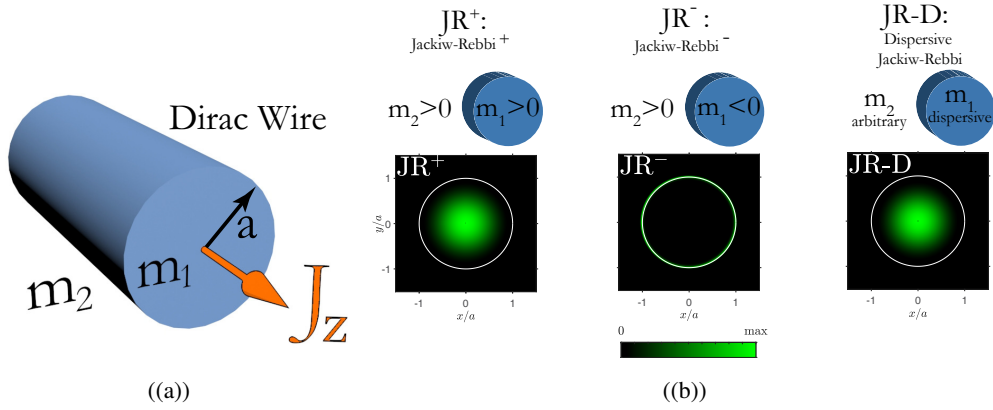


Figure 4.1: (a) Schematic of the Dirac wire. (b) The three Jackiw-Rebbi (JR) type domains considered here are  $JR^+$  with electron mass inside ( $m_1$ ) and outside ( $m_2$ ) the wire both positive,  $JR^-$  with positive mass inside and negative mass outside, and JR-D with a dispersive electronic mass inside [Eq. (4.5)] and an arbitrary mass outside. JR-D corresponds to the minimal topological insulator. Distribution of the probability density,  $\psi^\dagger\psi$ , for the three problems are shown in the three panels of (b). The fields are normalized such that  $\int \psi^\dagger\psi = 1$  when integrated over the entire cross section. Notice that the probability amplitude of the  $JR^-$  state is localized around the perimeter of the wire  $\rho = a$ . Also, in the case of the JR-D problem, the wave function is identically zero at the boundary and outside the wire  $\psi(\rho \geq a) = 0$ .

fiber. This system is the cylindrical generalization of the  $m > 0$ ,  $m < 0$  domain wall introduced by Jackiw and Rebbi [117]; the canonical planar system which spurred the field of topological materials. Important recent work has shown a null expectation value for the relativistic electron spin in the planar Jackiw-Rebbi problem [118]. In stark contrast, the confined geometry of a cylinder supports longitudinal fermionic spin along its axis [119, 120]. For completeness, we also mention that the two-dimensional (2D) photonic dual of the Jackiw-Rebbi domain wall was discovered only recently [121], and is described by the interface of positive/negative gyrotropic media. Comparing Maxwell's equations to the 2D Dirac equation, the gyrotropic non-reciprocity coefficient was shown to play the role of photonic mass [122–124].

The radius of the proposed Dirac wire is on the order of the Compton wavelength of the electron; fundamentally different from the well-known quantum wire limit [125, 126]. We directly capture the relativistic effects of spin-orbit coupling and spin quantization in the spatial dynamics of the electron wavefunction. This allows us to explicitly show the half-integer quantization of the total angular momentum in an inhomogeneous waveguide system. This presents a unique approach to analyzing spin-orbit coupling in confined geometries, compared to traditional bulk energy band structure [127, 128]. Solutions of the

Dirac equation in a cylindrical geometry have been studied in the context of quantum chromodynamics [129], Weyl fermions [119], and electrons in a step potential [120]. Existence of the longitudinal spin component as well as the spin-orbit coupling due to the confinement have been predicted in Refs. [119] and [120]. However the spatial dynamics of spin, as well as the connection to the Jackiw-Rebbi problem in a purely relativistic electronic problem have remained unexplored. Here, we analyze cylindrical generalizations of both the Jackiw-Rebbi domain wall and the minimal topological insulator [130, 131], which will be of interest in spintronics, majorana physics [132–134], and electron quantum optics [135]. Our work also motivates the concept of waveguide spin electrodynamics where the relativistic interaction of confined electrons and photons are manifested through the spin and OAM properties [22, 110].

## 4.2 Dirac Wire

We describe the Dirac wire as a cylinder with an effective electronic mass  $m_1$ , surrounded by a medium with an effective electronic mass  $m_2$  [Fig. 4.1(a)]. The wire radius  $a \approx \lambda_c$  is on the order of the Compton wavelength of the electron  $\lambda_c = h/(m_1 v_F)$ , where  $h$ ,  $m_1$ , and  $v_F$  are the Planck constant, electron mass, and Fermi velocity within the wire, respectively. We introduce three distinct classes of Jackiw-Rebbi (JR) domains labeled as  $\text{JR}^+$ ,  $\text{JR}^-$ , and  $\text{JR-D}$  [Fig. 4.1(b)]. We also show important fundamental differences between cylindrical JR solutions (Dirac wires) and the conventional planar interface problem [117] widely studied in the field of topological insulators and majorana physics [134]. The main differences between the cylindrical and planar JR problems are the emergence of a longitudinal component of spin and the existence of confined solutions for all-positive electronic mass.

For a cylindrical Dirac waveguide, the difference in electronic mass inside and outside the wire gives rise to bound fermionic waves. These solutions can be derived from the time-independent Dirac equation,

$$H\psi_\mu = (v_F \boldsymbol{\alpha} \cdot \mathbf{p} + m v_F^2 \beta) \psi_\mu = E\psi_\mu. \quad (4.1)$$

Eigenstates of the Dirac equation can be identified by five good quantum numbers which correspond to five commuting operators. In cylindrical coordinates, these operators are the Hamiltonian  $H$ , longitudinal total angular momentum  $J_z$ , longitudinal momentum  $p_z$ , transverse momentum  $p_\perp^2$ , and the transverse helicity  $h_\perp$  [129, 136]. The quantum numbers corresponding to these operators respectively are  $E$ ,  $\hbar\mu$ ,  $\hbar k_z$ ,  $\hbar k_\perp$ , and  $s = \pm 1$ , where

$\mu \in \mathbb{Z} + \frac{1}{2}$  is half-integer due to the fermionic nature of electrons. The two solutions corresponding to the two eigenvalues of transverse helicity  $s = \pm 1$  are (see Appendix C and, also, references [29, 136] therein),

$$\mathbf{u}_{\mu, M}^{(\pm)}(k) = \frac{C_\mu e^{ik_z z} e^{i\mu\phi}}{\sqrt{2}} \begin{pmatrix} Z_{n_+}(k_\perp \rho) e^{-i\phi/2} \\ \pm Z_{n_-}(k_\perp \rho) e^{+i\phi/2} \\ \mp i\hbar v_F \frac{k_\perp + ik_z}{M} Z_{n_+}(k_\perp \rho) e^{-i\phi/2} \\ i\hbar v_F \frac{k_\perp + ik_z}{M} Z_{n_-}(k_\perp \rho) e^{+i\phi/2} \end{pmatrix} \quad (4.2)$$

where  $C_\mu$  is the normalization factor,  $M = E + mv_F^2$ ,  $k_\perp = \sqrt{k^2 - k_z^2}$ , and  $n_+ - \frac{1}{2} = n_- + \frac{1}{2} = \mu$ . Here,  $\hbar^2 k^2$  are the eigenvalues of total momentum operator  $\mathbf{p}^2$ , and  $n_\pm \in \mathbb{Z}$  are integers. The  $s = \pm 1$  signs appearing in Eq. (4.2) refer to the eigenvalues of the transverse helicity operator,  $h_\perp$ .  $Z_n(k_\perp \rho)$  is a Bessel function of order  $n$  and argument  $k_\perp \rho$ , where  $\rho$  is the radial coordinate.

The vector spin operator of the Dirac equation is defined as

$$\hat{\Sigma} = \frac{\hbar}{2} \begin{pmatrix} \boldsymbol{\sigma} & 0 \\ 0 & \boldsymbol{\sigma} \end{pmatrix}, \quad (4.3)$$

where  $\boldsymbol{\sigma} = (\sigma_x, \sigma_y, \sigma_z)$  are the Pauli matrices expressed in vector operator form. The longitudinal component of the orbital angular momentum (OAM) operator is

$$\hat{L}_z = -i\hbar \frac{\partial}{\partial \phi}. \quad (4.4)$$

Together with the spin operator, we obtain the longitudinal total angular momentum  $\hat{J}_z = \hat{\Sigma}_z + \hat{L}_z$ . In the subsequent sections we will use these operators to find the expectation values of the spin and orbital angular momentum of the modes.

#### 4.2.1 Cylindrical Jackiw-Rebbi domain wall

We now solve the cylindrical wire geometry with an effective electronic mass  $m_1$  surrounded by a medium with an effective electronic mass  $m_2$ . This is the cylindrical analogue of the 1D Jackiw-Rebbi (JR) domain wall [117, 130, 131]. Unlike the 1D problem, however, solutions of the cylindrical geometry are not limited to the condition  $m_1 m_2 < 0$ . Therefore, we analyze two separate cases; the case when  $m_1, m_2 > 0$  and label it as  $\text{JR}^+$ , and the case when  $m_1 < 0, m_2 > 0$  and label it as  $\text{JR}^-$ .

For the case of  $m_1, m_2 > 0$  ( $\text{JR}^+$ ), solutions of Eq. (4.1) only exist when  $m_2 > m_1$  which requires a larger mass (bandgap) outside the wire to confine the waves. This condition is analogous to total internal reflection in an optical fiber, which necessitates a lower refractive index outside the fiber [137]. For the  $\text{JR}^+$  problem, the solutions are characterized by  $k_{\perp 1}$  real and  $k_{\perp 2}$  imaginary where  $k_{\perp i} = \sqrt{k_i^2 - k_z^2}$  are the transverse (to the

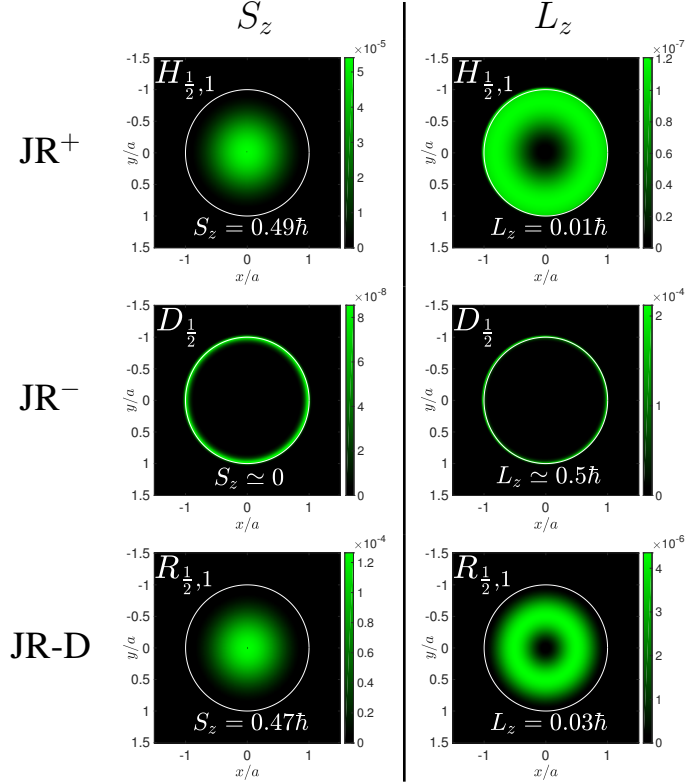


Figure 4.2: Spin and orbital angular momentum densities for the three Jackiw-Rebbi (JR) domains (Fig. 4.1). As an example,  $a = 20 \text{ \AA}$ ,  $\mu = \frac{1}{2}$ , and  $k_z = 0$ .  $|m_1|v_F^2$  and  $m_2v_F^2$  are 1 eV and 2 eV, respectively. For the JR-D problem,  $m_0v_F^2 = 1 \text{ eV}$  and  $B\hbar^2 = 50 \text{ eV\AA}^2$  [138]. In all three scenarios we have assumed a Fermi velocity of  $v_F \simeq 1.52 \times 10^5 \text{ m/s}$ , such that the Compton wavelength is  $\lambda_c \simeq 8 \text{ \AA}$ . The values at the bottom of each figure are the integrated quantities of the respective distribution over the entire cross-section of the problem. Note that the spin and OAM are not individually conserved but their summation ( $J_z = S_z + L_z$ ) is. Although not individually conserved, the difference in the distribution of spin and OAM makes them locally distinguishable. This means that one can, in principle, couple exclusively to spin or OAM locally.

$z$ -axis) propagation constants.  $k_1$  and  $k_2$  being the characteristic wavelengths inside and outside of the wire, respectively. Being comprised of evanescent waves outside the wire and standing waves inside, we denote these solutions as hybrid modes  $H_{\mu,\nu}$ . The subscripts  $\mu$  and  $\nu$  correspond to the total angular momentum eigenvalue and the order of the radial zero of the Bessel function.

Figure 4.1(b) (left panel) shows the amplitude of the wavefunction,  $\psi^\dagger\psi$ , for the dominant  $H_{\frac{1}{2},1}$  mode. Note that for the JR<sup>+</sup> problem, the solutions vanish at  $\rho \rightarrow \infty$  as the wavefunction is evanescent outside the wire. Figure 4.2 (first row) displays the spatial distribution of longitudinal spin and orbital angular momentum densities for this mode. Note that the azimuthal  $\hat{\phi}$  and radial  $\hat{\rho}$  components of the spin and OAM are identically zero –

the angular momentum is purely longitudinal (directed along  $\hat{z}$ ). The integrated values of spin and OAM over the entire  $x - y$  plane is recorded at the bottom of each figure. For the  $H_{\frac{1}{2},1}$  mode these values are not quantized,  $S_z \simeq 0.49\hbar$  and  $L_z \simeq 0.01\hbar$ , respectively. Their sum, however, gives the half-integral value of  $J_z = S_z + L_z = \frac{\hbar}{2} = \mu\hbar$  of the total angular momentum. These results show that while the spin and OAM are not separately conserved quantities, their sum, the total angular momentum, is conserved with an eigenvalue  $\hbar\mu$ . In other words, the wavefunctions  $\psi_\mu$  are also eigenfunctions of the  $\hat{J}_z$  operator [139].

Solutions for the Jackiw-Rebbi Dirac wire with  $m_1 < 0$  and  $m_2 > 0$  ( $\text{JR}^-$ ) are similar to that of the  $\text{JR}^+$  problem with the difference that, in addition to the hybrid  $H_{\mu,\nu}$  modes, another set of solutions exists. These are characterized by decaying solutions outside and inside the wire ( $k_{\perp 1}$  and  $k_{\perp 2}$  both imaginary). We label these waves as decaying  $D_\mu$  modes. In contrast to the hybrid modes, the decaying modes have only one possible solution for a given  $\mu$  and are therefore labeled by only one quantum number. As shown in Fig. 4.1(b) (middle panel), the wavefunction of this mode is predominantly concentrated around the perimeter of the wire and is therefore the cylindrical analogue of the surface states in the planar Jackiw-Rebbi domain [117]. In fact, as shown later, the gapless edge states of the planar geometry emerge when  $a \rightarrow \infty$ . The second row in Fig. 4.2 shows the spatial distribution of longitudinal spin and orbital angular momentum densities of the dominant mode,  $D_{\frac{1}{2}}$ , for the  $\text{JR}^-$  problem. Here also, the spin and OAM are purely longitudinal due to the confinement. This is in stark contrast with the plane wave solutions of Dirac equation where the propagation direction of the electron does not put any constraint on the direction of spin. In the Dirac wire, however, the direction of spin of the electron is fixed by the axis of the wire. The integrated values of spin and OAM give  $S_z \simeq 0$  and  $L_z \simeq 0.5\hbar$ , respectively, which again produces  $J_z = S_z + L_z = \frac{\hbar}{2}$ .

## 4.2.2 Dispersive Jackiw-Rebbi (topological insulator)

We now solve the Dirac Hamiltonian in Eq. (4.1) when the electronic mass inside the wire is dispersive [130, 140],

$$m_1 v_F^2 = m_0 v_F^2 - B \hbar^2 k^2, \quad (4.5)$$

where  $m_0$  is the electron rest mass in the wire and  $B$  is the dispersion factor. Denoted by JR-D, the dispersive mass gives rise to solutions satisfying open boundary conditions ( $\psi_\mu = 0$ ) on the surface of the wire, irrespective of the mass outside. This is confirmed by the plot of the probability density [right panel in Fig. 4.1(b)], where the wavefunction is identically zero for  $\rho \geq a$ . The dispersive mass considered here is the simplest model

that produces the gapless edge states on the surface of a topological insulator [140, 141]. The dispersive mass in Eq. (4.5) gives rise to non-trivial topological properties in the bulk [130] which, according to the bulk-edge correspondence [142], results in the appearance of gapless edge states. Existence of these edge states, irrespective of the surrounding material, implies the open boundary condition where the edge states vanish at the boundary of the topological insulator [143]. It can be shown that the bulk  $\mathbb{Z}_2$  invariant is nontrivial  $(-1)^\zeta = \text{sgn}(-m_0B)$  whenever  $m_0B > 0$ . Hence, the medium  $\rho < a$  is a topological insulator  $\zeta = 1$ . Note, we do not consider the inverse problem in this chapter, where the medium  $\rho > a$  is topological and the wire is treated as a cylindrical defect.

In the JR-D case, the eigenfunctions are of similar form as Eq. (4.2) with the difference that instead of two, there are four eigenfunctions:

$$\begin{aligned} \mathbf{u}_{\mu, M^{(1)}}^{(+)}(k^{(1)}), & \quad \mathbf{u}_{\mu, M^{(1)}}^{(-)}(k^{(1)}), \\ \mathbf{u}_{\mu, M^{(2)}}^{(+)}(k^{(2)}), & \quad \mathbf{u}_{\mu, M^{(2)}}^{(-)}(k^{(2)}), \end{aligned} \quad (4.6)$$

where  $M^{(i)} = E + m_0v_F^2 - B\hbar^2(k^{(i)})^2$  and  $\mathbf{u}_{\mu, M^{(i)}}^{(\pm)}(k^{(i)})$ 's are given by Eq. (4.2). Here  $k_{\perp}^{(i)} = \sqrt{(k^{(i)})^2 - k_z^2}$  with  $k^{(i)}$  being two possible propagation constants within the wire, resulting from the dispersive mass,

$$k^{(1,2)} = \frac{v_F}{\sqrt{2}B\hbar} \left[ (2m_0B - 1) \pm \sqrt{(1 - 4m_0B) + \frac{4B^2E^2}{v_F^4}} \right]^{\frac{1}{2}}. \quad (4.7)$$

Unlike 1D solutions of the topological insulator [130, 131], solutions of the cylindrical JR-D problem exist irrespective of the sign of  $m_0B$ . In this chapter, however, we only consider the scenario when  $m_0B > 0$  since the solutions of the trivial case  $\zeta = 0$  are similar to the  $\text{JR}^+$  domain and are not particularly interesting.

Like the  $\text{JR}^{\pm}$  states, we can label the modes depending on whether the two transverse propagation constants,  $k_{\perp}^{(1)}$  and  $k_{\perp}^{(2)}$  are real or imaginary. Note that  $k_{\perp}^{(1)}$  and  $k_{\perp}^{(2)}$  both belong to the interior of the wire  $\rho < a$  as there are now two characteristic wavelengths [Eq. (4.7)]. In addition to  $H_{\mu, \nu}$  and  $D_{\mu}$ , two other types of modes labeled as  $R_{\mu, \nu}$  and  $C_{\mu, \nu}$  exist in the JR-D problem. These modes refer to real ( $R_{\mu, \nu}$ ) and complex ( $C_{\mu, \nu}$ ) solutions for  $k_{\perp}^{(1,2)}$ , respectively. The third row of Fig. 4.2 shows the spin and orbital angular momenta densities for the dominant mode,  $R_{\frac{1}{2}, 1}$ , of the JR-D problem. Here also, the azimuthal and radial components of the spin and OAM are identically zero – only the longitudinal part is non-vanishing. Due to spin-orbit coupling, the spin and orbital angular momentum are not individually conserved. This means it is difficult to distinguish between the separate contributions of the total angular momentum in an experiment. The spatial

distributions of spin and OAM in Fig. 4.2, however, suggest a way to observe the spin or orbital parts locally. Analyzing the spin and orbital parts of  $R_{\frac{1}{2},1}$  for the JR-D problem, for instance, we observe that while the spin is dominantly at the center of the wire, the orbital angular momentum is zero here and is distributed closer to the perimeter. This shows that using a point contact at the center of the wire, one can exclusively couple to the local spin of the  $R_{\frac{1}{2},1}$  mode where the orbital angular momentum vanishes. This method is in analogy to the approach used in Refs. [20] and [100] where a trapped atom is used to probe the local spin of the photonic field in an optical fiber.

### 4.3 Dispersion of Dirac waveguides

The dispersion relation  $E = E(k_z)$  of the dominant modes is presented in Fig. 4.3(a) and shows significantly larger group velocities for  $JR^-$  and JR-D compared to  $JR^+$ , which implies higher conductivity. Anomalous dispersion for JR-D can be explained by the fact that, due to the dispersive electronic mass, charge transport is dominated by holes rather than electrons. This means that, in the regions where the group velocity becomes negative [inset of Fig. 4.3((a))], charge currents propagate along the negative  $\hat{z}$  direction for  $k_z > 0$ .

As shown in Fig. 4.3((b)), the bandgap in the  $JR^+$  problem plateaus to  $m_1$  (1 eV) for large radii. Since the  $H_{\mu,\nu}$  modes of the  $JR^+$  domain wall are mostly distributed within the bulk of the wire [Fig. 4.1(b)], these modes transform into bulk modes when  $a \rightarrow \infty$ . Note, however, that the spin dynamics in a fully bulk problem would be different from the spin in the  $JR^+$  problem due to the different rotational symmetries of the systems. The rotational symmetry around the  $z$ -axis in the Dirac wire problem would be replaced by the full rotational symmetry in the bulk problem in the limit  $a \rightarrow \infty$ . This means that a deterministic electronic spin along any particular direction would disappear.

For  $JR^-$ , on the other hand, the bandgap closes when  $a \rightarrow \infty$ . This can be explained by the fact that the mode is predominantly distributed around the perimeter of the wire [middle panel of Fig. 4.1(b)]. Therefore, the  $D_{\frac{1}{2}}$  mode transforms into the edge states of the conventional 1D Jackiw-Rebbi problem [117] when  $a \rightarrow \infty$ . The opening of the bandgap in the  $JR^-$  problem, for small wire radius, can be explained by the hybridization of the edge state modes [144].

More interesting is the bandgap of the topological insulator (JR-D) where for some finite values of radii, the bandgap closes and re-opens in an oscillatory fashion with  $a$  [inset of Fig. 4.3(b)]. For JR-D, spin also exhibits oscillatory behavior and passes through regions of

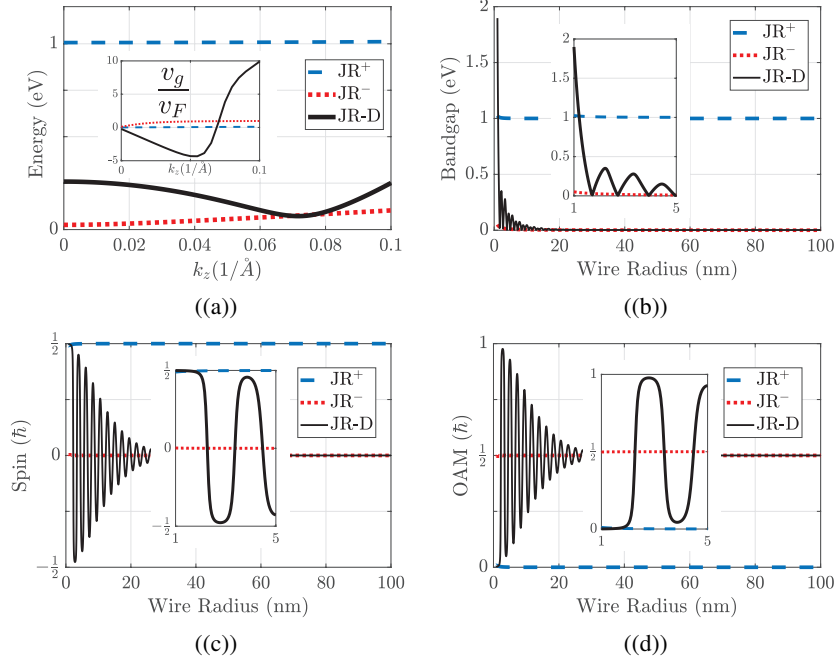


Figure 4.3: (a) Dispersion and group velocities (inset) for the dominant modes of  $JR^+$  (dashed blue),  $JR^-$  (dotted red), and  $JR-D$  (solid black). Group velocities are normalized to the Fermi velocity  $v_F \simeq 1.52 \times 10^5$  m/s. Wire radius dependence of (b) bandgaps, (c) spin, and (d) OAM for the three problems at  $k_z = 0$ . Here  $\mu = \frac{1}{2}$ ,  $k_z = 0$ ,  $|m_1|v_F^2 = 1$  eV,  $m_2v_F^2 = 2$  eV, and  $\lambda_c \simeq 8$  Å. The insets show the zoomed in region of the corresponding figure for wire radius between 1nm and 5nm. For the topological insulator ( $JR-D$ ),  $m_0v_F^2 = 1$  eV and  $B\hbar^2 = 50$  eVÅ<sup>2</sup>. Due to confinement in the cylindrical geometry, the bandgap is opened for all three problems. For  $JR-D$ , however, the bandgap closes and reopens for certain values of  $a$  as seen in the inset of panel (b). Note that the summation  $J_z = S_z + L_z$  produces the conserved value of  $\frac{1}{2}$  in all three cases. In the limit  $a \rightarrow \infty$ , OAM vanishes  $L_z \rightarrow 0$  for  $JR^+$ , while spin vanishes  $S_z \rightarrow 0$  for  $JR^-$  and  $JR-D$ .

positive and negative  $S_z$  upon increasing the wire radius [Fig. 4.3(c)]. However, as  $a \rightarrow \infty$ , angular momentum is dominated by spin for the  $JR^+$  problem and conversely dominated by OAM for  $JR^-$  and  $JR-D$ . This means the dominant  $JR^-$  and  $JR-D$  modes behave like edge states in the limit  $a \rightarrow \infty$  and circulate around the perimeter of the material. Another important observation in Fig. 4.3((c)) is that, although the spin is not conserved in any problem, its absolute value never exceeds  $\frac{1}{2}$ . This holds for all higher orders of  $\mu$  and  $\nu$  as well (see Appendix C. Note also, for all three cases, the total angular momentum is still conserved irrespective of the value of the wire radius.

## 4.4 Conclusion

Our results show important differences between the 1D JR [117, 130] and the cylindrical JR domain walls. In contrast to the 1D problem, the confined geometry of  $JR^\pm$  and JR-D display non-zero longitudinal spin and orbital angular momentum. Moreover, we have shown that a sign change in mass is not necessary for the existence of confined cylindrical solutions of the Dirac equation. Labeled by  $JR^+$ , these Dirac waveguide solutions are the electronic analogue of the guided modes of an optical fiber [137]. This observation makes wire geometry an excellent candidate as a Dirac waveguide, where electronic wave packets can propagate inside the wire with high confinement.

While the experimental observation of these effects is challenging for a wire of this radius, we believe our results will push current techniques further due to their importance in spintronics and electron transport. Topological insulator nanowires of radius  $a = 20$  nm have been reported in the literature [145]. Although the JR-D problem has the simplest model for topological insulators, the parameters used here are within the range of real materials. For  $Bi_2Se_3$ , for instance, a Fermi velocity of  $v_F \simeq 5.0 \times 10^5 m/s$ , a bandgap of about 0.28 eV, and dispersion factor of  $56.6 \text{ eV}\text{\AA}^2$  has been reported [138]. The parameters for other topological insulators such as  $Bi_2Te_3$  and  $Sb_2Te_3$  show that the Dirac wire is realizable using available materials [141]. The surrounding environment can be either vacuum or another material with a bandgap larger than that of the wire. While the difference between the bandgap in vacuum and these materials can be very large, the solutions still exist only with a higher confinement inside the wire. Smaller effective mass ratios between the cladding and core of the wire can be achieved by placing, for instance, the  $Bi_2Se_3$  wires of 0.28 eV bandgap inside or on top of a bulk  $Bi_2Te_3$  material of 0.3 eV bandgap. The study of such possibilities is the subject of more comprehensive future research.

It is important to note that the dispersive mass property in these 3D topological materials arises due to the spin-orbit coupling (SOC). Due to the atomic SOC in the Bi or Se atom, in the  $Bi_2Se_3$  lattice for instance, hybridization occurs between the p orbital of the Bi and Se atoms which results in momentum dependent nature of the effective mass in the model Hamiltonian [141]. This SOC is different from the Dresselhaus SOC [146] – which is mostly concerned with crystals lacking bulk inversion symmetry and consequently give rise only to terms dependent on odd exponents of momentum in Hamiltonian. The materials in the group of  $Bi_2Se_3$  preserve the inversion symmetry and thus the Dresselhaus SOC does not apply to them. The Hamiltonian for the surface states of these topological insulators,

however, resembles that of Rashba SOC Hamiltonian which most commonly applies to 2D materials or boundary of 3D materials where the inversion symmetry is broken perpendicular to the plane of the lattice [141, 147]. A comprehensive study of SOC in these and similar 3D topological insulator materials requires a point group theoretical approach towards the symmetry properties of these lattices and is out of scope of this study. A complete study of the Hamiltonian of materials belonging to the group  $\text{Bi}_2\text{Se}_3$  incorporating SOC interactions can be found in Ref. [141].

Table 4.1 summarizes the physical parameters of the problem discussed here.

Parameter	radius of of the wire	Fermi velocity	Compton wavelength	dispersion constant (JR-D problem)	Fermi energy
Value	$a = 20 \text{ \AA}$	$v_F = 1.52 \times 10^5 \text{ m/s}$	$\lambda_c = 8 \text{ \AA}$	$B\hbar^2 = 50 \text{ eV\AA}^2$	$m_0 v_F^2 = 1 \text{ eV}$

Table 4.1: Physical parameters of Dirac wire problem.

## Chapter 5

# Spin-Momentum Locking in Surface Acoustic Waves

In this chapter, we briefly discuss the local properties of angular momentum in mechanical waves of acoustic waves. We specifically study the Rayleigh-type surface acoustic waves (SAW) propagating on the surface of a slab of lithium niobate ( $\text{LiNbO}_3$ ). By numerically solving the equations of motion for Lithium Niobate, we show that the SAW gives rise to acoustic spin inside the material. Being a piezo-electric material, the propagation of SAW on lithium niobate also gives rise to a gyrating electric field. We show that both the acoustic waves and the gyrating electric field possess spin and have the spin-momentum locking property. This gyrating electric field can be detected and probed using advanced ultrafast nanophotonic techniques. The results of this chapter will be published in collaboration with professor Hubert Krenner. Here we only discuss the theoretical aspect of the spin in SAWs. Experimental methods and details will be accessed through the corresponding journal's portal once the manuscript has been published.

### 5.1 Introduction

Spin-momentum locking is a universal property observed in electromagnetic [94, 95] [22] as well as electronic [87] systems where the momentum of the waves, the decay direction, and the spin form a triplet in which the spin is locked to the momentum [Fig. 5.1(a)]. In condensed matter physics, spin-momentum locking leads to directional spin currents of electrons on the surface of topological insulators. In photonics, this directional transport of energy, dependent on local polarization of evanescent waves, has been observed in quantum dot emission near topological photonic crystals, scattering of surface plasmon polaritons in metasurfaces, and cold atoms coupled to an optical fiber. Moreover, in 2D materials, re-

cent experiments demonstrated that the coupling between the valley pseudospin of tungsten disulfide ( $\text{WS}_2$ ) and the optical spin of plasmons in a silver nanowire results in the directional propagation of circularly polarized excitations [148]. Similar phenomenon has also been observed in magnon modes of a spherical Yttrium Iron Garnett (YIG) resonator where the spin-orbit coupling in the whispering gallery modes leads to a strong nonreciprocity [149]. This opens the intriguing question of observing spin-momentum locking related phenomena in acoustic waves.

Acoustic waves, described by the motion of mechanical degrees of freedom, are fundamentally different excitations compared to photonic modes and fermionic states in electronic structures. Despite this fundamental difference, however, they show similar properties to other forms of waves [150–153], indicating the universal nature of properties such as spin-momentum locking [94]. More specifically, Rayleigh surface acoustic waves (SAWs), exhibit both transverse and longitudinal displacement, with respect to the propagation direction on the surface of a material, with an intrinsic phase difference between these two orthogonal components [154]. This is the manifestation of acoustic spin in Rayleigh SAWs in parallel to photonic edge waves and surface waves; making them an archetypical example of spin-momentum locking of elastic waves. These surface acoustic waves have the potential to be integrated on-chip alongside photonic and electronic technologies. They find a myriad of applications ranging from quantum technologies for information transduction between microwave and optical frequencies to the life sciences [155].

In this chapter, we show the spin-momentum locking for the Rayleigh SAWs. Unlike previous studies where a generic acoustic beam has been studied for spin properties [150, 152], here we have solved for the acoustic waves propagating on the surface of lithium niobate. Having a piezoelectric property, we have shown that the gyrating electric field produced as a result of the SAW on lithium niobate possesses the spin-momentum locking property and thus can be used to probe the spin-momentum locking of the acoustic wave. Our results can be experimentally tested by probing the gyrating electric field using quantum well nanowires placed on the surface of the lithium niobate [156].

## 5.2 Rayleigh Surface Acoustic Waves

Equations of motion for the surface electric and acoustic waves on the surface of a piezoelectric material are solved numerically for one of the technologically most relevant SAW substrate,  $\text{LiNbO}_3$  [154] with the parameters taken from reference [157]. We consider, with

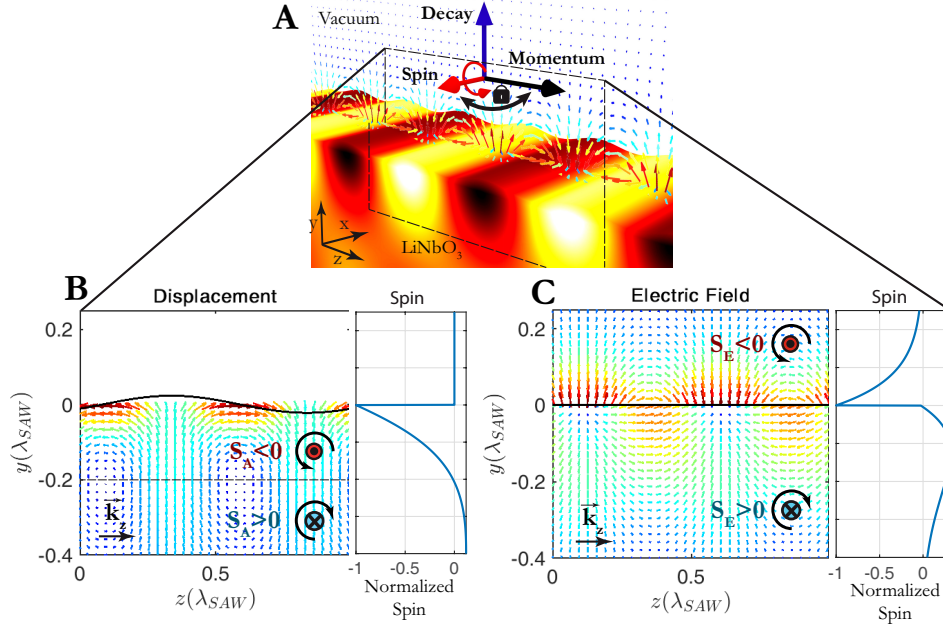


Figure 5.1: (a) Momentum, decay and spin of the gyrating electric field generated by a Rayleigh-type SAW form a right-handed triplet. The direction of spin for both electric field and displacement are locked to the propagation direction. (b) Calculated displacement and (c) electric field (main panels) of the Rayleigh SAW propagating along the Z-direction on a Y-cut LiNbO<sub>3</sub> crystal. The side panels show the normalized magnitude of the transverse spin normal to the surface ( $y = 0$ ). The mechanical spin shows a characteristic sign change at  $\approx \lambda_{SAW}$  below the surface, i.e. from being counterclockwise to clockwise, while the electrical spin changes from counterclockwise to clockwise exactly at the surface.

no loss of generality, that the Rayleigh SAW is propagating along the Z-direction of a Y-cut LiNbO<sub>3</sub> crystal. Equations of motion for acoustic waves in a piezoelectric material are given by [154],

$$c_{ijkl} \frac{\partial^2 u_l}{\partial x_j \partial x_k} + e_{kij} \frac{\partial^2 \Phi}{\partial x_j \partial x_k} = -\rho \omega^2 u_i, \quad i = 1, 2, 3 \quad (5.1a)$$

$$e_{jkl} \frac{\partial^2 u_l}{\partial x_j \partial x_k} - \epsilon_{jk} \frac{\partial^2 \Phi}{\partial x_j \partial x_k} = 0 \quad (5.1b)$$

where  $c_{ijk}$  is the stiffness tensor,  $u_l$  displacement vector indicating the displacement in the material along the three directions,  $\Phi$  the scalar electric potential,  $e_{ijk}$  the piezoelectric tensor relating the electric field components to the displacement vector,  $\rho$  the mass density of the material,  $\omega$  the oscillation frequency of the acoustic wave, and  $\epsilon_{jk}$  the permittivity tensor. Tensor properties of the material depends on the lattice structure and molecular build-up of the unit cells. For lithium niobate, these parameters can be found in [154] and [157]. See Appendix D for more detail.

Solutions of the Rayleigh SAW can be found by using the ansatz  $u_\mu = u_{\mu 0} e^{i(\omega t - kx_3)} e^{\chi k x_2}$ , where  $u_i, i = 1, 2, 3$  are the displacement components and  $u_4 = \Phi$ . Note that  $k$  is the momentum of the wave and  $\chi$  is the decay factor. The equations of motion in Eq. (5.1) have to be solved together with the boundary conditions in order to find the SAW solutions. Assuming that the crystal is a Y-cut lithium niobate, as shown in Fig. (5.1(a)), the interface of the material is normal to the  $y$  axis. Therefore the boundary conditions are

$$T_{i2} = 0, \quad D_{y0} = D_{y1} \quad (5.2)$$

where  $D_{y0}$  and  $D_{y1}$  are the electric displacement fields in vacuum and in the material, respectively. For Rayleigh SAWs we can assume that  $u_1 = \frac{\partial}{\partial x_1} = 0$ , meaning that the displacement component is zero along the  $x$  axis.

Therefore, by solving the Eq. (5.1) together with the boundary conditions Eq. (5.2), we can find the solutions for Rayleigh acoustic waves. We thus find the displacement vector components  $u_\mu$ , electric field components  $E_i$ , as well as the propagation velocity of the wave  $V = \omega/k$ . The solution of these equations is described in detail in Appendix D.

Figures 5.1(b) and 5.1(c) show the displacement and the electric fields found in the sagittal plane (the plane of propagation of SAW, the  $Z - Y$  plane). The displacement field vector indicates the amount of displacement in the crystal of lithium niobate at each point inside the material. The vector  $\vec{k}_z$  shows the direction of the propagation of SAW along the  $z$  axis. The  $y$  axis in both figures indicates the distance from the interface into the material and the vacuum as a function of the SAW wavelength  $\lambda_{\text{SAW}}$ . Note that the SAW wavelength is found to be  $\lambda_{\text{SAW}} = 18 \mu\text{m}$ . Since the same ansatz has been used for both the displacement vector and the electric field, we can conclude that the SAW and the gyrating electric field have the same oscillation frequency, wavelength, and propagation velocity.

The electromagnetic and acoustic spin are given by [106, 108, 109],

$$S_E = \frac{1}{2} \omega \text{Im} \{ \epsilon_0 \mathbf{E} \times \mathbf{E}^* + \mu_0 \mathbf{H} \times \mathbf{H}^* \} \quad (5.3)$$

and [150, 151],

$$S_A = \frac{1}{2} \omega \text{Im} \{ \rho \mathbf{v} \times \mathbf{v}^* \}, \quad (5.4)$$

respectively, where  $\mathbf{v}$  is the velocity vector and is equal to the time-derivative of the displacement vector. In solving the equations for the Rayleigh waves the electrostatic approximation has been assumed. Therefore, the contribution to the electric field spin  $S_E$  comes only from the electric field in our case. The side panels of Fig. 5.1(b) and 5.1(c) show the normalized acoustic and electromagnetic fields as a function of  $y$  coordinate for propagation

along positive  $z$  direction ( $k_z > 0$ ). The acoustic spin analyzed in side panel of Fig. 5.1(b) is pointing out of the sagittal plane close to the interface and it flips sign at about 0.2 wavelength away from the interface as shown by the dashed line. This shows that even though the direction of acoustic spin is locked to the direction momentum, it does not necessarily form a right-handed triplet with the momentum and decay, which is a unique property of Rayleigh-type SAWs. For the electric field spin, however, as shown in the side panel of Fig. 5.1(c), the spin is pointing out of the plane on top of the surface. Therefore, the momentum, decay, and spin form a right-handed triplet as indicated in Fig. 5.1(a). Inside the material, the electric field spin flips together with the decay direction. Thus, the right-hand momentum, decay, and spin triplet are preserved.

These results clearly show the spin-momentum locking in both the electric field and the displacement vector. This means that by changing the direction of the propagation (changing the sign of  $k_z$ ), all of the spin components flip. It is important to note that the electric fields generated here are different from SPPs or surface waves propagating on the surface of metallic interface. While the latter involves high-frequency electromagnetic oscillations, the former contains only electrostatic fields. This means that the gyrating electric field changes slowly with the frequency of the acoustic wave and does not give rise to electromagnetic propagation. All spatial and temporal components of the electric field thus follow the same patterns as the SAW.

### 5.3 Experimental Observation

In this section, we briefly discuss a possible experimental realization. This experiment has been performed by Prof. Hubert Krenner using a method similar to the one used in Ref. [156]. Figure 5.2 shows the experimental setup for the detection of spin of the SAW. The nanowire (NW) is designed such that it has two dislocated quantum wells. By probing the photoluminescence (PL) from the two quantum wells, we are able to track the time-evolution of the electric field, generated by the SAW, locally on the surface of the Lithium Niobate. The SAW is generated by an interdigital transducer (IDT) which is excited by an RF signal of 194 MHz with a wavelength of  $\lambda_{\text{SAW}} = 18\mu\text{m}$ . The NW is placed parallel to the propagation direction of the SAW. As shown in Fig. 5.2, we observe that the electric field spins counter-clockwise with time – demonstrating the electromagnetic spin as shown in Fig. 5.1(c).

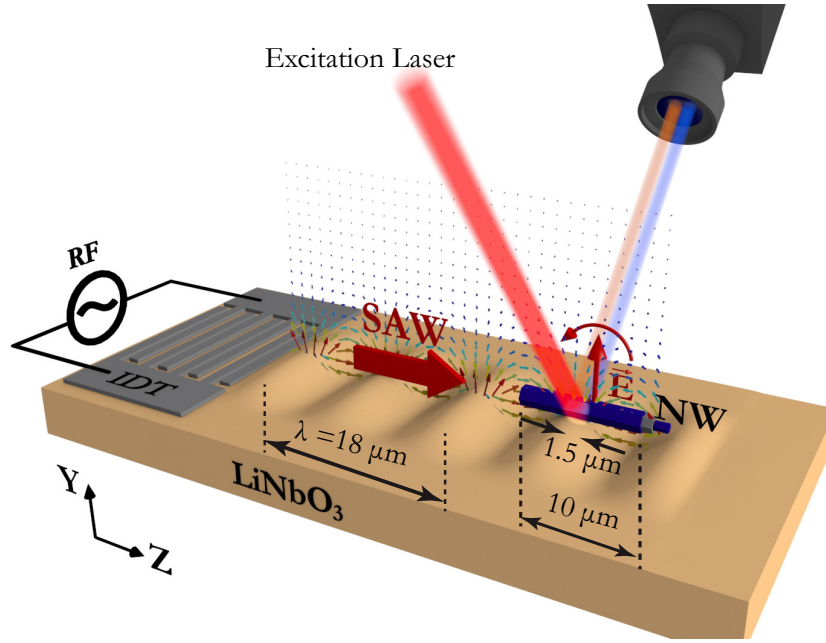


Figure 5.2: Experimental setup for the observation of spin of a Rayleigh-type SAW propagating on the surface of Lithium Niobate ( $\text{LiNbO}_3$ ). By probing PL from the two quantum wells inside the NW, we are able to track the time-evolution of the electric field generated by the SAW and thus confirm the spin of the acoustic wave.

## 5.4 Conclusion

In this chapter, we have shown the local angular momentum property of the surface acoustic waves. We did this by solving the equations of motion for SAWs propagating on the surface of the piezoelectric lithium niobate and evaluating the spin of the acoustic wave as well as the gyrating electric field. We have shown that both the displacement field and the electric field have the spin-momentum locking property meaning that the direction of spin is locked to the propagation direction of the SAW. Since the wavelength of the SAW is much smaller compared to the wavelength of radiation at 194 MHz ( $18\mu\text{m}$ ), the electrostatic approximation has been assumed. We have shown that the electric field has the same time-evolution, wavelength and decay constant as the SAW. Therefore by probing the spin of the electric field we can gain insight into the spin properties of the SAW. These results show the importance of local interaction between nanophotonics and nanoacoustic structures in detecting angular momenta phenomena that are typically challenging to observe.

## Chapter 6

# Colossal Vacuum Radiation from Spinning YIG Nanosphere

Observation of quantum vacuum radiation and quantum vacuum torque is a challenging task due to its negligible effect compared to other dominating effects in various experimental setups. Here we show that a spinning YIG nanosphere in vicinity of a aluminum or YIG slab exhibits colossal quantum vacuum radiation of about 8 orders of magnitude larger compared to other metallic or dielectric spinning nanoparticles. Our result show that, for experimentally feasible rotation speeds and particles sizes, this large quantum vacuum radiation or quantum vacuum torque is manifested in the clear observable effects such as balance rotation speeds or stopping times, for realistic experimental setups.

### 6.1 Introduction

The physics of moving and rotating bodies are gaining more attention as the technological and experimental aspect of this field is achieving higher speeds every day [8, 158]. Besides having implications in the fields of quantum gravity [159], dark energy detection [160] and superradiance [161, 162], trapping and rotation of nanoparticles at GHz speeds is a major breakthrough for the detection of quantum vacuum fluctuations [162, 163]. Although Casimir force, the force acting between plates as a result of quantum vacuum fluctuations, has been measured extensively [164–166], the sensitivity of the tools are only starting to reach the limit needed for the measurement of Casimir torque – the torque exerted on spinning objects as a result of quantum vacuum radiation [167]. Observation of direct consequence of quantum vacuum radiation, on the other hand, still remains a challenge due to intractability of the radiated photons.

Metals are known to exhibit a pronounced magnetic local density of states (LDOS) ,

compared to the electric LDOS, at wavelengths above a few microns down to GHz frequency, due to the dominance of the evanescent  $s$ -polarized over the  $p$ -polarized waves [168]. This leads to a higher coupling between magnetic dipoles and evanescent waves of metals, compared to the electric dipoles, at low frequencies. Moreover, here we show that the dominant magnetic LDOS property at GHz frequencies also extends to magnetic materials. This can have important implications in magnetometry [169] and spin measurements [170].

In this chapter, we investigate a Yttrium Iron Garnet (YIG) nanosphere spinning at 1 GHz frequency in the vicinity of a metallic or YIG interface. With YIG having a magnetic resonance at GHz frequencies [171], and due to the higher magnetic LDOS at these frequencies, the fluctuating magnetic dipoles of the YIG nanosphere couple strongly to the electromagnetic modes of the metallic or magnetic interface and give rise to a colossal quantum vacuum radiation. Emitting radiations of about 8 orders of magnitude larger than any other metallic or dielectric material, in the vicinity of a metallic slab [172], this setup proposes a unique tool for the detection and analysis of quantum vacuum radiation as well as quantum vacuum torque. In fact we show that, for experimentally accessible rotation speeds, particle size, temperatures, and vacuum pressures [8, 173], this large vacuum radiation and vacuum friction has direct experimental consequences. Here it is shown that these effects are readily observed in the balance speed, stopping time, as well as the balance temperature of the spinning YIG.

The source of the energy for this larger vacuum radiation is evidently the non-inertial motion of the sphere, which is transferred as a boost of energy of value  $\hbar\Omega$  to the fluctuating photons of the sphere, as seen from the lab frame. For a stationary sphere and equilibrium temperatures, the number of photons emitted by the fluctuating dipoles of the sphere is equal to the number of photons emitted by the fluctuating fields of the vacuum which are absorbed by the sphere; resulting in a net zero radiation. However, when the sphere is rotating, due to the extra boost of energy from mechanical rotation, the balance between the emitted and absorbed photons is broken and there is a net radiated power coming from the sphere [174]. This energy goes mostly into the lossy surface waves in both metallic and magnetic materials [175]. However, if the magnetic material is properly biased, as it is the case studied here with a bias magnetic field of 812 Oe for the YIG slab, the magnetic resonance in the magnetic slab can become resonant with the magnetic resonance in the magnetic sphere – meaning that most of the energy is transferred to surface magnon polaritons.

## 6.2 Quantum Vacuum Radiation

While in absence of any interface the spinning YIG particles do not present any substantial enhancement in the vacuum radiation, the presence of a metallic or magnetic interface drastically changes this observation (Fig. 6.1). While metallic particles are known to possess higher radiation rate compared to dielectric particles [174], here we observe that magnetic particles exhibit an even larger radiation rate, of about 8 orders of magnitude, compared metallic particles.

Using a similar approach to the methods used by Abajo and Manjavacas [162], we find the radiated power due to the magnetic fluctuations to be,

$$P_{\text{mag}} = \int_{-\infty}^{+\infty} \hbar\omega d\omega \Gamma^{\text{H}}(\omega) \quad (6.1)$$

where  $\Gamma^{\text{H}}(\omega)$  is the spectral density function due to magnetic dipole fluctuations given by (see Appendix E),

$$\Gamma^{\text{H}}(\omega) = (\omega\rho_0/8) \left\{ \begin{aligned} & \left[ g_{\perp,2}^{\text{H}}(\omega) + 2g_{\parallel}^{\text{H}}(\omega) + 2g_{g,2}^{\text{H}}(\omega) \right] \left[ \text{Im} \{ \alpha_{m,\perp}(\omega^-) \} - \text{Re} \{ \alpha_{m,g}(\omega^-) \} \right] \times \\ & \left[ n_1(\omega^-) - n_0(\omega) \right] \\ & + g_{\perp,1}^{\text{H}}(\omega) \text{Im} \{ \alpha_{m,\parallel}(\omega) \} \left[ n_1(\omega) - n_0(\omega) \right] \end{aligned} \right\} \quad (6.2)$$

where  $\rho_0 = \omega^2/c^2\pi^3$  is the vacuum density of states,  $g_{\perp,1}^{\text{H}}, g_{\perp,2}^{\text{H}}$  are the two perpendicular components of the magnetic Green's function in the plane of the interface (in this case the  $xx$  and  $zz$  respectively),  $g_{\parallel}^{\text{H}}$  the component normal to the interface ( $yy$  component here), and  $g_{g,2}^{\text{H}}$  the off-diagonal  $xy$  component (here between one in-plane and the normal component), all normalized to  $\pi\omega\rho_0/8$ .  $\alpha_{m,\perp}(\omega)$ ,  $\alpha_{m,g}(\omega)$ , and  $\alpha_{m,\parallel}(\omega)$  are the  $xx$  (or  $yy$ ),  $xy$ , and  $zz$  components of the magnetic polarizability tensor in the frame of the rotating sphere, respectively, where  $\omega^- = \omega - \Omega$  [162, 171, 176].  $n_1(\omega)$  and  $n_0(\omega)$  are the Planck's distributions pertinent to temperatures  $T_1$  and  $T_0$  of the sphere and the environment, respectively.

Due to the conservation of energy, the radiated power is equal to minus the change in the stored electromagnetic energy in the magnetic dipole moments. Therefore the total radiated power is found by finding the time-derivative of the inner product of the induced magnetic field due to the magnetic dipole fluctuations and the dipole fluctuations as well as the inner product of the induced magnetic dipoles due to the magnetic field fluctuations and the magnetic field fluctuations. Writing the induced dipole moments and fields in terms

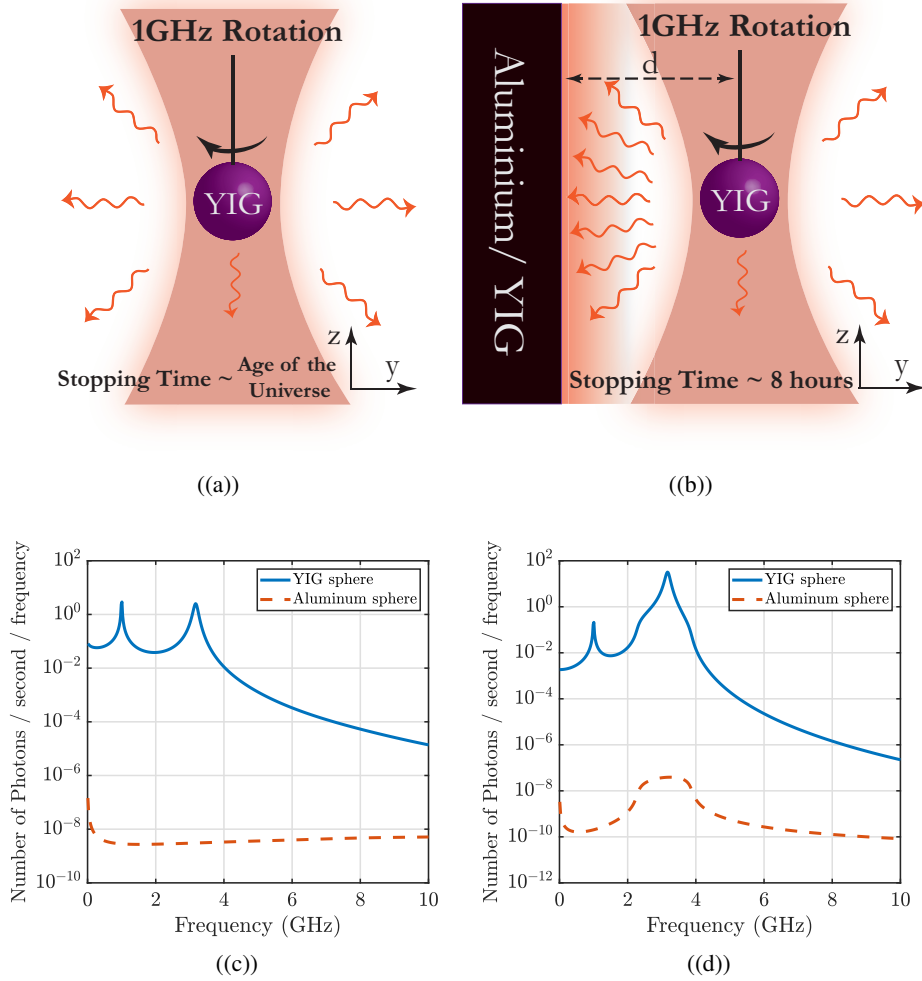


Figure 6.1: (a) A YIG sphere trapped in the laser beam and spinning at 1 GHz rotation frequency in vacuum. The stopping time for the sphere is on the order of age of the universe. (b) YIG sphere spinning the vicinity of an Aluminum or YIG interface exhibits colossal quantum vacuum radiation. The stopping time, due to the presence of the interface, is reduced to about 8 hours. (c) Number of photons emitted per second per radiation frequency, defined as  $\frac{1}{\hbar\omega} dP/d\omega = \Gamma(\omega) - \Gamma(-\omega)$ , for a YIG (blue solid curve) and Aluminum (dashed orange curve) nanosphere of radius 200 nm in the vicinity of an Aluminum slab, and (d) in the vicinity of a YIG slab. For the Al slab, non-local model has been used. The YIG slab in panel (d) is biased along y direction (panel (a)) with a magnetic field of  $H_0 = 812$  Oe. The distance between the sphere and both interfaces is chosen to be  $d = 0.5\mu\text{m}$ .

of the magnetic dipole and field fluctuations, and using the fluctuation-dissipation theorem (FDT) for finding the radiated energy due to the fluctuating dipoles and fields, we arrive at the total radiated power expression in terms of the Green's function, Planck's distribution, and polarizability tensor, as given by Eqs. (6.1) and (6.2). Note that all of the expressions are written in the lab frame. Therefore coordinate transformation between the rotating frame of

the sphere and the lab frame has been performed when necessary. A detailed derivation for all of these quantities, along with various orientations and bias magnetic field directions for the YIG interface, are provided in Appendix E.

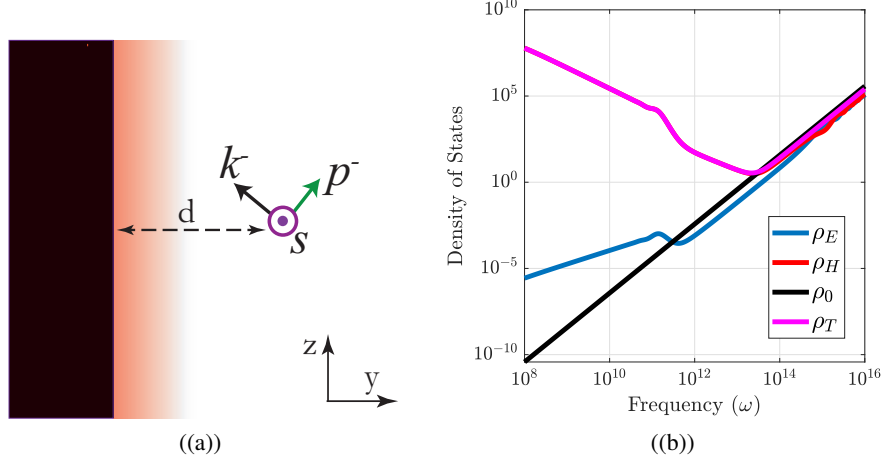


Figure 6.2: (a) Schematic for the  $s$  and  $p$  polarization. The  $k^-$  vector shows the propagation direction for waves propagating along  $-z$  direction.  $s$  and  $p^-$  polarization are defined with respect to this propagation direction. Similarly,  $k^+$  and  $p^+$  vectors can also be defined for waves propagating along  $+z$  direction. (b) Plots of the electric ( $\rho_E$ ), magnetic ( $\rho_H$ ), and total ( $\rho_T$ ) LDOS for a distance of  $d = 0.5\mu\text{m}$  from an Al interface. Note that non-local model has been used for the Al. As shown, the total LDOS is dominated by the magnetic LDOS since it is about 12 orders of magnitude larger than the electric LDOS.

As shown in Fig. 6.1(c) for Aluminium interface, and Fig. 6.1(d) for YIG interface, the radiation from spinning YIG sphere (blue curves) is much larger than that of the Al sphere (orange curves). This is explained by the difference in the electric and magnetic local density of states (LDOS) in the vicinity of a metal interface. As shown by Joulain *et al.* [168], LDOS is dominated by the magnetic LDOS at wavelengths above a few microns. We have extended this observation to GHz frequencies and taken into account the effect of non-locality in Al [175] (see Appendix E).

The reason behind higher magnetic LDOS at low frequencies is the difference in the reflection coefficients of the  $s$  and  $p$  polarizations (Fig. 6.2(a)). For the electric field, the LDOS is generally dominated by the  $p$  polarization for the evanescent fields since evanescent  $p$  polarized fields have stronger dependence on the momentum of the modes than  $s$  polarization. For the magnetic field the opposite is true since the magnetic field is perpendicular to the electric field and thus the contribution from the  $s$  polarization is dominant. Now, at GHz frequencies, the imaginary part of the  $s$  polarization reflection coefficient is close to unity meaning that the  $s$  polarized fields get reflected while for the  $p$  polariza-

tion the reflection is close to zero. Thus the  $s$  polarization contributes more to the LDOS than  $p$  polarization and since only the magnetic LDOS is dominated by  $s$  polarized evanescent fields, as discussed above, the magnetic LDOS is dominant at these frequencies for evanescent fields. Figure 6.2(b) shows the electric, magnetic, total, and vacuum LDOS for a distance of  $d = 0.5\mu\text{m}$  from an Al interface. As shown, the total LDOS is dominated by the magnetic LDOS since it is about 12 orders of magnitude larger than the electric LDOS at about GHz frequencies. Also, as shown, LDOS in presence of Al interface is about 16 orders of magnitude larger than the vacuum LDOS  $\rho_0$ . For a more in depth study of the LDOS in presence of metallic interfaces refer to the Ref. [168].

An important fact regarding spinning YIG is magnetization of the nanosphere due to the rotation in absence of any external magnetic field. Known as the Barnett effect, this occurs due to the conservation of angular momentum where the mechanical angular momentum of the sphere is transferred to the spin of the unpaired electrons in the magnetic material [177]. It is concluded that the Larmor precession frequency of the electrons inside the sphere, assuming that the magnetic field is parallel to the rotation axis, is given by [171],

$$\omega_0 = \Omega + \mu_0\gamma H_0 \quad (6.3)$$

for the rotation frequency  $\Omega$ , gyromagnetic ratio of the electron  $\gamma$ , vacuum permeability  $\mu_0$ , and applied external magnetic field  $H_0$ . This expression shows that, in absence of any external magnetic field, the nanosphere is magnetized with the Larmor frequency  $\Omega$ .

Radiated photons per second per frequency are calculated in Appendix E using the expressions given in Eqs. (6.1) and (6.2) for the radiated power as a function of frequency written in terms of positive frequencies only. This is expressed through  $\Gamma(\omega) - \Gamma(-\omega)$ , with  $\Gamma(\omega)$  being defined as the spectral distribution of the rate of emission or absorption [162], where the FDT is used as discussed above. Figures 6.1(c) and 6.1(d) show the total radiated photons per frequency per second for the case when the Al or YIG interface are in the  $x - z$  plane. We find that in the case of Al interface Fig. (6.1(c)), spinning YIG sphere radiates about 6 femto-Watts of power, compared to the Al sphere which radiates about  $6 \times 10^{-7}$  femto-Watts. In the case of a YIG interface, on the other hand, we find about 61.3 femto-Watts and  $4.63 \times 10^{-7}$  femto-Watts of radiated power for YIG and Al spheres, respectively. These results clearly show the advantage of YIG over Al nanoparticles for probing quantum vacuum radiation.

### 6.3 Quantum Vacuum Torque

We used a similar approach to find the vacuum torque exerted on the sphere [174] due to magnetic dipole and magnetic field fluctuations. The torque along the axis of rotation is given by  $M_z = \int_0^\infty d\omega \hbar [\Gamma_M^H(\omega) + \Gamma_M^H(-\omega)]$ , where the expression for  $\Gamma_M^H(\omega)$  is similar to the expression for  $\Gamma^H(\omega)$  in Eq. (6.2) with the difference that the last term on the second line is not present in  $\Gamma_M^H(\omega)$  [162]. One interesting fact about the case when the particle is spinning in vicinity of the YIG slab is that the other components of the torque ( $M_x$  and  $M_y$  components) are not necessarily zero as it is for the Al slab. Due to the anisotropy of the YIG slab,  $M_x$  and  $M_y$  do not vanish for some directions of the bias magnetic field. These cases are studied in Appendix E.

Figure 6.3 compares vacuum torques for the spinning YIG sphere (Figs. 6.3(a) and 6.3(c)) to vacuum torque for spinning Al sphere (Fig. 6.3(b) and 6.3(d)), sphere spinning in vicinity of YIG slab (Figs. 6.3(a) and 6.3(b)) and Al slab (Figs. 6.3(c) and 6.3(d)), as well as spinning in vicinity of slabs (solid colored curves) versus spinning in vacuum (dashed black curves). These figures show more than 10 orders of magnitude enhancement in the vacuum torque in the presence of YIG and Al slabs compared to the vacuum, and about 4 orders of magnitude enhancement due to use of YIG sphere compared to Al sphere. These results show the advantage of coupling to magnetic LDOS than the electric LDOS for the investigation of quantum vacuum torque at GHz frequencies. Note that in these figures the model used for the Al interface is a non-local model [175]. Moreover, these results include the torque due to magnetic and electric dipole and field fluctuations. However, note that in all cases the vacuum torque is dominated by the magnetic rather than the electric fluctuations (see Appendix E for more detail). Also, we have taken into account the effect of recoil torque [78] — the torque exerted on the sphere due to the scattering of vacuum field fluctuations off the particle. Being a second order torque, however, its effect is negligible compared to the effect of magnetic fluctuations for the studied cases (see Appendix E).

### 6.4 Experimental Considerations

The observation of consequences of quantum vacuum radiation and quantum vacuum torque comes down to the changes observed in the parameters of the experiments as a result of bringing the Al/YIG interface in the vicinity of the spinning particle. Figure 6.4(a) shows the proposed experimental setup for this observation where a YIG nanoparticle is trapped inside a Al or YIG ring. Note that the size of the ring is much greater than that of the particle

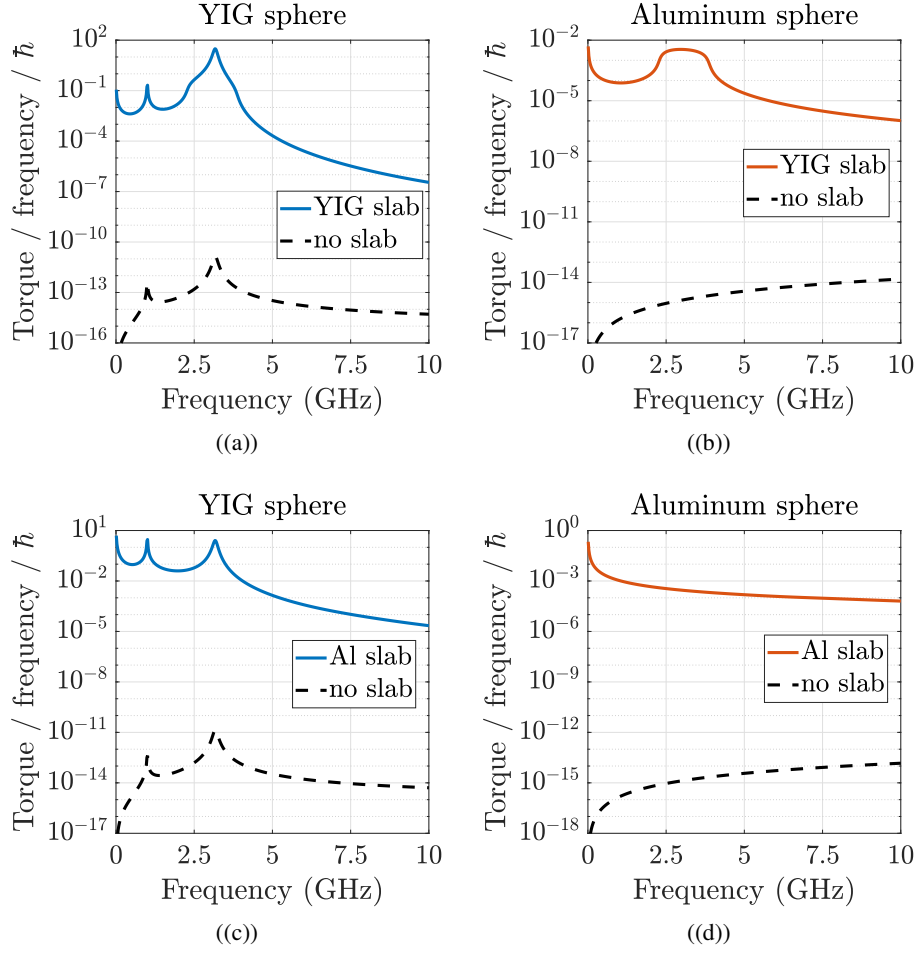


Figure 6.3: The negative quantum vacuum torque experienced by a YIG and Aluminum nanosphere of radius 200 nm at room temperature. (a) Torque experienced by a YIG sphere in vicinity of YIG slab (solid blue curve) and in vacuum (dashed black curve). (b) Torque exerted on an Al sphere in vicinity of YIG slab (solid orange curve) and in vacuum (dashed black curve). (c), (d) the same as (a) and (b) with YIG slab replaced by an Al slab. The YIG slab is biased along  $y$  direction with  $H_0 = 812$  Oe (see Fig. 1(a)). A non-local model is used for the Al slabs. The distance between the spinning spheres and slabs is  $d = 0.5\mu\text{m}$  for all cases. Placing the YIG or Al interface in vicinity of spinning sphere results in about 12 orders of magnitude increase in the exerted quantum vacuum torque.

and it does not lead to any resonant behaviour. However, for smaller ring size, LDOS can be further enhanced compared to the slab interface due to the presence of the interface on all sides.

We evaluated some of the observable experimental outcomes due to the higher quantum radiation and friction. This analysis is based on the values obtained from the experiments in Refs. [8, 173, 178]. Figure 6.4(b) shows the balanced rotation speed  $\Omega_b$  of the sphere, normalized to the rotation speed in the absence of any interface  $\Omega_0$  as a function of distance

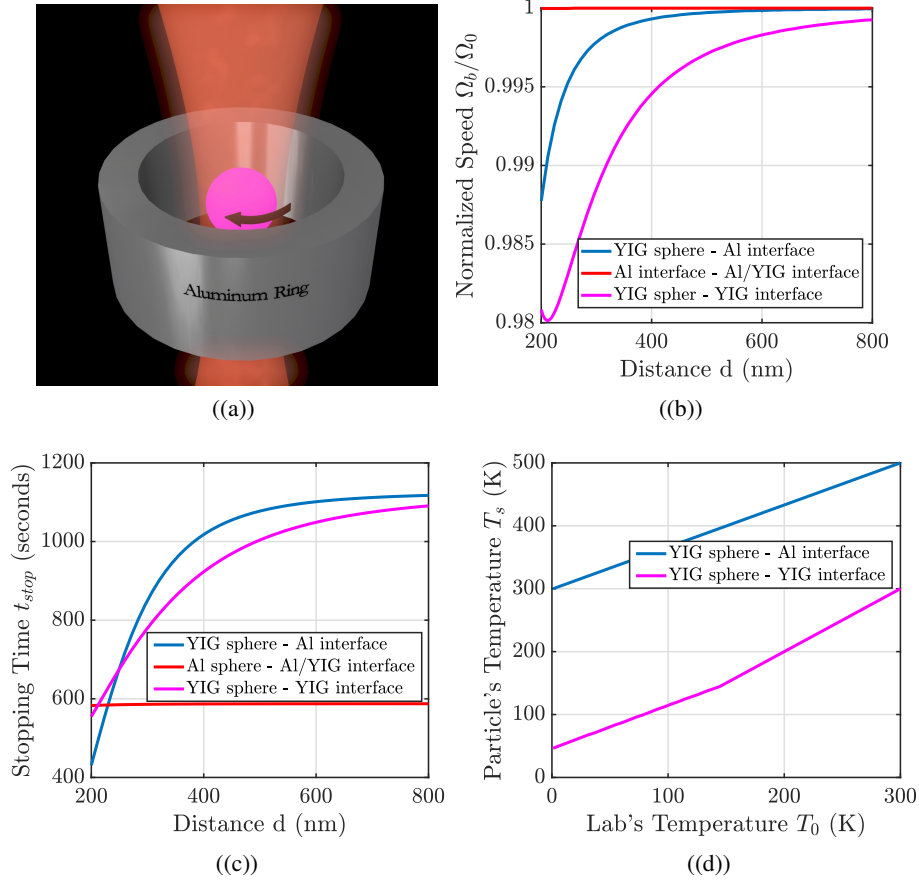


Figure 6.4: Experimental considerations of the setup. (a) Proposed experimental setup with nanosphere trapped inside a ring. (b) Balance speed  $\Omega_b$  for Al sphere (red curve) and YIG sphere in presence of Al (blue curve) and YIG (pink curve) interfaces, as a function of distance  $d$  from the interface for a 200 nm radius sphere at  $10^{-4}$  Torr vacuum pressure. The values are normalized to the vacuum balance speed  $\Omega_0$ . (c) Characteristic stopping time as a function of distance from the interface at vacuum pressure of  $10^{-6}$  Torr. (d) Balance temperature of the YIG sphere  $T_s$  at  $d = 500$  nm distance from Al (blue curve) and YIG (pink curve) interface as a function of lab temperature  $T_0$ , at vacuum pressure  $10^{-4}$  Torr. For Al interface there is no final temperature as the temperature keeps raising with time.

$d$  from the interface. In absence of any interface, due to the negligible value of quantum vacuum radiation, the balance rotation speed is obtained when the torque due to the trapping laser balances the negative drag torque due to the imperfect vacuum [8]. This indicates that the lower the vacuum pressure, the higher the rotation speed is going to be. Taking the driving torque to be constant and the drag force to have a simple linear velocity dependence [8], Fig. 6.4(b) shows that the balance rotation speed of the YIG sphere is reduced when the Al (blue curve) or the YIG (pink curve) interface is brought closer to the sphere, due to the negative torque resulting from vacuum fluctuations. Note however that, for the spinning Al

sphere in the vicinity of Al or YIG sphere (red curve), no observable change in the balance speed is manifested.

This signature is apparent in other experimental observables such as the stopping time as a function of distance (Fig. 6.4(c)) and the balance temperature of the sphere as a function of the vacuum temperature  $T_0$  (Fig. 6.4(d)). These results show that the quantum vacuum radiation and quantum vacuum torque can be experimentally measured through the measurement of the balance speed, balance temperature, and stopping time of the YIG nanoparticle. The Al particle (or any other metallic particle) however may not experience enough vacuum fluctuations to exhibit observable outcomes, unless for a very sensitive setup with very low vacuum pressure [8, 167].

## 6.5 Conclusion

Our results show that due to the dominance of magnetic LDOS over electric LDOS in the vicinity of metallic or magnetic materials in the GHz range, spinning magnetic materials can exhibit orders of magnitude larger quantum vacuum radiation and quantum vacuum torque compared to any metallic or dielectric material. By investigating the case of a YIG nanosphere spinning at 1 GHz speed, we have shown that the effect of quantum vacuum fluctuations are easily observed in a reasonably prepared experimental setup. These results set a new perspective for the observation and understanding of quantum vacuum fluctuations.

Table 6.1 summarizes the physical parameters of the problem discussed here.

Parameter	sphere radius	distance from the interface	rotation speed	bias magnetic field of the YIG interface	temperature
Value	$a = 200 \text{ nm}$	$d = 0.5 \mu\text{m}$	$\Omega = 1\text{GHz}$	$H_0 = 812 \text{ Oe}$	$T_0 = 300 \text{ K}$

Table 6.1: Physical parameters of the YIG nanosphere spinning in vicinity of the aluminum or YIG interface

## Chapter 7

# Conclusion and Future Work

In this chapter, we conclude our work by recapitulating the main points of the thesis. We further discuss possible future directions regarding the research in this area.

### 7.1 Conclusion and Summary

In this work we discussed the important implications of the emerging field of spin photonics. With a focus on local light-matter interactions, we discussed the importance of evanescent fields in providing various experimental possibilities and the role of angular momentum in the near-field interactions. We have presented for the first time a local conservation of angular momentum equation applicable to the light-matter interactions. We have moreover shown the importance of local interactions by studying a variety of systems incorporating the role of angular momentum in near-field interactions.

In chapter 2 we started from the QED Lagrangian and investigated its symmetry properties using Noether's theorem. With a focus on rotational symmetries of the full Lorentz transformation, in combination with the well-known angular momentum related terms such as spin, OAM, chirality, and helicity, we presented a set of new quantities that are responsible for the transfer and propagation of angular momentum. We further showed that these terms are connected through a local conservation equation. The new terms, such as spin-orbit torque and angular momentum current tensors, shed light on the local dynamics of near-field interactions. A complete understanding of the dynamics of the angular momentum of light-matter interactions in geometries with tight light confinement, such as optical fibers and SPPs, require this local treatment of angular momentum.

We explored the local interactions by studying the coupling of  $\sigma^\pm$  Zeeman transitions of a quantum source to a spherical resonator. By placing the quantum source in the evanescent fields of the WGMs of the resonator, we were able to demonstrate non-symmetric behaviour

that are manifested exclusively in the local, evanescently coupled, interactions.

The local properties of the angular momentum was further investigated for the confined electronic modes in chapter 4. We analyzed the solutions of the Dirac equation in the cylindrical geometry of a wire, made of a material with an effective electronic mass different than that of the surrounding. Calling this geometry a Dirac wire we showed that due to this confinement, electronic spin emerges along the axis of the wire. We have shown that this longitudinal spin emerges only in the confined geometry and vanishes as the size of the wire is increased.

Chapter 5 discussed the local angular momentum properties of mechanical waves. By finding the solutions of Rayleigh surface acoustic waves propagating on the surface of a slab of Lithium Niobate, we showed that the mechanical oscillations of the SAW also manifest spin-momentum locking property usually observed in the nanophotonic or electronic structures. This acoustic spin can be experimentally tracked by probing the gyrating electric field from the piezo-electric Lithium Niobate using a nanowire with a quantum well structure.

In chapter 6 we demonstrated an important consequence of local interactions between magnetic dipoles in a YIG sphere and optical modes of a metallic or magnetic material. When the sphere is spinning, due to the imbalance between the emitted and absorbed photons, the sphere emits radiations – transferring the mechanical energy of the particle to the energy of quantum vacuum radiation. While this has been a known effect for a long time, quantum vacuum radiation is usually very small compared to the noise levels which makes it hard to detect. We showed that by bringing a metallic or magnetic interface into the near-field of the YIG sphere, this radiation can be greatly enhanced. Our results show that, due to this colossal enhancement, the effect of quantum vacuum radiation and quantum vacuum torque can be experimentally observed; making this result a breakthrough in the field of quantum vacuum radiation.

## **7.2 Future work**

In this section, we briefly discuss the research directions that can be taken following the results presented in this work.

### **7.2.1 Study of Local Angular Momentum Electrodynamics**

In chapter 2, we discussed the importance of local conservation laws of angular momentum in describing near-field light-matter interactions. However, except for the two simple

electromagnetic problems discussed, we did not study a light-matter interacting system that can put these local laws into test. The platforms discussed in section 1.2 are a good starting point for this study. These platforms include atomic or quantum dot sources, with quantized transitions, trapped in the near-field of a photonic structure. Examples of these photonic structures include 2D or 3D optical resonators, optical fibers, SPPs, or photonic crystals where due to the confined light property near-field local light-matter interactions between the quantum source and optical modes can be probed.

Such systems will be studied in a future work and the local angular momentum dynamics of the optical and electronic fields will be analyzed. Due to the small size of atomic structures compared to currently available probes, local measurement of electronic spin is still a challenging task. However, measurement of local properties of optical fields are more feasible with the current technologies and, as discussed in section 2.5, a semi-local approach can reveal the importance of a local approach towards the angular momentum dynamics.

In addition to the methods discussed in section 1.2, a variety of methods are used to measure local properties of optical fields. Among these, nitrogen-vacancy center (NV center) in diamond lattices are promising nanoscale probes with nano-Tesla magnetic field sensitivity [179, 180]. NV centers are point defects in the crystal of diamond which give rise to a local multielectron system with stable energy transitions. Due to Zeeman splitting, a minuscule magnetic field can shift these energy transitions which then can be observed through the narrow-band photoluminescence of these transition. Experiments are currently being performed at our group, at Purdue university, where NV centers are used for the detection of optical spin and optically induced fictitious magnetic fields [181, 182].

### **7.2.2 Angular Momentum of Quantum Vacuum Radiation**

Chapter 6 discussed the importance of local interactions between a metallic or magnetic slab and the magnetic dipoles in a spinning YIG nanosphere. Our results showed a substantial increase in the quantum vacuum radiation due to this local coupling. However, properties of this radiation, such the radiation direction and polarization, were not discussed in that chapter.

This study requires calculation of Poynting vector and finding the angular momentum in the radiation. Although mathematically demanding, such a calculation would shed light on the transfer of angular momentum between the mechanical motion and the optical radiation. Instead of finding the field and dipole fluctuations only at the location of the sphere, this treatment requires an evaluation of these fluctuations at every point in space and then a

calculation of the Poynting vector [183]. This analysis will contribute to the emerging field of thermal spin photonics [184].

### 7.2.3 Two-body Dirac Equations

The conservation equations of chapter 2 are based on the Dirac equation which is a single-electron equation in the sense that it does not incorporate electron-electron interactions. While the conservation laws derived from this equation accurately describe the dynamics of angular momentum for optical fields interacting with a source modeled by a single electron, more complex interactions such as electron-electron interactions mediated by emission of photons or near-fields are not captured by this treatment.

In order to apply the method of chapter 2 to the problem of two-body fermionic system, the Lagrangian of the system is essential in deriving the angular momentum dynamics equation. Such an equation was initially proposed by Breit [185], where he extended the Dirac equation to include two sets of fields for two electrons plus an interaction Darwin term. Although successful in explaining magnetic effects, this equation is first order perturbative in QED and is not Lorentz invariant.

Beth and Salpeter proposed the famous Beth-Salpeter Hamiltonian which takes a full quantum field theory approach [186]. It is Lorentz invariant and has found applications in a wide range of areas from condensed matter to AMO and high energy physics. However, It was shown by Nakanishi [187] that the Beth-Salpeter equation gives rise to negative-norm solutions due to the relative time degree of freedom.

This problem was alleviated by Sazdjian [188] as well as Crater and Alstine [74], by writing two simultaneous Lorentz invariant Dirac equations for each of the two interacting fermions named two-body Dirac equations (TBDEs) . All of these methods for many-body interactions are being currently incorporated depending on the application and range of validity of the theory. Due to their manifest Lorentz covariance nature, TBDE are a good starting point for the investigation of symmetry properties and angular momentum dynamics in an interacting many-body electronic system. This study would shed light on the mechanism through which two electrons transfer angular momentum.

### 7.2.4 Atomic Selection Rules in Near-Field Interactions

Atomic transitions in vacuum are dominated by the electric dipolar transitions where there is a strong coupling between the dipolar field distribution of the atom and the free photon field. Because of a weaker coupling between the atom and radiation, higher order multi-

polar transitions (e.g. magnetic dipole, electric quadruple, magnetic quadruple, and so on) are orders of magnitude slower compared to the electric dipole transition. For instance, magnetic dipole transitions are about  $1/137$  slower than electric dipole transitions in a Hydrogen atom [189]. Due to the fact that atomic transitions are dominated by the electric dipole, higher order transitions are considered *forbidden*.

In a study by Rivera *et al* [24], it was shown that forbidden atomic transitions can be greatly enhanced by bringing the atom close to a surface with high LDOS through evanescent coupling with surface modes. This happens due to the matching between the field profile of the evanescent fields and higher atomic transitions. This leads to a stronger coupling between multi-polar electronic wavefunction profiles and the electromagnetic field. These higher order transitions can become as large as the electric dipole transitions and thus are experimentally more accessible.

Selection rules are quantum mechanical rules governing allowable atomic transitions based on the conservation of angular momentum as well as wave properties of the electronic wavefunction. Since these selection rules are governed by the electric dipole transition, it is expected that these rules would also change by coupling to electromagnetic evanescent waves. Atomic multipolar transitions are governed by different set of selection rules compared to the electric dipole transitions. Therefore, by enhancing the multipolar transitions in near-field couplings, atomic selection rules normally dominated by the electric dipole transitions can be altered by the multipolar selection rules [189].

# Bibliography

- [1] J. B. Scarborough, *The Gyroscope*. New York: Interscience Publ., 1958.
- [2] W. M. Macek and D. T. M. Davis, “Rotation rate sensing with traveling-wave ring lasers,” *Applied Physics Letters*, vol. 2, no. 3, pp. 67–68, 1963.
- [3] C. Kittel and P. McEuen, *Introduction to solid state physics*. Wiley New York, 1976, vol. 8.
- [4] W. Happer and A. C. Tam, “Effect of rapid spin exchange on the magnetic-resonance spectrum of alkali vapors,” *Phys. Rev. A*, vol. 16, pp. 1877–1891, Nov 1977. [Online]. Available: <https://link.aps.org/doi/10.1103/PhysRevA.16.1877>
- [5] U. Fano, K. W. McVoy, and J. R. Albers, “Interference of orbital and spin currents in bremsstrahlung and photoelectric effect,” *Phys. Rev.*, vol. 116, pp. 1159–1167, Dec 1959. [Online]. Available: <https://link.aps.org/doi/10.1103/PhysRev.116.1159>
- [6] L. Allen, M. W. Beijersbergen, R. J. C. Spreeuw, and J. P. Woerdman, “Orbital angular momentum of light and the transformation of laguerre-gaussian laser modes,” *Phys. Rev. A*, vol. 45, pp. 8185–8189, Jun 1992. [Online]. Available: <https://link.aps.org/doi/10.1103/PhysRevA.45.8185>
- [7] P. Genevet, J. Lin, M. A. Kats, and F. Capasso, “Holographic detection of the orbital angular momentum of light with plasmonic photodiodes,” *Nature Communications*, vol. 3, no. 1, p. 1278, Dec 2012. [Online]. Available: <https://doi.org/10.1038/ncomms2293>
- [8] J. Ahn, Z. Xu, J. Bang, Y.-H. Deng, T. M. Hoang, Q. Han, R.-M. Ma, and T. Li, “Optically levitated nanodumbbell torsion balance and ghz nanomechanical rotor,” *Phys. Rev. Lett.*, vol. 121, p. 033603, Jul 2018. [Online]. Available: <https://link.aps.org/doi/10.1103/PhysRevLett.121.033603>
- [9] G. Molina-Terriza, J. P. Torres, and L. Torner, “Twisted photons,” *Nature Physics*, vol. 3, no. 5, pp. 305–310, May 2007. [Online]. Available: <https://doi.org/10.1038/nphys607>
- [10] P. Delaney, J. C. Greer, and J. A. Larsson, “Spin-polarization mechanisms of the nitrogen-vacancy center in diamond,” *Nano Letters*, vol. 10, no. 2, pp. 610–614, 2010, pMID: 20085271. [Online]. Available: <https://doi.org/10.1021/nl903646p>
- [11] J. Wertz, *Electron spin resonance: elementary theory and practical applications*. Netherlands: Springer Science & Business Media, 2012.
- [12] D. I. Hoult and B. Bhakar, “Nmr signal reception: Virtual photons and coherent spontaneous emission,” *Concepts in Magnetic Resonance*, vol. 9, no. 5, pp. 277–297, 1997. [Online]. Available: <https://onlinelibrary.wiley.com/doi/abs/10.1002/%28SICI%291099-0534%281997%299%3A5%3C277%3A%3AAID-CMR1%3E3.0.CO%3B2-W>
- [13] D. W. McRobbie, E. A. Moore, M. J. Graves, and M. R. Prince, *MRI from Picture to Proton*. Cambridge: Cambridge university press, 2017.

- [14] J. K. LL.D., “Xliii. on rotation of the plane of polarization by reflection from the pole of a magnet,” *The London, Edinburgh, and Dublin Philosophical Magazine and Journal of Science*, vol. 3, no. 19, pp. 321–343, 1877. [Online]. Available: <https://doi.org/10.1080/14786447708639245>
- [15] S. Mancuso and S. R. Spangler, “Faraday rotation and models for the plasma structure of the solar corona,” *The Astrophysical Journal*, vol. 539, no. 1, pp. 480–491, aug 2000. [Online]. Available: <https://doi.org/10.1086%2F309205>
- [16] R. Mitsch, C. Sayrin, B. Albrecht, P. Schneeweiss, and A. Rauschenbeutel, “Quantum state-controlled directional spontaneous emission of photons into a nanophotonic waveguide,” *Nature Commun.*, vol. 5, p. 5713, 2014.
- [17] I. Shomroni, S. Rosenblum, Y. Lovsky, O. Bechler, G. Guendelman, and B. Dayan, “All-optical routing of single photons by a one-atom switch controlled by a single photon,” *Science*, vol. 345, no. 6199, pp. 903–906, 2014.
- [18] F. J. Rodríguez-Fortuño, G. Marino, P. Ginzburg, D. O’Connor, A. Martínez, G. A. Wurtz, and A. V. Zayats, “Near-field interference for the unidirectional excitation of electromagnetic guided modes,” *Science*, vol. 340, no. 6130, pp. 328–330, 2013.
- [19] I. Söllner, S. Mahmoodian, S. L. Hansen, L. Midolo, A. Javadi, G. Kiršanskė, T. Pregnolato, H. El-Ella, E. H. Lee, J. D. Song, S. Stobbe, and P. Lodahl, “Deterministic photon–emitter coupling in chiral photonic circuits,” *Nature Nanotechnol.*, vol. 10, no. 9, pp. 775–778, 2015.
- [20] J. Petersen, J. Volz, and A. Rauschenbeutel, “Chiral nanophotonic waveguide interface based on spin-orbit interaction of light,” *Science*, vol. 346, no. 6205, pp. 67–71, 2014.
- [21] T. Aoki, B. Dayan, E. Wilcut, W. P. Bowen, A. S. Parkins, T. Kippenberg, K. Vahala, and H. Kimble, “Observation of strong coupling between one atom and a monolithic microresonator,” *Nature*, vol. 443, no. 7112, pp. 671–674, 2006.
- [22] F. Khosravi, C. L. Cortes, and Z. Jacob, “Spin photonics in 3d whispering gallery mode resonators,” *Opt. Express*, vol. 27, no. 11, pp. 15 846–15 855, May 2019. [Online]. Available: <http://www.opticsexpress.org/abstract.cfm?URI=oe-27-11-15846>
- [23] L. S. Langsjoen, A. Poudel, M. G. Vavilov, and R. Joynt, “Qubit relaxation from evanescent-wave johnson noise,” *Phys. Rev. A*, vol. 86, p. 010301, Jul 2012. [Online]. Available: <https://link.aps.org/doi/10.1103/PhysRevA.86.010301>
- [24] N. Rivera, I. Kaminer, B. Zhen, J. D. Joannopoulos, and M. Soljačić, “Shrinking light to allow forbidden transitions on the atomic scale,” *Science*, vol. 353, no. 6296, pp. 263–269, 2016. [Online]. Available: <https://science.sciencemag.org/content/353/6296/263>
- [25] E. Noether, “Invariant variation problems,” *Transport Theory and Statistical Physics*, vol. 1, no. 3, pp. 186–207, 1971. [Online]. Available: <https://doi.org/10.1080/00411457108231446>
- [26] C. Gerry and P. Knight, *Introductory quantum optics*. Cambridge: Cambridge university press, 2005.
- [27] C. Cohen-Tannoudji, J. Dupont-Roc, and G. Grynberg, *Photons and Atoms: Introduction to Quantum Electrodynamics*. Wiley, New York, 1997.
- [28] L.-P. Yang, F. Khosravi, and Z. Jacob, “Quantum spin operator of the photon,” *arXiv preprint arXiv:2004.03771*, 2020. [Online]. Available: <https://arxiv.org/abs/2004.03771>

- [29] L. H. Ryder, *Quantum field theory*. Cambridge: Cambridge university press, 1996.
- [30] W.-K. Tung, *Group theory in physics: an introduction to symmetry principles, group representations, and special functions in classical and quantum physics*. World Scientific Publishing Company, 1985.
- [31] I. Kaplan, “The pauli exclusion principle. can it be proved?” *Foundations of Physics*, vol. 43, no. 10, pp. 1233–1251, 2013.
- [32] D. J. Griffiths, “Introduction to electrodynamics,” Boston, MA, 2005.
- [33] K. Y. Bliokh, A. Y. Bekshaev, and F. Nori, “Dual electromagnetism: helicity, spin, momentum and angular momentum,” *New Journal of Physics*, vol. 15, no. 3, p. 033026, mar 2013. [Online]. Available: <https://doi.org/10.1088%2F1367-2630%2F15%2F3%2F033026>
- [34] F. Crimin, N. Mackinnon, J. Götte, and S. Barnett, “Optical helicity and chirality: Conservation and sources,” *Applied Sciences*, vol. 9, no. 5, p. 828, Feb 2019. [Online]. Available: <http://dx.doi.org/10.3390/app9050828>
- [35] M. V. Berry, “Optical currents,” *J. Opt. A: Pure Appl. Opt.*, vol. 11, no. 9, p. 094001, aug 2009. [Online]. Available: <https://doi.org/10.1088%2F1464-4258%2F11%2F9%2F094001>
- [36] I. Fernandez-Corbaton, X. Zambrana-Puyalto, N. Tischler, X. Vidal, M. L. Juan, and G. Molina-Terriza, “Electromagnetic duality symmetry and helicity conservation for the macroscopic maxwell’s equations,” *Phys. Rev. Lett.*, vol. 111, p. 060401, Aug 2013. [Online]. Available: <https://link.aps.org/doi/10.1103/PhysRevLett.111.060401>
- [37] J. Schwinger, “Gauge invariance and mass,” *Phys. Rev.*, vol. 125, pp. 397–398, Jan 1962. [Online]. Available: <https://link.aps.org/doi/10.1103/PhysRev.125.397>
- [38] —, “Gauge invariance and mass. ii,” *Phys. Rev.*, vol. 128, pp. 2425–2429, Dec 1962. [Online]. Available: <https://link.aps.org/doi/10.1103/PhysRev.128.2425>
- [39] D. M. Lipkin, “Existence of a new conservation law in electromagnetic theory,” *Journal of Mathematical Physics*, vol. 5, no. 5, pp. 696–700, 1964. [Online]. Available: <https://doi.org/10.1063/1.1704165>
- [40] G. Malinowski, F. Dalla Longa, J. Rietjens, P. Paluskar, R. Huijink, H. Swagten, and B. Koopmans, “Control of speed and efficiency of ultrafast demagnetization by direct transfer of spin angular momentum,” *Nature Physics*, vol. 4, no. 11, p. 855, 2008. [Online]. Available: <https://doi.org/10.1038/nphys1092>
- [41] C. T. Schmiegelow, J. Schulz, H. Kaufmann, T. Ruster, U. G. Poschinger, and F. Schmidt-Kaler, “Transfer of optical orbital angular momentum to a bound electron,” *Nature communications*, vol. 7, p. 12998, 2016. [Online]. Available: <https://doi.org/10.1038/ncomms12998>
- [42] A. B. Young, A. Thijssen, D. M. Beggs, P. Androvitsaneas, L. Kuipers, J. G. Rarity, S. Hughes, and R. Oulton, “Polarization engineering in photonic crystal waveguides for spin-photon entanglers,” *Phys. Rev. Lett.*, vol. 115, no. 15, p. 153901, 2015.
- [43] S. Barik, A. Karasahin, S. Mittal, E. Waks, and M. Hafezi, “Chiral quantum optics using a topological resonator,” 2019.
- [44] Y. Tang and A. E. Cohen, “Optical chirality and its interaction with matter,” *Phys. Rev. Lett.*, vol. 104, p. 163901, Apr 2010. [Online]. Available: <https://link.aps.org/doi/10.1103/PhysRevLett.104.163901>
- [45] G. Nienhuis, “Conservation laws and symmetry transformations of the electromagnetic field with sources,” *Phys. Rev. A*, vol. 93, p. 023840, Feb 2016. [Online]. Available: <https://link.aps.org/doi/10.1103/PhysRevA.93.023840>

- [46] I. Fernandez-Corbaton, X. Zambrana-Puyalto, N. Tischler, X. Vidal, M. L. Juan, and G. Molina-Terriza, “Electromagnetic duality symmetry and helicity conservation for the macroscopic maxwell’s equations,” *Phys. Rev. Lett.*, vol. 111, p. 060401, Aug 2013. [Online]. Available: <https://link.aps.org/doi/10.1103/PhysRevLett.111.060401>
- [47] T. G. Philbin, “Lipkin’s conservation law, noether’s theorem, and the relation to optical helicity,” *Phys. Rev. A*, vol. 87, p. 043843, Apr 2013. [Online]. Available: <https://link.aps.org/doi/10.1103/PhysRevA.87.043843>
- [48] W. Greiner *et al.*, *Relativistic quantum mechanics*. Springer, Berlin, 1990, vol. 3.
- [49] S. M. Barnett, “Optical dirac equation,” *New J. Phys.*, vol. 16, no. 9, p. 093008, sep 2014. [Online]. Available: <https://doi.org/10.1088%2F1367-2630%2F16%2F9%2F093008>
- [50] I. Bialynicki-Birula, “The photon wave function,” in *Coherence and Quantum Optics VII*, J. H. Eberly, L. Mandel, and E. Wolf, Eds. Boston, MA: Springer US, 1996, pp. 313–322.
- [51] F. Khosravi, T. Van Mechelen, and Z. Jacob, “Dirac wire: Fermionic waveguides with longitudinal spin,” *Phys. Rev. B*, vol. 100, p. 155105, Oct 2019. [Online]. Available: <https://link.aps.org/doi/10.1103/PhysRevB.100.155105>
- [52] T. Van Mechelen and Z. Jacob, “Nonlocal topological electromagnetic phases of matter,” *Phys. Rev. B*, vol. 99, p. 205146, May 2019. [Online]. Available: <https://link.aps.org/doi/10.1103/PhysRevB.99.205146>
- [53] ———, “Unidirectional maxwellian spin waves,” *Nanophotonics*, vol. 8, no. 8, pp. 1399–1416, 2019. [Online]. Available: <https://www.degruyter.com/view/j/nanoph.2019.8.issue-8/nanoph-2019-0092/nanoph-2019-0092.xml>
- [54] W. Greiner, B. Müller, and D. A. Bromley, *Gauge theory of weak interactions*. Springer, Berlin, 1996, vol. 5.
- [55] S. M. Barnett, “Optical angular-momentum flux\*,” *Journal of Optics B: Quantum and Semiclassical Optics*, vol. 4, no. 2, pp. S7–S16, jan 2002.
- [56] M. G. Calkin, “An invariance property of the free electromagnetic field,” *American Journal of Physics*, vol. 33, no. 11, pp. 958–960, 1965. [Online]. Available: <https://doi.org/10.1119/1.1971089>
- [57] X. Ji, “Gauge-invariant decomposition of nucleon spin,” *Phys. Rev. Lett.*, vol. 78, pp. 610–613, Jan 1997. [Online]. Available: <https://link.aps.org/doi/10.1103/PhysRevLett.78.610>
- [58] X.-S. Chen, X.-F. Lü, W.-M. Sun, F. Wang, and T. Goldman, “Spin and orbital angular momentum in gauge theories: Nucleon spin structure and multipole radiation revisited,” *Phys. Rev. Lett.*, vol. 100, p. 232002, Jun 2008. [Online]. Available: <https://link.aps.org/doi/10.1103/PhysRevLett.100.232002>
- [59] E. Leader and C. Lorcé, “The angular momentum controversy: What’s it all about and does it matter?” *Physics Reports*, vol. 541, no. 3, pp. 163 – 248, 2014, the angular momentum controversy: What’s it all about and does it matter? [Online]. Available: <http://www.sciencedirect.com/science/article/pii/S0370157314001185>
- [60] E. Leader, “The photon angular momentum controversy: Resolution of a conflict between laser optics and particle physics,” *Physics Letters B*, vol. 756, pp. 303–308, 2016.
- [61] W. Greiner and J. Reinhardt, *Field quantization*. Springer Science & Business Media, Berlin, 2013.

- [62] H. Kleinert, *Particles and quantum fields*. World Scientific, Singapore, 2016.
- [63] J. D. Jackson, *Classical electrodynamics*. Wiley, New York, 1999, 3rd Edition, Chap. 6.7.
- [64] L. Woltjer, “A theorem on force-free magnetic fields,” *Proc. Natl. Acad. Sci. USA*, vol. 44, no. 6, p. 489, 1958. [Online]. Available: <https://www.ncbi.nlm.nih.gov/pubmed/16590226>
- [65] M. M. Coles and D. L. Andrews, “Chirality and angular momentum in optical radiation,” *Phys. Rev. A*, vol. 85, p. 063810, Jun 2012. [Online]. Available: <https://link.aps.org/doi/10.1103/PhysRevA.85.063810>
- [66] J. M. Leeder, H. T. Haniewicz, and D. L. Andrews, “Point source generation of chiral fields: measures of near- and far-field optical helicity,” *J. Opt. Soc. Am. B*, vol. 32, no. 11, pp. 2308–2313, Nov 2015. [Online]. Available: <http://josab.osa.org/abstract.cfm?URI=josab-32-11-2308>
- [67] L. Meredith, “Helicity, chirality, and the dirac equation in the non-relativistic limit,” 2018. [Online]. Available: [https://www.pas.rochester.edu/assets/pdf/undergraduate/helicity\\_chirality\\_and\\_the\\_dirac\\_equation\\_in\\_the\\_non-relativistic\\_limit.pdf](https://www.pas.rochester.edu/assets/pdf/undergraduate/helicity_chirality_and_the_dirac_equation_in_the_non-relativistic_limit.pdf)
- [68] K. M. McCreary, A. G. Swartz, W. Han, J. Fabian, and R. K. Kawakami, “Magnetic moment formation in graphene detected by scattering of pure spin currents,” *Phys. Rev. Lett.*, vol. 109, p. 186604, Nov 2012. [Online]. Available: <https://link.aps.org/doi/10.1103/PhysRevLett.109.186604>
- [69] H. Zhao, E. J. Loren, H. M. van Driel, and A. L. Smirl, “Coherence control of hall charge and spin currents,” *Phys. Rev. Lett.*, vol. 96, p. 246601, Jun 2006. [Online]. Available: <https://link.aps.org/doi/10.1103/PhysRevLett.96.246601>
- [70] S. A. Wolf, D. D. Awschalom, R. A. Buhrman, J. M. Daughton, S. von Molnár, M. L. Roukes, A. Y. Chtchelkanova, and D. M. Treger, “Spintronics: A spin-based electronics vision for the future,” *Science*, vol. 294, no. 5546, pp. 1488–1495, 2001. [Online]. Available: <https://science.sciencemag.org/content/294/5546/1488>
- [71] P. Sharma, “How to create a spin current,” *Science*, vol. 307, no. 5709, pp. 531–533, 2005. [Online]. Available: <https://science.sciencemag.org/content/307/5709/531>
- [72] S. K. Watson, R. M. Potok, C. M. Marcus, and V. Umansky, “Experimental realization of a quantum spin pump,” *Phys. Rev. Lett.*, vol. 91, p. 258301, Dec 2003. [Online]. Available: <https://link.aps.org/doi/10.1103/PhysRevLett.91.258301>
- [73] S. Kashiwaya, Y. Tanaka, N. Yoshida, and M. R. Beasley, “Spin current in ferromagnet-insulator-superconductor junctions,” *Phys. Rev. B*, vol. 60, pp. 3572–3580, Aug 1999. [Online]. Available: <https://link.aps.org/doi/10.1103/PhysRevB.60.3572>
- [74] H. W. Crater and P. V. Alstine], “Two-body dirac equations,” *Annals of Physics*, vol. 148, no. 1, pp. 57 – 94, 1983. [Online]. Available: <http://www.sciencedirect.com/science/article/pii/0003491683903305>
- [75] E. E. Salpeter and H. A. Bethe, “A relativistic equation for bound-state problems,” *Phys. Rev.*, vol. 84, pp. 1232–1242, Dec 1951. [Online]. Available: <https://link.aps.org/doi/10.1103/PhysRev.84.1232>
- [76] A. Manchon, H. C. Koo, J. Nitta, S. Frolov, and R. Duine, “New perspectives for rashba spin–orbit coupling,” *Nature materials*, vol. 14, no. 9, pp. 871–882, 2015. [Online]. Available: <https://doi.org/10.1038/nmat4360>
- [77] S. V. Enk and G. Nienhuis, “Commutation rules and eigenvalues of spin and orbital angular momentum of radiation fields,” *Journal of Modern Optics*, vol. 41, no. 5, pp. 963–977, 1994. [Online]. Available: <https://doi.org/10.1080/09500349414550911>

- [78] M. Nieto-Vesperinas, “Optical torque on small bi-isotropic particles,” *Opt. Lett.*, vol. 40, no. 13, pp. 3021–3024, Jul 2015. [Online]. Available: <http://ol.osa.org/abstract.cfm?URI=ol-40-13-3021>
- [79] D. M. Wolkow, “Über eine klasse von lösungen der diracschen gleichung,” *Zeitschrift für Physik*, vol. 94, no. 3, pp. 250–260, Mar 1935. [Online]. Available: <https://doi.org/10.1007/BF01331022>
- [80] P. J. Redmond, “Solution of the klein-gordon and dirac equations for a particle with a plane electromagnetic wave and a parallel magnetic field,” *Journal of Mathematical Physics*, vol. 6, no. 7, pp. 1163–1169, 1965.
- [81] A. H. MacDonald and S. H. Vosko, “A relativistic density functional formalism,” *Journal of Physics C: Solid State Physics*, vol. 12, no. 15, pp. 2977–2990, aug 1979. [Online]. Available: <https://doi.org/10.1088%2F0022-3719%2F12%2F15%2F007>
- [82] H. Eschrig and V. D. P. Servedio, “Relativistic density functional approach to open shells,” *Journal of Computational Chemistry*, vol. 20, no. 1, pp. 23–30, 1999. [Online]. Available: <https://onlinelibrary.wiley.com/doi/abs/10.1002/%28SICI%291096-987X%2819990115%2920%3A1%3C23%3A%3AAID-JCC5%3E3.0.CO%3B2-N>
- [83] R. Mondal, M. Berritta, and P. M. Oppeneer, “Unified theory of magnetization dynamics with relativistic and nonrelativistic spin torques,” *Phys. Rev. B*, vol. 98, p. 214429, Dec 2018. [Online]. Available: <https://link.aps.org/doi/10.1103/PhysRevB.98.214429>
- [84] J. Lin, J. B. Mueller, Q. Wang, G. Yuan, N. Antoniou, X. C. Yuan, and F. Capasso, “Polarization-controlled tunable directional coupling of surface plasmon polaritons,” *Science*, vol. 340, no. 6130, pp. 331–334, 2013.
- [85] K. Y. Bliokh, A. Y. Bekshaev, and F. Nori, “Extraordinary momentum and spin in evanescent waves,” *Nature Commun.*, vol. 5, p. 3300, 2014.
- [86] S. Barik, A. Karasahin, C. Flower, T. Cai, H. Miyake, W. DeGottardi, M. Hafezi, and E. Waks, “A topological quantum optics interface,” *Science*, vol. 359, no. 6376, pp. 666–668, 2018.
- [87] C. Li, O. van’t Erve, J. Robinson, Y. Liu, L. Li, and B. Jonker, “Electrical detection of charge-current-induced spin polarization due to spin-momentum locking in  $\text{Bi}_2\text{Se}_3$ ,” *Nature Nanotechnol.*, vol. 9, no. 3, pp. 218–224, 2014.
- [88] B. Le Feber, N. Rotenberg, and L. Kuipers, “Nanophotonic control of circular dipole emission,” *Nature Commun.*, vol. 6, p. 6695, 2015.
- [89] A. Aiello, N. Lindlein, C. Marquardt, and G. Leuchs, “Transverse angular momentum and geometric spin hall effect of light,” *Phys. Rev. Lett.*, vol. 103, no. 10, p. 100401, 2009.
- [90] C. Li, O. van’t Erve, Y. Li, L. Li, and B. Jonker, “Electrical detection of the helical spin texture in a p-type topological insulator  $\text{Sb}_2\text{Te}_3$ ,” *Sci. Rep.*, vol. 6, p. 29533, 2016.
- [91] L. Huang, X. Chen, B. Bai, Q. Tan, G. Jin, T. Zentgraf, and S. Zhang, “Helicity dependent directional surface plasmon polariton excitation using a metasurface with interfacial phase discontinuity,” *Light Sci. Appl.*, vol. 2, no. 3, p. e70, 2013.
- [92] B. Redding, L. Ge, Q. Song, J. Wiersig, G. S. Solomon, and H. Cao, “Local chirality of optical resonances in ultrasmall resonators,” *Phys. Rev. Lett.*, vol. 108, no. 25, p. 253902, 2012.

- [93] S. Maayani, R. Dahan, Y. Kligerman, E. Moses, A. U. Hassan, H. Jing, F. Nori, D. N. Christodoulides, and T. Carmon, “Flying couplers above spinning resonators generate irreversible refraction,” *Nature*, vol. 558, no. 7711, pp. 569–572, 2018.
- [94] T. Van Mechelen and Z. Jacob, “Universal spin-momentum locking of evanescent waves,” *Optica*, vol. 3, no. 2, pp. 118–126, 2016.
- [95] F. Kalhor, T. Thundat, and Z. Jacob, “Universal spin-momentum locked optical forces,” *Appl. Phys. Lett.*, vol. 108, no. 6, p. 061102, 2016.
- [96] M. Alizadeh and B. M. Reinhard, “Transverse chiral optical forces by chiral surface plasmon polaritons,” *ACS Photonics*, vol. 2, no. 12, pp. 1780–1788, 2015.
- [97] S. Wang and C. Chan, “Lateral optical force on chiral particles near a surface,” *Nature Commun.*, vol. 5, p. 3307, 2014.
- [98] A. Hayat, J. B. Mueller, and F. Capasso, “Lateral chirality-sorting optical forces,” *Proc. Natl. Acad. Sci.*, vol. 112, no. 43, pp. 13 190–13 194, 2015.
- [99] S. M. Barnett, L. Allen, R. P. Cameron, C. R. Gilson, M. J. Padgett, F. C. Speirits, and A. M. Yao, “On the natures of the spin and orbital parts of optical angular momentum,” *J. Opt.*, vol. 18, no. 6, p. 064004, 2016.
- [100] G. Sagué, E. Vetsch, W. Alt, D. Meschede, and A. Rauschenbeutel, “Cold-atom physics using ultrathin optical fibers: Light-induced dipole forces and surface interactions,” *Phys. Rev. Lett.*, vol. 99, no. 16, p. 163602, 2007.
- [101] M. Bayer, G. Ortner, O. Stern, A. Kuther, A. Gorbunov, A. Forchel, P. Hawrylak, S. Fafard, K. Hinzer, T. Reinecke, S. Walck, J. Reithmaier, F. Klopff, and F. Schafer, “Fine structure of neutral and charged excitons in self-assembled in (ga) as/(al) gaas quantum dots,” *Phys. Rev. B*, vol. 65, no. 19, p. 195315, 2002.
- [102] T. Setälä, A. Shevchenko, M. Kaivola, and A. T. Friberg, “Degree of polarization for optical near fields,” *Phys. Rev. E*, vol. 66, no. 1, p. 016615, 2002.
- [103] K. J. Vahala, “Optical microcavities,” *Nature*, vol. 424, no. 6950, pp. 839–846, 2003.
- [104] J. D. Jackson, *Classical electrodynamics*. New York: John Wiley & Sons, 2012.
- [105] A. Chiasera, Y. Dumeige, P. Feron, M. Ferrari, Y. Jestin, G. Nunzi Conti, S. Pelli, S. Soria, and G. C. Righini, “Spherical whispering-gallery-mode microresonators,” *Laser Photonics Rev.*, vol. 4, no. 3, pp. 457–482, 2010.
- [106] S. M. Barnett and L. Allen, “Orbital angular momentum and nonparaxial light beams,” *Opt. Commun.*, vol. 110, no. 5-6, pp. 670–678, 1994.
- [107] M. V. Berry, “Paraxial beams of spinning light,” *SPIE*, vol. 3487, pp. 6–11, 1998.
- [108] M. F. Picardi, A. V. Zayats, and F. J. Rodríguez-Fortuño, “Janus and Huygens dipoles: near-field directionality beyond spin-momentum locking,” *Phys. Rev. Lett.*, vol. 120, no. 11, p. 117402, 2018.
- [109] M. Picardi, K. Bliokh, F. Rodríguez-Fortuño, F. Alpegiani, and F. Nori, “Angular momenta, helicity, and other properties of dielectric-fiber and metallic-wire modes,” *Optica*, vol. 5, no. 8, pp. 1016–1026, 2018.
- [110] S. Pendharker, F. Kalhor, T. Van Mechelen, S. Jahani, N. Nazemifard, T. Thundat, and Z. Jacob, “Spin photonic forces in non-reciprocal waveguides,” *Opt. Express*, vol. 26, no. 18, pp. 23 898–23 910, 2018.
- [111] T. Van Mechelen and Z. Jacob, “Dirac-maxwell correspondence: Spin-1 bosonic topological insulator,” in *2018 Conference on Lasers and Electro-Optics (CLEO)*. IEEE, 2018, pp. 1–2.

- [112] C. T. Tai, *Dyadic Green functions in electromagnetic theory*. Institute of Electrical & Electronics Engineers (IEEE), 1994.
- [113] L. W. Li, P. S. Kooi, M. S. Leong, and T. S. Yee, “Electromagnetic dyadic green’s function in spherically multilayered media,” *IEEE Trans. Microw. Theory Tech.*, vol. 42, no. 12, pp. 2302–2310, 1994.
- [114] L. Novotny and B. Hecht, *Principles of nano-optics*. Cambridge university press, 2012.
- [115] S. Rosenblum, Y. Lovsky, L. Arazi, F. Vollmer, and B. Dayan, “Cavity ring-up spectroscopy for ultrafast sensing with optical microresonators,” *Nature Commun.*, vol. 6, p. 6788, 2015.
- [116] A. N. Oraevsky, “Whispering-gallery waves,” *Quantum Electron.*, vol. 32, no. 5, pp. 377–400, 2002.
- [117] R. Jackiw and C. Rebbi, “Solitons with fermion number  $1/2$ ,” *Phys. Rev. D*, vol. 13, pp. 3398–3409, Jun 1976. [Online]. Available: <https://link.aps.org/doi/10.1103/PhysRevD.13.3398>
- [118] K. Y. Bliokh, D. Smirnova, and F. Nori, “Quantum spin hall effect of light,” *Science*, vol. 348, no. 6242, pp. 1448–1451, 2015. [Online]. Available: <https://science.sciencemag.org/content/348/6242/1448>
- [119] M. Erementchouk and P. Mazumder, “Weyl fermions in cylindrical wires,” *Phys. Rev. B*, vol. 97, p. 035429, Jan 2018. [Online]. Available: <https://link.aps.org/doi/10.1103/PhysRevB.97.035429>
- [120] C. C. Leary, D. Reeb, and M. G. Raymer, “Self-spin-controlled rotation of spatial states of a dirac electron in a cylindrical potential via spin–orbit interaction,” *New J. Phys.*, vol. 10, no. 10, p. 103022, oct 2008. [Online]. Available: <https://doi.org/10.1088%2F1367-2630%2F10%2F10%2F103022>
- [121] A. A. Gorlach, D. V. Zhirihin, A. P. Slobozhanyuk, A. B. Khanikaev, and M. A. Gorlach, “Photonic jackiw-rebbi states in all-dielectric structures controlled by bianisotropy,” *Phys. Rev. B*, vol. 99, p. 205122, May 2019. [Online]. Available: <https://link.aps.org/doi/10.1103/PhysRevB.99.205122>
- [122] T. Van Mechelen and Z. Jacob, “Quantum gyroelectric effect: Photon spin-1 quantization in continuum topological bosonic phases,” *Phys. Rev. A*, vol. 98, p. 023842, Aug 2018. [Online]. Available: <https://link.aps.org/doi/10.1103/PhysRevA.98.023842>
- [123] ———, “Photonic dirac monopoles and skyrmions: spin-1 quantization [invited],” *Opt. Mater. Express*, vol. 9, no. 1, pp. 95–111, Jan 2019. [Online]. Available: <http://www.osapublishing.org/ome/abstract.cfm?URI=ome-9-1-95>
- [124] S. A. R. Horsley, “Topology and the optical dirac equation,” *Phys. Rev. A*, vol. 98, p. 043837, Oct 2018. [Online]. Available: <https://link.aps.org/doi/10.1103/PhysRevA.98.043837>
- [125] S. Datta, *Electronic Transport in Mesoscopic Systems*, ser. Cambridge Studies in Semiconductor Physics and Microelectronic Engineering. Cambridge University Press, 1995, Cambridge.
- [126] Y. I. Latyshev, A. V. Frolov, V. A. Volkov, T. Wade, V. A. Prudkoglyad, A. P. Orlov, V. M. Pudalov, and M. Konczykowski, “Manifestations of surface states in the longitudinal magnetoresistance of an array of bi nanowires,” *JETP Lett.*, vol. 107, no. 3, pp. 192–195, Feb 2018. [Online]. Available: <https://doi.org/10.1134/S0021364018030104>

- [127] L. Fu, C. L. Kane, and E. J. Mele, “Topological insulators in three dimensions,” *Phys. Rev. Lett.*, vol. 98, p. 106803, Mar 2007. [Online]. Available: <https://link.aps.org/doi/10.1103/PhysRevLett.98.106803>
- [128] M. Z. Hasan and C. L. Kane, “Colloquium: Topological insulators,” *Rev. Mod. Phys.*, vol. 82, pp. 3045–3067, Nov 2010. [Online]. Available: <https://link.aps.org/doi/10.1103/RevModPhys.82.3045>
- [129] Y. Jiang and J. Liao, “Pairing phase transitions of matter under rotation,” *Phys. Rev. Lett.*, vol. 117, p. 192302, Nov 2016. [Online]. Available: <https://link.aps.org/doi/10.1103/PhysRevLett.117.192302>
- [130] S.-Q. Shen, W.-Y. Shan, and H.-Z. Lu, “Topological insulator and the dirac equation,” in *Spin*, vol. 1, no. 01. World Scientific, 2011, pp. 33–44.
- [131] S.-Q. Shen, *Topological insulators*. Springer, 2012, vol. 174, Berlin, Heidelberg.
- [132] Y. Fan and K. L. Wang, “Spintronics based on topological insulators,” *SPIN*, vol. 06, no. 02, p. 1640001, 2016. [Online]. Available: <https://doi.org/10.1142/S2010324716400014>
- [133] H. Larocque, I. Kaminer, V. Grillo, G. Leuchs, M. J. Padgett, R. W. Boyd, M. Segev, and E. Karimi, “‘twisted’ electrons,” *Contemp. Phys.*, vol. 59, no. 2, pp. 126–144, 2018. [Online]. Available: <https://doi.org/10.1080/00107514.2017.1418046>
- [134] S. R. Elliott and M. Franz, “Colloquium: Majorana fermions in nuclear, particle, and solid-state physics,” *Rev. Mod. Phys.*, vol. 87, pp. 137–163, Feb 2015. [Online]. Available: <https://link.aps.org/doi/10.1103/RevModPhys.87.137>
- [135] E. Bocquillon, V. Freulon, F. D. Parmentier, J.-M. Berroir, B. Plaçais, C. Wahl, J. Rech, T. Jonckheere, T. Martin, C. Grenier, D. Ferraro, P. Degiovanni, and G. Fève, “Electron quantum optics in ballistic chiral conductors,” *Annalen der Physik*, vol. 526, no. 1-2, pp. 1–30, 2014. [Online]. Available: <https://onlinelibrary.wiley.com/doi/abs/10.1002/andp.201300181>
- [136] A. Balantekin and A. DeWeerd, “Second quantization of the dirac equation in cylindrical coordinates,” 1995.
- [137] K. Okamoto, *Fundamentals of optical waveguides*. Academic press, 2006, Burlington.
- [138] H. Zhang, C.-X. Liu, X.-L. Qi, X. Dai, Z. Fang, and S.-C. Zhang, “Topological insulators in bi 2 se 3, bi 2 te 3 and sb 2 te 3 with a single dirac cone on the surface,” *Nat. Phys.*, vol. 5, no. 6, p. 438, 2009. [Online]. Available: <https://doi.org/10.1038/nphys1270>
- [139] I. Bialynicki-Birula and Z. Bialynicka-Birula, *Phys. Rev. Lett.*, vol. 118, p. 114801, Mar 2017. [Online]. Available: <https://link.aps.org/doi/10.1103/PhysRevLett.118.114801>
- [140] B. A. Bernevig and T. L. Hughes, *Topological insulators and topological superconductors*. Oxford: Princeton university press, 2013.
- [141] C.-X. Liu, X.-L. Qi, H. Zhang, X. Dai, Z. Fang, and S.-C. Zhang, “Model hamiltonian for topological insulators,” *Phys. Rev. B*, vol. 82, p. 045122, Jul 2010. [Online]. Available: <https://link.aps.org/doi/10.1103/PhysRevB.82.045122>
- [142] X.-L. Qi, Y.-S. Wu, and S.-C. Zhang, “General theorem relating the bulk topological number to edge states in two-dimensional insulators,” *Phys. Rev. B*, vol. 74, p. 045125, Jul 2006. [Online]. Available: <https://link.aps.org/doi/10.1103/PhysRevB.74.045125>

- [143] X.-L. Qi and S.-C. Zhang, “Topological insulators and superconductors,” *Rev. Mod. Phys.*, vol. 83, pp. 1057–1110, Oct 2011. [Online]. Available: <https://link.aps.org/doi/10.1103/RevModPhys.83.1057>
- [144] H.-Z. Lu, W.-Y. Shan, W. Yao, Q. Niu, and S.-Q. Shen, “Massive dirac fermions and spin physics in an ultrathin film of topological insulator,” *Phys. Rev. B*, vol. 81, p. 115407, Mar 2010. [Online]. Available: <https://link.aps.org/doi/10.1103/PhysRevB.81.115407>
- [145] M. Tian, W. Ning, Z. Qu, H. Du, J. Wang, and Y. Zhang, “Dual evidence of surface dirac states in thin cylindrical topological insulator bi 2 te 3 nanowires,” *Sci. Rep.*, vol. 3, p. 1212, 2013. [Online]. Available: <https://doi.org/10.1038/srep01212>
- [146] G. Dresselhaus, “Spin-orbit coupling effects in zinc blende structures,” *Phys. Rev.*, vol. 100, pp. 580–586, Oct 1955. [Online]. Available: <https://link.aps.org/doi/10.1103/PhysRev.100.580>
- [147] Y. A. Bychkov and E. I. Rashba, “Oscillatory effects and the magnetic susceptibility of carriers in inversion layers,” *Journal of Physics C: Solid State Physics*, vol. 17, no. 33, pp. 6039–6045, nov 1984. [Online]. Available: <https://doi.org/10.1088%2F0022-3719%2F17%2F33%2F015>
- [148] S.-H. Gong, F. Alpegiani, B. Sciacca, E. C. Garnett, and L. Kuipers, “Nanoscale chiral valley-photon interface through optical spin-orbit coupling,” *Science*, vol. 359, no. 6374, pp. 443–447, 2018. [Online]. Available: <https://science.sciencemag.org/content/359/6374/443>
- [149] A. Osada, R. Hisatomi, A. Noguchi, Y. Tabuchi, R. Yamazaki, K. Usami, M. Sadgrove, R. Yalla, M. Nomura, and Y. Nakamura, “Cavity optomagnonics with spin-orbit coupled photons,” *Physical review letters*, vol. 116, no. 22, p. 223601, 2016.
- [150] K. Y. Bliokh and F. Nori, “Spin and orbital angular momenta of acoustic beams,” *Phys. Rev. B*, vol. 99, p. 174310, May 2019. [Online]. Available: <https://link.aps.org/doi/10.1103/PhysRevB.99.174310>
- [151] C. Shi, R. Zhao, Y. Long, S. Yang, Y. Wang, H. Chen, J. Ren, and X. Zhang, “Observation of acoustic spin,” *National Science Review*, vol. 6, no. 4, pp. 707–712, 05 2019. [Online]. Available: <https://doi.org/10.1093/nsr/nwz059>
- [152] Y. Long, J. Ren, and H. Chen, “Intrinsic spin of elastic waves,” *Proceedings of the National Academy of Sciences*, vol. 115, no. 40, pp. 9951–9955, 2018. [Online]. Available: <https://www.pnas.org/content/115/40/9951>
- [153] F. J. R. Schulein, E. Zallo, P. Atkinson, O. G. Schmidt, R. Trotta, A. Rastelli, A. Wixforth, and H. J. Krenner, “Fourier synthesis of radiofrequency nanomechanical pulses with different shapes,” *Nature Nanotechnology*, vol. 10, no. 6, pp. 512–516, Jun 2015. [Online]. Available: <https://doi.org/10.1038/nnano.2015.72>
- [154] D. Royer and E. Dieulesaint, *Elastic waves in solids I: Free and guided propagation*. Berlin, Heidelberg: Springer Science & Business Media, 1999.
- [155] P. Delsing, A. N. Cleland, M. J. A. Schuetz, J. Knörzer, G. Giedke, J. I. Cirac, K. Srinivasan, M. Wu, K. C. Balram, C. Bäuerle, T. Meunier, C. J. B. Ford, P. V. Santos, E. Cerda-Méndez, H. Wang, H. J. Krenner, E. D. S. Nysten, M. Weiß, G. R. Nash, L. Thevenard, C. Gourdon, P. Rovillain, M. Marangolo, J.-Y. Duquesne, G. Fischerauer, W. Ruile, A. Reiner, B. Paschke, D. Denysenko, D. Volkmer, A. Wixforth, H. Bruus, M. Wiklund, J. Reboud, J. M. Cooper, Y. Fu, M. S. Brugger, F. Rehfeldt, and C. Westerhausen, “The 2019 surface acoustic waves roadmap,” *Journal of Physics D: Applied Physics*, vol. 52, no. 35, p. 353001, jul 2019. [Online]. Available: <https://doi.org/10.1088%2F1361-6463%2Fab1b04>

- [156] M. Weiß, J. B. Kinzel, F. J. R. Schülein, M. Heigl, D. Rudolph, S. Morkötter, M. Döblinger, M. Bichler, G. Abstreiter, J. J. Finley, G. Koblmüller, A. Wixforth, and H. J. Krenner, “Dynamic acoustic control of individual optically active quantum dot-like emission centers in heterostructure nanowires,” *Nano Letters*, vol. 14, no. 5, pp. 2256–2264, 2014, pMID: 24678960. [Online]. Available: <https://doi.org/10.1021/nl4040434>
- [157] G. Gautschi, “Piezoelectric sensors,” in *Piezoelectric Sensorics*. Springer, 2002, pp. 73–91, Berlin, Heidelberg.
- [158] R. Reimann, M. Doderer, E. Hebestreit, R. Diehl, M. Frimmer, D. Windey, F. Tebbenjohanns, and L. Novotny, “Ghz rotation of an optically trapped nanoparticle in vacuum,” *Phys. Rev. Lett.*, vol. 121, p. 033602, Jul 2018. [Online]. Available: <https://link.aps.org/doi/10.1103/PhysRevLett.121.033602>
- [159] C. Marletto and V. Vedral, “Gravitationally induced entanglement between two massive particles is sufficient evidence of quantum effects in gravity,” *Phys. Rev. Lett.*, vol. 119, p. 240402, Dec 2017. [Online]. Available: <https://link.aps.org/doi/10.1103/PhysRevLett.119.240402>
- [160] A. D. Rider, D. C. Moore, C. P. Blakemore, M. Louis, M. Lu, and G. Gratta, “Search for screened interactions associated with dark energy below the 100  $\mu\text{m}$  length scale,” *Phys. Rev. Lett.*, vol. 117, p. 101101, Aug 2016. [Online]. Available: <https://link.aps.org/doi/10.1103/PhysRevLett.117.101101>
- [161] J. D. Bekenstein and M. Schiffer, “The many faces of superradiance,” *Phys. Rev. D*, vol. 58, p. 064014, Aug 1998. [Online]. Available: <https://link.aps.org/doi/10.1103/PhysRevD.58.064014>
- [162] A. Manjavacas and F. J. García de Abajo, “Vacuum friction in rotating particles,” *Phys. Rev. Lett.*, vol. 105, p. 113601, Sep 2010. [Online]. Available: <https://link.aps.org/doi/10.1103/PhysRevLett.105.113601>
- [163] Y. Guo and Z. Jacob, “Giant non-equilibrium vacuum friction: role of singular evanescent wave resonances in moving media,” *Journal of Optics*, vol. 16, no. 11, p. 114023, nov 2014. [Online]. Available: <https://doi.org/10.1088%2F2040-8978%2F16%2F11%2F114023>
- [164] R. S. Decca, D. López, E. Fischbach, and D. E. Krause, “Measurement of the casimir force between dissimilar metals,” *Phys. Rev. Lett.*, vol. 91, p. 050402, Jul 2003. [Online]. Available: <https://link.aps.org/doi/10.1103/PhysRevLett.91.050402>
- [165] U. Mohideen and A. Roy, “Precision measurement of the casimir force from 0.1 to 0.9  $\mu\text{m}$ ,” *Phys. Rev. Lett.*, vol. 81, pp. 4549–4552, Nov 1998. [Online]. Available: <https://link.aps.org/doi/10.1103/PhysRevLett.81.4549>
- [166] C. F. Munday, J. N. and V. A. Parsegian, “Measured long-range repulsive casimir-lifshitz forces,” *Nature*, vol. 457, pp. 170–173, Jan 2009. [Online]. Available: <https://doi.org/10.1038/nature07610>
- [167] Z. Xu and T. Li, “Detecting casimir torque with an optically levitated nanorod,” *Phys. Rev. A*, vol. 96, p. 033843, Sep 2017. [Online]. Available: <https://link.aps.org/doi/10.1103/PhysRevA.96.033843>
- [168] K. Joulain, R. Carminati, J.-P. Mulet, and J.-J. Greffet, “Definition and measurement of the local density of electromagnetic states close to an interface,” *Phys. Rev. B*, vol. 68, p. 245405, Dec 2003. [Online]. Available: <https://link.aps.org/doi/10.1103/PhysRevB.68.245405>
- [169] J. Sloan, N. Rivera, J. D. Joannopoulos, I. Kaminer, and M. Soljačić, “Controlling spins with surface magnon polaritons,” *Phys. Rev. B*, vol. 100, p. 235453, Dec 2019. [Online]. Available: <https://link.aps.org/doi/10.1103/PhysRevB.100.235453>

- [170] H. J. Mamin, M. Kim, M. H. Sherwood, C. T. Rettner, K. Ohno, D. D. Awschalom, and D. Rugar, “Nanoscale nuclear magnetic resonance with a nitrogen-vacancy spin sensor,” *Science*, vol. 339, no. 6119, pp. 557–560, 2013. [Online]. Available: <https://science.sciencemag.org/content/339/6119/557>
- [171] D. M. Pozar, *Microwave Engineering 3e*. Hoboken, NJ: Wiley, 2006.
- [172] R. Zhao, A. Manjavacas, F. J. García de Abajo, and J. B. Pendry, “Rotational quantum friction,” *Phys. Rev. Lett.*, vol. 109, p. 123604, Sep 2012. [Online]. Available: <https://link.aps.org/doi/10.1103/PhysRevLett.109.123604>
- [173] T. Seberson, J. Ahn, J. Bang, T. Li, and F. Robicheaux, “Optical levitation of a yig nanoparticle and simulation of sympathetic cooling via coupling to a cold atomic gas,” *arXiv preprint arXiv:1910.05371*, 2019.
- [174] A. Manjavacas and F. J. García de Abajo, “Thermal and vacuum friction acting on rotating particles,” *Phys. Rev. A*, vol. 82, p. 063827, Dec 2010. [Online]. Available: <https://link.aps.org/doi/10.1103/PhysRevA.82.063827>
- [175] G. Ford and W. Weber, “Electromagnetic interactions of molecules with metal surfaces,” *Physics Reports*, vol. 113, no. 4, pp. 195 – 287, 1984. [Online]. Available: <http://www.sciencedirect.com/science/article/pii/037015738490098X>
- [176] A. H. Sihvola, “Dielectric polarizability of a sphere with arbitrary anisotropy,” *Opt. Lett.*, vol. 19, no. 7, pp. 430–432, Apr 1994. [Online]. Available: <http://ol.osa.org/abstract.cfm?URI=ol-19-7-430>
- [177] S. J. Barnett, “Magnetization by rotation,” *Phys. Rev.*, vol. 6, pp. 239–270, Oct 1915. [Online]. Available: <https://link.aps.org/doi/10.1103/PhysRev.6.239>
- [178] T. Seberson and F. Robicheaux, “Distribution of laser shot noise energy delivered to a levitated nanoparticle,” *arXiv preprint arXiv:1909.06469*, 2019.
- [179] D. A. Golter, T. Oo, M. Amezcua, K. A. Stewart, and H. Wang, “Optomechanical quantum control of a nitrogen-vacancy center in diamond,” *Phys. Rev. Lett.*, vol. 116, p. 143602, Apr 2016. [Online]. Available: <https://link.aps.org/doi/10.1103/PhysRevLett.116.143602>
- [180] M. W. Doherty, F. Dolde, H. Fedder, F. Jelezko, J. Wrachtrup, N. B. Manson, and L. C. L. Hollenberg, “Theory of the ground-state spin of the  $nv^-$  center in diamond,” *Phys. Rev. B*, vol. 85, p. 205203, May 2012. [Online]. Available: <https://link.aps.org/doi/10.1103/PhysRevB.85.205203>
- [181] W. Happer and B. S. Mathur, “Effective operator formalism in optical pumping,” *Phys. Rev.*, vol. 163, pp. 12–25, Nov 1967. [Online]. Available: <https://link.aps.org/doi/10.1103/PhysRev.163.12>
- [182] C. Cohen-Tannoudji, “The quantum theory of the optical pumping cycle. experimental verification of the new planned effects,” Ph.D. dissertation, 1962.
- [183] L. D. Landau and E. M. Lifshitz, *Statistical Physics: Volume 5*. Elsevier, 2013, vol. 5, Butterworth-Heinemann.
- [184] C. Khandekar and Z. Jacob, “Thermal spin photonics in the near-field of nonreciprocal media,” *New Journal of Physics*, vol. 21, no. 10, p. 103030, oct 2019. [Online]. Available: <https://doi.org/10.1088%2F1367-2630%2Fab494d>
- [185] G. Breit, “Dirac’s equation and the spin-spin interactions of two electrons,” *Phys. Rev.*, vol. 39, pp. 616–624, Feb 1932. [Online]. Available: <https://link.aps.org/doi/10.1103/PhysRev.39.616>

- [186] E. E. Salpeter and H. A. Bethe, “A relativistic equation for bound-state problems,” *Phys. Rev.*, vol. 84, pp. 1232–1242, Dec 1951. [Online]. Available: <https://link.aps.org/doi/10.1103/PhysRev.84.1232>
- [187] N. Nakanishi, “A General Survey of the Theory of the Bethe-Salpeter Equation,” *Progress of Theoretical Physics Supplement*, vol. 43, pp. 1–81, 01 1969. [Online]. Available: <https://doi.org/10.1143/PTPS.43.1>
- [188] H. Sazdjian, “N-body bound state relativistic wave equations,” *Annals of Physics*, vol. 191, no. 1, pp. 52 – 77, 1989. [Online]. Available: <http://www.sciencedirect.com/science/article/pii/0003491689903369>
- [189] F. Schwabl, *Quantum mechanics*. Springer., 2007, Berlin, Heidelberg.
- [190] F. Belinfante, “On the current and the density of the electric charge, the energy, the linear momentum and the angular momentum of arbitrary fields,” *Physica*, vol. 7, no. 5, pp. 449–474, 1940.
- [191] L. J. H. C. Rosenfeld, *Sur le tenseur d’impulsion-énergie*. Bruxelles: Palais des Académies, 1940.
- [192] C. F. Bohren and D. R. Huffman, *Absorption and scattering of light by small particles*. John Wiley & Sons, 2008, Weinheim, Germany.
- [193] G. W. Ford and W. H. Weber, “Electromagnetic interactions of molecules with metal surfaces,” *Physics Reports*, vol. 113, no. 4, pp. 195–287, 1984.
- [194] J. Corson, G. W. Mulholland, and M. R. Zachariah, “Calculating the rotational friction coefficient of fractal aerosol particles in the transition regime using extended kirkwood-riseman theory,” *Physical Review E*, vol. 96, no. 1, p. 013110, 2017.
- [195] C. H. Kruger and W. Vincenti, “Introduction to physical gas dynamics,” *John Wiley & Sons*, p. 414, 1965, London.

# Appendix A

## Proofs for Chapter 2

### A.1 Conserved Angular Momentum Tensor

In this section, by starting from the Lagrangian of QED, we derive the conservation of angular momentum equation using Noether's theorem [25]. Symmetrized Dirac Lagrangian, with the minimal coupling term [61], is written as

$$\mathcal{L} = \bar{\psi} \left[ c\gamma^\mu \left( \frac{i\hbar}{2} \overleftrightarrow{\partial}_\mu - eA_\mu \right) - mc^2 \right] \psi - \frac{1}{4\mu_0} F_{\mu\nu} F^{\mu\nu} \quad (\text{A.1})$$

where  $\overleftrightarrow{\partial} = \overleftarrow{\partial} + \overrightarrow{\partial}$  with  $\overleftarrow{\partial}$  and  $\overrightarrow{\partial}$  acting only on  $\bar{\psi}$  and  $\psi$ , respectively,

$$F_{\mu\nu} = \partial_\mu A_\nu - \partial_\nu A_\mu = \begin{pmatrix} 0 & E_x/c & E_y/c & E_z/c \\ -E_x/c & 0 & -B_z & B_y \\ -E_y/c & B_z & 0 & -B_x \\ -E_z/c & -B_y & B_x & 0 \end{pmatrix} \quad (\text{A.2})$$

is the electromagnetic tensor, and  $\gamma^\mu$  are the Dirac gamma matrices with the property  $\{\gamma^\mu, \gamma^\nu\} = \eta^{\mu\nu}$ , where

$$\eta^{\mu\nu} = \begin{pmatrix} 1 & 0 & 0 & 0 \\ 0 & -1 & 0 & 0 \\ 0 & 0 & -1 & 0 \\ 0 & 0 & 0 & -1 \end{pmatrix} \quad (\text{A.3})$$

is the Minkowski metric tensor with the signature  $(+ - - -)$ . We can get the conserved currents related to the rotational symmetry of the Lagrangian, using the Noether's theorem, as [25, 61]:

$$\begin{aligned} \mathcal{M}^{\mu\nu,\lambda} = & \left( -\frac{i}{2} \frac{\partial \mathcal{L}}{\partial(\partial_\lambda \psi)} \hat{M}_D^{\mu\nu} \psi \right) + \left( -\frac{i}{2} \bar{\psi} \hat{M}_D^{\mu\nu} \frac{\partial \mathcal{L}}{\partial(\partial_\lambda \bar{\psi})} \right) + \left( -\frac{i}{2} \frac{\partial \mathcal{L}}{\partial(\partial_\lambda A^\kappa)} \right) (\hat{M}_{\text{em}}^{\mu\nu})^\kappa{}_\sigma A^\sigma \\ & + \frac{1}{2} \left( \eta^{\lambda\mu} \mathcal{L} x^\nu - \eta^{\lambda\nu} \mathcal{L} x^\mu \right) \end{aligned} \quad (\text{A.4})$$

where

$$\hat{M}_D^{\mu\nu} = \hat{L}^{\mu\nu} + \hat{\Sigma}^{\mu\nu} \quad (\text{A.5})$$

is the angular momentum operator for the Dirac fields with

$$\hat{\Sigma}^{\mu\nu} = \frac{1}{2}\sigma^{\mu\nu}, \quad \sigma^{\mu\nu} = \frac{i}{2}[\gamma^\mu, \gamma^\nu] \quad (\text{A.6})$$

$$\hat{L}^{\mu\nu} = x^\mu \partial^\nu - x^\nu \partial^\mu, \quad (\text{A.7})$$

and

$$(\hat{M}_{\text{em}}^{\mu\nu})^\kappa{}_\sigma = \hat{L}^{\mu\nu} \delta_\sigma^\kappa + (\hat{S}^{\mu\nu})^\kappa{}_\sigma \quad (\text{A.8})$$

is the angular momentum operator for the electromagnetic fields with  $\hat{L}^{\mu\nu}$  given by Eq. (A.7),  $\delta_\sigma^\kappa$  being the Kronecker delta function, and

$$(\hat{S}^{\mu\nu})^\kappa{}_\sigma = i(\eta^{\mu\kappa}\eta^\nu{}_\sigma - \eta^\mu{}_\sigma\eta^{\nu\kappa}). \quad (\text{A.9})$$

Plugging these equations into Eq. (A.4), we get for the angular momentum currents

$$\mathcal{M}^{\mu\nu,\lambda} = \mathcal{M}_{\text{D}}^{\mu\nu,\lambda} + \mathcal{M}_{\text{em}}^{\mu\nu,\lambda} \quad (\text{A.10})$$

where

$$\mathcal{M}_{\text{D}}^{\mu\nu,\lambda} = \mathcal{S}_{\text{D}}^{\mu\nu,\lambda} + \mathcal{L}_{\text{D}}^{\mu\nu,\lambda} \quad (\text{A.11a})$$

$$\mathcal{S}_{\text{D}}^{\mu\nu,\lambda} = \frac{\hbar c}{4} \bar{\psi} \left( \gamma^\lambda \sigma^{\mu\nu} + \sigma^{\mu\nu} \gamma^\lambda \right) \psi \quad (\text{A.11b})$$

$$\mathcal{L}_{\text{D}}^{\mu\nu,\lambda} = \hbar c \mathcal{R} \left\{ \bar{\psi} \gamma^\lambda (x^\mu \partial^\nu - x^\nu \partial^\mu) \psi \right\} + (\eta^{\lambda\mu} x^\nu - \eta^{\lambda\nu} x^\mu) \mathfrak{L}_{\text{D}} \quad (\text{A.11c})$$

$$\mathfrak{L}_{\text{D}} = \bar{\psi} \left[ i\hbar c \frac{1}{2} \gamma^\mu \overleftrightarrow{\partial}_\mu - mc^2 \right] \psi - ce \bar{\psi} \gamma^\mu \psi A_\mu \quad (\text{A.11d})$$

is the contribution due to the Dirac field and

$$\mathcal{M}_{\text{em}}^{\mu\nu,\lambda} = \mathcal{S}_{\text{em}}^{\mu\nu,\lambda} + \mathcal{L}_{\text{em}}^{\mu\nu,\lambda} \quad (\text{A.12a})$$

$$\mathcal{S}_{\text{em}}^{\mu\nu,\lambda} = -\frac{1}{\mu_0} \left( F^{\lambda\mu} A^\nu - F^{\lambda\nu} A^\mu \right) \quad (\text{A.12b})$$

$$\mathcal{L}_{\text{em}}^{\mu\nu,\lambda} = -\frac{1}{\mu_0} \left[ F^\lambda{}_\kappa (x^\mu \partial^\nu - x^\nu \partial^\mu) A^\kappa \right] + (\eta^{\lambda\mu} x^\nu - \eta^{\lambda\nu} x^\mu) \mathfrak{L}_{\text{em}} \quad (\text{A.12c})$$

$$\mathfrak{L}_{\text{em}} = -\frac{1}{4\mu_0} F_{\mu\nu} F^{\mu\nu} = \frac{1}{2\mu_0} \left( \frac{\mathbf{E} \cdot \mathbf{E}}{c^2} - \mathbf{B} \cdot \mathbf{B} \right) \quad (\text{A.12d})$$

is the contribution due to the electromagnetic field. As a consequence of Noether theorem, the angular momentum tensor  $\mathcal{M}^{\mu\nu,\lambda}$  is conserved. In other words,

$$\partial_\lambda \mathcal{M}^{\mu\nu,\lambda} = 0. \quad (\text{A.13})$$

For the tensors given in Eqs. (A.11) and (A.12), and using Maxwell and Dirac equations, one can show that Eq. (A.13) holds for the total angular momentum tensor.

For the case that  $\mu\nu = ij$ , where  $i, j = 1, 2, 3$ , we find the angular momentum currents due to rotations. We find for the spin and OAM currents of the Dirac field

$$\partial_\lambda \mathcal{S}_D^{ij,\lambda} = \varepsilon_{ijk} \left[ \hbar \frac{\partial}{\partial t} (\psi^\dagger \Sigma \psi) + \frac{\hbar c}{2} \nabla (\psi^\dagger \gamma^5 \psi) \right]_k, \quad (\text{A.14a})$$

$$\partial_\lambda \mathcal{L}_D^{ij,\lambda} = \varepsilon_{ijk} \left[ -\hbar \frac{\partial}{\partial t} \mathcal{R} \left\{ i \psi^\dagger (\mathbf{r} \times \nabla) \psi \right\} - \hbar c \nabla \cdot \mathcal{R} \left\{ i \bar{\psi} \boldsymbol{\gamma} (\mathbf{r} \times \nabla) \psi \right\} \right]_k \quad (\text{A.14b})$$

where

$$\Sigma_i = \frac{1}{2} \varepsilon_{ijk} \sigma^{jk} = \frac{i}{4} \varepsilon_{ijk} [\gamma^j, \gamma^k] = \frac{1}{2} \begin{pmatrix} \sigma_i & 0 \\ 0 & \sigma_i \end{pmatrix}, \quad (\text{A.15})$$

with  $\sigma_i$  being the Pauli matrices,  $\mathcal{R}\{\dots\}$  takes the real part of its argument,  $\gamma^5 = i\gamma^0\gamma^1\gamma^2\gamma^3$  is the chirality operator in the Dirac equation [61], and

$$\boldsymbol{\gamma} = \gamma^1 \hat{x} + \gamma^2 \hat{y} + \gamma^3 \hat{z}. \quad (\text{A.16})$$

Note that we have used the fact that, using the Dirac equation,

$$(i\hbar\gamma^\mu \partial_\mu - e\gamma^\mu A_\mu - mc)\psi = 0, \quad (\text{A.17})$$

we get  $\mathcal{L}_D = 0$  for the fields that follow Dirac equation of motion. This is straightforward to show by multiplying Eq. (A.17) from left by  $c\bar{\psi}$ . For the spin and OAM currents of the electromagnetic field we find

$$\partial_\lambda \mathcal{S}_{\text{em}}^{ij,\lambda} = \varepsilon_{ijk} \left[ \epsilon \frac{\partial}{\partial t} (\mathbf{E} \times \mathbf{A}) - \frac{1}{\mu_0} \nabla \cdot (\mathbf{A}\mathbf{B}) + \frac{1}{\mu_0} \nabla (\mathbf{A} \cdot \mathbf{B}) \right]_k \quad (\text{A.18a})$$

$$\partial_\lambda \mathcal{L}_{\text{em}}^{ij,\lambda} = \varepsilon_{ijk} \left\{ \epsilon \frac{\partial}{\partial t} [\mathbf{E} \cdot (\mathbf{r} \times \nabla) \mathbf{A}] - \nabla \cdot \left[ \frac{1}{\mu_0} \mathbf{B} \times (\mathbf{r} \times \nabla) \mathbf{A} - \epsilon \mathbf{E} (\mathbf{r} \times \nabla \phi) \right] + (\mathbf{r} \times \nabla) \mathcal{L}_{\text{em}} \right\}_k \quad (\text{A.18b})$$

The problem with Eqs. (A.14b) and (A.18) is that they are gauge-dependent, which means that under the transformations  $\psi \rightarrow \psi e^{i\zeta}$  and  $A_\mu \rightarrow A_\mu + \partial_\mu \zeta$  these expressions change. Therefore, the individual terms do not represent any physically meaningful quantity. The fundamental equation to hold is Eq. (A.13). Therefore, as long as this relation is satisfied, we can cast Eqs. (A.14b) and (A.18) into gauge-independent forms. To do so, we break  $\mathbf{A}$  into two longitudinal and transverse parts as  $\mathbf{A} = \mathbf{A}^\parallel + \mathbf{A}^\perp$ , where  $\nabla \cdot \mathbf{A}^\perp = 0$  and  $\nabla \times \mathbf{A}^\parallel = 0$  by definition. After some algebra, we find for the new spin and OAM tensors of Dirac and electromagnetic field

$$\partial_\lambda \mathcal{S}_D^{ij,\lambda} = \varepsilon_{ijk} \left[ \hbar \frac{\partial}{\partial t} (\psi^\dagger \Sigma \psi) + \frac{\hbar c}{2} \nabla (\psi^\dagger \gamma^5 \psi) \right]_k, \quad (\text{A.19a})$$

$$\partial_\lambda \mathcal{L}_D^{ij,\lambda} = \varepsilon_{ijk} \left[ \frac{\partial}{\partial t} \mathcal{R} \left\{ \psi^\dagger (\mathbf{r} \times \mathbf{p}_\parallel) \psi \right\} + c \nabla \cdot \mathcal{R} \left\{ \bar{\psi} \boldsymbol{\gamma} (\mathbf{r} \times \mathbf{p}_\parallel) \psi \right\} \right]_k, \quad (\text{A.19b})$$

$$\partial_\lambda \mathbf{S}_{\text{em}}^{ij,\lambda} = \varepsilon_{ijk} \left[ \epsilon \frac{\partial}{\partial t} (\mathbf{E} \times \mathbf{A}^\perp) - \frac{1}{\mu_0} \nabla \cdot (\mathbf{A}^\perp \mathbf{B}) + \frac{1}{\mu_0} \nabla (\mathbf{A}^\perp \cdot \mathbf{B}) \right]_k, \quad (\text{A.19c})$$

$$\begin{aligned} \partial_\lambda \mathbf{L}_{\text{em}}^{ij,\lambda} = & \varepsilon_{ijk} \left\{ \epsilon \frac{\partial}{\partial t} \left[ \mathbf{E} \cdot (\mathbf{r} \times \nabla) \mathbf{A}^\perp \right] - \nabla \cdot \left[ \frac{1}{\mu_0} \mathbf{B} \times (\mathbf{r} \times \nabla) \mathbf{A}^\perp + \epsilon \mathbf{E} (\mathbf{r} \times \mathbf{E}^\parallel) \right] \right. \\ & \left. + (\mathbf{r} \times \nabla) \mathfrak{L}_{\text{em}} \right\}_k. \end{aligned} \quad (\text{A.19d})$$

where  $\mathbf{p}_\parallel = -i\hbar\nabla - e\mathbf{A}^\parallel$  is the gauge-independent covariant momentum operator of electron. We can further separate the contribution of longitudinal electric field  $\mathbf{E}^\parallel$  to the angular momentum. This contribution can be written as

$$\mathbf{E}^\parallel \times \mathbf{A}^\perp + E_i^\parallel (\mathbf{r} \times \nabla) A_i^\perp = -\nabla \times \left[ \mathbf{r} (\mathbf{E}^\parallel \cdot \mathbf{A}^\perp) \right] - \nabla \cdot \left[ \mathbf{A}^\perp (\mathbf{r} \times \mathbf{E}^\parallel) \right] \quad (\text{A.20})$$

When integrated over the entire space, both of these terms on r.h.s of this expression become zero due to the Stokes theorem and thus the longitudinal electric field does not contribute to the global angular momentum of the electromagnetic field. For this reason, we move this term into the angular momentum current terms so that the global angular momentum represents the integrated angular momentum density. Making this change, we get for the new components of the electromagnetic angular momentum currents

$$\partial_\lambda \mathbf{S}_{\text{em}}^{ij,\lambda} = \varepsilon_{ijk} \left[ \epsilon \frac{\partial}{\partial t} (\mathbf{E}^\perp \times \mathbf{A}^\perp) - \frac{1}{\mu_0} \nabla \cdot (\mathbf{A}^\perp \mathbf{B}) + \frac{1}{\mu_0} \nabla (\mathbf{A}^\perp \cdot \mathbf{B}) \right]_k, \quad (\text{A.21a})$$

$$\begin{aligned} \partial_\lambda \mathbf{L}_{\text{em}}^{ij,\lambda} = & \varepsilon_{ijk} \left\{ \epsilon \frac{\partial}{\partial t} \left[ \mathbf{E}^\perp \cdot (\mathbf{r} \times \nabla) \mathbf{A}^\perp \right] - \nabla \cdot \left[ \frac{1}{\mu_0} \mathbf{B} \times (\mathbf{r} \times \nabla) \mathbf{A}^\perp + \epsilon_0 \mathbf{A}^\perp \left( \mathbf{r} \times \frac{\partial \mathbf{E}^\parallel}{\partial t} \right) \right] \right. \\ & \left. + (\mathbf{r} \times \nabla) \left[ -\frac{1}{2\mu_0} \mathbf{B} \cdot \mathbf{B} + \frac{\epsilon_0}{2} \mathbf{E}^\perp \cdot \mathbf{E}^\perp + \epsilon_0 \frac{\partial \mathbf{E}^\parallel}{\partial t} \cdot \mathbf{A}^\perp \right] \right\}_k. \end{aligned} \quad (\text{A.21b})$$

Adding these four equations together we get Eq. (2.6),

$$\frac{\partial \mathbf{M}}{\partial t} + \nabla_i J_{ij} + \nabla \chi + \nabla_i N_{ij} = 0 \quad (\text{A.22})$$

where the terms are given in Eq. (2.7) and (2.8). Eq. (A.22) can be written as

$$\frac{\partial \mathbf{M}}{\partial t} + \nabla \cdot \overleftarrow{\mathbf{T}} = 0 \quad (\text{A.23})$$

where

$$\overleftarrow{\mathbf{T}} = \chi \overleftarrow{\mathbf{I}} + \overleftarrow{\mathbf{J}} + \overleftarrow{\mathbf{N}} \quad (\text{A.24})$$

with  $\overleftarrow{\mathbf{I}} = \hat{x}\hat{x} + \hat{y}\hat{y} + \hat{z}\hat{z} = \delta_{ij}\hat{x}_i\hat{x}_j$ , and

$$\begin{aligned} \overleftarrow{\mathbf{N}} = & \varepsilon_{ijk} \hat{x}_i \hat{x}_j x_k \mathfrak{N}_{\text{em}} = \begin{pmatrix} 0 & z & -y \\ -z & 0 & x \\ y & -x & 0 \end{pmatrix} \mathfrak{N}_{\text{em}}, \\ \mathfrak{N}_{\text{em}} = & \frac{\epsilon_0}{2} \mathbf{E}^\perp \cdot \mathbf{E}^\perp - \frac{1}{2\mu_0} \mathbf{B} \cdot \mathbf{B} + \epsilon_0 \frac{\partial \mathbf{E}^\parallel}{\partial t} \cdot \mathbf{A}^\perp. \end{aligned} \quad (\text{A.25})$$

Note that the first two terms of  $\mathfrak{N}_{em}$  describe the Lagrangian due to the transverse electric field, which can be interpreted as the Lagrangian of the free photon [28], while the last term shows the interaction between the transverse vector potential and the currents due to the longitudinal electric fields. Note that the term  $\frac{\epsilon_0}{2} \mathbf{E}^{\parallel} \cdot \mathbf{E}^{\parallel}$  in the Lagrangian of the electromagnetic field cancels out with the same term coming from  $\nabla_i J_{ij}$ . The expressions for  $\overleftrightarrow{\mathbf{J}}$  and  $\chi$  are given in Eq. (2.8).

Also note that the EM Lagrangian does not include the interaction term  $j_C^\mu A_\mu$  because it appears in the Dirac part of the Lagrangian  $\mathfrak{L}_D$ . Dirac Lagrangian, as mentioned earlier, vanishes from the expression for the OAM of the Dirac field since it satisfies the Dirac equation. For this reason, the contribution from the Dirac Lagrangian  $\mathfrak{L}_D$  disappears from the conservation equations.

Equation (A.23) describes the local conservation law for the angular momentum currents  $\overleftrightarrow{\mathbf{T}}$  and the angular momentum density (charge)  $M$ . When integrated over the entire space, and assuming that the fields vanish on the boundary of the this surface, the second term becomes an integral over this surface and thus vanishes. In this case, we arrive at the usual global conservation of angular momentum equation which states that the total angular momentum of the Dirac and Maxwell fields is a constant. However, in situations where the problem under consideration is an open dissipative system, this simplification cannot be made and surface terms of the angular momentum current can carry angular momentum out of the system.

## A.2 Spin-Orbit Torque

In this section we show that Eq. (A.19) leads to Eq. (2.9). Starting with the equation for the spin of the Dirac fields, we get for the  $z$  component for instance,

$$\partial_\lambda \mathbf{S}_D^{12,\lambda} = \frac{\hbar}{2} \partial_t (\psi^\dagger \Sigma_z \psi) + \frac{\hbar c}{2} \partial_z (\psi^\dagger \gamma^5 \psi) \quad (\text{A.26})$$

where  $\partial_t \equiv \frac{\partial}{\partial t}$  and  $\partial_i \equiv \frac{\partial}{\partial x_i}$ . Using Dirac equation we get

$$\hbar \partial_t \psi = -\hbar c \gamma^0 (\boldsymbol{\gamma} \cdot \nabla \psi) - ice A_\mu \gamma^0 \gamma^\mu \psi - imc^2 \gamma^0 \psi \quad (\text{A.27a})$$

$$\hbar \partial_t \psi^\dagger = \hbar c (\nabla \psi^\dagger \cdot \boldsymbol{\gamma}) \gamma^0 + ice A_\mu \psi^\dagger \gamma^0 \gamma^\mu + imc^2 \psi^\dagger \gamma^0 \quad (\text{A.27b})$$

Using these equations we find

$$\begin{aligned}
\partial_\lambda \mathbf{S}_D^{12,\lambda} &= \frac{\hbar}{2} \left\{ (\partial_t \psi^\dagger) \Sigma_z \psi + \psi^\dagger \Sigma_z (\partial_t \psi) + c \partial_z (\psi^\dagger \gamma^5 \psi) \right\} \\
&+ \frac{1}{2} \left\{ \hbar c (\nabla \psi^\dagger \cdot \boldsymbol{\gamma}) i \gamma^0 \gamma^1 \gamma^2 \psi - c e A_\mu \psi^\dagger \gamma^0 \gamma^\mu \gamma^1 \gamma^2 \psi - m c^2 \psi^\dagger \gamma^0 \gamma^1 \gamma^2 \psi \right. \\
&- i \hbar c \psi^\dagger \gamma^1 \gamma^2 \gamma^0 (\boldsymbol{\gamma} \cdot \nabla \psi) + c e A_\mu \psi^\dagger \gamma^1 \gamma^2 \gamma^0 \gamma^\mu \psi + m c^2 \psi^\dagger \gamma^1 \gamma^2 \gamma^0 \psi + \hbar c \partial_z (\psi^\dagger \gamma^5 \psi) \left. \right\} \\
&= \frac{1}{2} \left\{ -\hbar c \partial_z (\psi^\dagger \gamma^5 \psi) + i \hbar c (\partial_x \psi^\dagger) \gamma^0 \gamma^2 \psi - i \hbar c \psi^\dagger \gamma^0 \gamma^2 (\partial_x \psi) - i \hbar c (\partial_y \psi^\dagger) \gamma^0 \gamma^1 \psi \right. \\
&+ i \hbar c \psi^\dagger \gamma^0 \gamma^1 (\partial_y \psi) + 2 c e A_1 \psi^\dagger \gamma^0 \gamma^2 \psi - 2 c e A_2 \psi^\dagger \gamma^0 \gamma^1 \psi + \hbar c \partial_z (\psi^\dagger \gamma^5 \psi) \left. \right\} \\
&= \hbar c \mathcal{R} \left\{ i \bar{\psi} (\gamma^1 \partial_y - \gamma^2 \partial_x) \psi \right\} - c e (A_x^\parallel \bar{\psi} \gamma^2 \psi - A_y^\parallel \bar{\psi} \gamma^1 \psi) - (A_x^\perp j_{c,y} - A_y^\perp j_{c,x}) \\
&= -c \mathcal{R} \left\{ \bar{\psi} \left[ \gamma^1 (-i \hbar \partial_y - e A_y^\parallel) - \gamma^2 (-i \hbar \partial_x - e A_x^\parallel) \right] \psi \right\} - (A_x^\perp j_{c,y} - A_y^\perp j_{c,x}) \\
&= -c \mathcal{R} \left\{ \bar{\psi} (\boldsymbol{\gamma} \times \mathbf{p}_\parallel)_z \psi \right\} + (\mathbf{j}_c \times \mathbf{A}^\perp)_z.
\end{aligned} \tag{A.28}$$

In this derivation we have used the facts that  $\{\gamma^\mu, \gamma^\nu\} = 2\eta^{\mu\nu}$ ,  $(\gamma^i)^2 = -1$ ,  $A_1 = -A_x$ ,  $A_2 = -A_y$ , and  $\mathbf{j}_c = c e \bar{\psi} \boldsymbol{\gamma} \psi$ . We can do a similar derivation for other components of  $\partial_\lambda \mathbf{S}_D^{ij,\lambda}$ . Doing so we find Eq. (2.9a). Note that the first term on the r.h.s. of Eq. (A.28) is nothing but the spin-orbit torque of the Dirac field  $\boldsymbol{\tau}_D$  given in Eq. (2.10).

We now turn into the equation for the OAM of the Dirac field Eq. (A.19b). We get for the  $z$  component, for instance

$$\begin{aligned}
\partial_\lambda L_D^{12,\lambda} &= \partial_t \mathcal{R} \left\{ \psi^\dagger (xp_{\parallel,y} - yp_{\parallel,x}) \psi \right\} + c \nabla \cdot \mathcal{R} \left\{ \bar{\psi} \boldsymbol{\gamma} (xp_{\parallel,y} - yp_{\parallel,x}) \psi \right\} \\
&= \mathcal{R} \left\{ (\partial_t \psi^\dagger) (xp_{\parallel,y} - yp_{\parallel,x}) \psi + \psi^\dagger (xp_{\parallel,y} - yp_{\parallel,x}) (\partial_t \psi) + c \nabla \cdot \bar{\psi} \boldsymbol{\gamma} (xp_{\parallel,y} - yp_{\parallel,x}) \psi \right. \\
&\quad \left. - e \psi^\dagger \psi (x \partial_t A_y^\parallel - y \partial_t A_x^\parallel) \right\} \\
&= \mathcal{R} \left\{ c (\nabla \psi^\dagger \cdot \boldsymbol{\gamma}) \gamma^0 (xp_{\parallel,y} - yp_{\parallel,x}) \psi + \frac{ice}{\hbar} A_\mu \psi^\dagger \gamma^0 \gamma^\mu (xp_{\parallel,y} - yp_{\parallel,x}) \psi + \frac{imc^2}{\hbar} \psi^\dagger \gamma^0 (xp_{\parallel,y} - yp_{\parallel,x}) \psi \right. \\
&\quad \left. - c \psi^\dagger (xp_{\parallel,y} - yp_{\parallel,x}) \gamma^0 (\boldsymbol{\gamma} \cdot \nabla \psi) - \frac{ice}{\hbar} \psi^\dagger (xp_{\parallel,y} - yp_{\parallel,x}) \gamma^0 \gamma^\mu (A_\mu \psi) - \frac{imc^2}{\hbar} \psi^\dagger (xp_{\parallel,y} - yp_{\parallel,x}) \gamma^0 \psi \right. \\
&\quad \left. + c \nabla \cdot \bar{\psi} \boldsymbol{\gamma} (xp_{\parallel,y} - yp_{\parallel,x}) \psi - e \psi^\dagger \psi (x \partial_t A_y^\parallel - y \partial_t A_x^\parallel) \right\} \\
&= \mathcal{R} \left\{ -c \nabla \cdot \bar{\psi} \boldsymbol{\gamma} (xp_{\parallel,y} - yp_{\parallel,x}) \psi + c \bar{\psi} [\boldsymbol{\gamma} \cdot \nabla (xp_{\parallel,y} - yp_{\parallel,x})] \psi - ce \bar{\psi} \gamma^\mu \psi (x \partial_y - y \partial_x) A_\mu \right. \\
&\quad \left. + c \nabla \cdot \bar{\psi} \boldsymbol{\gamma} (xp_{\parallel,y} - yp_{\parallel,x}) \psi - e \psi^\dagger \psi (x \partial_t A_y^\parallel - y \partial_t A_x^\parallel) \right\} \\
&= \mathcal{R} \left\{ c \bar{\psi} (\gamma^1 p_{\parallel,y} - \gamma^2 p_{\parallel,x}) \psi \right\} - ce \bar{\psi} \boldsymbol{\gamma} \psi (x \nabla A_y^\parallel - y \nabla A_x^\parallel) - ce \bar{\psi} \gamma^\mu \psi (x \partial_y - y \partial_x) A_\mu \\
&\quad - e \psi^\dagger \psi (x \partial_t A_y^\parallel - y \partial_t A_x^\parallel) \\
&= \mathcal{R} \left\{ c \bar{\psi} (\gamma^1 p_{\parallel,y} - \gamma^2 p_{\parallel,x}) \psi \right\} - ce \bar{\psi} \left[ \gamma^1 (x \partial_x A_y^\parallel - y \partial_x A_x^\parallel) + \gamma^2 (x \partial_y A_y^\parallel - y \partial_y A_x^\parallel) \right. \\
&\quad \left. + \gamma^3 (x \partial_z A_y^\parallel - y \partial_z A_x^\parallel) - \gamma^1 (x \partial_y A_x - y \partial_x A_x) - \gamma^2 (x \partial_y A_y - y \partial_x A_y) - \gamma^3 (x \partial_y A_z - y \partial_x A_z) \right. \\
&\quad \left. + \frac{1}{c} \gamma^0 (x \partial_y \phi - y \partial_x \phi) + \frac{1}{c} \psi^\dagger (x \partial_t A_y^\parallel - y \partial_t A_x^\parallel) \right] \psi \\
&= \mathcal{R} \left\{ c \bar{\psi} (\gamma^1 p_{\parallel,y} - \gamma^2 p_{\parallel,x}) \psi \right\} - ce \bar{\psi} \gamma^1 \psi x (\partial_x A_y^\parallel - \partial_y A_x^\parallel) + ce \bar{\psi} \gamma^1 \psi (x \partial_y - y \partial_x) A_x^\perp \\
&\quad - ce \bar{\psi} \gamma^2 \psi y (\partial_x A_y^\parallel - \partial_y A_x^\parallel) + ce \bar{\psi} \gamma^2 \psi (x \partial_y - y \partial_x) A_y^\perp - ce \bar{\psi} \gamma^3 \psi x (\partial_z A_y^\parallel - \partial_y A_z^\parallel) \\
&\quad + ce \bar{\psi} \gamma^3 \psi y (\partial_z A_x^\parallel - \partial_x A_z^\parallel) + ce \bar{\psi} \gamma^3 \psi (x \partial_y - y \partial_x) A_z^\perp + e \psi^\dagger \psi \left[ x (-\partial_y \phi - \partial_t A_y^\parallel) - y (-\partial_x \phi - \partial_t A_x^\parallel) \right] \\
&= c \mathcal{R} \left\{ \bar{\psi} (\boldsymbol{\gamma} \times \mathbf{p}_{\parallel})_z \psi \right\} + j_{c,i} (\mathbf{r} \times \nabla)_z A_i^\perp + \rho (\mathbf{r} \times \mathbf{E}^\parallel)_z
\end{aligned} \tag{A.29}$$

where we have used the facts that  $\nabla \times \mathbf{A}^\parallel = 0$  and  $\mathbf{E}^\parallel = -\nabla \phi - \partial_t \mathbf{A}^\parallel$ . Writing similar equations for the other components we get Eq. (2.9b).

We can repeat this derivation for the electromagnetic spin and OAM currents as well.

Using Eq. (A.21a) we find, again for the  $z$  component for instance,

$$\begin{aligned}
\partial_\lambda \mathbf{S}_{\text{em}}^{12,\lambda} &= \epsilon_0 \partial_t (\mathbf{E}^\perp \times \mathbf{A}^\perp)_z - \frac{1}{\mu_0} \nabla \cdot (\mathbf{A}^\perp B_z) + \frac{1}{\mu_0} \partial_z (\mathbf{A}^\perp \cdot \mathbf{B}) \\
&= \epsilon_0 \partial_t (\mathbf{E}^\perp \times \mathbf{A}^\perp)_z - \frac{1}{\mu_0} B_z (\nabla \cdot \mathbf{A}^\perp) - \frac{1}{\mu_0} (\mathbf{A}^\perp \cdot \nabla) B_z \\
&\quad + \frac{1}{\mu_0} \left\{ (\mathbf{A}^\perp \cdot \nabla) B_z + (\mathbf{B} \cdot \nabla) A_z^\perp + [\mathbf{A}^\perp \times (\nabla \times \mathbf{B})]_z + [\mathbf{B} \times (\nabla \times \mathbf{A}^\perp)]_z \right\} \\
&= \epsilon_0 \partial_t (\mathbf{E}^\perp \times \mathbf{A}^\perp)_z + \frac{1}{\mu_0} (\mathbf{B} \cdot \nabla) A_z^\perp - \epsilon_0 [(\partial_t \mathbf{E}) \times \mathbf{A}^\perp]_z - (\mathbf{j}_c \times \mathbf{A}^\perp)_z \\
&= \epsilon_0 [\mathbf{E}^\perp \times (\partial_t \mathbf{A}^\perp)]_z + \frac{1}{\mu_0} (\mathbf{B} \cdot \nabla) A_z^\perp - \epsilon_0 \left[ \frac{\partial \mathbf{E}^\parallel}{\partial t} \times \mathbf{A}^\perp \right]_z - (\mathbf{j}_c \times \mathbf{A}^\perp)_z \\
&= \frac{1}{\mu_0} (\mathbf{B} \cdot \nabla) A_z^\perp - \epsilon_0 \left( \frac{\partial \mathbf{E}^\parallel}{\partial t} \times \mathbf{A}^\perp \right)_z - (\mathbf{j}_c \times \mathbf{A}^\perp)_z,
\end{aligned} \tag{A.30}$$

where we have used the facts that  $\nabla \cdot \mathbf{A}^\perp = 0$ ,  $\mathbf{B} = \nabla \times \mathbf{A}^\perp$ ,  $\mathbf{E}^\perp = -\partial_t \mathbf{A}^\perp$ , and  $\nabla \times \mathbf{B} = \frac{1}{c^2} \partial_t \mathbf{E} + \mu_0 \mathbf{j}_c$ . By repeating this derivation for the other components we get Eq. (2.9c). Note that the first two terms are the spin-orbit torque of the electromagnetic field,  $\tau_{\text{em}}$ , given in Eq. (2.11).

We can repeat this derivation to find the equation for  $\partial_\lambda \mathbf{L}_{\text{em}}^{ij,\lambda}$ . However, using the continuity condition,

$$\partial_\lambda (\mathbf{S}_{\text{D}}^{ij,\lambda} + \mathbf{L}_{\text{D}}^{ij,\lambda} + \mathbf{S}_{\text{em}}^{ij,\lambda} + \mathbf{L}_{\text{em}}^{ij,\lambda}) = 0, \tag{A.31}$$

it is straightforward to show that Eq. (2.9d) holds.

### A.3 Semi-Local Conservation Law

We can get the semi-local conservation laws by integrating the terms in Eqs. (A.19a), (A.19b), and (A.21) over the volume  $V'$ , on which surface the Dirac eigenfunctions  $\psi$  become zero. Using Gauss's theorem, the integral of the terms  $\nabla \cdot (\psi^\dagger \boldsymbol{\gamma}^5 \psi)$  and  $\nabla \cdot \mathcal{R}\{\bar{\psi} \boldsymbol{\gamma} (\mathbf{r} \times \mathbf{p}) \psi\}$  vanish because they become surface integrals of functions of  $\psi$ . We therefore arrive at the semi-local conservation law

$$\frac{\partial \tilde{\mathbf{M}}_{\text{D}}}{\partial t} + \frac{\partial \tilde{\mathbf{M}}_{\text{em}}}{\partial t} + \tilde{\mathbf{J}}_{\text{A}} + \tilde{\mathbf{h}} + \int_{V'} \nabla \times (\mathbf{r} \mathfrak{N}_{\text{em}}) dV' = 0 \tag{A.32}$$

where  $\tilde{\mathbf{M}}_{\text{D}}$  is the total angular momentum of the electron given by

$$\tilde{\mathbf{M}}_{\text{D}} = \hbar \int_{V'} \left[ \frac{1}{2} (\psi^\dagger \boldsymbol{\Sigma} \psi) + \mathcal{R}\{\psi^\dagger (\mathbf{r} \times \mathbf{p}) \psi\} \right] dV', \tag{A.33}$$

$\tilde{\mathbf{M}}_{\text{em}}$  is the EM total angular momentum in the volume  $V'$ ,

$$\tilde{\mathbf{M}}_{\text{em}} = \int_{V'} \epsilon (\mathbf{E}^\perp \times \mathbf{A}^\perp) d^3x + \int_{V'} \epsilon \left[ \mathbf{E}^\perp \cdot (\mathbf{r} \times \nabla) \mathbf{A}^\perp \right] d^3x, \tag{A.34}$$

and

$$\tilde{\mathbf{J}}_A = - \int_{V'} \nabla \cdot \left[ \frac{1}{\mu_0} \mathbf{A}^\perp \mathbf{B} + \frac{1}{\mu_0} \mathbf{B} \times (\mathbf{r} \times \nabla) \mathbf{A}^\perp + \epsilon \mathbf{A}^\perp \left( \mathbf{r} \times \frac{\partial E^\parallel}{\partial t} \right) \right] dV', \quad (\text{A.35a})$$

$$\tilde{\mathbf{h}} = \int_{V'} \nabla (\mathbf{A}^\perp \cdot \mathbf{B}) dV'. \quad (\text{A.35b})$$

Using Gauss's theorem the volume integrals in Eqs. (A.32), (A.35a) and (A.35b) can be converted into surface integrals. We find

$$\tilde{\mathbf{J}}_A = - \int_{S'} \hat{n}_i \left[ A_i^\perp \mathbf{B} + \epsilon_{ijk} B_j (\mathbf{r} \times \nabla) A_k^\perp + \epsilon A_i^\perp \left( \mathbf{r} \times \frac{\partial E^\parallel}{\partial t} \right) \right] da \quad (\text{A.36a})$$

$$\tilde{\mathbf{h}} = \int_{S'} \hat{n} (\mathbf{A}^\perp \cdot \mathbf{B}) da \quad (\text{A.36b})$$

where  $\hat{n}$  is the unit vector normal to the surface of the volume  $V'$ , and  $da$  its surface element. Equation (A.32) presents an equation for the time evolution of angular momentum of the electron in terms of the EM fields.

## A.4 Symmetrized Angular Momentum Tensor

In our derivation, we have used the canonical form of the angular momentum tensor which is derived directly from the application of Noether theorem to the QED Lagrangian in Eq. (A.1). The angular momentum tensor can be written in terms of the canonical energy-momentum tensor,  $T^{\mu\nu}$ , as

$$\mathcal{M}^{\mu\nu,\lambda} = x^\mu T^{\lambda\nu} - x^\nu T^{\lambda\mu} + S^{\mu\nu,\lambda}. \quad (\text{A.37})$$

Conservation of angular momentum implies that, when  $\partial_\lambda S^{\mu\nu,\lambda} \neq 0$ ,

$$T^{\mu\nu} \neq T^{\nu\mu} \quad (\text{A.38})$$

This is unpleasant because in general relativity, the energy-momentum tensor is directly proportional to the metric tensor which is symmetric in  $\mu$  and  $\nu$ . To overcome this problem, the energy momentum tensor can be modified to the so-called Bellifante-Resenfeld energy-momentum tensor as [190, 191]

$$T'^{\mu\nu} = T^{\mu\nu} + \frac{1}{2} \partial_\lambda (S^{\nu\lambda,\mu} + S^{\mu\lambda,\nu} - S^{\nu\mu,\lambda}) \quad (\text{A.39})$$

It can be shown that this new energy-momentum tensor is symmetric and does not change the conservation law of the energy-momentum tensor,  $\partial_\mu T'^{\mu\nu} = 0$ . We can therefore write a new symmetrized angular momentum tensor,  $M'^{\mu\nu,\lambda}$  as

$$\mathcal{M}'^{\mu\nu,\lambda} = x^\mu T'^{\lambda\nu} - x^\nu T'^{\lambda\mu} \quad (\text{A.40})$$

where we do not need to include the additional spin tensor because it is already present in the symmetric energy-momentum tensor. This symmetrized angular momentum tensor is of course different from the canonical one we derived in Eqs. (A.11) and (A.12). However, it is still not gauge invariant and the conservation law of angular momentum still holds. In other words

$$\partial_\lambda \mathcal{M}'^{\mu\nu,\lambda} = \partial_\lambda \mathcal{M}^{\mu\nu,\lambda} = 0 \quad (\text{A.41})$$

We can follow a similar procedure as we did in the previous section to derive the expression for the gauge-independent forms of the symmetrized angular momentum tensor for the electromagnetic and Dirac fields. We find, setting  $\mu, \nu = i, j$ ,

$$\frac{\partial \mathbf{M}'}{\partial t} + \nabla \cdot \overleftrightarrow{\mathbf{J}} + \nabla \chi' - \nabla \times (\mathbf{r} \mathcal{U}_{\text{em}}) = 0 \quad (\text{A.42})$$

where

$$\mathbf{M}' = \frac{\hbar}{2} (\psi^\dagger \boldsymbol{\Sigma} \psi) + \mathcal{R} \left\{ \psi^\dagger (\mathbf{r} \times \mathbf{p}_\parallel) \psi \right\} + \epsilon_0 \mathbf{r} \times (\mathbf{E} \times \mathbf{B}) - \rho (\mathbf{r} \times \mathbf{A}^\perp) \quad (\text{A.43a})$$

$$\nabla \cdot \overleftrightarrow{\mathbf{J}} = c \nabla_i \mathcal{R} \{ \bar{\psi} \gamma^i (\mathbf{r} \times \mathbf{p}_\parallel) \psi \} + \epsilon_0 \nabla_i E_i (\mathbf{r} \times \mathbf{E}) + \frac{1}{\mu_0} \nabla_i [B_i (\mathbf{r} \times \mathbf{B})] - \nabla_i [J_i (\mathbf{r} \times \mathbf{A}^\perp)] \quad (\text{A.43b})$$

$$\tilde{\chi} = \frac{\hbar c}{2} (\psi^\dagger \gamma^5 \psi) \quad (\text{A.43c})$$

$$\mathcal{U}_{\text{em}} = \frac{1}{2} \left( \epsilon_0 \mathbf{E} \cdot \mathbf{E} + \frac{1}{\mu_0} \mathbf{B} \cdot \mathbf{B} \right) \quad (\text{A.43d})$$

We emphasize that Eq. (A.42) is identical to the conservation Eq. (2.6). In fact, the terms related to the Dirac field are exactly the same as the one with the four-divergence of the canonical angular momentum tensor. The main difference is that we lose separate physically observable expressions for the spin and OAM densities and currents of the electromagnetic field and instead we get expressions for the total angular momentum,

$$\epsilon_0 \mathbf{r} \times (\mathbf{E} \times \mathbf{B}) - \rho (\mathbf{r} \times \mathbf{A}^\perp), \quad (\text{A.44})$$

and total angular momentum currents,

$$\epsilon_0 \mathbf{E} (\mathbf{r} \times \mathbf{E}) + \frac{1}{\mu_0} \mathbf{B} (\mathbf{r} \times \mathbf{B}) - \mathbf{J} (\mathbf{r} \times \mathbf{A}^\perp), \quad (\text{A.45})$$

of the electromagnetic field. Assuming that the symmetric energy-momentum tensor is more fundamental than the canonical one, however, does not prevent us from writing conservation laws that involve canonical angular momentum tensor and taking its gauge-independent terms as physically meaningful quantities.

## A.5 Boost Conservation Relations

We started our derivation by applying the Noether's theorem to the Dirac-Maxwell fields under the Lorentz transformation. To derive the angular momentum conservation equations, however, we only focused on the spatial rotations of the coordinates i.e. the space-space components of the angular momentum tensor current  $\mathcal{M}^{\mu\nu,\lambda}$ . In this section, we look at the conservation equations for the time-space components of the Lorentz transformations, namely the boosts, of the Dirac-Maxwell fields.

Using a similar approach to the one used in the first section, the conservation equation resulting from the boost components of the Lorentz transformation is given by,

$$\begin{aligned}
\partial_\lambda \mathcal{M}^{i0,\lambda} &= \partial_\lambda (\mathcal{M}_D)^{i0,\lambda} + \partial_\lambda (\mathcal{M}_E)^{i0,\lambda} \\
&= \frac{\partial}{\partial t} \mathcal{R} \left\{ i\psi^\dagger \left[ \frac{\mathbf{r}}{c} p_0 - ct\mathbf{p}_\parallel \right] \psi \right\} - c\nabla \times \left( \frac{\hbar}{2} \psi^\dagger \boldsymbol{\Sigma} \psi \right) + c\nabla \cdot \mathcal{R} \left\{ i\bar{\psi} \boldsymbol{\gamma} \left[ \frac{\mathbf{r}}{c} p_0 - ct\mathbf{p}_\parallel \right] \psi \right\} \\
&\quad - \epsilon \frac{\partial}{\partial t} \left[ \mathbf{E} \cdot \left( \frac{\mathbf{r}}{c} \partial_t + ct\nabla \right) \mathbf{A}^\perp \right] + \frac{1}{\mu_0} \nabla \cdot \left[ \mathbf{B} \times \left( \frac{\mathbf{r}}{c} \partial_t + ct\nabla \right) \mathbf{A}^\perp \right] + \frac{1}{\mu_0 c} \mathbf{B} \times \mathbf{E}^\perp + \frac{1}{\mu_0 c} \mathbf{E} \cdot (\nabla) \mathbf{A}^\perp \\
&\quad + c\rho \mathbf{A}^\perp - \left( \frac{\mathbf{r}}{c} \right) \mathbf{J} \cdot \mathbf{E}^\parallel + ct\rho \mathbf{E}^\parallel + \epsilon \mathbf{E} \cdot \left( \frac{\mathbf{r}}{c} \partial_t + ct\nabla \right) \mathbf{E}^\parallel + c \left( \frac{\mathbf{r}}{c^2} \partial_t + t\nabla \right) \mathcal{L}_E = 0
\end{aligned} \tag{A.46}$$

where  $p_0 = i\hbar\partial_t - e\phi$  and  $\mathbf{p}_\parallel = -i\hbar\nabla - e\mathbf{A}^\parallel$  are the gauge-independent time-derivative and momentum operators of the Dirac field, respectively. It is a matter of straightforward algebra to show that  $\mathbf{r} \times \partial_\lambda \mathcal{M}^{0,\lambda} = \epsilon_{ijk} x_j \partial_\lambda \mathcal{M}^{k0,\lambda}$  gives the conservation equation of the angular momentum in Eq. (A.23).

## A.6 Two Plane Wave Interference

We now evaluate the terms in Eq. (2.9c) for the interference of two plane waves at different frequencies. For a plane wave propagating along  $\mathbf{k}/|\mathbf{k}|$ , with the wavevector  $k$  we have  $\mathbf{k} \cdot \mathbf{E} = \mathbf{k} \cdot \mathbf{A}^\perp = \mathbf{k} \cdot \mathbf{B} = 0$ . Therefore we get

$$\nabla \cdot (\mathbf{A}^\perp \mathbf{B}) = (\mathbf{k} \cdot \mathbf{A}^\perp) \mathbf{B} = 0. \tag{A.47}$$

Note also that the EM spin-orbit torque  $\boldsymbol{\tau}_{\text{em}}$  also vanishes for plane waves because

$$(\mathbf{B} \cdot \nabla) \mathbf{A}^\perp = (\mathbf{B} \cdot \mathbf{k}) \mathbf{A}^\perp = 0. \tag{A.48}$$

Thus the only relevant terms in finding the conservation law for the spin current of the two plane wave interference are the time-derivative of spin and gradient of helicity.

The electric field for two plane waves propagating along  $z$  direction can be written as

$$\mathbf{E} = \mathcal{R}\{\mathcal{E}_1 e^{-i(\omega_1 t - k_1 z)} + \mathcal{E}_2 e^{-i(\omega_2 t - k_2 z)}\} \quad (\text{A.49})$$

where  $\mathcal{E}_i = \frac{\mathcal{E}_i}{\sqrt{2}}(\hat{x} + i\hat{y})$  are the complex electric field amplitudes of the two modes with frequencies  $\omega_i/c = k_i$ . Using Maxwell equation  $\nabla \times \mathbf{E} = -\frac{\partial \mathbf{B}}{\partial t}$  and  $\mathbf{E} = -\frac{\partial \mathbf{A}}{\partial t}$ , we get

$$\mathbf{B} = \mathcal{R}\left\{-\frac{k_1}{i\omega_1}\mathcal{E}_1 e^{-i(\omega_1 t - k_1 z)} - \frac{k_2}{i\omega_2}\mathcal{E}_2 e^{-i(\omega_2 t - k_2 z)}\right\} \quad (\text{A.50a})$$

$$\mathbf{A}^\perp = \mathcal{R}\left\{\frac{1}{i\omega_1}\mathcal{E}_1 e^{-i(\omega_1 t - k_1 z)} + \frac{1}{i\omega_2}\mathcal{E}_2 e^{-i(\omega_2 t - k_2 z)}\right\} \quad (\text{A.50b})$$

Using these equations we get for the spin of the two plane waves

$$\epsilon(\mathbf{E}^\perp \times \mathbf{A}^\perp) = \frac{\epsilon}{2} \left[ \frac{1}{\omega_1} \mathcal{I}\{\mathcal{E}_1^* \times \mathcal{E}_1\} + \frac{1}{\omega_2} \mathcal{I}\{\mathcal{E}_2^* \times \mathcal{E}_2\} + \left(\frac{1}{\omega_1} + \frac{1}{\omega_2}\right) \mathcal{I}\{\mathcal{E}_1^* \times \mathcal{E}_2 e^{+i[(\omega_1 - \omega_2)t - (k_1 - k_2)z]}\} \right] \quad (\text{A.51})$$

and thus we get

$$\begin{aligned} \epsilon \frac{\partial}{\partial t}(\mathbf{E}^\perp \times \mathbf{A}^\perp) &= -\epsilon \frac{\omega_1^2 - \omega_2^2}{2\omega_1\omega_2} \mathcal{R}\left\{\mathcal{E}_1^* \times \mathcal{E}_2 e^{+i[(\omega_1 - \omega_2)t - (k_1 - k_2)z]}\right\} \\ &= -\epsilon \frac{\omega_1^2 - \omega_2^2}{2\omega_1\omega_2} \mathcal{I}\left\{\mathcal{E}_1 \mathcal{E}_2^* e^{-i[(\omega_1 - \omega_2)t - (k_1 - k_2)z]}\right\} \hat{z} \end{aligned} \quad (\text{A.52})$$

For the helicity density we find

$$\mathbf{A}^\perp \cdot \mathbf{B} = -\frac{k_1}{\omega_1^2} |\mathcal{E}_1|^2 - \frac{k_2}{\omega_2^2} |\mathcal{E}_2|^2 - \frac{k_1 + k_2}{2\omega_1\omega_2} \mathcal{R}\left\{\mathcal{E}_1 \mathcal{E}_2^* e^{-i[(\omega_1 - \omega_2)t - (k_1 - k_2)z]}\right\} \quad (\text{A.53})$$

and thus

$$\begin{aligned} \frac{1}{\mu_0} \nabla(\mathbf{A}^\perp \cdot \mathbf{B}) &= \frac{1}{\mu_0} \frac{k_1^2 - k_2^2}{2\omega_1\omega_2} \mathcal{I}\left\{\mathcal{E}_1 \mathcal{E}_2^* e^{-i[(\omega_1 - \omega_2)t - (k_1 - k_2)z]}\right\} \hat{z} \\ &= \epsilon \frac{\omega_1^2 - \omega_2^2}{2\omega_1\omega_2} \mathcal{I}\left\{\mathcal{E}_1 \mathcal{E}_2^* e^{-i[(\omega_1 - \omega_2)t - (k_1 - k_2)z]}\right\} \end{aligned} \quad (\text{A.54})$$

which confirms the conservation Eq. (2.14).

## A.7 Meaning of the Notations

Throughout chapter 2, the usual expressions for dot and cross product are assumed. Terms like  $\mathbf{A}^\perp \cdot \mathbf{B}$  are tensorial expressions which can be expanded as

$$\begin{aligned} \mathbf{A}^\perp \cdot \mathbf{B} &= A_x^\perp B_x \hat{x}\hat{x} + A_x^\perp B_y \hat{x}\hat{y} + A_x^\perp B_z \hat{x}\hat{z} \\ &\quad + A_y^\perp B_x \hat{y}\hat{x} + A_y^\perp B_y \hat{y}\hat{y} + A_y^\perp B_z \hat{y}\hat{z} \\ &\quad + A_z^\perp B_x \hat{z}\hat{x} + A_z^\perp B_y \hat{z}\hat{y} + A_z^\perp B_z \hat{z}\hat{z} \end{aligned} \quad (\text{A.55})$$

Similar expressions can be written the terms like  $\mathbf{E}(\mathbf{r} \times \mathbf{E})$ ,  $\mathbf{E}(\mathbf{r} \times \mathbf{E})$ ,  $\mathbf{J}(\mathbf{r} \times \mathbf{A}^\perp)$ , and so on. Therefore, the expression  $\nabla \cdot (\mathbf{A}^\perp \mathbf{B})$  means

$$\begin{aligned} \nabla \cdot (\mathbf{A}^\perp \mathbf{B}) &= \left[ \partial_x(A_x^\perp B_x) + \partial_y(A_y^\perp B_x) + \partial_z(A_z^\perp B_x) \right] \hat{x} \\ &\quad + \left[ \partial_x(A_x^\perp B_y) + \partial_y(A_y^\perp B_y) + \partial_z(A_z^\perp B_y) \right] \hat{y} \\ &\quad + \left[ \partial_x(A_x^\perp B_z) + \partial_y(A_y^\perp B_z) + \partial_z(A_z^\perp B_z) \right] \hat{z} \end{aligned} \quad (\text{A.56})$$

which is a vector. We can similar expand

$$\begin{aligned} \mathbf{B} \times (\mathbf{r} \times \nabla) \mathbf{A}^\perp &= \left[ B_y(y\partial_z - z\partial_y)A_z^\perp - B_z(y\partial_z - z\partial_y)A_y^\perp \right] \hat{x}\hat{x} \\ &\quad + \left[ B_z(y\partial_z - z\partial_y)A_x^\perp - B_x(y\partial_z - z\partial_y)A_z^\perp \right] \hat{y}\hat{x} \\ &\quad + \left[ B_x(y\partial_z - z\partial_y)A_y^\perp - B_y(y\partial_z - z\partial_y)A_x^\perp \right] \hat{z}\hat{x} \\ &\quad + \left[ B_y(z\partial_x - x\partial_z)A_z^\perp - B_z(z\partial_x - x\partial_z)A_y^\perp \right] \hat{x}\hat{y} \\ &\quad + \left[ B_z(z\partial_x - x\partial_z)A_x^\perp - B_x(z\partial_x - x\partial_z)A_z^\perp \right] \hat{y}\hat{y} \\ &\quad + \left[ B_x(z\partial_x - x\partial_z)A_y^\perp - B_y(z\partial_x - x\partial_z)A_x^\perp \right] \hat{z}\hat{y} \\ &\quad + \left[ B_y(x\partial_y - y\partial_x)A_z^\perp - B_z(x\partial_y - y\partial_x)A_y^\perp \right] \hat{x}\hat{z} \\ &\quad + \left[ B_z(x\partial_y - y\partial_x)A_x^\perp - B_x(x\partial_y - y\partial_x)A_z^\perp \right] \hat{y}\hat{z} \\ &\quad + \left[ B_x(x\partial_y - y\partial_x)A_y^\perp - B_y(x\partial_y - y\partial_x)A_x^\perp \right] \hat{z}\hat{z} \end{aligned} \quad (\text{A.57})$$

and we can take its divergence similar to Eq. (A.56).

## Appendix B

# Proofs for Chapter 3

### B.1 Spherical Solutions of Scalar Helmholtz Equation

In this section, we derive the solutions to the source-free Maxwell's equations in the spherical coordinates. The Helmholtz equation

$$(\nabla^2 + k^2)\psi = 0 \quad (\text{B.1})$$

in the spherical coordinates can be written as

$$\frac{\partial^2 \psi}{\partial r^2} + \frac{2}{r} \frac{\partial \psi}{\partial r} + \frac{1}{r^2 \sin \theta} \frac{\partial}{\partial \theta} \left( \sin \theta \frac{\partial \psi}{\partial \theta} \right) + \frac{1}{r^2 \sin^2 \theta} \frac{\partial^2 \psi}{\partial \phi^2} + k^2 \psi = 0 \quad (\text{B.2})$$

Separating the variable into angular and radial terms by

$$\psi = \sum_{l,m} f_{lm}(r) Y(\theta, \phi) \quad (\text{B.3})$$

and plugging these solutions back into wave equations we get

$$\frac{r^2}{f_{lm}} \frac{d^2 f_{lm}}{dr^2} + \frac{2r}{f_{lm}} \frac{df_{lm}}{dr} + k^2 r^2 = -\frac{1}{Y \sin \theta} \frac{\partial}{\partial \theta} \left( \sin \theta \frac{\partial Y}{\partial \theta} \right) - \frac{1}{\sin^2 \theta} \frac{1}{Y} \frac{\partial^2 Y}{\partial \phi^2} \quad (\text{B.4})$$

LHS and RHS are only functions of  $r$  and  $(\theta, \phi)$ , respectively, and therefore they both should be constant, say  $\lambda$ . Defining the angular momentum operators as

$$L_{\pm} = L_x \pm iL_y = \pm e^{\pm i\phi} \left( \frac{\partial}{\partial \theta} \pm i \cot \theta \frac{\partial}{\partial \phi} \right) \quad (\text{B.5a})$$

$$L_z = -i \frac{\partial}{\partial \phi} \quad (\text{B.5b})$$

$$L^2 = - \left[ \frac{1}{\sin \theta} \frac{\partial}{\partial \theta} \left( \sin \theta \frac{\partial}{\partial \theta} \right) + \frac{1}{\sin^2 \theta} \frac{\partial^2}{\partial \phi^2} \right] \quad (\text{B.5c})$$

We can write for the RHS of equation B.4

$$L^2 Y(\theta, \phi) = \lambda Y(\theta, \phi) \quad (\text{B.6})$$

Taking  $Y(\theta, \phi)$  be simultaneous eigenfunctions of  $L^2$  and  $L_z$ , with eigenvalues  $\lambda$  and  $m$ , respectively, we require

$$L_z Y_{\lambda m} = m Y_{\lambda m} \quad (\text{B.7})$$

Using commutation relations of  $J_z$  and  $L_{\pm}$  we find that  $L_+$  increases the eigenvalue  $m$  of  $Y_{\lambda m}$  by one. But we cannot increase the projection of  $L$  on  $z$  forever since the total angular momentum is constant. Taking the maximum value of  $m$  as  $l$  we have for the state with  $l = m$ . Therefore

$$L^2 Y_{\lambda l} = (L_- L_+ + L_z^2 + L_z) Y_{\lambda, l} = (0 + l^2 + l) Y_{\lambda, l} = l(l+1) Y_{\lambda, l} \quad (\text{B.8})$$

and thus  $\lambda = l(l+1)$ . Therefore writing  $Y_{lm}(\theta, \phi) = \Theta(\theta)\Phi(\phi)$  we get two separate equations for  $\theta$  and  $\phi$

$$\frac{d^2 \Phi(\phi)}{d\phi^2} = -m^2 \Phi(\phi) \quad (\text{B.9a})$$

$$\left[ \frac{1}{\sin \theta} \frac{\partial}{\partial \theta} \left( \sin \theta \frac{\partial}{\partial \theta} \right) + \left( l(l+1) - \frac{m^2}{\sin^2 \theta} \right) \right] \Theta(\theta) = 0 \quad (\text{B.9b})$$

which gives for  $\Phi(\phi) = e^{\pm im\phi}$  with  $m$  integer, and solutions in terms of Legendre polynomials  $P_l^m(\cos \theta)$  for  $\theta$  dependence. Therefore  $Y_{lm}(\theta, \phi)$  (spherical harmonics) are

$$Y_{lm}(\theta, \phi) = (-1)^m \sqrt{\frac{(2l+1)(l-m)!}{4\pi(l+m)!}} P_l^m(\cos \theta) e^{im\phi}, \quad -l < m < l. \quad (\text{B.10})$$

Note that  $P_l^{-m} = (-1)^m \frac{(l-m)!}{(l+m)!} P_l^m$ . For the radial part we get

$$\left[ \frac{d^2}{dr^2} + \frac{2}{r} \frac{d}{dr} + k^2 - \frac{l(l+1)}{r^2} \right] f_l(r) = 0 \quad (\text{B.11})$$

whose solutions are spherical bessel functions  $j_l(kr)$ ,  $y_l(kr)$ ,  $h_l^{(1)}(kr)$ , and  $h_l^{(2)}(kr)$ .

## B.2 Spherical Solutions of Vector Helmholtz Equation

The solutions for the Helmholtz Eq. (B.1), when the fields are vector fields, can be determined from the solutions of the scalar equation by defining the following operators

$$\nabla = \hat{\mathbf{x}} \frac{\partial}{\partial x} + \hat{\mathbf{y}} \frac{\partial}{\partial y} + \hat{\mathbf{z}} \frac{\partial}{\partial z} \quad (\text{B.12a})$$

$$\mathbf{L} = -i\mathbf{r} \times \nabla \quad (\text{B.12b})$$

$$\nabla \times \mathbf{L}. \quad (\text{B.12c})$$

Using these operators, we can build a complete set of three vector fields from the solutions of scalar Helmholtz equation as

$$\mathbf{A}^r = \frac{1}{ik} \nabla \psi \quad (\text{B.13a})$$

$$\mathbf{A}^e = \frac{1}{k\sqrt{l(l+1)}} \nabla \times \mathbf{L}\psi \quad (\text{B.13b})$$

$$\mathbf{A}^m = \frac{1}{\sqrt{l(l+1)}} \mathbf{L}\psi \quad (\text{B.13c})$$

where  $\psi$  is given by equation B.3. The components  $\mathbf{A}^e$  and  $\mathbf{A}^m$  are related to each other by

$$\mathbf{A}^e = \frac{1}{k} \nabla \times \mathbf{A}^m \quad \mathbf{A}^m = \frac{1}{k} \nabla \times \mathbf{A}^e \quad (\text{B.14})$$

### B.3 Whispering-Gallery Modes in a Spherical Resonator

In order to find the eigen modes of a spherical resonator, we need to find the fields for a dielectric sphere in vacuum and match the boundary conditions. For a general well-behaved field  $T$  we can write

$$\nabla^2(\mathbf{r} \cdot \mathbf{T}) = \mathbf{r} \cdot (\nabla^2 \mathbf{T}) + 2\nabla \cdot \mathbf{T} \quad (\text{B.15})$$

Therefore, using source-free Maxwell's equations it can be shown for the electric,  $\mathbf{E}$ , and magnetic,  $\mathbf{H}$ , fields that

$$(\nabla^2 + k^2)(\mathbf{r} \cdot \mathbf{E}) = 0, \quad (\nabla^2 + k^2)(\mathbf{r} \cdot \mathbf{H}) = 0 \quad (\text{B.16})$$

and therefore,  $\mathbf{r} \cdot \mathbf{E}$  and  $\mathbf{r} \cdot \mathbf{H}$  have the solutions of scalar Helmholtz equation given in equation B.3. Therefore, we can write two sets of solutions as

$$\begin{aligned} \mathbf{r} \cdot \mathbf{H}_{lm}^{TE} &= \frac{l(l+1)}{k} g_l(kr) Y_{lm}(\theta, \phi) \\ \mathbf{r} \cdot \mathbf{E}_{lm}^{TE} &= 0 \end{aligned} \quad (\text{B.17})$$

where

$$g_l(kr) = A_l^{(1)} h_l^{(1)}(kr) + A_l^{(2)} h_l^{(2)}(kr) \quad (\text{B.18})$$

We can find the electric field from the longitudinal magnetic field from the Maxwell's equation as

$$\omega \mu \mathbf{r} \cdot \mathbf{H}_{lm}^{TE} = -i \mathbf{r} \cdot (\nabla \times \mathbf{E}_{lm}^{TE}) = -i (\mathbf{r} \times \nabla) \cdot \mathbf{E}_{lm}^{TE} = \mathbf{L} \cdot \mathbf{E}_{lm}^{TE} = l(l+1) \sqrt{\frac{\mu}{\epsilon}} g_l(kr) Y_{lm}(\theta, \phi) \quad (\text{B.19})$$

Since  $\mathbf{L}$  only operates on  $\theta$  and  $\phi$ , and using the fact that  $\mathbf{L}^2 Y_{lm}(\theta, \phi) = l(l+1) Y_{lm}(\theta, \phi)$ , we can prove that

$$\mathbf{E}_{lm}^{TE}(r, \theta, \phi) = \sqrt{\frac{\mu}{\epsilon}} g_l(kr) \mathbf{L} Y_{lm}(\theta, \phi) \quad (\text{B.20})$$

Together with

$$\mathbf{H}_{lm}^{TE} = -\frac{i}{\omega\mu} \nabla \times \mathbf{E}_{lm}^{TE} \quad (\text{B.21})$$

we can determine electric and magnetic  $TE$  fields solely from the longitudinal magnetic field. Similarly, we get for the  $TM$  mode

$$\mathbf{r} \cdot \mathbf{E}_{lm}^{TM} = -\sqrt{\frac{\mu}{\epsilon}} \frac{l(l+1)}{k} f_l(kr) Y_{lm}(\theta, \phi) \quad (\text{B.22a})$$

$$\mathbf{r} \cdot \mathbf{H}_{lm}^{TM} = 0 \quad (\text{B.22b})$$

$$\mathbf{H}_{lm}^{TM} = f_l(kr) \mathbf{L} Y_{lm}(\theta, \phi) \quad (\text{B.22c})$$

$$\mathbf{E}_{lm}^{TM} = \frac{i}{\omega\epsilon} \nabla \times \mathbf{H}_{lm}^{TM} \quad (\text{B.22d})$$

Putting  $\mathbf{Y}_{lm} = \mathbf{L} Y_{lm}$  we can show that

$$\mathbf{Y}_{lm} = i \left[ \frac{1}{\sin \theta} \frac{\partial Y_{lm}(\theta, \phi)}{\partial \phi} \hat{\theta} - \frac{\partial Y_{lm}(\theta, \phi)}{\partial \theta} \hat{\phi} \right] = Y_{lm,\theta} \hat{\theta} + Y_{lm,\phi} \hat{\phi} \quad (\text{B.23})$$

Therefore, we can write

$$\mathbf{E}_{lm}^{TM} = \frac{i}{\omega\epsilon} \nabla \times [f_l(kr) \mathbf{Y}_{lm}] = \frac{i}{\omega\epsilon} \{ \nabla f_l(kr) \times \mathbf{Y}_{lm} + f_l(kr) \nabla \times \mathbf{Y}_{lm} \} \quad (\text{B.24})$$

which gives

$$\mathbf{E}_{lm}^{TM} = -\hat{r} \sqrt{\frac{\mu}{\epsilon}} \frac{l(l+1)}{kr} f_l(kr) Y_{lm}(\theta, \phi) + \frac{i}{\omega\epsilon} \left\{ \frac{df_l(kr)}{dr} + \frac{1}{r} f_l(kr) \right\} (\hat{\phi} Y_{lm,\theta} - \hat{\theta} Y_{lm,\phi}) \quad (\text{B.25})$$

Next, we solve the eigen modes for a sphere of radius  $a$  with the dielectric constant  $\epsilon = \epsilon_1 \epsilon_0$ . The boundary conditions are matched by matching the radial parts of the fields. For the  $TE$  mode, the radial part of the electric field is in term of  $j_l(k_1 r)$  inside the sphere due to the finiteness of the solutions, and it is in terms of  $A_l^{(1)} h_l^{(1)}(k_0 r) + A_l^{(2)} h_l^{(2)}(k_0 r)$  outside the sphere, according to Eq. (B.20). Applying continuity condition for the fields at the interface we get for  $TE$  mode

$$\frac{1}{\sqrt{\epsilon_1}} j_l(k_1 a) = A_l^{(1)} h_l^{(1)}(k_0 a) + A_l^{(2)} h_l^{(2)}(k_0 a) \quad (\text{B.26a})$$

$$j_l'(k_1 a) = A_l^{(1)} h_l^{(1)'}(k_0 a) + A_l^{(2)} h_l^{(2)'}(k_0 a) \quad (\text{B.26b})$$

and

$$j_l(k_1 a) = A_l^{(1)} h_l^{(1)}(k_0 a) + A_l^{(2)} h_l^{(2)}(k_0 a) \quad (\text{B.27a})$$

$$\frac{1}{\sqrt{\epsilon_1}} j_l'(k_1 a) = A_l^{(1)} h_l^{(1)'}(k_0 a) + A_l^{(2)} h_l^{(2)'}(k_0 a) \quad (\text{B.27b})$$

These equations are not enough to find the eigen modes (i.e. Whispering Gallery Modes). In other words, the general case of a sphere dielectric cannot produce WGM modes. The extra condition comes from the fact that fields cannot come from infinity. The solutions outside the sphere in this case can then only be written in terms of Hankel function of the first kind which are outgoing waves. Therefore, the coefficient  $A_l^{(2)}$  are zero in Eq. (B.26) and (B.27) and thus we get transcendental equations for  $TE$  and  $TM$  modes

$$\frac{j_l(k_1 a)}{\sqrt{\epsilon_1} j_l'(k_1 a)} = \frac{h_l^{(1)}(k_0 a)}{h_l'^{(1)}(k_0 a)} \quad (\text{B.28})$$

$$\frac{\sqrt{\epsilon_1} j_l(k_1 a)}{j_l'(k_1 a)} = \frac{h_l^{(1)}(k_0 a)}{h_l'^{(1)}(k_0 a)} \quad (\text{B.29})$$

## B.4 Spin of WGMs

In this section we demonstrate the coupling between the spin of WGMs and the spin of the source by studying the coupling coefficient between the dipole moment of the source and the local fields of the WGM. The coupling coefficient between the dipole and WGMs can be written as

$$C_{lm} = \mathbf{E}_{lm} \cdot \mathbf{d} \quad (\text{B.30})$$

where  $\mathbf{E}_{lm}$  is the electric field of the TE or TM mode and  $\mathbf{d}$  is the dipole moment. Assuming the dipole with the dipole moment

$$\mathbf{d} = \frac{d_0}{\sqrt{2}} (\hat{r} + i\hat{\phi}) \quad (\text{B.31})$$

we find for the TM modes

$$\begin{aligned} C_{lm}^{TM} &= \mathbf{E}_{lm}^{TM} \cdot \mathbf{d} \\ &= \frac{d_0}{\sqrt{2}} \sqrt{\frac{\mu}{\epsilon}} Y_{lm}(\theta, \phi) \left\{ -\frac{l(l+1)}{kr} f_l(kr) + \frac{m}{\sin \theta} \left[ \frac{df_l(kr)}{kdr} + \frac{1}{kr} f_l(kr) \right] \right\} \\ &= \frac{d_0}{\sqrt{2}} \sqrt{\frac{\mu}{\epsilon}} Y_{lm}(\theta, \phi) \left\{ \frac{f_l(kr)}{kr} (l+1) \left[ \frac{m}{\sin \theta} - l \right] - \frac{m}{\sin \theta} f_{l+1}(kr) \right\} \end{aligned} \quad (\text{B.32})$$

We can see that first of all it is larger for higher  $l$ . Secondly, the magnitude of  $C_m^{TM}$  is larger for  $m < 0$  than for  $m > 0$ . It can become very small for  $m = l$  and very large for  $m = -l$ . Looking at the TM electric fields,

$$\mathbf{E}_{lm}^{TM} = -\hat{r} \sqrt{\frac{\mu}{\epsilon}} \frac{l(l+1)}{kr} f_l(kr) Y_{lm} + \frac{i}{\omega \epsilon} \sqrt{\frac{\mu}{\epsilon}} \left\{ \frac{l+1}{kr} f_l(kr) - f_{l+1}(kr) \right\} \left( -\frac{m}{\sin \theta} Y_{lm} \hat{\phi} + i \frac{\partial Y_{lm}}{\partial \theta} \hat{\theta} \right) \quad (\text{B.33})$$

we can see that  $E_r$  and  $E_\phi$  are out of phase while  $E_r$  and  $E_\theta$  are in phase. This would generate a nonzero spin along  $\hat{\theta}$  and a zero spin component along  $\hat{\phi}$ . Essentially  $C_{lm}^{TM}$  are nonzero for  $\mathbf{d} = \frac{d_0}{\sqrt{2}}(\hat{r} + i\hat{\phi})$  which means that the spin of the dipole is aligning with the spin of the TM WGMs.

Using the same argument, having  $\mathbf{d} = \frac{d_0}{\sqrt{2}}(\hat{r} + i\hat{\theta})$ , would give zero  $C_{lm}^{TM}$  because the spin of the dipole (along  $\hat{\theta}$ ) aligns with the  $\hat{\phi}$  component of the spin of TM WGM. However the  $\hat{\phi}$  component of the spin for the TM WGMs is zero as explained above. Thus we get zero  $C_{lm}^{TM}$  for when  $\mathbf{d} = \frac{d_0}{\sqrt{2}}(\hat{r} + i\hat{\theta})$ .

## B.5 Electric Field Green's Function

In this section we derive the Green's function for a source placed at an arbitrary location  $r'$  outside of a sphere. The Green function can be written in terms of the homogeneous and scattered Green's functions as

$$\overline{\mathbf{G}}_e(\mathbf{r}, \mathbf{r}') = \overline{\mathbf{G}}_{0e}(\mathbf{r}, \mathbf{r}') + \overline{\mathbf{G}}_{es}(\mathbf{r}, \mathbf{r}') \quad (\text{B.34})$$

The homogeneous solution in Eq. B.34 can be written as:

$$\begin{aligned} \overline{\mathbf{G}}_{0e}(\mathbf{r}, \mathbf{r}') &= \frac{\hat{r}\hat{r}}{k_0^2} \delta(r - r') + \frac{ik_0}{4\pi} \sum_{n=0}^{\infty} \sum_{m=0}^n (2 - \delta_m^0) \frac{2n+1}{n(n+1)} \frac{(n-m)!}{n+m} \\ &\times \begin{cases} \mathbf{M}_{mn}^{(1)}(k_0)\mathbf{M}'_{mn}(k_0) + \mathbf{N}_{mn}^{(1)}(k_0)\mathbf{N}'_{mn}(k_0) & r \geq r', \\ \mathbf{M}_{mn}(k_0)\mathbf{M}'_{mn}^{(1)}(k_0) + \mathbf{N}_{mn}(k_0)\mathbf{N}'_{mn}^{(1)}(k_0) & r \leq r' \end{cases} \end{aligned} \quad (\text{B.35})$$

Where  $k_0$  is the wavevector outside the sphere (where the dipole exists) and

$$\mathbf{M}_{mn}(k) = \mp \frac{m}{\sin \theta} z_n(kr) P_n^m(\cos \theta) \frac{\sin m\phi\hat{\theta} - z_n(kr)}{\cos \theta} \frac{dP_n^m(\cos \theta)}{d\theta} \frac{\cos m\phi\hat{\phi}}{\sin \theta} \quad (\text{B.36a})$$

$$\begin{aligned} \mathbf{N}_{mn}(k) &= \frac{n(n+1)}{kr} z_n(kr) P_n^m(\cos \theta) \frac{\cos m\phi\hat{r}}{\sin \theta} \\ &+ \frac{1}{kr} \frac{d[rz_n(kr)]}{dr} \left[ \frac{dP_n^m(\cos \theta)}{d\theta} \frac{\cos m\phi\hat{\theta}}{\sin \theta} \mp \frac{m}{\sin \theta} P_n^m(\cos \theta) \frac{\sin \theta}{\cos \theta} \frac{m\phi\hat{\phi}}{\cos \theta} \right] \end{aligned} \quad (\text{B.36b})$$

The (1) superscripts in Eq. B.35 indicates that the  $z_n$ 's should be spherical Hankel functions of first kind. Otherwise, they are the spherical bessel functions of the first kind. The prime sign also indicates that the coordinates belong to the location of the source  $\mathbf{r}'$ .

Similarly, the scattered part of the Green function can be written as :

$$\overline{\mathbf{G}}_{es}^{(11)}(\mathbf{r}, \mathbf{r}') = \frac{ik_0}{4\pi} \sum_{n=0}^{\infty} \sum_{m=0}^n (2 - \delta_m^0) \frac{2n+1}{n(n+1)} \frac{(n-m)!}{(n+m)!} \left[ \mathcal{B}_M \mathbf{M}_{mn}^{(1)}(k_0) \mathbf{M}'_{mn}^{(1)}(k_0) + \mathcal{B}_N \mathbf{N}_{mn}^{(1)}(k_0) \mathbf{N}'_{mn}^{(1)}(k_0) \right] \quad (\text{B.37a})$$

$$\overline{\mathbf{G}}_{es}^{(21)}(\mathbf{r}, \mathbf{r}') = \frac{ik_0}{4\pi} \sum_{n=0}^{\infty} \sum_{m=0}^n (2-\delta_m^0) \frac{2n+1}{n(n+1)} \frac{(n-m)!}{(n+m)!} \left[ \mathcal{D}_M \mathbf{M}_{mn}(k_1) \mathbf{M}'_{mn}(k_0) + \mathcal{D}_N \mathbf{N}_{mn}(k_1) \mathbf{N}'_{mn}(k_0) \right] \quad (\text{B.37b})$$

where  $k_1$  is the wavevector inside the sphere. The first equation is the scattered fields outside the sphere and the second equation is the scattered fields inside the sphere. Where

$$\mathcal{B}_{M,N} = -R_F^{H,V}, \quad \mathcal{D}_{M,N} = \frac{1}{T_P^{H,V}} \left[ 1 - R_F^{H,V} R_P^{H,V} \right] \quad (\text{B.38})$$

with

$$R_F^H = \frac{\partial \mathcal{J}_1 \mathcal{J}_0 - \partial \mathcal{J}_0 \mathcal{J}_1}{\partial \mathcal{J}_1 \mathcal{H}_0 - \partial \mathcal{H}_0 \mathcal{J}_1} \quad (\text{B.39a})$$

$$R_F^V = \frac{\epsilon_1 \partial \mathcal{J}_0 \mathcal{J}_1 - \epsilon_0 \partial \mathcal{J}_1 \mathcal{J}_0}{\epsilon_1 \partial \mathcal{H}_0 \mathcal{J}_1 - \epsilon_0 \partial \mathcal{J}_1 \mathcal{H}_0} \quad (\text{B.39b})$$

$$R_P^H = \frac{\partial \mathcal{H}_1 \mathcal{H}_0 - \partial \mathcal{H}_0 \mathcal{H}_1}{\partial \mathcal{H}_1 \mathcal{J}_0 - \partial \mathcal{J}_0 \mathcal{H}_1} \quad (\text{B.39c})$$

$$R_P^V = \frac{\epsilon_1 \partial \mathcal{H}_0 \mathcal{H}_1 - \epsilon_0 \partial \mathcal{H}_1 \mathcal{H}_0}{\epsilon_1 \partial \mathcal{J}_0 \mathcal{H}_1 - \epsilon_0 \partial \mathcal{H}_1 \mathcal{J}_0} \quad (\text{B.39d})$$

$$T_P^H = \frac{\partial \mathcal{H}_1 \mathcal{J}_1 - \partial \mathcal{J}_1 \mathcal{H}_1}{\partial \mathcal{H}_1 \mathcal{J}_0 - \partial \mathcal{J}_0 \mathcal{H}_1} \quad (\text{B.39e})$$

$$T_P^V = \sqrt{\epsilon_0 \epsilon_1} \frac{\partial \mathcal{J}_1 \mathcal{H}_1 - \partial \mathcal{H}_1 \mathcal{J}_1}{\epsilon_1 \partial \mathcal{J}_0 \mathcal{H}_1 - \epsilon_0 \partial \mathcal{H}_1 \mathcal{J}_0} \quad (\text{B.39f})$$

where

$$\mathcal{J}_i = j_n(k_i a), \quad \mathcal{H}_i = h_n^{(1)}(k_i a), \quad \partial \mathcal{J}_i = \left. \frac{d[\rho j_n(\rho)]}{d\rho} \right|_{\rho=k_i a}, \quad \partial \mathcal{H}_i = \left. \frac{d[\rho h_n^{(1)}(\rho)]}{d\rho} \right|_{\rho=k_i a} \quad (\text{B.39g})$$

I have assumed that the magnetic permeability equals  $\mu_0$  inside and outside the sphere and also the dielectric permittivity equals  $\epsilon_1$  and  $\epsilon_0$  inside and outside the sphere, respectively.

We can rewrite Eq. B.35 as:

$$\begin{aligned} \overline{\mathbf{G}}_{0e}(\mathbf{r}, \mathbf{r}') = & \frac{\hat{r}\hat{r}}{k_0^2} \delta(r-r') + \left\{ G_{0e,rr} \hat{r}\hat{r} + G_{0e,r\theta} \hat{r}\hat{\theta} + G_{0e,\theta r} \hat{\theta}\hat{r} + G_{0e,r\phi} \hat{r}\hat{\phi} + G_{0e,\phi r} \hat{\phi}\hat{r} \right. \\ & \left. + G_{0e,\theta\theta} \hat{\theta}\hat{\theta} + G_{0e,\theta\phi} \hat{\theta}\hat{\phi} + G_{0e,\phi\theta} \hat{\phi}\hat{\theta} + G_{0e,\phi\phi} \hat{\phi}\hat{\phi} \right\} \end{aligned} \quad (\text{B.39h})$$

where

$$\begin{aligned} G_{0e,rr} = & \frac{ik_0}{4\pi} \sum_{n=0}^{\infty} \sum_{m=0}^n C_{mn} \\ & \times \frac{n^2(n+1)^2}{x_0 x_0'} P_n^m(\cos \theta) P_n^m(\cos \theta') \begin{matrix} \cos & \cos \\ \sin & \sin \end{matrix} \begin{matrix} m\phi & m\phi' \end{matrix} \begin{cases} h_n^{(1)}(x_0) j_n(x_0') & r \geq r' \\ j_n(x_0) h_n^{(1)}(x_0') & r \leq r' \end{cases} \end{aligned} \quad (\text{B.40a})$$

$$\begin{aligned}
G_{0e,r\theta} &= \frac{ik_0}{4\pi} \sum_{n=0}^{\infty} \sum_{m=0}^n C_{mn} \\
&\times \frac{n(n+1)}{x_0 x'_0} P_n^m(\cos \theta) \frac{dP_n^m(\cos \theta')}{d\theta'} \begin{matrix} \cos & \cos \\ \sin & \sin \end{matrix} \begin{matrix} m\phi & m\phi' \end{matrix} \left\{ \begin{array}{l} h_n^{(1)}(x_0) \frac{d[r' j_n(x'_0)]}{dr'} \quad r \geq r' \\ j_n(x_0) \frac{d[r' h_n^{(1)}(x'_0)]}{dr'} \quad r \leq r' \end{array} \right. \\
&\hspace{15em} \text{(B.40b)}
\end{aligned}$$

$$\begin{aligned}
G_{0e,\theta r} &= \frac{ik_0}{4\pi} \sum_{n=0}^{\infty} \sum_{m=0}^n C_{mn} \\
&\times \frac{n(n+1)}{x_0 x'_0} P_n^m(\cos \theta') \frac{dP_n^m(\cos \theta)}{d\theta} \begin{matrix} \cos & \cos \\ \sin & \sin \end{matrix} \begin{matrix} m\phi & m\phi' \end{matrix} \left\{ \begin{array}{l} \frac{d[rh_n^{(1)}(x_0)]}{dr} j_n(x'_0) \quad r \geq r' \\ \frac{d[rj_n(x_0)]}{dr} h_n^{(1)}(x'_0) \quad r \leq r' \end{array} \right. \\
&\hspace{15em} \text{(B.40c)}
\end{aligned}$$

$$\begin{aligned}
G_{0e,r\phi} &= \frac{ik_0}{4\pi} \sum_{n=0}^{\infty} \sum_{m=0}^n C_{mn} \\
&\times \mp \frac{mn(n+1)}{x_0 x'_0 \sin \theta'} P_n^m(\cos \theta) P_n^m(\cos \theta') \begin{matrix} \cos & \sin \\ \sin & \cos \end{matrix} \begin{matrix} m\phi & m\phi' \end{matrix} \left\{ \begin{array}{l} h_n^{(1)}(x_0) \frac{d[r' j_n(x'_0)]}{dr'} \quad r \geq r' \\ j_n(x_0) \frac{d[r' h_n^{(1)}(x'_0)]}{dr'} \quad r \leq r' \end{array} \right. \\
&\hspace{15em} \text{(B.40d)}
\end{aligned}$$

$$\begin{aligned}
G_{0e,\phi r} &= \frac{ik_0}{4\pi} \sum_{n=0}^{\infty} \sum_{m=0}^n C_{mn} \\
&\times \mp \frac{mn(n+1)}{x_0 x'_0 \sin \theta} P_n^m(\cos \theta) P_n^m(\cos \theta') \begin{matrix} \sin & \cos \\ \cos & \sin \end{matrix} \begin{matrix} m\phi' & m\phi \end{matrix} \left\{ \begin{array}{l} \frac{d[rh_n^{(1)}(x_0)]}{dr} j_n(x'_0) \quad r \geq r' \\ \frac{d[rj_n(x_0)]}{dr} h_n^{(1)}(x'_0) \quad r \leq r' \end{array} \right. \\
&\hspace{15em} \text{(B.40e)}
\end{aligned}$$

$$\begin{aligned}
G_{0e,\theta\theta} &= \frac{ik_0}{4\pi} \sum_{n=0}^{\infty} \sum_{m=0}^n C_{mn} \\
&\times \left\{ \frac{1}{x_0 x'_0} \frac{dP_n^m(\cos \theta)}{d\theta} \frac{dP_n^m(\cos \theta')}{d\theta'} \begin{matrix} \cos & \cos \\ \sin & \sin \end{matrix} \begin{matrix} m\phi & m\phi' \end{matrix} \left\{ \begin{array}{l} \frac{d[rh_n^{(1)}(x_0)]}{dr} \frac{d[r' j_n(x'_0)]}{dr'} \quad r \geq r' \\ \frac{d[rj_n(x_0)]}{dr} \frac{d[r' h_n^{(1)}(x'_0)]}{dr'} \quad r \leq r' \end{array} \right. \right. \\
&+ \left. \frac{m^2}{\sin \theta \sin \theta'} P_n^m(\cos \theta) P_n^m(\cos \theta') \begin{matrix} \sin & \sin \\ \cos & \cos \end{matrix} \begin{matrix} m\phi & m\phi' \end{matrix} \left\{ \begin{array}{l} h_n^{(1)}(x_0) j_n(x'_0) \quad r \geq r' \\ j_n(x_0) h_n^{(1)}(x'_0) \quad r \leq r' \end{array} \right. \right\} \\
&\hspace{15em} \text{(B.40f)}
\end{aligned}$$

$$\begin{aligned}
G_{0e,\theta\phi} &= \frac{ik_0}{4\pi} \sum_{n=0}^{\infty} \sum_{m=0}^n C_{mn} \\
&\times \left\{ \mp \frac{m}{x_0 x'_0 \sin \theta'} \frac{dP_n^m(\cos \theta)}{d\theta} P_n^m(\cos \theta') \begin{matrix} \cos & \sin \\ \sin & \cos \end{matrix} \begin{matrix} m\phi & m\phi' \end{matrix} \left\{ \begin{array}{l} \frac{d[rh_n^{(1)}(x_0)]}{dr} \frac{d[r' j_n(x'_0)]}{dr'} \quad r \geq r' \\ \frac{d[rj_n(x_0)]}{dr} \frac{d[r' h_n^{(1)}(x'_0)]}{dr'} \quad r \leq r' \end{array} \right. \right. \\
&\pm \left. \frac{m}{\sin \theta} P_n^m(\cos \theta) \frac{dP_n^m(\cos \theta')}{d\theta'} \begin{matrix} \sin & \cos \\ \cos & \sin \end{matrix} \begin{matrix} m\phi & m\phi' \end{matrix} \left\{ \begin{array}{l} h_n^{(1)}(x_0) j_n(x'_0) \quad r \geq r' \\ j_n(x_0) h_n^{(1)}(x'_0) \quad r \leq r' \end{array} \right. \right\} \\
&\hspace{15em} \text{(B.40g)}
\end{aligned}$$

$$\begin{aligned}
G_{0e,\phi\theta} &= \frac{ik_0}{4\pi} \sum_{n=0}^{\infty} \sum_{m=0}^n C_{mn} \\
&\times \left\{ \mp \frac{m}{x_0 x'_0 \sin \theta} P_n^m(\cos \theta) \frac{dP_n^m(\cos \theta')}{d\theta'} \begin{matrix} \sin & \cos \\ \cos & \sin \end{matrix} \begin{matrix} m\phi & m\phi' \end{matrix} \left\{ \begin{matrix} \frac{d[rh_n^{(1)}(x_0)]}{dr} \frac{d[r'j_n(x'_0)]}{dr'} & r \geq r' \\ \frac{d[rj_n(x_0)]}{dr} \frac{d[r'h_n^{(1)}(x'_0)]}{dr'} & r \leq r' \end{matrix} \right. \right. \\
&\pm \frac{m}{\sin \theta'} \frac{dP_n^m(\cos \theta)}{d\theta} P_n^m(\cos \theta') \begin{matrix} \cos & \sin \\ \sin & \cos \end{matrix} \begin{matrix} m\phi & m\phi' \end{matrix} \left. \left\{ \begin{matrix} h_n^{(1)}(x_0) j_n(x'_0) & r \geq r' \\ j_n(x_0) h_n^{(1)}(x'_0) & r \leq r' \end{matrix} \right. \right\} \right. \\
&\hspace{15em} \text{(B.40h)}
\end{aligned}$$

$$\begin{aligned}
G_{0e,\phi\phi} &= \frac{ik_0}{4\pi} \sum_{n=0}^{\infty} \sum_{m=0}^n C_{mn} \\
&\times \left\{ \frac{m^2}{x_0 x'_0 \sin \theta \sin \theta'} P_n^m(\cos \theta) P_n^m(\cos \theta') \begin{matrix} \sin & \sin \\ \cos & \cos \end{matrix} \begin{matrix} m\phi & m\phi' \end{matrix} \left\{ \begin{matrix} \frac{d[rh_n^{(1)}(x_0)]}{dr} \frac{d[r'j_n(x'_0)]}{dr'} & r \geq r' \\ \frac{d[rj_n(x_0)]}{dr} \frac{d[r'h_n^{(1)}(x'_0)]}{dr'} & r \leq r' \end{matrix} \right. \right. \\
&+ \frac{dP_n^m(\cos \theta)}{d\theta} \frac{dP_n^m(\cos \theta')}{d\theta'} \begin{matrix} \cos & \cos \\ \sin & \sin \end{matrix} \begin{matrix} m\phi & m\phi' \end{matrix} \left. \left\{ \begin{matrix} h_n^{(1)}(x_0) j_n(x'_0) & r \geq r' \\ j_n(x_0) h_n^{(1)}(x'_0) & r \leq r' \end{matrix} \right. \right\} \right. \\
&\hspace{15em} \text{(B.40i)}
\end{aligned}$$

where

$$C_{mn} = (2 - \delta_m^0) \frac{2n+1}{n(n+1)} \frac{(n-m)!}{(n+m)!} \quad \text{(B.41)}$$

and  $x_0 = k_0 r$ ,  $x'_0 = k_0 r'$ . Using some Legendre theorems we can simplify these equations as:

$$G_{0e,rr} = \frac{ik_0}{4\pi} \sum_{n=0}^{\infty} \frac{n(n+1)(2n+1)}{x_0 x'_0} P_n(\cos \gamma) \left\{ \begin{matrix} h_n^{(1)}(x_0) j_n(x'_0) & r \geq r' \\ j_n(x_0) h_n^{(1)}(x'_0) & r \leq r' \end{matrix} \right. \quad \text{(B.42a)}$$

$$G_{0e,r\theta} = \frac{ik_0}{4\pi} \sum_{n=0}^{\infty} \frac{(2n+1)}{x_0 x'_0} \frac{dP_n(\cos \gamma)}{d\gamma} \cos \chi_2 \left\{ \begin{matrix} h_n^{(1)}(x_0) \frac{d[r'j_n(x'_0)]}{dr'} & r \geq r' \\ j_n(x_0) \frac{d[r'h_n^{(1)}(x'_0)]}{dr'} & r \leq r' \end{matrix} \right. \quad \text{(B.42b)}$$

$$G_{0e,\theta r} = \frac{ik_0}{4\pi} \sum_{n=0}^{\infty} \frac{(2n+1)}{x_0 x'_0} \frac{dP_n(\cos \gamma)}{d\gamma} \cos \chi_1 \left\{ \begin{matrix} \frac{d[rh_n^{(1)}(x_0)]}{dr} j_n(x'_0) & r \geq r' \\ \frac{d[rj_n(x_0)]}{dr} h_n^{(1)}(x'_0) & r \leq r' \end{matrix} \right. \quad \text{(B.42c)}$$

$$G_{0e,r\phi} = -\frac{ik_0}{4\pi} \sum_{n=0}^{\infty} \frac{(2n+1)}{x_0 x'_0} \frac{dP_n(\cos \gamma)}{d\gamma} \sin \chi_2 \left\{ \begin{matrix} h_n^{(1)}(x_0) \frac{d[r'j_n(x'_0)]}{dr'} & r \geq r' \\ j_n(x_0) \frac{d[r'h_n^{(1)}(x'_0)]}{dr'} & r \leq r' \end{matrix} \right. \quad \text{(B.42d)}$$

$$G_{0e,\phi r} = -\frac{ik_0}{4\pi} \sum_{n=0}^{\infty} \frac{(2n+1)}{x_0 x'_0} \frac{dP_n(\cos \gamma)}{d\gamma} \sin \chi_1 \left\{ \begin{matrix} \frac{d[rh_n^{(1)}(x_0)]}{dr} j_n(x'_0) & r \geq r' \\ \frac{d[rj_n(x_0)]}{dr} h_n^{(1)}(x'_0) & r \leq r' \end{matrix} \right. \quad \text{(B.42e)}$$

$$\begin{aligned}
G_{0e,\theta\theta} &= \frac{ik_0}{4\pi} \sum_{n=0}^{\infty} \frac{2n+1}{n(n+1)} \left\{ \frac{1}{x_0 x'_0} P_n^{(1)} \left\{ \begin{matrix} \frac{d[rh_n^{(1)}(x_0)]}{dr} \frac{d[r'j_n(x'_0)]}{dr'} & r \geq r' \\ \frac{d[rj_n(x_0)]}{dr} \frac{d[r'h_n^{(1)}(x'_0)]}{dr'} & r \leq r' \end{matrix} \right. \right. \\
&\left. \left. + P_n^{(2)} \left\{ \begin{matrix} h_n^{(1)}(x_0) j_n(x'_0) & r \geq r' \\ j_n(x_0) h_n^{(1)}(x'_0) & r \leq r' \end{matrix} \right. \right\} \right\} \\
&\hspace{15em} \text{(B.42f)}
\end{aligned}$$

$$G_{0e,\theta\phi} = \frac{ik_0}{4\pi} \sum_{n=0}^{\infty} \frac{2n+1}{n(n+1)} \left\{ P_n^{(3)} \frac{1}{x_0 x'_0} \begin{cases} \frac{d[rh_n^{(1)}(x_0)]}{dr} \frac{d[r'j_n(x'_0)]}{dr'} & r \geq r' \\ \frac{d[rj_n(x_0)]}{dr} \frac{d[r'h_n^{(1)}(x'_0)]}{dr'} & r \leq r' \end{cases} \right. \\ \left. - P_n^{(4)} \begin{cases} h_n^{(1)}(x_0) j_n(x'_0) & r \geq r' \\ j_n(x_0) h_n^{(1)}(x'_0) & r \leq r' \end{cases} \right\} \quad (\text{B.42g})$$

$$G_{0e,\phi\theta} = \frac{ik_0}{4\pi} \sum_{n=0}^{\infty} \frac{2n+1}{n(n+1)} \left\{ P_n^{(4)} \frac{1}{x_0 x'_0} \begin{cases} \frac{d[rh_n^{(1)}(x_0)]}{dr} \frac{d[r'j_n(x'_0)]}{dr'} & r \geq r' \\ \frac{d[rj_n(x_0)]}{dr} \frac{d[r'h_n^{(1)}(x'_0)]}{dr'} & r \leq r' \end{cases} \right. \\ \left. - P_n^{(3)} \begin{cases} h_n^{(1)}(x_0) j_n(x'_0) & r \geq r' \\ j_n(x_0) h_n^{(1)}(x'_0) & r \leq r' \end{cases} \right\} \quad (\text{B.42h})$$

$$G_{0e,\phi\phi} = \frac{ik_0}{4\pi} \sum_{n=0}^{\infty} \frac{2n+1}{n(n+1)} \left\{ \frac{1}{x_0 x'_0} P_n^{(2)} \begin{cases} \frac{d[rh_n^{(1)}(x_0)]}{dr} \frac{d[r'j_n(x'_0)]}{dr'} & r \geq r' \\ \frac{d[rj_n(x_0)]}{dr} \frac{d[r'h_n^{(1)}(x'_0)]}{dr'} & r \leq r' \end{cases} \right. \\ \left. + P_n^{(1)} \begin{cases} h_n^{(1)}(x_0) j_n(x'_0) & r \geq r' \\ j_n(x_0) h_n^{(1)}(x'_0) & r \leq r' \end{cases} \right\} \quad (\text{B.42i})$$

where

$$P_n^{(1)} = \frac{d^2 P_n(\cos \gamma)}{d\gamma^2} \cos \chi_1 \cos \chi_2 - \frac{dP_n(\cos \gamma)}{d\gamma} \frac{\sin \chi_1 \sin \chi_2}{\sin \gamma} \quad (\text{B.43a})$$

$$P_n^{(2)} = -\frac{d^2 P_n(\cos \gamma)}{d\gamma^2} \sin \chi_1 \sin \chi_2 + \frac{dP_n(\cos \gamma)}{d\gamma} \frac{\cos \chi_1 \cos \chi_2}{\sin \gamma} \quad (\text{B.43b})$$

$$P_n^{(3)} = -\frac{d^2 P_n(\cos \gamma)}{d\gamma^2} \cos \chi_1 \sin \chi_2 - \frac{dP_n(\cos \gamma)}{d\gamma} \frac{\sin \chi_1 \cos \chi_2}{\sin \gamma} \quad (\text{B.43c})$$

$$P_n^{(4)} = \frac{d^2 P_n(\cos \gamma)}{d\gamma^2} \cos \chi_2 \sin \chi_1 + \frac{dP_n(\cos \gamma)}{d\gamma} \frac{\sin \chi_2 \cos \chi_1}{\sin \gamma} \quad (\text{B.43d})$$

Similarly, we can write components of Eq. (B.37a) as

$$G_{es,rr}^{(11)} = \frac{ik_0}{4\pi} \sum_{n=0}^{\infty} \mathcal{B}_N \frac{n(n+1)(2n+1)}{x_0 x'_0} P_n(\cos \gamma) h_n^{(1)}(x_0) h_n^{(1)}(x'_0) \quad (\text{B.44a})$$

$$G_{es,r\theta}^{(11)} = \frac{ik_0}{4\pi} \sum_{n=0}^{\infty} \mathcal{B}_N \frac{(2n+1)}{x_0 x'_0} \frac{dP_n(\cos \gamma)}{d\gamma} \cos \chi_2 h_n^{(1)}(x_0) \frac{d[r'h_n^{(1)}(x'_0)]}{dr'} \quad (\text{B.44b})$$

$$G_{es,\theta r}^{(11)} = \frac{ik_0}{4\pi} \sum_{n=0}^{\infty} \mathcal{B}_N \frac{(2n+1)}{x_0 x'_0} \frac{dP_n(\cos \gamma)}{d\gamma} \cos \chi_1 \frac{d[rh_n^{(1)}(x_0)]}{dr} h_n^{(1)}(x'_0) \quad (\text{B.44c})$$

$$G_{es,r\phi}^{(11)} = -\frac{ik_0}{4\pi} \sum_{n=0}^{\infty} \mathcal{B}_N \frac{(2n+1)}{x_0 x'_0} \frac{dP_n(\cos \gamma)}{d\gamma} \sin \chi_2 h_n^{(1)}(x_0) \frac{d[r'h_n^{(1)}(x'_0)]}{dr'} \quad (\text{B.44d})$$

$$G_{es,\phi r}^{(11)} = -\frac{ik_0}{4\pi} \sum_{n=0}^{\infty} \mathcal{B}_N \frac{(2n+1)}{x_0 x'_0} \frac{dP_n(\cos \gamma)}{d\gamma} \sin \chi_1 \frac{d[rh_n^{(1)}(x_0)]}{dr} h_n^{(1)}(x'_0) \quad (\text{B.44e})$$

$$G_{es,\theta\theta}^{(11)} = \frac{ik_0}{4\pi} \sum_{n=0}^{\infty} \frac{2n+1}{n(n+1)} \left\{ \mathcal{B}_N \frac{1}{x_0 x'_0} P_n^{(1)} \frac{d[rh_n^{(1)}(x_0)]}{dr} \frac{d[r'h_n^{(1)}(x'_0)]}{dr'} \right. \\ \left. + \mathcal{B}_M P_n^{(2)} h_n^{(1)}(x_0) h_n^{(1)}(x'_0) \right\} \quad (\text{B.44f})$$

$$G_{es,\theta\phi}^{(11)} = \frac{ik_0}{4\pi} \sum_{n=0}^{\infty} \frac{2n+1}{n(n+1)} \left\{ P_n^{(3)} \mathcal{B}_N \frac{1}{x_0 x'_0} \frac{d[rh_n^{(1)}(x_0)]}{dr} \frac{d[r'h_n^{(1)}(x'_0)]}{dr'} \right. \\ \left. - P_n^{(4)} \mathcal{B}_M h_n^{(1)}(x_0) h_n^{(1)}(x'_0) \right\} \quad (\text{B.44g})$$

$$G_{es,\phi\theta}^{(11)} = \frac{ik_0}{4\pi} \sum_{n=0}^{\infty} \frac{2n+1}{n(n+1)} \left\{ P_n^{(4)} \mathcal{B}_N \frac{1}{x_0 x'_0} \frac{d[rh_n^{(1)}(x_0)]}{dr} \frac{d[r'h_n^{(1)}(x'_0)]}{dr'} \right. \\ \left. - P_n^{(3)} \mathcal{B}_M h_n^{(1)}(x_0) h_n^{(1)}(x'_0) \right\} \quad (\text{B.44h})$$

$$G_{es,\phi\phi}^{(11)} = \frac{ik_0}{4\pi} \sum_{n=0}^{\infty} \frac{2n+1}{n(n+1)} \left\{ \mathcal{B}_N \frac{1}{x_0 x'_0} P_n^{(2)} \frac{d[rh_n^{(1)}(x_0)]}{dr} \frac{d[r'h_n^{(1)}(x'_0)]}{dr'} \right. \\ \left. + \mathcal{B}_M P_n^{(1)} h_n^{(1)}(x_0) h_n^{(1)}(x'_0) \right\} \quad (\text{B.44i})$$

and for Eq. (B.37b)

$$G_{es,rr}^{(21)} = \frac{ik_0}{4\pi} \sum_{n=0}^{\infty} \mathcal{D}_N \frac{n(n+1)(2n+1)}{x_1 x'_0} P_n(\cos \gamma) j(x_1) h_n^{(1)}(x'_0) \quad (\text{B.45a})$$

$$G_{es,r\theta}^{(21)} = \frac{ik_0}{4\pi} \sum_{n=0}^{\infty} \mathcal{D}_N \frac{(2n+1)}{x_1 x'_0} \frac{dP_n(\cos \gamma)}{d\gamma} \cos \chi_2 j_n(x_1) \frac{d[r'h_n^{(1)}(x'_0)]}{dr'} \quad (\text{B.45b})$$

$$G_{es,\theta r}^{(21)} = \frac{ik_0}{4\pi} \sum_{n=0}^{\infty} \mathcal{D}_N \frac{(2n+1)}{x_1 x'_0} \frac{dP_n(\cos \gamma)}{d\gamma} \cos \chi_1 \frac{d[rj_n(x_1)]}{dr} h_n^{(1)}(x'_0) \quad (\text{B.45c})$$

$$G_{es,r\phi}^{(21)} = -\frac{ik_0}{4\pi} \sum_{n=0}^{\infty} \mathcal{D}_N \frac{(2n+1)}{x_1 x'_0} \frac{dP_n(\cos \gamma)}{d\gamma} \sin \chi_2 j_n(x_1) \frac{d[r'h_n^{(1)}(x'_0)]}{dr'} \quad (\text{B.45d})$$

$$G_{es,\phi r}^{(21)} = -\frac{ik_0}{4\pi} \sum_{n=0}^{\infty} \mathcal{D}_N \frac{(2n+1)}{x_1 x'_0} \frac{dP_n(\cos \gamma)}{d\gamma} \sin \chi_1 \frac{d[rj_n(x_1)]}{dr} h_n^{(1)}(x'_0) \quad (\text{B.45e})$$

$$G_{es,\theta\theta}^{(21)} = \frac{ik_0}{4\pi} \sum_{n=0}^{\infty} \frac{2n+1}{n(n+1)} \left\{ \mathcal{D}_N \frac{1}{x_1 x'_0} P_n^{(1)} \frac{d[rj_n(x_1)]}{dr} \frac{d[r'h_n^{(1)}(x'_0)]}{dr'} \right. \\ \left. + \mathcal{D}_M P_n^{(2)} j_n(x_1) h_n^{(1)}(x'_0) \right\} \quad (\text{B.45f})$$

$$G_{es,\theta\phi}^{(21)} = \frac{ik_0}{4\pi} \sum_{n=0}^{\infty} \frac{2n+1}{n(n+1)} \left\{ P_n^{(3)} \mathcal{D}_N \frac{1}{x_1 x'_0} \frac{d[rj_n(x_1)]}{dr} \frac{d[r'h_n^{(1)}(x'_0)]}{dr'} \right. \\ \left. - P_n^{(4)} \mathcal{D}_M j_n(x_1) h_n^{(1)}(x'_0) \right\} \quad (\text{B.45g})$$

$$G_{es,\phi\theta}^{(21)} = \frac{ik_0}{4\pi} \sum_{n=0}^{\infty} \frac{2n+1}{n(n+1)} \left\{ P_n^{(4)} \mathcal{D}_N \frac{1}{x_1 x'_0} \frac{d[rj_n(x_1)]}{dr} \frac{d[r'h_n^{(1)}(x'_0)]}{dr'} \right. \\ \left. - P_n^{(3)} \mathcal{D}_M j_n(x_1) h_n^{(1)}(x'_0) \right\} \quad (\text{B.45h})$$

$$G_{es,\phi\phi}^{(21)} = \frac{ik_0}{4\pi} \sum_{n=0}^{\infty} \frac{2n+1}{n(n+1)} \left\{ \mathcal{B}_N \frac{1}{x_1 x'_0} P_n^{(2)} \frac{d[rj_n(x_1)]}{dr} \frac{d[r'h_n^{(1)}(x'_0)]}{dr'} \right. \\ \left. + \mathcal{B}_M P_n^{(1)} j_n(x_1) h_n^{(1)}(x'_0) \right\} \quad (\text{B.45i})$$

## B.6 Magnetic Field Green Function

In order to find the total magnetic field for the source placed in the vicinity of the sphere, we need to find the magnetic Green's function due to the electric dipole. The Green function for the magnetic field is expressed as

$$\mathbf{H} = \int (\nabla \times \bar{\mathbf{G}}_e(\mathbf{r}, \mathbf{r}')) \mathbf{J}(\mathbf{r}') d^3 \mathbf{r}' \quad (\text{B.46})$$

Therefore  $\bar{\mathbf{G}}_m = \nabla \times \bar{\mathbf{G}}_e$  where

$$\bar{\mathbf{G}}_m = \bar{\mathbf{G}}_{0m} + \bar{\mathbf{G}}_{ms} \quad (\text{B.47})$$

where  $\bar{\mathbf{G}}_{0m} = \nabla \times \bar{\mathbf{G}}_{0e}$  and can be expressed as:

$$\bar{\mathbf{G}}_{0m}(\mathbf{r}, \mathbf{r}') = \frac{ik_0}{4\pi} \sum_{n=0}^{\infty} \sum_{m=0}^n (2 - \delta_m^0) \frac{2n+1}{n(n+1)} \frac{(n-m)!}{n+m} \\ \times \begin{cases} \nabla \times \mathbf{M}_{mn}^{(1)}(k_0) \mathbf{M}'_{mn}(k_0) + \nabla \times \mathbf{N}_{mn}^{(1)}(k_0) \mathbf{N}'_{mn}(k_0) & r \geq r', \\ \nabla \times \mathbf{M}_{mn}(k_0) \mathbf{M}'_{mn}{}^{(1)}(k_0) + \nabla \times \mathbf{N}_{mn}(k_0) \mathbf{N}'_{mn}{}^{(1)}(k_0) & r \leq r' \end{cases}. \quad (\text{B.48})$$

Knowing that the operation  $\nabla \times$  acts only on the  $\mathbf{r}$  coordinates and using the identities

$$\nabla \times \mathbf{M}_{mn}(k) = k \mathbf{N}_{mn}(k) \quad (\text{B.49a})$$

$$\nabla \times \mathbf{N}_{mn}(k) = k \mathbf{M}_{mn}(k), \quad (\text{B.49b})$$

we can rewrite Eq. B.48 as:

$$\bar{\mathbf{G}}_{0m}(\mathbf{r}, \mathbf{r}') = \frac{ik_0^2}{4\pi} \sum_{n=0}^{\infty} \sum_{m=0}^n (2 - \delta_m^0) \frac{2n+1}{n(n+1)} \frac{(n-m)!}{n+m} \\ \times \begin{cases} \mathbf{N}_{mn}^{(1)}(k_0) \mathbf{M}'_{mn}(k_0) + \mathbf{M}_{mn}^{(1)}(k_0) \mathbf{N}'_{mn}(k_0) & r \geq r', \\ \mathbf{N}_{mn}(k_0) \mathbf{M}'_{mn}{}^{(1)}(k_0) + \mathbf{M}_{mn}(k_0) \mathbf{N}'_{mn}{}^{(1)}(k_0) & r \leq r' \end{cases}. \quad (\text{B.50})$$

Similarly we can write the scattered Green functions for the magnetic field as

$$\bar{\mathbf{G}}_{ms}^{(11)}(\mathbf{r}, \mathbf{r}') = \frac{ik_0}{4\pi} \sum_{n=0}^{\infty} \sum_{m=0}^n (2 - \delta_m^0) \frac{2n+1}{n(n+1)} \frac{(n-m)!}{(n+m)!} \left[ \mathcal{B}_M \mathbf{N}_{mn}^{(1)}(k_0) \mathbf{M}'_{mn}{}^{(1)}(k_0) + \mathcal{B}_N \mathbf{M}_{mn}^{(1)}(k_0) \mathbf{N}'_{mn}{}^{(1)}(k_0) \right] \quad (\text{B.51a})$$

$$\bar{\mathbf{G}}_{ms}^{(21)}(\mathbf{r}, \mathbf{r}') = \frac{ik_0^2}{4\pi} \sum_{n=0}^{\infty} \sum_{m=0}^n (2 - \delta_m^0) \frac{2n+1}{n(n+1)} \frac{(n-m)!}{(n+m)!} \left[ \mathcal{D}_M \mathbf{N}_{mn}(k_1) \mathbf{M}'_{mn}{}^{(1)}(k_0) + \mathcal{D}_N \mathbf{M}_{mn}(k_1) \mathbf{N}'_{mn}{}^{(1)}(k_0) \right] \quad (\text{B.51b})$$

We can write the elements of Eq. (B.50) as:

$$G_{0m,rr} = 0 \quad (\text{B.52a})$$

$$G_{0m,r\theta} = \frac{ik_0^2}{4\pi} \sum_{n=0}^{\infty} \sum_{m=0}^n C_{mn} \times \mp \frac{n(n+1)}{x_0} P_n^m(\cos \theta) \frac{m}{\sin \theta'} P_n^m(\cos \theta') \begin{matrix} \cos & \sin \\ \sin & \cos \end{matrix} \begin{matrix} m\phi & m\phi' \end{matrix} \begin{cases} h_n^{(1)}(x_0) j_n(x'_0) & r \geq r' \\ j_n(x_0) h_n^{(1)}(x'_0) & r \leq r' \end{cases} \quad (\text{B.52b})$$

$$G_{0m,\theta r} = \frac{ik_0^2}{4\pi} \sum_{n=0}^{\infty} \sum_{m=0}^n C_{mn} \times \mp \frac{n(n+1)}{x'_0} \frac{m}{\sin \theta} P_n^m(\cos \theta) P_n^m(\cos \theta') \begin{matrix} \sin & \cos \\ \cos & \sin \end{matrix} \begin{matrix} m\phi & m\phi' \end{matrix} \begin{cases} h_n^{(1)}(x_0) j_n(x'_0) & r \geq r' \\ j_n(x_0) h_n^{(1)}(x'_0) & r \leq r' \end{cases} \quad (\text{B.52c})$$

$$G_{0m,r\phi} = \frac{ik_0^2}{4\pi} \sum_{n=0}^{\infty} \sum_{m=0}^n C_{mn} \times - \frac{n(n+1)}{x_0} P_n^m(\cos \theta) \frac{dP_n^m(\cos \theta')}{d\theta'} \begin{matrix} \cos & \cos \\ \sin & \sin \end{matrix} \begin{matrix} m\phi & m\phi' \end{matrix} \begin{cases} h_n^{(1)}(x_0) j_n(x'_0) & r \geq r' \\ j_n(x_0) h_n^{(1)}(x'_0) & r \leq r' \end{cases} \quad (\text{B.52d})$$

$$G_{0m,\phi r} = \frac{ik_0^2}{4\pi} \sum_{n=0}^{\infty} \sum_{m=0}^n C_{mn} \times - \frac{n(n+1)}{x'_0} \frac{dP_n^m(\cos \theta)}{d\theta} P_n^m(\cos \theta') \begin{matrix} \cos & \cos \\ \sin & \sin \end{matrix} \begin{matrix} m\phi & m\phi' \end{matrix} \begin{cases} h_n^{(1)}(x_0) j_n(x'_0) & r \geq r' \\ j_n(x_0) h_n^{(1)}(x'_0) & r \leq r' \end{cases} \quad (\text{B.52e})$$

$$G_{0m,\theta\theta} = \frac{ik_0^2}{4\pi} \sum_{n=0}^{\infty} \sum_{m=0}^n C_{mn} \times \left\{ \mp \frac{1}{x_0} \frac{dP_n^m(\cos \theta)}{d\theta} \frac{m}{\sin \theta'} P_n^m(\cos \theta') \begin{matrix} \cos & \sin \\ \sin & \cos \end{matrix} \begin{matrix} m\phi & m\phi' \end{matrix} \begin{cases} \frac{d[rh_n^{(1)}(x_0)]}{dr} j_n(x'_0) & r \geq r' \\ \frac{d[rj_n(x_0)]}{dr} h_n^{(1)}(x'_0) & r \leq r' \end{cases} \right. \\ \left. \mp \frac{1}{x'_0} \frac{m}{\sin \theta} P_n^m(\cos \theta) \frac{dP_n^m(\cos \theta')}{d\theta'} \begin{matrix} \sin & \cos \\ \cos & \sin \end{matrix} \begin{matrix} m\phi & m\phi' \end{matrix} \begin{cases} h_n^{(1)}(x_0) \frac{d[rj_n(x'_0)]}{dr'} & r \geq r' \\ j_n(x_0) \frac{d[rh_n^{(1)}(x'_0)]}{dr'} & r \leq r' \end{cases} \right\} \quad (\text{B.52f})$$

$$G_{0m,\theta\phi} = \frac{ik_0^2}{4\pi} \sum_{n=0}^{\infty} \sum_{m=0}^n C_{mn} \times \left\{ - \frac{1}{x_0} \frac{dP_n^m(\cos \theta)}{d\theta} \frac{dP_n^m(\cos \theta')}{d\theta'} \begin{matrix} \cos & \cos \\ \sin & \sin \end{matrix} \begin{matrix} m\phi & m\phi' \end{matrix} \begin{cases} \frac{d[rh_n^{(1)}(x_0)]}{dr} j_n(x'_0) & r \geq r' \\ \frac{d[rj_n(x_0)]}{dr} h_n^{(1)}(x'_0) & r \leq r' \end{cases} \right. \\ \left. + \frac{1}{x'_0} \frac{m}{\sin \theta} P_n^m(\cos \theta) \frac{m}{\sin \theta'} P_n^m(\cos \theta') \begin{matrix} \sin & \sin \\ \cos & \cos \end{matrix} \begin{matrix} m\phi & m\phi' \end{matrix} \begin{cases} h_n^{(1)}(x_0) \frac{d[rj_n(x'_0)]}{dr'} & r \geq r' \\ j_n(x_0) \frac{d[rh_n^{(1)}(x'_0)]}{dr'} & r \leq r' \end{cases} \right\} \quad (\text{B.52g})$$

$$\begin{aligned}
G_{0m,\phi\theta} &= \frac{ik_0^2}{4\pi} \sum_{n=0}^{\infty} \sum_{m=0}^n C_{mn} \\
&\times \left\{ \frac{1}{x_0} \frac{m}{\sin \theta} P_n^m(\cos \theta) \frac{m}{\sin \theta'} P_n^m(\cos \theta') \frac{\sin m\phi}{\cos m\phi} \frac{\sin m\phi'}{\cos m\phi'} \begin{cases} \frac{d[rh_n^{(1)}(x_0)]}{dr} j_n(x'_0) & r \geq r' \\ \frac{d[rj_n(x_0)]}{dr} h_n^{(1)}(x'_0) & r \leq r' \end{cases} \right. \\
&\left. - \frac{1}{x'_0} \frac{dP_n^m(\cos \theta)}{d\theta} \frac{dP_n^m(\cos \theta')}{d\theta'} \frac{\cos m\phi}{\sin m\phi} \frac{\cos m\phi'}{\sin m\phi'} \begin{cases} h_n^{(1)}(x_0) \frac{d[rj_n(x'_0)]}{dr'} & r \geq r' \\ j_n(x_0) \frac{d[rh_n^{(1)}(x'_0)]}{dr'} & r \leq r' \end{cases} \right\} \\
&\hspace{15em} \text{(B.52h)}
\end{aligned}$$

$$\begin{aligned}
G_{0m,\phi\phi} &= \frac{ik_0^2}{4\pi} \sum_{n=0}^{\infty} \sum_{m=0}^n C_{mn} \\
&\times \left\{ \pm \frac{1}{x_0} \frac{m}{\sin \theta} P_n^m(\cos \theta) \frac{dP_n^m(\cos \theta')}{d\theta'} \frac{\sin m\phi}{\cos m\phi} \frac{\cos m\phi'}{\sin m\phi'} \begin{cases} \frac{d[rh_n^{(1)}(x_0)]}{dr} j_n(x'_0) & r \geq r' \\ \frac{d[rj_n(x_0)]}{dr} h_n^{(1)}(x'_0) & r \leq r' \end{cases} \right. \\
&\left. \pm \frac{1}{x'_0} \frac{dP_n^m(\cos \theta)}{d\theta} \frac{m}{\sin \theta'} P_n^m(\cos \theta') \frac{\cos m\phi}{\sin m\phi} \frac{\sin m\phi'}{\cos m\phi'} \begin{cases} h_n^{(1)}(x_0) \frac{d[rj_n(x'_0)]}{dr'} & r \geq r' \\ j_n(x_0) \frac{d[rh_n^{(1)}(x'_0)]}{dr'} & r \leq r' \end{cases} \right\} \\
&\hspace{15em} \text{(B.52i)}
\end{aligned}$$

where can be simplified to

$$G_{0m,rr} = 0 \quad \text{(B.53a)}$$

$$G_{0m,r\theta} = -\frac{ik_0^2}{4\pi} \sum_{n=0}^{\infty} \frac{2n+1}{x_0} \frac{dP_n(\cos \gamma)}{d\gamma} \sin \chi_2 \begin{cases} h_n^{(1)}(x_0) j_n(x'_0) & r \geq r' \\ j_n(x_0) h_n^{(1)}(x'_0) & r \leq r' \end{cases} \quad \text{(B.53b)}$$

$$G_{0m,\theta r} = \frac{ik_0^2}{4\pi} \sum_{n=0}^{\infty} \frac{2n+1}{x'_0} \frac{dP_n(\cos \gamma)}{d\gamma} \sin \chi_1 \begin{cases} h_n^{(1)}(x_0) j_n(x'_0) & r \geq r' \\ j_n(x_0) h_n^{(1)}(x'_0) & r \leq r' \end{cases} \quad \text{(B.53c)}$$

$$G_{0m,r\phi} = -\frac{ik_0^2}{4\pi} \sum_{n=0}^{\infty} \frac{2n+1}{x_0} \frac{dP_n(\cos \gamma)}{d\gamma} \cos \chi_2 \begin{cases} h_n^{(1)}(x_0) j_n(x'_0) & r \geq r' \\ j_n(x_0) h_n^{(1)}(x'_0) & r \leq r' \end{cases} \quad \text{(B.53d)}$$

$$G_{0m,\phi r} = -\frac{ik_0^2}{4\pi} \sum_{n=0}^{\infty} \frac{2n+1}{x'_0} \frac{dP_n(\cos \gamma)}{d\gamma} \cos \chi_1 \begin{cases} h_n^{(1)}(x_0) j_n(x'_0) & r \geq r' \\ j_n(x_0) h_n^{(1)}(x'_0) & r \leq r' \end{cases} \quad \text{(B.53e)}$$

$$\begin{aligned}
G_{0m,\theta\theta} &= \frac{ik_0^2}{4\pi} \sum_{n=0}^{\infty} \frac{2n+1}{n(n+1)} \left\{ \frac{1}{x_0} P_n^{(3)} \begin{cases} \frac{d[rh_n^{(1)}(x_0)]}{dr} j_n(x'_0) & r \geq r' \\ \frac{d[rj_n(x_0)]}{dr} h_n^{(1)}(x'_0) & r \leq r' \end{cases} \right. \\
&\left. + \frac{1}{x'_0} P_n^{(4)} \begin{cases} h_n^{(1)}(x_0) \frac{d[rj_n(x'_0)]}{dr'} & r \geq r' \\ j_n(x_0) \frac{d[rh_n^{(1)}(x'_0)]}{dr'} & r \leq r' \end{cases} \right\} \\
&\hspace{15em} \text{(B.53f)}
\end{aligned}$$

$$\begin{aligned}
G_{0m,\theta\phi} &= \frac{ik_0^2}{4\pi} \sum_{n=0}^{\infty} \frac{2n+1}{n(n+1)} \left\{ -\frac{1}{x_0} P_n^{(1)} \begin{cases} \frac{d[rh_n^{(1)}(x_0)]}{dr} j_n(x'_0) & r \geq r' \\ \frac{d[rj_n(x_0)]}{dr} h_n^{(1)}(x'_0) & r \leq r' \end{cases} \right. \\
&\left. + \frac{1}{x'_0} P_n^{(2)} \begin{cases} h_n^{(1)}(x_0) \frac{d[rj_n(x'_0)]}{dr'} & r \geq r' \\ j_n(x_0) \frac{d[rh_n^{(1)}(x'_0)]}{dr'} & r \leq r' \end{cases} \right\} \\
&\hspace{15em} \text{(B.53g)}
\end{aligned}$$

$$G_{0m,\phi\theta} = \frac{ik_0^2}{4\pi} \sum_{n=0}^{\infty} \frac{2n+1}{n(n+1)} \left\{ \frac{1}{x_0} P_n^{(2)} \begin{cases} \frac{d[rh_n^{(1)}(x_0)]}{dr} j_n(x'_0) & r \geq r' \\ \frac{d[rj_n(x_0)]}{dr} h_n^{(1)}(x'_0) & r \leq r' \end{cases} \right. \\ \left. - \frac{1}{x'_0} P_n^{(1)} \begin{cases} h_n^{(1)}(x_0) \frac{d[rj_n(x'_0)]}{dr'} & r \geq r' \\ j_n(x_0) \frac{d[rh_n^{(1)}(x'_0)]}{dr'} & r \leq r' \end{cases} \right\} \quad (\text{B.53h})$$

$$G_{0m,\phi\phi} = -\frac{ik_0^2}{4\pi} \sum_{n=0}^{\infty} \frac{2n+1}{n(n+1)} \left\{ \frac{1}{x_0} P_n^{(4)} \begin{cases} \frac{d[rh_n^{(1)}(x_0)]}{dr} j_n(x'_0) & r \geq r' \\ \frac{d[rj_n(x_0)]}{dr} h_n^{(1)}(x'_0) & r \leq r' \end{cases} \right. \\ \left. + \frac{1}{x'_0} P_n^{(3)} \begin{cases} h_n^{(1)}(x_0) \frac{d[rj_n(x'_0)]}{dr'} & r \geq r' \\ j_n(x_0) \frac{d[rh_n^{(1)}(x'_0)]}{dr'} & r \leq r' \end{cases} \right\} \quad (\text{B.53i})$$

Similarly, we can write the elements of Green functions in Eq. (B.51)

$$G_{ms,rr}^{(11)} = 0 \quad (\text{B.54a})$$

$$G_{ms,r\theta}^{(11)} = -\frac{ik_0^2}{4\pi} \sum_{n=0}^{\infty} \mathcal{B}_M \frac{2n+1}{x_0} \frac{dP_n(\cos \gamma)}{d\gamma} \sin \chi_2 h_n^{(1)}(x_0) h_n^{(1)}(x'_0) \quad (\text{B.54b})$$

$$G_{ms,\theta r}^{(11)} = \frac{ik_0^2}{4\pi} \sum_{n=0}^{\infty} \mathcal{B}_N \frac{2n+1}{x'_0} \frac{dP_n(\cos \gamma)}{d\gamma} \sin \chi_1 h_n^{(1)}(x_0) h_n^{(1)}(x'_0) \quad (\text{B.54c})$$

$$G_{ms,r\phi}^{(11)} = -\frac{ik_0^2}{4\pi} \sum_{n=0}^{\infty} \mathcal{B}_M \frac{2n+1}{x_0} \frac{dP_n(\cos \gamma)}{d\gamma} \cos \chi_2 h_n^{(1)}(x_0) h_n^{(1)}(x'_0) \quad (\text{B.54d})$$

$$G_{ms,\phi r}^{(11)} = -\frac{ik_0^2}{4\pi} \sum_{n=0}^{\infty} \mathcal{B}_N \frac{2n+1}{x'_0} \frac{dP_n(\cos \gamma)}{d\gamma} \cos \chi_1 h_n^{(1)}(x_0) h_n^{(1)}(x'_0) \quad (\text{B.54e})$$

$$G_{ms,\theta\theta}^{(11)} = \frac{ik_0^2}{4\pi} \sum_{n=0}^{\infty} \frac{2n+1}{n(n+1)} \left\{ \mathcal{B}_M \frac{1}{x_0} P_n^{(3)} \frac{d[rh_n^{(1)}(x_0)]}{dr} h_n^{(1)}(x'_0) + \mathcal{B}_N \frac{1}{x'_0} P_n^{(4)} h_n^{(1)}(x_0) \frac{d[rh_n^{(1)}(x'_0)]}{dr'} \right\} \quad (\text{B.54f})$$

$$G_{ms,\theta\phi}^{(11)} = \frac{ik_0^2}{4\pi} \sum_{n=0}^{\infty} \frac{2n+1}{n(n+1)} \left\{ -\mathcal{B}_M \frac{1}{x_0} P_n^{(1)} \frac{d[rh_n^{(1)}(x_0)]}{dr} h_n^{(1)}(x'_0) + \mathcal{B}_N \frac{1}{x'_0} P_n^{(2)} h_n^{(1)}(x_0) \frac{d[rh_n^{(1)}(x'_0)]}{dr'} \right\} \quad (\text{B.54g})$$

$$G_{ms,\phi\theta}^{(11)} = \frac{ik_0^2}{4\pi} \sum_{n=0}^{\infty} \frac{2n+1}{n(n+1)} \left\{ \mathcal{B}_M \frac{1}{x_0} P_n^{(2)} \frac{d[rh_n^{(1)}(x_0)]}{dr} h_n^{(1)}(x'_0) - \mathcal{B}_N \frac{1}{x'_0} P_n^{(1)} h_n^{(1)}(x_0) \frac{d[rh_n^{(1)}(x'_0)]}{dr'} \right\} \quad (\text{B.54h})$$

$$G_{ms,\phi\phi}^{(11)} = -\frac{ik_0^2}{4\pi} \sum_{n=0}^{\infty} \frac{2n+1}{n(n+1)} \left\{ \mathcal{B}_M \frac{1}{x_0} P_n^{(4)} \frac{d[rh_n^{(1)}(x_0)]}{dr} h_n^{(1)}(x'_0) + \mathcal{B}_N \frac{1}{x'_0} P_n^{(3)} h_n^{(1)}(x_0) \frac{d[rh_n^{(1)}(x'_0)]}{dr'} \right\} \quad (\text{B.54i})$$

and

$$G_{ms,rr}^{(21)} = 0 \quad (\text{B.55a})$$

$$G_{ms,r\theta}^{(21)} = -\frac{ik_0^2}{4\pi} \sum_{n=0}^{\infty} \mathcal{D}_M \frac{2n+1}{x_1} \frac{dP_n(\cos \gamma)}{d\gamma} \sin \chi_2 j_n(x_1) h_n^{(1)}(x'_0) \quad (\text{B.55b})$$

$$G_{ms,\theta r}^{(21)} = \frac{ik_0^2}{4\pi} \sum_{n=0}^{\infty} \mathcal{D}_N \frac{2n+1}{x'_0} \frac{dP_n(\cos \gamma)}{d\gamma} \sin \chi_1 j_n(x_1) h_n^{(1)}(x'_0) \quad (\text{B.55c})$$

$$G_{ms,r\phi}^{(21)} = -\frac{ik_0^2}{4\pi} \sum_{n=0}^{\infty} \mathcal{D}_M \frac{2n+1}{x_1} \frac{dP_n(\cos \gamma)}{d\gamma} \cos \chi_2 j_n(x_1) h_n^{(1)}(x'_0) \quad (\text{B.55d})$$

$$G_{ms,\phi r}^{(11)} = -\frac{ik_0^2}{4\pi} \sum_{n=0}^{\infty} \mathcal{D}_N \frac{2n+1}{x'_0} \frac{dP_n(\cos \gamma)}{d\gamma} \cos \chi_1 j_n(x_1) h_n^{(1)}(x'_0) \quad (\text{B.55e})$$

$$G_{ms,\theta\theta}^{(21)} = \frac{ik_0^2}{4\pi} \sum_{n=0}^{\infty} \frac{2n+1}{n(n+1)} \left\{ \mathcal{D}_M \frac{1}{x_1} P_n^{(3)} \frac{d[rj_n(x_1)]}{dr} h_n^{(1)}(x'_0) + \mathcal{D}_N \frac{1}{x'_0} P_n^{(4)} j_n(x_1) \frac{d[rh_n^{(1)}(x'_0)]}{dr'} \right\} \quad (\text{B.55f})$$

$$G_{ms,\theta\phi}^{(21)} = \frac{ik_0^2}{4\pi} \sum_{n=0}^{\infty} \frac{2n+1}{n(n+1)} \left\{ -\mathcal{D}_M \frac{1}{x_1} P_n^{(1)} \frac{d[rj_n(x_1)]}{dr} h_n^{(1)}(x'_0) + \mathcal{D}_N \frac{1}{x'_0} P_n^{(2)} j_n(x_1) \frac{d[rh_n^{(1)}(x'_0)]}{dr'} \right\} \quad (\text{B.55g})$$

$$G_{ms,\phi\theta}^{(21)} = \frac{ik_0^2}{4\pi} \sum_{n=0}^{\infty} \frac{2n+1}{n(n+1)} \left\{ \mathcal{D}_M \frac{1}{x_1} P_n^{(2)} \frac{d[rj_n(x_1)]}{dr} h_n^{(1)}(x'_0) - \mathcal{D}_N \frac{1}{x'_0} P_n^{(1)} j_n(x_1) \frac{d[rh_n^{(1)}(x'_0)]}{dr'} \right\} \quad (\text{B.55h})$$

$$G_{ms,\phi\phi}^{(21)} = -\frac{ik_0^2}{4\pi} \sum_{n=0}^{\infty} \frac{2n+1}{n(n+1)} \left\{ \mathcal{D}_M \frac{1}{x_1} P_n^{(4)} \frac{d[rj_n(x_0)]}{dr} h_n^{(1)}(x'_0) + \mathcal{D}_N \frac{1}{x'_0} P_n^{(3)} j_n(x_0) \frac{d[rh_n^{(1)}(x'_0)]}{dr'} \right\} \quad (\text{B.55i})$$

## B.7 Electric and Magnetic Dipoles

Having found the electric and magnetic Green's function, it is a matter of substitution to find the electric and magnetic fields of the dipole placed outside of the sphere. The fields from an electric dipole is simply the dipole moment times the Green's functions. Therefore, assuming an electric dipole moment of  $\mathbf{p}$ , we get:

$$\mathbf{E}_e(\mathbf{r}) = \omega^2 \mu_0 \overline{\mathbf{G}}_e(\mathbf{r}, \mathbf{r}') \mathbf{p}(\mathbf{r}') \quad (\text{B.56a})$$

$$\mathbf{H}_e(\mathbf{r}) = -i\omega \overline{\mathbf{G}}_m(\mathbf{r}, \mathbf{r}') \mathbf{p}(\mathbf{r}') \quad (\text{B.56b})$$

where the subscript  $e$  refers to fields due to an electric dipole.

The fields due to a magnetic dipole can be found from the results of an electric dipole by performing a dual transformation. Since the Maxwell equations are dual symmetric, the equations will be the same if we do the transformation:

$$\mathbf{E} \rightarrow Z_0 \mathbf{H}, \quad Z_0 \mathbf{H} \rightarrow -\mathbf{E}, \quad \mathbf{p} \rightarrow \mathbf{m}/c \quad (\text{B.57})$$

where  $Z_0 = \sqrt{\frac{\mu_0}{\epsilon_0}} \simeq 376.73\Omega$ . Therefore, for a magnetic dipole with the dipole moment  $\mathbf{m}$  we get

$$\mathbf{E}_m(\mathbf{r}) = i\omega \mu_0 \overline{\mathbf{G}}_m(\mathbf{r}, \mathbf{r}') \mathbf{m}(\mathbf{r}') \quad (\text{B.58a})$$

$$\mathbf{H}_m(\mathbf{r}) = \frac{\omega^2}{c^2} \overline{\mathbf{G}}_e(\mathbf{r}, \mathbf{r}') \mathbf{m}(\mathbf{r}'), \quad (\text{B.58b})$$

where the subscript  $m$  refers to fields due to a magnetic dipole. Here, we have assumed that the medium does not have any magnetic property.

The interaction Hamiltonian between two electric dipoles can be written as:

$$V_{ee} = -\mathbf{p}_A \cdot \mathbf{E}_{eD} = -\omega^2 \mu_0 \mathbf{p}_A(\mathbf{r}) \cdot \overline{\mathbf{G}}_e(\mathbf{r}, \mathbf{r}') \cdot \mathbf{p}_D(\mathbf{r}') \quad (\text{B.59})$$

where the  $ee$  subscript refers to electric dipole-electric dipole interaction, and  $\mathbf{p}_A$  and  $\mathbf{p}_D$  are the dipole moments of the acceptor and donor, respectively. Similarly, we can write the interaction Hamiltonian between two magnetic dipoles as:

$$V_{mm} = -\mathbf{m}_A \cdot \mathbf{B}_{mD} = -\frac{\omega^2 \mu_0}{c^2} \mathbf{m}_A(\mathbf{r}) \cdot \overline{\mathbf{G}}_e(\mathbf{r}, \mathbf{r}') \cdot \mathbf{m}_D(\mathbf{r}') \quad (\text{B.60})$$

For interactions between an electric and magnetic dipole we can write

$$V_{em} = -\mathbf{p}_A \cdot \mathbf{E}_{mD} = -i\omega \mu_0 \mathbf{p}_A(\mathbf{r}) \cdot \overline{\mathbf{G}}_m(\mathbf{r}, \mathbf{r}') \cdot \mathbf{m}_D(\mathbf{r}') \quad (\text{B.61a})$$

$$V_{me} = -\mathbf{m}_A \cdot \mathbf{B}_{eD} = +i\omega \mu_0 \mathbf{m}_A(\mathbf{r}) \cdot \overline{\mathbf{G}}_m(\mathbf{r}, \mathbf{r}') \cdot \mathbf{p}_D(\mathbf{r}') \quad (\text{B.61b})$$

## B.8 Properties of Legendre Polynomials

Here we present two of the important properties of the Legendre polynomials used in this chapter. These give recursion equations for the first- and second-order derivatives of the polynomials as,

$$\frac{d^2 P_n(x)}{dx^2} = \frac{n}{(x^2 - 1)^2} \{ [x^2(n-1) - n - 1] P_n(x) + 2x P_{n-1}(x) \} \quad (\text{B.62})$$

$$\frac{dP_n(x)}{dx} = \frac{n}{(x^2 - 1)} (x P_n(x) - P_{n-1}(x)) \quad (\text{B.63})$$

Therefore we find

$$\frac{d^2 P_n(\cos \gamma)}{d\gamma^2} = \sin^2 \gamma \frac{d^2 P_n(\cos \gamma)}{d(\cos \gamma)^2} - \cos \gamma \frac{dP_n(\cos \gamma)}{d(\cos \gamma)} \quad (\text{B.64})$$

## Appendix C

# Proofs for Chapter 4

### C.1 Cylindrical Dirac Equation

In this section we aim to find the solution of the Dirac's equation in cylindrical coordinates.

The time-independent Dirac equation is written as:

$$(v_F \boldsymbol{\alpha} \cdot \mathbf{p} + m v_F^2 \beta) \psi_\mu = E \psi_\mu, \quad (\text{C.1})$$

where

$$\boldsymbol{\alpha} = \begin{pmatrix} 0 & \boldsymbol{\sigma} \\ \boldsymbol{\sigma} & 0 \end{pmatrix}, \quad \beta = \begin{pmatrix} I_{2 \times 2} & 0 \\ 0 & -I_{2 \times 2} \end{pmatrix}, \quad (\text{C.2})$$

and  $\boldsymbol{\sigma}$ 's are the Pauli matrices written as

$$\sigma_x = \begin{pmatrix} 0 & 1 \\ 1 & 0 \end{pmatrix}, \quad \sigma_y = \begin{pmatrix} 0 & -i \\ i & 0 \end{pmatrix}, \quad \sigma_z = \begin{pmatrix} 1 & 0 \\ 0 & -1 \end{pmatrix}. \quad (\text{C.3})$$

The Dirac equation can be separated into two equations as:

$$(E - m v_F^2) \phi = -i \hbar v_F \vec{\sigma} \cdot \vec{\nabla} \chi \quad (\text{C.4})$$

$$(E + m v_F^2) \chi = -i \hbar v_F \vec{\sigma} \cdot \vec{\nabla} \phi \quad (\text{C.5})$$

where  $\mathbf{u} = \begin{pmatrix} \phi \\ \chi \end{pmatrix}$  is the four-component eigen bi-spinor solution. These two equations together give the familiar Helmholtz equation

$$(\nabla^2 + k^2) \phi = 0 \quad (\text{C.6})$$

where

$$k = \sqrt{\frac{E^2 - m^2 v_F^4}{\hbar^2 v_F^2}}. \quad (\text{C.7})$$

Since  $\chi$  is a spinor, Eq. (C.6) contains two independent solutions. Therefore, we can write these two solutions in cylindrical coordinates as  $\phi = \begin{pmatrix} \phi^+ \\ \phi^- \end{pmatrix}$  with

$$\phi^\pm = (A_{n\pm} J_{n\pm}(k_\perp \rho) + B_{n\pm} Y_{n\pm}(k_\perp \rho)) e^{i k_z z} e^{i n \pm \phi} \quad (\text{C.8})$$

where  $n_+$  and  $n_-$  are two integers,  $k_\perp = \sqrt{k^2 - k_z^2}$ , and  $J$  and  $Y$  are Bessel functions of first and second kind, respectively. We require the solutions to be eigenfunctions of total angular momentum along the  $z$  direction,  $J_z$ , with eigenvalue  $\mu\hbar$ . This can be written as

$$J_z\phi = \left(-i\hbar\frac{\partial}{\partial\phi}I_{2\times 2} + \frac{\hbar}{2}\sigma_z\right)\phi = \hbar\mu\phi \quad (\text{C.9})$$

which gives

$$n_+ + \frac{1}{2} = n_- - \frac{1}{2} = \mu \quad (\text{C.10})$$

We also require the solutions to be eigenfunctions of transverse helicity defined as [136],

$$h_\perp = i\hbar\gamma_3 \frac{\alpha_x\partial_x + \alpha_y\partial_y}{p_\perp} = \frac{1}{k_\perp} \begin{pmatrix} 0 & \partial_x - i\partial_y & 0 & 0 \\ -\partial_x - i\partial_y & 0 & 0 & 0 \\ 0 & 0 & 0 & -\partial_x + i\partial_y \\ 0 & 0 & \partial_x + i\partial_y & 0 \end{pmatrix}, \quad (\text{C.11})$$

where  $\gamma_3 = \beta\alpha_z$ . We can see that the spinors

$$\phi_\mu^+ = \frac{e^{ik_z z}}{\sqrt{2}} \begin{pmatrix} (A_{n_+}J_{n_+}(k_\perp\rho) + B_{n_+}Y_{n_+}(k_\perp\rho))e^{in_+\phi} \\ (A_{n_-}J_{n_-}(k_\perp\rho) + B_{n_-}Y_{n_-}(k_\perp\rho))e^{in_-\phi} \end{pmatrix} \quad (\text{C.12})$$

and

$$\phi_\mu^- = \frac{e^{ik_z z}}{\sqrt{2}} \begin{pmatrix} (A_{n_+}J_{n_+}(k_\perp\rho) + B_{n_+}Y_{n_+}(k_\perp\rho))e^{in_+\phi} \\ -(A_{n_-}J_{n_-}(k_\perp\rho) + B_{n_-}Y_{n_-}(k_\perp\rho))e^{in_-\phi} \end{pmatrix} \quad (\text{C.13})$$

are eigenfunctions of the  $2 \times 2$  matrix on the diagonal of the  $h_\perp$  matrix in Eq. (C.11), assuming that  $A_{n_+} = A_{n_-} = A_\mu$  and  $B_{n_+} = B_{n_-} = B_\mu$ . We can use Eq. (C.5) to find the other two components of the eigenfunctions as

$$\chi_\mu = \frac{-i\hbar v_F \vec{\sigma} \cdot \vec{\nabla}}{(E + mv_F^2)} \phi_\mu. \quad (\text{C.14})$$

This would give the two solutions as

$$\chi_\mu^\pm = \frac{\mp i\hbar v_F e^{ik_z z} e^{i\mu\phi} (k_\perp \pm ik_z)}{\sqrt{2}(E + mv_F^2)} \begin{pmatrix} (A_\mu J_{n_+}(k_\perp\rho) + B_\mu Y_{n_+}(k_\perp\rho))e^{-i\phi/2} \\ \mp (A_\mu J_{n_-}(k_\perp\rho) + B_\mu Y_{n_-}(k_\perp\rho))e^{+i\phi/2} \end{pmatrix}. \quad (\text{C.15})$$

Therefore, we can write the bi-spinor solutions as

$$\mathbf{u}_{\mu,M}^{(s)} = \frac{e^{ik_z z} e^{i\mu\phi}}{\sqrt{2}} \begin{pmatrix} \phi_\mu^{(s)} \\ -is\hbar v_F \frac{k_\perp + ik_z}{M} \phi_\mu^{(-s)} \end{pmatrix} \quad (\text{C.16})$$

where  $s = \pm 1$  is the eigenvalue of the transverse helicity operator,

$$h_\perp \psi_\mu^{(s)} = s\psi_\mu^{(s)}, \quad (\text{C.17})$$

and  $M = E + mv_F^2$ . For solutions that include  $\rho = 0$ ,  $B_\mu$  should become zero so that the solutions do not diverge at  $\rho = 0$ . On the other hand, for solutions that include  $\rho \rightarrow \infty$ , only  $K_n(k_\perp\rho)$  solutions should remain. Since we only face either of these two scenarios, these observations give the solutions in Eq. (4.2).

## C.2 Cylindrical Jackiw-Rebbi problem

We now apply the general solutions of the previous section to the cylindrical Jackiw-Rebbi problem with the electronic mass inside and outside the wire  $m_1$  and  $m_2$ , respectively. We look at the two cases of  $\text{JR}^+$  and  $\text{JR}^-$  for which  $m_1 > 0$  and  $m_1 < 0$ , respectively. For both cases  $m_2$  is positive. In order to get physical solutions outside of the wire we require the solutions to vanish as  $\rho \rightarrow \infty$ . This means that the radial solutions outside of the wire should be in the form of modified Bessel functions of the second kind  $K_n(k_{\perp}\rho)$ . Writing the  $\rho > a$  solutions in this form and applying the continuity boundary condition to the four components of the Dirac bi-spinors, we arrive at the transcendental equation,

$$\left[ -k_{\rho_1} \gamma_2 \left( \frac{J_{n_-}(k_{\perp_1} a) K_{n_+}(\gamma_2 a)}{J_{n_+}(k_{\perp_1} a) K_{n_-}(\gamma_2 a)} - \frac{J_{n_+}(k_{\perp_1} a) K_{n_-}(\gamma_2 a)}{J_{n_-}(k_{\perp_1} a) K_{n_+}(\gamma_2 a)} \right) \right] + 2k_z^2 = \frac{M_1^2 k_2^2 + M_2^2 k_1^2}{M_1 M_2} \quad (\text{C.18})$$

where  $k_{\perp_1} = \sqrt{k_1^2 - k_z^2}$ ,  $\gamma_2 = -ik_{\perp_2} = \sqrt{k_z^2 - k_2^2}$ , and  $M_i = E + m_i v_F^2$  with  $k_i = \frac{\sqrt{E^2 - m_i^2 v_F^4}}{\hbar v_F}$  being the propagation constants inside and outside of the wire for  $i = 1$  and  $i = 2$ , respectively.

### C.2.1 Solutions of $\text{JR}^+$ Dirac Wire problem

For the  $\text{JR}^+$  problem ( $m_1, m_2 > 0$ ), the solutions only exist when  $m_2 > m_1$ . This corresponds to the condition that  $E_1 < E < E_2$ , where

$$E_i = \sqrt{m_i^2 v_F^4 + \hbar^2 v_F^2 k_z^2}, \quad i = 1, 2. \quad (\text{C.19})$$

In this range,  $k_{\perp_1}$  is real while  $k_{\perp_2}$  is imaginary; therefore giving the hybrid mode label  $H_{\mu,\nu}$ . Figure C.1 shows the calculated amplitude for the wavefunctions ( $\psi^\dagger \psi$ ) of the first six modes of the  $\text{JR}^+$  problem. Note that these distributions integrate to one over the entire  $x - y$  plane. Figure C.2 shows the dispersions as well as the integrated values of spin and OAM of the  $\text{JR}^+$  problem for the first six modes. As shown in the dispersion diagram in Fig. C.2(a), the  $H_{\frac{1}{2},2}$  and  $H_{\frac{3}{2},1}$  as well as the  $H_{\frac{3}{2},2}$  and  $H_{\frac{5}{2},1}$  modes are degenerate. Spin and OAM of these modes are shown in Fig. C.2(b). Note that spin and OAM are not dispersive (they are independent of  $k_z$ ). Also, the values of spin are not exactly  $\pm \frac{1}{2}$  which shows the non-quantization of spin. The summation of spin and OAM, however, is always quantized.

### C.2.2 Solutions of $\text{JR}^-$ Dirac Wire problem

In the case of  $\text{JR}^-$  problem, in addition to  $H_{\mu,\nu}$  modes, another type of mode exists due to the negative mass inside the wire. These solutions exist in the range  $E < E_1$  with  $E_1$  given

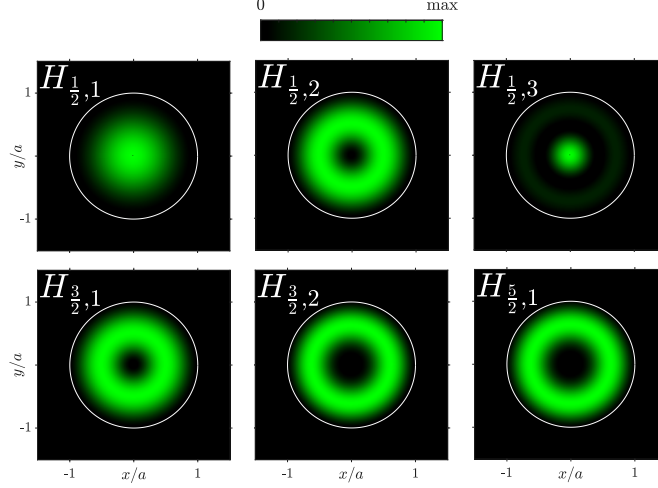


Figure C.1: Spatial distribution of probability densities,  $\psi^\dagger\psi$ , for the first six modes of the  $\text{JR}^+$  problem. The radius of the wire is  $a = 20 \text{ \AA}$ ,  $m_1 v_F^2 = 1 \text{ eV}$ , and  $m_2 v_F^2 = 2 \text{ eV}$ .

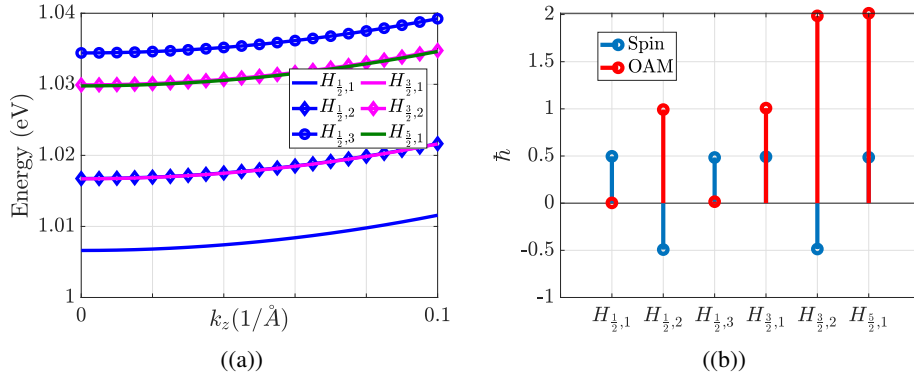


Figure C.2: Properties of the first six modes of the  $\text{JR}^+$  problem for  $a = 20 \text{ \AA}$ . (a) dispersion and (b) spin and OAM of the first six modes.

by Eq. (C.19). These modes are characterized by imaginary values of  $k_{\perp 1}$  and  $k_{\perp 2}$ . Since the solutions are evanescent inside and outside of the wire, there is only one possibility for the continuity boundary condition to be satisfied. In other words, unlike the  $H_{\mu,\nu}$  modes, the radial function has only one possible solution in this case. Therefore, we label these modes as  $D_\mu$ .

Figure C.3 shows the spatial distribution of  $\psi^\dagger\psi$  for the first six modes of the  $\text{JR}^-$  problem with  $|m_1|v_F^2 = 1 \text{ eV}$ ,  $m_2 v_F^2 = 2 \text{ eV}$ , and  $a = 20 \text{ \AA}$ . Note that these six modes are not ordered in terms of energy because all of the  $D_\mu$  modes have lower energy than the  $H_{\mu,\nu}$  modes, as seen in Fig. C.4(a). As shown in Fig. C.4(b), similar to the  $\text{JR}^+$  problem, the spin and OAM add up to the quantized value for the total angular momentum. Note that

although the spin is not conserved in these problems, its absolute value does not exceed  $\frac{1}{2}$ .

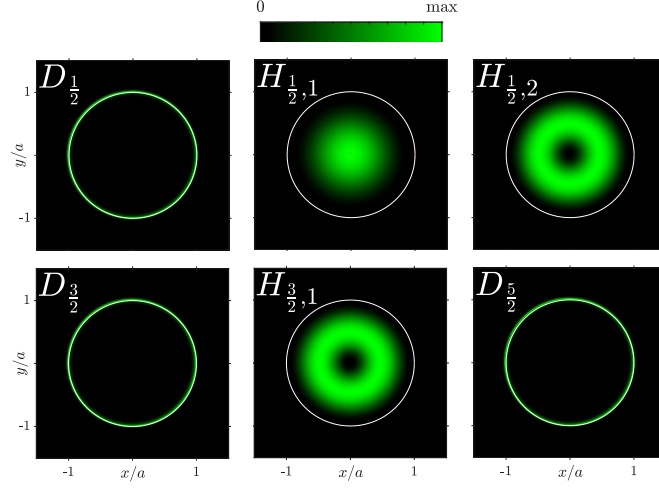


Figure C.3: Spatial distribution of probability densities,  $\psi^\dagger\psi$ , for  $\mu = \frac{1}{2}$  and for the first six modes of the  $JR^-$  problem. The radius of the wire is  $a = 20\text{\AA}$ ,  $|m_1|v_F^2 = 1\text{eV}$ , and  $m_2v_F^2 = 2\text{eV}$ .

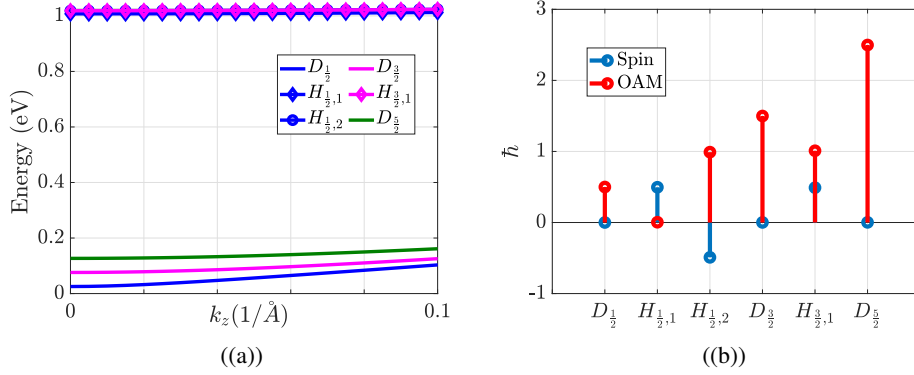


Figure C.4: Properties of the first six modes of the  $JR^-$  problem for  $a = 20\text{\AA}$ . (a) Dispersion and (b) spin and OAM of the first six modes.

### C.3 Dirac Equation with dispersive mass

The method used in the previous section can be also applied here to find the solutions of the Dirac Eq. (C.1) for the dispersive Jackiw-Rebbi (JR-D) problem. Using the dispersive mass,

$$mv_F^2 = m_0v_F^2 - B\hbar^2k^2, \quad (\text{C.20})$$

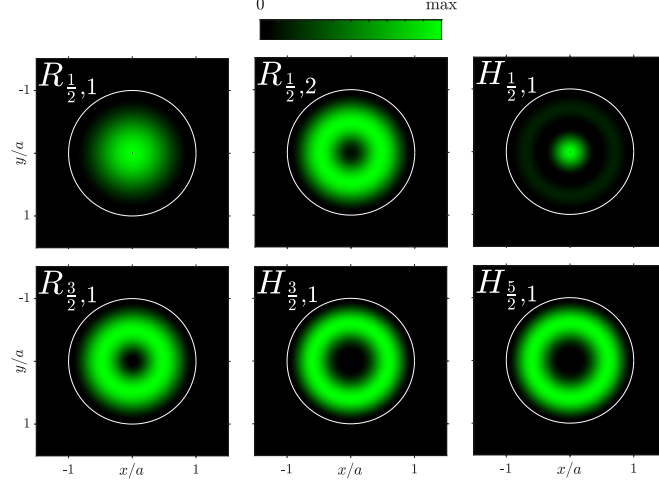


Figure C.5: Spatial distribution of probability densities,  $\psi^\dagger\psi$ , for the first six modes of the JR-D problem. The radius of the wire is  $a = 20 \text{ \AA}$ ,  $m_1v_F^2 = 1 \text{ eV}$ , and  $m_2v_F^2 = 2 \text{ eV}$ .

we find for the JR-D problem,

$$\left[ \nabla^2 + \left( \frac{E^2 - (m_0v_F^2 - B\hbar^2k^2)^2}{\hbar^2v_F^2} \right) \right] \phi = 0. \quad (\text{C.21})$$

Using the fact that  $[\mathbf{p}^2, H] = 0$ , we arrive at the solutions for propagation constant as,

$$k^{(1,2)} = \frac{v_F}{\sqrt{2}B\hbar} \left[ (2m_0B - 1) \pm \sqrt{(1 - 4m_0B) + \frac{4B^2E^2}{v_F^4}} \right]^{\frac{1}{2}}. \quad (\text{C.22})$$

where  $k^{(1)}$  and  $k^{(2)}$  are both propagation constants inside the wire. The dispersive mass in the JR-D problem, splits the propagation constant into two non-degenerate solutions. This breaks the solutions given in Eq. (C.16) into four eigenfunctions instead of two, written as,

$$\begin{aligned} \mathbf{u}_{\mu, M^{(1)}}^{(+)} &= \frac{e^{ik_z z} e^{i\mu\phi}}{\sqrt{2}} \begin{pmatrix} \phi_\mu^{(+)} \\ -i\hbar v_F \frac{k_\perp + ik_z}{M^{(1)}} \phi_\mu^{(-)} \end{pmatrix}, & \mathbf{u}_{\mu, M^{(1)}}^{(-)} &= \frac{e^{ik_z z} e^{i\mu\phi}}{\sqrt{2}} \begin{pmatrix} \phi_\mu^{(-)} \\ +i\hbar v_F \frac{k_\perp + ik_z}{M^{(1)}} \phi_\mu^{(+)} \end{pmatrix} \\ \mathbf{u}_{\mu, M^{(2)}}^{(+)} &= \frac{e^{ik_z z} e^{i\mu\phi}}{\sqrt{2}} \begin{pmatrix} \phi_\mu^{(+)} \\ -i\hbar v_F \frac{k_\perp + ik_z}{M^{(2)}} \phi_\mu^{(-)} \end{pmatrix}, & \mathbf{u}_{\mu, M^{(2)}}^{(-)} &= \frac{e^{ik_z z} e^{i\mu\phi}}{\sqrt{2}} \begin{pmatrix} \phi_\mu^{(-)} \\ +i\hbar v_F \frac{k_\perp + ik_z}{M^{(2)}} \phi_\mu^{(+)} \end{pmatrix} \end{aligned} \quad (\text{C.23})$$

where  $M^{(i)} = E + m_0v^2 - B\hbar^2(k^{(i)})^2$ . These four eigenfunctions can combine together to satisfy the open boundary condition,  $\psi_\mu = 0$ , on the surface of the wire. By applying this boundary condition, we arrive at the following transcendental equation:

$$k_\perp^{(1)} k_\perp^{(2)} \left( \frac{J_{n_-}(k_\perp^{(1)} a) J_{n_+}(k_\perp^{(2)} a)}{J_{n_+}(k_\perp^{(1)} a) J_{n_-}(k_\perp^{(2)} a)} + \frac{J_{n_+}(k_\perp^{(1)} a) J_{n_-}(k_\perp^{(2)} a)}{J_{n_-}(k_\perp^{(1)} a) J_{n_+}(k_\perp^{(2)} a)} \right) + 2k_z^2 = \frac{(M^{(1)} k^{(2)})^2 + (M^{(2)} k^{(1)})^2}{M^{(1)} M^{(2)}}. \quad (\text{C.24})$$

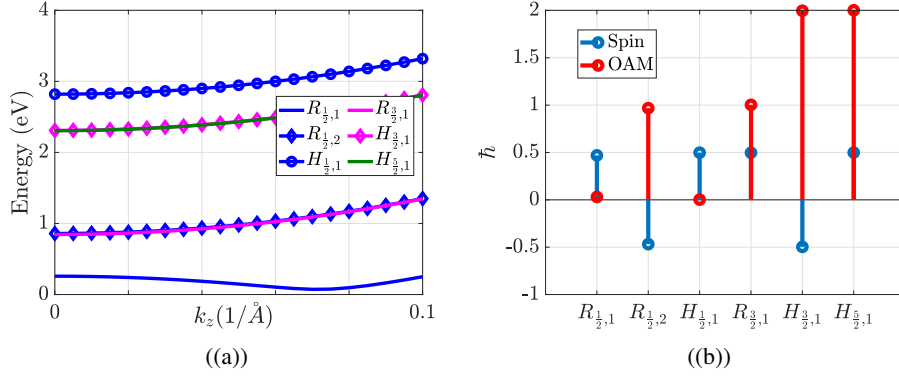


Figure C.6: Properties of the first six modes of the JR-D problem. (a) Dispersion of the first six modes and (b) spin and OAM of the first six modes.

### C.3.1 Modal Behaviour of Solutions

Modal behaviour in the solutions of the transcendental Eq. (C.24) refers to the regions where the solutions have different field distributions and properties. This modal behaviour can be analyzed by looking at Eq. (C.22). We define  $E_1$  and  $E_2$  as,

$$E_1 = \sqrt{\frac{v_F^4(4m_0B - 1)}{4B^2}} \quad (\text{C.25a})$$

$$E_2 = \sqrt{m_0^2v_F^4 + k_z^2\hbar^2(k_z^2\hbar^2B^2 + v_F^2 - 2m_0Bv_F^2)}, \quad (\text{C.25b})$$

and  $X_1$  and  $X_2$  as,

$$X_{1,2} = \frac{m_0v_F^2 \pm v_F\sqrt{m_0^2v_F^2 - 2k_z^2\hbar^2}}{k_z^2\hbar^2}. \quad (\text{C.26})$$

We can categorize the modes depending on the relationship of the eigenvalues,  $E$ , with respect to  $E_1$ ,  $E_2$ ,  $X_1$ ,  $X_2$ , and also values of  $k_z$  and  $B$ , as follows:

- $C_\mu$  Modes:  $E < E_1 \Rightarrow k_\perp^{(1)}$  and  $k_\perp^{(2)}$  are complex.
- $D_\mu$  Modes:  $E_1 < E < E_2$  &  $\{(k_z > \frac{m_0v_F}{2\hbar})$  or  $[k_z < \frac{m_0v_F}{2\hbar}$  &  $(B < X_1$  or  $B > X_2)]\}$   
 $\Rightarrow k_\perp^{(1)}$  and  $k_\perp^{(2)}$  are imaginary.
- $R_{\mu,\nu}$  Modes:  $E_1 < E < E_2$  &  $(k_z < \frac{m_0v_F}{2\hbar}$  &  $X_1 < B < X_2)$   $\Rightarrow k_\perp^{(1)}$  and  $k_\perp^{(2)}$  are real.
- $H_{\mu,\nu}$  Modes:  $E > E_2 \Rightarrow k_\perp^{(1)}$  is real and  $k_\perp^{(2)}$  is imaginary.

Figure C.5 shows the spatial distribution of  $\psi^\dagger\psi$  for the first six modes the JR-D problem. Dispersion diagrams of these modes in Fig. C.6, show that the  $R_{\frac{1}{2},2}$  and  $R_{\frac{3}{2},1}$  modes,

as well as the  $H_{\frac{3}{2},1}$  and  $H_{\frac{5}{2},1}$  modes, are degenerate. Unlike the two  $JR^+$  and  $JR^-$  problems, for JR-D the spin and OAM are dispersive. The total angular momentum, however, is still conserved and independent of  $k_z$ . Also note that although the spin is dispersive here, its absolute value does not exceed  $\frac{1}{2}$ .

### C.3.2 Group Velocity

As shown in the inset of Fig. 4.3(a) in section 4.3, group velocity becomes negative at some values of  $k_z$  for the dominant mode of the JR-D problem. Group velocity can be found by either taking the derivative of the dispersion or finding the expectation value of the velocity operator, defined in the Dirac equation as,

$$\hat{v} = \frac{\partial H}{\partial \mathbf{p}} = v_F \boldsymbol{\alpha} - 2\beta \hbar \mathbf{k}. \quad (\text{C.27})$$

Therefore, we find for the expectation value of  $\hat{z}$  component,  $\psi^\dagger \hat{v}_z \psi$ ,

$$v_z = v_F \psi \alpha_z \psi - 2\hbar k_z \psi^\dagger \beta \psi. \quad (\text{C.28})$$

Note that in Dirac equation,  $\mathbf{I} = e\psi^\dagger \hat{\mathbf{v}}\psi$  also represents the conserved charge currents [29]. This means that in the regions where the group velocity becomes negative, charge currents propagate along negative  $\hat{z}$  direction  $I_z < 0$ . In other words, charge transport is dominated by the holes rather than electrons.

## Appendix D

# Proofs for Chapter 5

### D.1 Equations of Motion

The equations of motions governing the acoustic waves in source-free regions are given by

$$\frac{\partial T_{ij}}{\partial x_j} = \rho \frac{\partial^2 u_i}{\partial t^2} \quad (\text{D.1})$$

where  $T_{ij}$  is the stress tensor,  $u_i$  the displacement vector, and  $\rho$  is the mass density of the medium. For piezoelectric material, the stress tensor can be written in terms of the strain tensor and electric field as

$$T_{ij} = c_{ijkl} S_{kl} - e_{kij} E_k \quad (\text{D.2})$$

while the displacement electric field is given by

$$D_i = \epsilon_{ij} E_j + e_{ijk} S_{jk} \quad (\text{D.3})$$

where  $c_{ijkl}$  is the stiffness tensor,  $e_{ijk}$  is the piezoelectric tensor,  $\epsilon_{ij}$  is the permittivity tensor.  $e_{ijk}$  is symmetric in the last two indices  $e_{ijk} = e_{ikj}$ . Due to the symmetry properties, these tensors are symmetric in pairs of indices. Therefore, the tensor  $c_{ijkl}$  can be written in the form of a  $6 \times 6$  matrix as  $c_{\alpha\beta}$  by following rules

$$\begin{aligned} \alpha = 1 \rightarrow ij = 11, \quad \alpha = 2 \rightarrow ij = 22, \quad \alpha = 3 \rightarrow ij = 33, \\ \alpha = 4 \rightarrow ij = 23, \quad \alpha = 5 \rightarrow ij = 31, \quad \alpha = 6 \rightarrow ij = 12. \end{aligned} \quad (\text{D.4})$$

This way it is common to write the matrices as  $c_{\alpha\beta} = c_{ijkl}$ ,  $e_{ijk} = e_{i\alpha}$ , and  $T_{ij} = T_\alpha$ .

On the other hand, the strain tensor  $S_{ij}$  is given by

$$S_{ij} = \frac{1}{2} \left( \frac{\partial u_i}{\partial x_j} + \frac{\partial u_j}{\partial x_i} \right), \quad (\text{D.5})$$

and

$$\mathbf{E} = -\nabla\Phi, \quad \Phi = u_4. \quad (\text{D.6})$$

We thus get, together with the equation  $\nabla \cdot \mathbf{D} = 0$ , equations of motion for source-free regions

$$c_{ijkl} \frac{\partial^2 u_l}{\partial x_j \partial x_k} + e_{kij} \frac{\partial^2 \Phi}{\partial x_j \partial x_k} = -\rho \omega^2 u_i, \quad i = 1, 2, 3 \quad (\text{D.7a})$$

$$e_{jkl} \frac{\partial^2 u_l}{\partial x_j \partial x_k} - \epsilon_{jk} \frac{\partial^2 \Phi}{\partial x_j \partial x_k} = 0 \quad (\text{D.7b})$$

where we have assumed that the solutions are of the form  $u_i = u_{i0}(x_i) e^{i\omega t}$ .

## D.2 Rayleigh Surface Wave

For a Rayleigh wave propagating along  $z$  direction, with an interface along  $y$  direction, we can write the solutions as

$$u_\mu = u_{\mu 0} e^{i(\omega t - kx_3)} e^{\chi k x_2}, \quad \mu = 1, 2, 3, 4 \quad \text{and} \quad u_4 = \Phi. \quad (\text{D.8})$$

Since  $\frac{\partial}{\partial x_1} = 0$ ,  $\frac{\partial}{\partial x_2} = \chi k$ , and  $\frac{\partial}{\partial x_3} = -ik$ , we get by plugging this into the equations of motion

$$[c_{i22l} \chi^2 k^2 - c_{i33l} k^2 - i\chi k^2 (c_{i23l} + c_{i32l})] u_l + [e_{2i2} \chi^2 k^2 u_4 - e_{3i3} k^2 - ik^2 \chi (e_{2i3} + e_{3i2})] u_4 + \rho \omega^2 u_i = 0 \quad (\text{D.9})$$

and

$$[e_{22l} \chi^2 k^2 - e_{33l} k^2 - i\chi k^2 (e_{23l} + e_{32l})] u_l - [e_{22} \chi^2 k^2 - e_{33} k^2 - i\chi k^2 (\epsilon_{23} + \epsilon_{32})] u_4 = 0 \quad (\text{D.10})$$

defining

$$\Gamma_{il} = c_{i33l} - c_{i22l} \chi^2 + i\chi (c_{i23l} + c_{i32l}) \quad (\text{D.11a})$$

$$\gamma_l = e_{33l} - e_{22l} \chi^2 + i\chi (e_{23l} + e_{32l}) \quad (\text{D.11b})$$

$$\epsilon = e_{33} - e_{22} \chi^2 + i\chi (\epsilon_{23} + \epsilon_{32}) \quad (\text{D.11c})$$

and  $v = \omega/k$  as the speed of the wave, we can write the system of four equations in matrix form as

$$\begin{pmatrix} \Gamma_{11} - \rho v^2 & \Gamma_{12} & \Gamma_{13} & \gamma_1 \\ \Gamma_{21} & \Gamma_{22} - \rho v^2 & \Gamma_{23} & \gamma_2 \\ \Gamma_{31} & \Gamma_{32} & \Gamma_{33} - \rho v^2 & \gamma_3 \\ \gamma_1 & \gamma_2 & \gamma_3 & -\epsilon \end{pmatrix} \begin{pmatrix} u_1 \\ u_2 \\ u_3 \\ u_4 \end{pmatrix} = 0. \quad (\text{D.12})$$

### D.3 Lithium Niobate Crystal Properties

The crystal of Lithium Niobate ( $\text{LiNO}_3$ ) belongs to the class  $3m$  which has a trigonal lattice.

The stiffness tensor for this class is

$$c_{\alpha\beta} = \begin{pmatrix} c_{11} & c_{12} & c_{13} & c_{14} & 0 & 0 \\ c_{12} & c_{11} & c_{13} & -c_{14} & 0 & 0 \\ c_{13} & c_{13} & c_{33} & 0 & 0 & 0 \\ c_{14} & -c_{14} & 0 & c_{44} & 0 & 0 \\ 0 & 0 & 0 & 0 & c_{44} & c_{14} \\ 0 & 0 & 0 & 0 & c_{14} & \frac{c_{11}-c_{22}}{2} \end{pmatrix} \quad (\text{D.13})$$

Where we have assumed that the (triad) principal axis (the axis that has the symmetry for a rotation of  $2\pi/3$  denoted by  $A_3$ ) is along  $z$  direction. For classes  $32$ ,  $3m$ , and  $\bar{3}m$  the dyad axis (the axis that has the symmetry for a rotation of  $\pi$ ) imposes extra conditions. Assuming that this axis, which is perpendicular to the principal axis, is along  $x$  direction, the constants  $c_{ijkl}$  with an odd number of indices equal to 1 become zero. Therefore in the above matrix, we have  $c_{25} = 0$ .

The class  $3m$  is distinguished by  $A_33M'$  which is one  $A_3$  triad axis and three mirror planes  $M'$  perpendicular to the  $A_3$  axis. If the sagittal plane is parallel to any of these three planes, we get a piezo-electric Rayleigh surface mode denoted by  $\bar{R}_2$ . In our case, the sagittal plane (the plane of propagation of surface wave) is the  $Y - Z$  plane. Therefore, if the wave propagates along the  $Z$  direction for a  $Y$ -cut crystal, we get the  $\bar{R}_2$  wave. For the matrix given in Eq. (D.13) the  $A_3$  axis is assumed to be along  $Z$  direction, while the mirror plane is assumed to be parallel  $Y - Z$  plane, i.e. the sagittal plane. We thus only need to plug in this matrix into the Eqs. (D.12) and (D.11) for the propagation of surface wave. Before doing so, we also need the piezo-electricity and permittivity tensors for Lithium Niobate. They are given by

$$e = \begin{pmatrix} 0 & 0 & 0 & 0 & e_{15} & -e_{22} \\ -e_{22} & e_{22} & 0 & e_{15} & 0 & 0 \\ e_{31} & e_{31} & e_{33} & 0 & 0 & 0 \end{pmatrix} \quad (\text{D.14})$$

and

$$\epsilon = \begin{pmatrix} \epsilon_{11} & 0 & 0 \\ 0 & \epsilon_{11} & 0 \\ 0 & 0 & \epsilon_{33} \end{pmatrix} \quad (\text{D.15})$$

Using these matrices, we get for the parameters in Eq. (D.11),

$$\begin{aligned} \Gamma_{11} &= c_{44} - \frac{1}{2}(c_{11} - c_{22})\chi^2 + 2i\chi c_{14}, & \Gamma_{12} &= 0, & \Gamma_{13} &= 0 \\ \Gamma_{21} &= 0, & \Gamma_{22} &= c_{44} - c_{11}\chi^2 - 2i\chi c_{14}, & \Gamma_{23} &= c_{14}\chi^2 + i\chi(c_{13} + c_{44}) \\ \Gamma_{31} &= 0, & \Gamma_{32} &= c_{14}\chi^2 + i\chi(c_{44} + c_{13}), & \Gamma_{33} &= c_{33} - c_{44}\chi^2 \end{aligned} \quad (\text{D.16a})$$

$$\gamma_1 = 0, \quad \gamma_2 = -e_{22}\chi^2 + i\chi(e_{15} + e_{31}), \quad \gamma_3 = e_{33} - e_{15}\chi^2 \quad (\text{D.16b})$$

$$\epsilon = \epsilon_{33} - \epsilon_{11}\chi^2 \quad (\text{D.16c})$$

These relations simplify Eq. (D.12) to

$$\begin{pmatrix} \Gamma_{22} - \rho v^2 & \Gamma_{23} & \gamma_2 \\ \Gamma_{23} & \Gamma_{33} - \rho v^2 & \gamma_3 \\ \gamma_2 & \gamma_3 & -\epsilon \end{pmatrix} \begin{pmatrix} u_2 \\ u_3 \\ u_4 \end{pmatrix} = 0, \quad (\text{D.17})$$

and

$$(\Gamma_{11} - \rho v^2) u_1 = 0 \quad (\text{D.18})$$

The second equation is decoupled from the first one and gives an independent transverse horizontal wave  $TH$  which is non-piezoelectric. We thus focus on the first equation and take  $u_1 = 0$ .

## D.4 Boundary Conditions

The mechanical boundary conditions on the surface normal to the axis  $x_2$  are for the surface stresses  $T_{i2}$  which states that  $T_{i2} = 0$ . We have using  $u_1 = 0$  and  $\partial/\partial x_1 = 0$ ,

$$\begin{aligned} T_{12} = & c_{12kl} \frac{1}{2} \left( \frac{\partial u_k}{\partial x_l} + \frac{\partial u_l}{\partial x_k} \right) + e_{k12} \frac{\partial u_4}{\partial x_k} = c_{1222} \frac{\partial u_2}{\partial x_2} + c_{1223} \left( \frac{\partial u_2}{\partial x_3} + \frac{\partial u_3}{\partial x_2} \right) \\ & + c_{1233} \frac{\partial u_3}{\partial x_3} + e_{212} \frac{\partial u_4}{\partial x_2} + e_{312} \frac{\partial u_4}{\partial x_3} = 0 \end{aligned} \quad (\text{D.19a})$$

$$\begin{aligned} T_{22} = & c_{22kl} \frac{1}{2} \left( \frac{\partial u_k}{\partial x_l} + \frac{\partial u_l}{\partial x_k} \right) + e_{k22} \frac{\partial u_4}{\partial x_k} = c_{2222} \frac{\partial u_2}{\partial x_2} + c_{2223} \left( \frac{\partial u_2}{\partial x_3} + \frac{\partial u_3}{\partial x_2} \right) \\ & + c_{2233} \frac{\partial u_3}{\partial x_3} + e_{222} \frac{\partial u_4}{\partial x_2} + e_{322} \frac{\partial u_4}{\partial x_3} \\ = & c_{11}\chi k u_2 - c_{14}(-iku_2 + \chi k u_3) - ikc_{13}u_3 + (e_{22}\chi k - e_{31}ik)u_4 \end{aligned} \quad (\text{D.19b})$$

$$\begin{aligned} T_{32} = & c_{32kl} \frac{1}{2} \left( \frac{\partial u_k}{\partial x_l} + \frac{\partial u_l}{\partial x_k} \right) + e_{k32} \frac{\partial u_4}{\partial x_k} = c_{3222} \frac{\partial u_2}{\partial x_2} + c_{3223} \left( \frac{\partial u_2}{\partial x_3} + \frac{\partial u_3}{\partial x_2} \right) \\ & + c_{3233} \frac{\partial u_3}{\partial x_3} + e_{232} \frac{\partial u_4}{\partial x_2} + e_{332} \frac{\partial u_4}{\partial x_3} \\ = & -c_{14}\chi k u_2 + c_{44}(-iku_2 + \chi k u_3) + e_{15}\chi k u_4 \end{aligned} \quad (\text{D.19c})$$

Setting these to zero we get the

$$T_{22} = c_{11}\chi k u_2 - c_{14}(-iku_2 + \chi k u_3) - ikc_{13}u_3 + (e_{22}\chi k - e_{31}ik)u_4 = 0 \quad (\text{D.20a})$$

$$T_{32} = -c_{14}\chi k u_2 + c_{44}(-iku_2 + \chi k u_3) + e_{15}\chi k u_4 = 0 \quad (\text{D.20b})$$

We also have the boundary condition for the normal component of the displacement electric field to be continuous  $D_{y0} = D_{y1}$ . We first write the electric field in the vacuum half space in terms of  $\Phi'$  in this medium as

$$\mathbf{E} = -\nabla\Phi = -\nabla \left( e^{-\chi' k x_2} e^{i(\omega t - k x_3)} \right) \quad (\text{D.21})$$

where the propagation constant  $k$  should be the same in the two media because of the boundary condition for the transverse electric field  $E_t = E'_t$ . The electric potential in vacuum follows the wave equation. It gives

$$\left[ k^2 \left( 1 - \chi'^2 \right) - \frac{\omega^2}{c^2} \right] \Phi = 0 \quad (\text{D.22})$$

which means that the wave propagates at the speed of light. However,  $\omega/k = V$  is equal to the speed of acoustic wave. We thus have

$$V = \frac{\omega}{k} = c\sqrt{1 - \chi'^2} \quad (\text{D.23})$$

But the acoustic wave speed is much less than the speed of light ( $V/c \sim 10^{-5}$ ). This means that  $\chi' \simeq 1$ . This is equivalent to the electrostatic condition. Therefore the potential in vacuum becomes

$$\Phi' = u_{40} e^{-k x_2} e^{i(\omega t - k x_3)} \quad (\text{D.24})$$

This gives for the continuity of normal component of the  $D$

$$\epsilon_0 \frac{\partial \Phi'}{\partial x_2} = \epsilon_{22} \frac{\partial u_4}{\partial x_2} - e_{2jk} \frac{1}{2} \left( \frac{\partial u_j}{\partial x_k} + \frac{\partial u_k}{\partial x_j} \right) \quad (\text{D.25})$$

and thus

$$-\epsilon_0 k u_{40} = \epsilon_{22} \chi k u_{40} - [e_{222} \chi k u_2 + e_{223} (-i k u_2 + \chi k u_3)] \quad (\text{D.26})$$

or

$$k u_{40} (\epsilon_0 + \epsilon_{22} \chi) = e_{22} \chi k u_{20} + e_{24} k (-i u_2 + \chi u_3) \quad (\text{D.27})$$

## D.5 Solving the Equations

To find the solutions for the Rayleigh waves, we need to solve the system of equations

$$\begin{pmatrix} \Gamma_{22} - \rho V^2 & \Gamma_{23} & \gamma_2 \\ \Gamma_{23} & \Gamma_{33} - \rho V^2 & \gamma_3 \\ \gamma_2 & \gamma_3 & -\epsilon \end{pmatrix} \begin{pmatrix} u_2 \\ u_3 \\ u_4 \end{pmatrix} = 0, \quad (\text{D.28})$$

with the parameters gives in Eq. (D.11) together with the boundary conditions

$$c_{11} \chi k u_2 - c_{14} (-i k u_2 + \chi k u_3) - i k c_{13} u_3 + (e_{22} \chi k - e_{31} i k) u_4 = 0 \quad (\text{D.29a})$$

$$-c_{14}\chi k u_2 + c_{44}(-iku_2 + \chi k u_3) + e_{15}\chi k u_4 = 0 \quad (\text{D.29b})$$

$$k u_{40}(\epsilon_0 + \epsilon_{22}\chi) = e_{22}\chi k u_{20} + e_{24}k(-iu_2 + \chi u_3) \quad (\text{D.29c})$$

Plus a normalization constant (taking  $u_{20} = 1$ ) to solve for the four unknowns  $u_{30}$ ,  $u_{40}$ ,  $\chi$ , and  $V = \omega/k$ .

For Eq. (D.28), the determinant of coefficients must be zero for a non-trivial solutions. This gives

$$\gamma_2 [\Gamma_{23}\gamma_3 - (\Gamma_{33} - \rho V^2)\gamma_2] - \gamma_3 [(\Gamma_{22} - \rho V^2)\gamma_3 - \Gamma_{23}\gamma_2] - \epsilon [(\Gamma_{22} - \rho V^2)(\Gamma_{33} - \rho V^2) - \Gamma_{23}^2] = 0 \quad (\text{D.30})$$

This equation has three physical solutions denoted as  $\chi^{(i)}$ ,  $i = 1, 2, 3$ . Therefore the solutions should be written as the sum of these three solutions as

$$u_\mu = \left( \sum_{i=1}^3 u_{\mu 0}^{(i)} e^{\chi^{(i)} k x_2} \right) e^{i(\omega t - k x_3)} \quad (\text{D.31})$$

From Eq. (D.28) we get

$$\frac{u_2^{(i)}}{u_3^{(i)}} = a^{(i)} = -\frac{(\gamma_3^{(i)})^2 + \epsilon^{(i)} (\Gamma_{33}^{(i)} - \rho V^2)}{\epsilon^{(i)} \Gamma_{23}^{(i)} + \gamma_2^{(i)} \gamma_3^{(i)}} = -\frac{\gamma_3^{(i)} \gamma_2^{(i)} + \epsilon^{(i)} \Gamma_{23}^{(i)}}{\epsilon^{(i)} (\Gamma_{22}^{(i)} - \rho V^2) + (\gamma_2^{(i)})^2} \quad (\text{D.32a})$$

$$\frac{u_4^{(i)}}{u_3^{(i)}} = b^{(i)} = -\frac{\gamma_2^{(i)} (\Gamma_{33}^{(i)} - \rho V^2) - \Gamma_{23}^{(i)} \gamma_3^{(i)}}{\epsilon^{(i)} \Gamma_{23}^{(i)} + \gamma_2^{(i)} \gamma_3^{(i)}} = -\frac{\Gamma_{23}^{(i)} \gamma_2^{(i)} - (\Gamma_{22}^{(i)} - \rho V^2) \gamma_3^{(i)}}{\epsilon^{(i)} (\Gamma_{22}^{(i)} - \rho V^2) + (\gamma_2^{(i)})^2} \quad (\text{D.32b})$$

where the parameters with the superscript  $(i)$  are given in Eq. (D.16) for each solution of  $\chi^{(i)}$ . Therefore, the boundary conditions become

$$\sum_{i=1}^3 t_1^{(i)} u_{30}^{(i)} = 0, \quad \sum_{i=1}^3 t_2^{(i)} u_{30}^{(i)} = 0, \quad \sum_{i=1}^3 t_3^{(i)} u_{30}^{(i)} = 0 \quad (\text{D.33})$$

with

$$t_1^{(i)} = c_{11}\chi^{(i)} a^{(i)} + i c_{14} a^{(i)} - c_{14}\chi^{(i)} - i c_{13} + e_{22}\chi^{(i)} b^{(i)} - i e_{31} b^{(i)} \quad (\text{D.34a})$$

$$t_2^{(i)} = -c_{14}\chi^{(i)} a^{(i)} - i c_{44} a^{(i)} + c_{44}\chi^{(i)} + e_{15}\chi^{(i)} b^{(i)} \quad (\text{D.34b})$$

$$t_3^{(i)} = e_{22}\chi^{(i)} a^{(i)} - i e_{15} a^{(i)} + e_{15}\chi^{(i)} - \epsilon_0 b^{(i)} - \epsilon_{11}\chi^{(i)} b^{(i)} \quad (\text{D.34c})$$

From the first two boundary conditions, assuming that  $u_{30}^{(1)} = 1$ , we can find  $u_{30}^{(2)}$  and  $u_{30}^{(3)}$ . Plugging these into the third equation, we can get the velocity of propagation. Solving these equations, we find the velocity of propagation to be  $V = 3491.985$  m/s.

## Appendix E

# Proofs for Chapter 6

### E.1 Radiated Power due to Magnetic Fluctuations

In this section we derive the total radiated power from the spinning sphere due to the fluctuating dipoles and fields. Using an approach similar to the one taken by Abajo *et al* [162, 174], we can write the radiated power due to the magnetic fluctuations of dipoles and fields as,

$$P_{\text{mag}} = -\langle \mathbf{H}^{\text{ind}} \cdot \partial \mathbf{m}^{\text{fl}} / \partial t + \mathbf{H}^{\text{fl}} \cdot \partial \mathbf{m}^{\text{ind}} / \partial t \rangle \quad (\text{E.1})$$

where  $\mathbf{H}^{\text{ind}}$  is the induced magnetic field due to the magnetic dipole fluctuations  $\mathbf{m}^{\text{fl}}$  of the particle and  $\mathbf{m}^{\text{ind}}$  is the induced magnetic dipole in the particle due to the fluctuations of the vacuum magnetic field  $\mathbf{H}^{\text{fl}}$ . Note that all of these quantities are written in the lab frame. For the sphere spinning at the rotation frequency  $\Omega$ , we can write,

$$\begin{aligned} m_x^{\text{fl}} &= m_x^{\prime\text{fl}} \cos \Omega t - m_y^{\prime\text{fl}} \sin \Omega t \\ m_y^{\text{fl}} &= m_x^{\prime\text{fl}} \sin \Omega t + m_y^{\prime\text{fl}} \cos \Omega t \\ m_z^{\text{fl}} &= m_z^{\prime\text{fl}} \end{aligned} \quad (\text{E.2})$$

where the primed quantities are written in the rotating frame. Performing a Fourier transformation as  $\mathbf{m}^{\text{fl}}(t) = \int \frac{d\omega}{2\pi} e^{-i\omega t} \mathbf{m}^{\text{fl}}(\omega)$ , we can write in the frequency domain

$$\begin{aligned} m_x^{\text{fl}}(\omega) &= \frac{1}{2} \left[ m_x^{\prime\text{fl}}(\omega^-) + m_x^{\prime\text{fl}}(\omega^+) + im_y^{\prime\text{fl}}(\omega^+) - im_y^{\prime\text{fl}}(\omega^-) \right] \\ m_y^{\text{fl}}(\omega) &= \frac{1}{2} \left[ im_x^{\prime\text{fl}}(\omega^-) - im_x^{\prime\text{fl}}(\omega^+) + m_y^{\prime\text{fl}}(\omega^+) + m_y^{\prime\text{fl}}(\omega^-) \right] \end{aligned} \quad (\text{E.3})$$

where  $\omega^\pm = \omega \pm \Omega$ . We can similarly write for the magnetic fields

$$\begin{aligned} H_x^{\text{fl}}(\omega) &= \frac{1}{2} \left[ H_x^{\text{fl}}(\omega^+) + H_x^{\text{fl}}(\omega^-) - iH_y^{\text{fl}}(\omega^+) + iH_y^{\text{fl}}(\omega^-) \right] \\ H_y^{\text{fl}}(\omega) &= \frac{1}{2} \left[ iH_x^{\text{fl}}(\omega^+) - iH_x^{\text{fl}}(\omega^-) + H_y^{\text{fl}}(\omega^+) + H_y^{\text{fl}}(\omega^-) \right]. \end{aligned} \quad (\text{E.4})$$

Thus, using the fact that,

$$\mathbf{m}'^{\text{ind}}(\omega) = \bar{\boldsymbol{\alpha}}_m(\omega) \cdot \mathbf{H}'^{\text{fl}}(\omega), \quad (\text{E.5})$$

with

$$\bar{\boldsymbol{\alpha}}_m(\omega) = \begin{pmatrix} \alpha_{m,\perp}(\omega) & -\alpha_{m,g}(\omega) & 0 \\ \alpha_{m,g}(\omega) & \alpha_{m,\perp}(\omega) & 0 \\ 0 & 0 & \alpha_{m,\parallel}(\omega) \end{pmatrix} \quad (\text{E.6})$$

being the magnetic polarizability tensor of the YIG sphere biased along the  $z$  axis, we find in the lab frame

$$\mathbf{m}^{\text{ind}}(\omega) = \bar{\boldsymbol{\alpha}}_m^{\text{eff}}(\omega) \cdot \mathbf{H}^{\text{fl}}(\omega) \quad (\text{E.7})$$

where

$$\bar{\boldsymbol{\alpha}}_m^{\text{eff}} = \begin{pmatrix} \alpha_{m,\perp}^{\text{eff}}(\omega) & -\alpha_{m,g}^{\text{eff}}(\omega) & 0 \\ \alpha_{m,g}^{\text{eff}}(\omega) & \alpha_{m,\perp}^{\text{eff}}(\omega) & 0 \\ 0 & 0 & \alpha_{m,\parallel}^{\text{eff}}(\omega) \end{pmatrix} \quad (\text{E.8})$$

and

$$\alpha_{m,\perp}^{\text{eff}}(\omega) = \frac{1}{2} [\alpha_{m,\perp}(\omega^+) + \alpha_{m,\perp}(\omega^-) + i\alpha_{m,g}(\omega^+) - i\alpha_{m,g}(\omega^-)] \quad (\text{E.9a})$$

$$\alpha_{m,g}^{\text{eff}}(\omega) = -\frac{i}{2} [\alpha_{m,\perp}(\omega^+) - \alpha_{m,\perp}(\omega^-) + i\alpha_{m,g}(\omega^+) + i\alpha_{m,g}(\omega^-)] \quad (\text{E.9b})$$

$$\alpha_{m,\parallel}^{\text{eff}} = \alpha_{m,\parallel}(\omega). \quad (\text{E.9c})$$

Note that we have used an expression similar to Eq. (E.3) but written for the induced magnetic dipole moments. Expression for  $\alpha_{m,\perp}(\omega)$  and  $\alpha_{m,g}(\omega)$  are given in section E.4. Using the fluctuation-dissipation theorem (FDT) [183],

$$\langle H_i^{\text{fl}}(\omega) H_j^{\text{fl}}(\omega') \rangle = 4\pi\hbar [n_0(\omega) + 1] \left\{ \frac{G_{ij}^{\text{H}}(\omega) - G_{ji}^{\text{H}*}(\omega)}{2i} \right\} \delta(\omega + \omega'), \quad (\text{E.10})$$

with  $G_{ij}^{\text{H}}(\omega) = G_{ij}^{\text{H}}(\mathbf{r}, \mathbf{r}' = \mathbf{r}, \omega)$  defined as the equal-frequency magnetic Green's function of the environment defined through the equation,

$$H_i(\mathbf{r}, \mathbf{r}', \omega) = G_{ij}^{\text{H}}(\mathbf{r}, \mathbf{r}', \omega) m_j(\mathbf{r}', \omega), \quad (\text{E.11})$$

we find, using Eqs. (E.5) and (E.4), for the second term in Eq. (E.1),

$$\begin{aligned} \langle H_i^{\text{fl}}(\omega) \partial m_i^{\text{ind}}(\omega') / \partial t \rangle &= -i\omega' 2\pi\hbar [n_0(\omega) + 1] \delta(\omega + \omega') \times \\ &\left\{ (\text{Im} \{G_{xx}^{\text{H}}(\omega)\} + \text{Im} \{G_{yy}^{\text{H}}(\omega)\}) [\alpha_{m,\perp}(\omega'^+) + \alpha_{m,\perp}(\omega'^-) + i\alpha_{m,g}(\omega'^+) - i\alpha_{m,g}(\omega'^-)] \right. \\ &+ (\text{Re} \{G_{xy}^{\text{H}}(\omega)\} - \text{Re} \{G_{yx}^{\text{H}*}(\omega)\}) [\alpha_{m,\perp}(\omega'^+) - \alpha_{m,\perp}(\omega'^-) + i\alpha_{m,g}(\omega'^+) + i\alpha_{m,g}(\omega'^-)] \\ &\left. + 2\text{Im} \{G_{zz}^{\text{H}}(\omega)\} \alpha_{m,\parallel}(\omega') \right\} \end{aligned} \quad (\text{E.12})$$

Note that

$$n_0(\omega) = \frac{1}{e^{\frac{\hbar\omega}{k_B T_0}} - 1} \quad (\text{E.13})$$

is the Planck's distribution at the temperature of the lab  $T_0$ . Writing FDT for the fluctuating dipoles,

$$\langle m_i^{\text{fl}}(\omega) m_j^{\text{fl}}(\omega') \rangle = 4\pi\hbar [n_1(\omega) + 1] \left( \frac{\alpha_{m,ij}(\omega) - \alpha_{m,ji}^*(\omega)}{2i} \right) \delta(\omega + \omega') \quad (\text{E.14})$$

we arrive at, for the first term in Eq. (E.1),

$$\begin{aligned} \langle H_i^{\text{ind}}(\omega) \partial m_i^{\text{fl}}(\omega') / \partial t \rangle = & -2\pi\hbar i \omega' [n_1(\omega^-) + 1] \left\{ \delta(\omega + \omega') \left[ G_{xx}^{\text{H}}(\omega) \text{Im} \{ \alpha_{m,\perp}(\omega^-) \} - G_{xx}^{\text{H}}(\omega) \text{Re} \{ \alpha_{m,g}(\omega^-) \} \right. \right. \\ & - G_{yy}^{\text{H}}(\omega) \text{Re} \{ \alpha_{m,g}(\omega^-) \} + G_{yy}^{\text{H}}(\omega) \text{Im} \{ \alpha_{m,\perp}(\omega^-) \} + i G_{xy}^{\text{H}}(\omega) \text{Im} \{ \alpha_{m,\perp}(\omega^-) \} \\ & \left. \left. - i G_{xy}^{\text{H}}(\omega) \text{Re} \{ \alpha_{m,g}(\omega^-) \} + i G_{yx}^{\text{H}}(\omega) \text{Re} \{ \alpha_{m,g}(\omega^-) \} - i G_{yx}^{\text{H}}(\omega) \text{Im} \{ \alpha_{m,\perp}(\omega^-) \} \right] \right\} \\ & - 2\pi\hbar i \omega' [n_1(\omega^+) + 1] \left\{ \delta(\omega + \omega') \left[ G_{xx}^{\text{H}}(\omega) \text{Im} \{ \alpha_{m,\perp}(\omega^+) \} + G_{xx}^{\text{H}}(\omega) \text{Re} \{ \alpha_{m,g}(\omega^+) \} \right. \right. \\ & + G_{yy}^{\text{H}}(\omega) \text{Re} \{ \alpha_{m,g}(\omega^+) \} + G_{yy}^{\text{H}}(\omega) \text{Im} \{ \alpha_{m,\perp}(\omega^+) \} - i G_{xy}^{\text{H}}(\omega) \text{Im} \{ \alpha_{m,\perp}(\omega^+) \} \\ & \left. \left. - i G_{xy}^{\text{H}}(\omega) \text{Re} \{ \alpha_{m,g}(\omega^+) \} + i G_{yx}^{\text{H}}(\omega) \text{Re} \{ \alpha_{m,g}(\omega^+) \} + i G_{yx}^{\text{H}}(\omega) \text{Im} \{ \alpha_{m,\perp}(\omega^+) \} \right] \right\} \\ & - 4\pi\hbar i \omega' [n_1(\omega) + 1] \left\{ \delta(\omega + \omega') G_{zz}^{\text{H}}(\omega) \text{Im} \{ \alpha_{m,\parallel}(\omega) \} \right\} \end{aligned} \quad (\text{E.15})$$

where we have used Eqs. (E.3) and,

$$H_i^{\text{ind}}(\omega) = G_{ij}^{\text{H}}(\omega) m_j^{\text{fl}}(\omega). \quad (\text{E.16})$$

Note that  $n_1(\omega)$  is the Planck distribution given in Eq. (E.13). Taking the inverse Fourier transform, adding Eqs. (E.12) and (E.15), taking the real part of the radiated power, and performing some change of integral variables, we find after some algebra,

$$\begin{aligned} P_{\text{mag}} = & \frac{\hbar}{\pi} \int_{-\infty}^{+\infty} \omega d\omega \left\{ [n_1(\omega^-) - n_0(\omega)] \left( \text{Im} \{ G_{xx}^{\text{H}}(\omega) \} + \text{Im} \{ G_{yy}^{\text{H}}(\omega) \} + \text{Re} \{ G_{xy}^{\text{H}}(\omega) \} - \text{Re} \{ G_{yx}^{\text{H}}(\omega) \} \right) \times \right. \\ & \left. \left[ \text{Im} \{ \alpha_{m,\perp}(\omega^-) \} - \text{Re} \{ \alpha_{m,g}(\omega^-) \} \right] + [n_1(\omega) - n_0(\omega)] \text{Im} \{ G_{zz}^{\text{H}}(\omega) \} \text{Im} \{ \alpha_{m,\parallel}(\omega) \} \right\}. \end{aligned} \quad (\text{E.17})$$

In this derivation, we have used the property  $\alpha_m(-\omega) = \alpha_m^*(\omega)$ . The expressions for Green's functions in different arrangements of the YIG and aluminium interface are given in section E.2. Plugging these expressions into Eq. (E.17), we obtain Eq. (6.2).

## E.2 Green's Function Near an Anisotropic Magnetic Material

In the case when the interface is a magnetic material, the density of states would change due to anisotropy of the material. In this section we derive the Green's function near a half-space of magnetic material. We study two cases when the interface is the  $x - y$  plane and

$x - z$  plane, as shown in Fig. E.1. We can write the electric and magnetic fields in vacuum as

$$\mathbf{E} = \mathbf{E}^i + \mathbf{E}^r, \quad \mathbf{H} = \mathbf{H}^i + \mathbf{H}^r \quad (\text{E.18a})$$

$$\mathbf{E}^i = (E_{0s}\hat{s}_- + E_{0p}\hat{p}_-)e^{i\mathbf{k}_-\cdot\mathbf{r}} \quad (\text{E.18b})$$

$$\mathbf{E}^r = (E_{0s}r_{ss}\hat{s}_+ + E_{0p}r_{pp}\hat{p}_+ + E_{0s}r_{ps}\hat{p}_+ + E_{0p}r_{sp}\hat{s}_+)e^{i\mathbf{k}_+\cdot\mathbf{r}} \quad (\text{E.18c})$$

$$\mathbf{H}^i = \frac{1}{\eta_0} (-E_{0s}\hat{p}_- + E_{0p}\hat{s}_-)e^{i\mathbf{k}_-\cdot\mathbf{r}} \quad (\text{E.18d})$$

$$\mathbf{H}^r = \frac{1}{\eta_0} (-E_{0s}r_{ss}\hat{p}_+ + E_{0p}r_{pp}\hat{s}_+ + E_{0s}r_{ps}\hat{s}_+ - E_{0p}r_{sp}\hat{p}_+)e^{i\mathbf{k}_+\cdot\mathbf{r}} \quad (\text{E.18e})$$

where  $\hat{s}_\pm$ ,  $\hat{p}_\pm$ , and  $\hat{k}_\pm/k_0$  form a triplet with

$$\hat{k}_\pm = k_0 (\kappa \cos \phi \hat{x} + \kappa \sin \phi \hat{y} \pm k_z \hat{z}), \quad \hat{s}_\pm = \sin \phi \hat{x} - \cos \phi \hat{y}, \quad \hat{p}_\pm = -(\pm k_z \cos \phi \hat{x} \pm k_z \sin \phi - \kappa \hat{z}) \quad (\text{E.19})$$

and  $\eta_0 = \sqrt{\mu_0/\epsilon_0}$ . Similarly, we can write the electric and magnetic fields inside the magnetic material as

$$\mathbf{E}' = \mathbf{E}^t, \quad \mathbf{H}' = \mathbf{H}^t \quad (\text{E.20a})$$

$$\mathbf{E}^t = (E_{0s}t_{ss}\hat{s}'_- + E_{0p}t_{pp}\hat{p}'_- + E_{0s}t_{ps}\hat{p}'_- + E_{0p}t_{sp}\hat{s}'_-)e^{i\mathbf{k}'_-\cdot\mathbf{r}} \quad (\text{E.20b})$$

$$\bar{\boldsymbol{\mu}}\mathbf{H}^t = \frac{\sqrt{\kappa^2 + k_z'^2}}{\eta_0} [-E_{0s}t_{ss}\hat{p}'_- + E_{0p}t_{pp}\hat{s}'_- + E_{0s}t_{ps}\hat{s}'_- - E_{0p}t_{sp}\hat{p}'_-]e^{i\mathbf{k}'_-\cdot\mathbf{r}} \quad (\text{E.20c})$$

where

$$\mathbf{k}'_\pm = k_0 \hat{k}'_\pm = k_0 (\kappa \cos \phi \hat{x} + \kappa \sin \phi \hat{y} \pm k'_z \hat{z}), \quad \hat{s}'_\pm = \sin \phi \hat{x} - \cos \phi \hat{y}, \quad \hat{p}'_\pm = -\frac{\pm k'_z \cos \phi \hat{x} \pm k'_z \sin \phi \hat{y} - \kappa \hat{z}}{\sqrt{\kappa^2 + k_z'^2}} \quad (\text{E.21})$$

Note that  $\kappa$  is the same in the two media due to the boundary conditions. Also  $\hat{k}'_\pm \times \hat{p}'_\pm = \hat{s}'_\pm$  and so on. We can write the Maxwell's equations in the magnetic material in matrix form as

$$(M + M_k) \psi = \left[ \begin{pmatrix} \bar{\boldsymbol{\epsilon}} & 0 \\ 0 & \bar{\boldsymbol{\mu}} \end{pmatrix} + \begin{pmatrix} 0 & \bar{\boldsymbol{\kappa}} \\ -\bar{\boldsymbol{\kappa}} & 0 \end{pmatrix} \right] \begin{pmatrix} \mathbf{E}^t \\ \eta_0 \mathbf{H}^t \end{pmatrix} = 0 \quad (\text{E.22})$$

where

$$\bar{\boldsymbol{\kappa}} = \begin{pmatrix} 0 & -k'_z & \kappa \sin \phi \\ k'_z & 0 & -\kappa \cos \phi \\ -\kappa \sin \phi & \kappa \cos \phi & 0 \end{pmatrix} \quad (\text{E.23})$$

Setting the  $\det(M + M_k) = 0$  we get the solutions for  $k'_z$  in terms of  $\kappa$  and  $\phi$ . From these solutions and applying the boundary conditions, we can find the values of  $r_{ss}$ ,  $r_{sp}$ ,  $r_{ps}$ ,  $r_{pp}$  for a given  $\kappa$  and  $\phi$  (see section E.10). Note that different bias directions for the magnetic field of the YIG slab change the  $\bar{\boldsymbol{\mu}}$  tensor and thus change the Fresnel coefficients

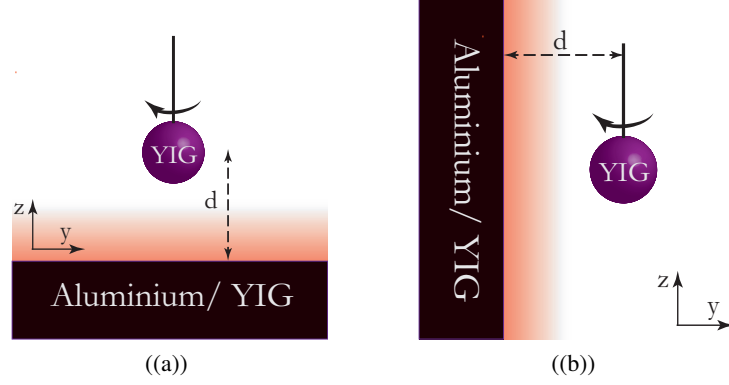


Figure E.1: Schematic of the problem for the two cases of when the interface is in (a)  $x - y$  plane and (b)  $x - z$  plane.

respectively. This can be done since no assumption on the direction and components of the permeability tensor has been assumed in our derivations.

We write the Green's function for a source located at  $z' = d$ . Here, since we take the spinning sphere to be at the origin and to simplify the derivations, we move  $z = 0$  to  $z' = d$ . This would not change the Fresnel reflection coefficients. The incident magnetic Green's function at the location of the source is thus,

$$\bar{\mathbf{G}}_i^{\text{H}}(z = z', \omega) = \frac{ik_0^2}{8\pi^2\epsilon_m} \int \frac{dk_x dk_y}{k_z} (\hat{s}\hat{s} + \hat{p}_-\hat{p}_-) e^{ik_x(x-x') + ik_y(y-y')} \quad (\text{E.24})$$

We can thus write the reflected magnetic Green's function at the location of the source, when the interface is in the  $x - y$  plane (Fig. E.1(a)), as

$$\bar{\mathbf{G}}_r^{\text{H}}(z = z', \omega) = \frac{ik_0^2}{8\pi\epsilon_m} \int \frac{dk_x dk_y}{k_z} (\hat{s}r_{pp}\hat{s} + \hat{p}_+r_{sp}\hat{s} + \hat{s}r_{ps}\hat{p}_- + \hat{p}_+r_{ss}\hat{p}_-) e^{2ik_z d} \quad (\text{E.25})$$

Here we take  $k_x = \kappa \cos \phi$  and  $k_y = \kappa \sin \phi$ . Note that here, however, the Fresnel reflection coefficients in general depend on the angle of incidence  $\phi$ . For the special case of magnetization along  $z$  axis they become independent of  $\phi$ . We can write the total magnetic Green's function, using Eq. (E.21), at the location of source as,

$$\begin{aligned} \bar{\mathbf{G}}^{\text{H}}(\mathbf{r}, \mathbf{r}, \omega) &= \frac{ik_0^2}{8\pi^2} \int \frac{dk_x dk_y}{k_z} \left[ \hat{s}\hat{s} (1 + r_{pp}e^{2ik_z d}) + \hat{p}_-\hat{p}_- + (r_{ss}\hat{p}_+\hat{p}_- + r_{ps}\hat{s}\hat{p}_- + r_{sp}\hat{p}_+\hat{s}) e^{2ik_z d} \right] \\ &= \frac{ik_0^3}{8\pi^2\epsilon_m} \int_0^{2\pi} d\phi \int_0^{+\infty} \frac{\kappa d\kappa}{p} \left\{ [\sin^2 \phi \hat{x}\hat{x} + \cos^2 \phi \hat{y}\hat{y} - \sin \phi \cos \phi (\hat{x}\hat{y} + \hat{y}\hat{x})] (1 + r_{pp}e^{2ik_z d}) \right. \\ &\quad + p^2 \cos^2 \phi \hat{x}\hat{x} + p^2 \sin^2 \phi \hat{y}\hat{y} + \kappa^2 \hat{z}\hat{z} + p^2 \cos \phi \sin \phi (\hat{x}\hat{y} + \hat{y}\hat{x}) + p\kappa \cos \phi (\hat{x}\hat{z} + \hat{z}\hat{x}) + p\kappa \sin \phi (\hat{y}\hat{z} + \hat{z}\hat{y}) \\ &\quad + e^{2ik_0 p d} r_{ss} [-p^2 \cos^2 \phi \hat{x}\hat{x} - p^2 \sin^2 \phi \hat{y}\hat{y} + \kappa^2 \hat{z}\hat{z} - p^2 \cos \phi \sin \phi (\hat{x}\hat{y} + \hat{y}\hat{x}) \\ &\quad \left. - p\kappa \cos \phi (\hat{x}\hat{z} - \hat{z}\hat{x}) - p\kappa \sin \phi (\hat{y}\hat{z} - \hat{z}\hat{y}) \right] \\ &\quad + e^{2ik_0 p d} r_{ps} [p \sin \phi \cos \phi (\hat{x}\hat{x} - \hat{y}\hat{y}) + p \sin^2 \phi \hat{x}\hat{y} - p \cos^2 \phi \hat{y}\hat{x} - \kappa \sin \phi \hat{x}\hat{z} + \kappa \cos \phi \hat{y}\hat{z}] \\ &\quad \left. + e^{2ik_0 p d} r_{sp} [-p \cos \phi \sin \phi (\hat{x}\hat{x} - \hat{y}\hat{y}) + p \cos^2 \phi \hat{x}\hat{y} - p \sin^2 \phi \hat{y}\hat{x} + \kappa \sin \phi \hat{z}\hat{x} - \kappa \cos \phi \hat{z}\hat{y}] \right\} \quad (\text{E.26}) \end{aligned}$$

Dropping the terms which vanish after integration over  $\phi$ , we get

$$\begin{aligned}
\bar{G}^H(\mathbf{r}, \mathbf{r}, \omega) = & \frac{ik_0^3}{8\pi^2} \int_0^{2\pi} d\phi \int_0^{+\infty} \frac{\kappa d\kappa}{p} \left\{ [\sin^2 \phi \hat{x}\hat{x} + \cos^2 \phi \hat{y}\hat{y} - \sin \phi \cos \phi (\hat{x}\hat{y} + \hat{y}\hat{x})] \left( 1 + r_{pp} e^{2ik_z d} \right) \right. \\
& + p^2 \cos^2 \phi \hat{x}\hat{x} + p^2 \sin^2 \phi \hat{y}\hat{y} + \kappa^2 \hat{z}\hat{z} \\
& + e^{2ik_0 p d} r_{ss} [-p^2 \cos^2 \phi \hat{x}\hat{x} - p^2 \sin^2 \phi \hat{y}\hat{y} + \kappa^2 \hat{z}\hat{z} - p^2 \cos \phi \sin \phi (\hat{x}\hat{y} + \hat{y}\hat{x}) \\
& - p\kappa \cos \phi (\hat{x}\hat{z} - \hat{z}\hat{x}) - p\kappa \sin \phi (\hat{y}\hat{z} - \hat{z}\hat{y})] \\
& + e^{2ik_0 p d} r_{ps} [p \sin \phi \cos \phi (\hat{x}\hat{x} - \hat{y}\hat{y}) + p \sin^2 \phi \hat{x}\hat{y} - p \cos^2 \phi \hat{y}\hat{x} + \kappa \sin \phi \hat{x}\hat{z} - \kappa \cos \phi \hat{y}\hat{z}] \\
& \left. + e^{2ik_0 p d} r_{sp} [-p \cos \phi \sin \phi (\hat{x}\hat{x} - \hat{y}\hat{y}) + p \cos^2 \phi \hat{x}\hat{y} - p \sin^2 \phi \hat{y}\hat{x} + \kappa \sin \phi \hat{z}\hat{x} - \kappa \cos \phi \hat{z}\hat{y}] \right\} \\
\end{aligned} \tag{E.27}$$

Note that the electric Green's function is obtained by dividing by  $\epsilon_0$  and changing  $r_{ss}$  to  $r_{pp}$ , and vice versa, as well as changing  $r_{sp}$  to  $r_{ps}$  and vice versa. In general, the non-diagonal parts of the Green's function are not zero. Note that this expression only applies to the case when the interface is the  $x - y$  plane. Using this equation, we find,

$$\text{Im} \{ G_{xx}^H(\omega) \} = \frac{\pi\omega\rho_0}{8} g_{\perp,1}^H(\omega) \tag{E.28a}$$

$$\text{Im} \{ G_{yy}^H(\omega) \} = \frac{\pi\omega\rho_0}{8} g_{\perp,2}^H(\omega) \tag{E.28b}$$

$$\text{Re} \{ G_{xy}^H(\omega) \} - \text{Re} \{ G_{yx}^H(\omega) \} = \frac{\pi\omega\rho_0}{4} g_{g,1}^H(\omega) \tag{E.28c}$$

$$\text{Im} \{ G_{zz}^H(\omega) \} = \frac{\pi\omega\rho_0}{4} g_{\parallel}^H(\omega) \tag{E.28d}$$

where  $\rho_0 = \omega^2/\pi^2 c^3$  is the vacuum density of states and,

$$\begin{aligned}
g_{\perp,1}^H(\omega) = & \frac{1}{\pi} \int_0^{2\pi} d\phi \left\{ \int_0^1 \frac{\kappa d\kappa}{p} [1 + \sin^2 \phi \text{Re} \{ r_{pp} e^{2ik_0 p d} \}] - \kappa^2 \cos^2 \phi + \cos^2 \phi (\kappa^2 - 1) \text{Re} \{ r_{ss} e^{2ik_0 p d} \} \right. \\
& \left. + p \sin \phi \cos \phi \text{Re} \{ e^{2ik_0 p d} (r_{ps} - r_{sp}) \} \right] \\
& + \int_1^\infty \frac{\kappa d\kappa}{|p|} [\sin^2 \phi \text{Im} \{ r_{pp} \} + \cos^2 \phi (\kappa^2 - 1) \text{Im} \{ r_{ss} \} + |p| \sin \phi \cos \phi \text{Re} \{ r_{ps} - r_{sp} \}] e^{-2k_0 |p| d} \left. \right\} \\
\end{aligned} \tag{E.29a}$$

$$\begin{aligned}
g_{\perp,2}^H(\omega) = & \frac{1}{\pi} \int_0^{2\pi} d\phi \left\{ \int_0^1 \frac{\kappa d\kappa}{p} [1 + \cos^2 \phi \text{Re} \{ r_{pp} e^{2ik_0 p d} \}] - \kappa^2 \sin^2 \phi + \sin^2 \phi (\kappa^2 - 1) \text{Re} \{ r_{ss} e^{2ik_0 p d} \} \right. \\
& \left. - p \sin \phi \cos \phi \text{Re} \{ e^{2ik_0 p d} (r_{ps} - r_{sp}) \} \right] \\
& + \int_1^\infty \frac{\kappa d\kappa}{|p|} [\cos^2 \phi \text{Im} \{ r_{pp} \} + \sin^2 \phi (\kappa^2 - 1) \text{Im} \{ r_{ss} \} - |p| \sin \phi \cos \phi \text{Re} \{ r_{ps} - r_{sp} \}] e^{-2k_0 |p| d} \left. \right\} \\
\end{aligned} \tag{E.29b}$$

$$\begin{aligned}
g_{g,1}^H(\omega) = & -\frac{1}{\pi} \int_0^{2\pi} d\phi \int_0^1 \kappa d\kappa [\sin^2 \phi \text{Im} \{ r_{ps} e^{2ik_0 p d} \} + \cos^2 \phi \text{Im} \{ r_{sp} e^{2ik_0 p d} \}] \\
& + \int_1^\infty \kappa d\kappa [\sin^2 \phi \text{Im} \{ r_{ps} \} + \cos^2 \phi \text{Im} \{ r_{sp} \}] e^{-2k_0 |p| d} \left. \right\} \\
\end{aligned} \tag{E.29c}$$

$$g_{\parallel}^{\text{H}}(\omega) = \frac{1}{2\pi} \int_0^{2\pi} d\phi \left\{ \int_0^1 \frac{\kappa^3 d\kappa}{p} \left( 1 + \text{Re} \left\{ r_{ss} e^{2ik_0pd} \right\} \right) + \int_1^{\infty} \frac{\kappa^3 d\kappa}{|p|} e^{-2k_0|p|d} \text{Im} \left\{ r_{ss} \right\} \right\} \quad (\text{E.29d})$$

Plugging Eqs. (E.28) into Eq. (E.17), we find,

$$P_{\text{mag}} = \int_{\infty}^{\infty} d\omega \hbar \omega \Gamma^{\text{H}}(\omega) \quad (\text{E.30})$$

with,

$$\Gamma^{\text{H}}(\omega) = (\omega \rho_0 / 8) \left\{ \left[ g_{\perp,1}^{\text{H}}(\omega) + g_{\perp,2}^{\text{H}}(\omega) + 2g_{g,1}^{\text{H}}(\omega) \right] \left[ \text{Im} \left\{ \alpha_{m,\perp}(\omega^-) \right\} - \text{Re} \left\{ \alpha_{m,g}(\omega^-) \right\} \right] \left[ n_1(\omega^-) - n_0(\omega) \right] \right. \\ \left. + 2g_{\parallel}^{\text{H}}(\omega) \text{Im} \left\{ \alpha_{m,\parallel}(\omega) \right\} \left[ n_1(\omega) - n_0(\omega) \right] \right\} \quad (\text{E.31})$$

For the case when the YIG interface is the  $x - z$  plane instead (Fig. E.1(b)), we find the radiated power by exchanging the axes  $\hat{x} \rightarrow \hat{z}$ ,  $\hat{y} \rightarrow \hat{x}$ , and  $\hat{z} \rightarrow \hat{y}$  in Eq. (E.27). In this case, we have

$$\text{Im} \left\{ G_{xx}^{\text{H}}(\omega) \right\} = \frac{\pi \omega \rho_0}{8} g_{\perp,2}^{\text{H}}(\omega) \quad (\text{E.32a})$$

$$\text{Im} \left\{ G_{yy}^{\text{H}}(\omega) \right\} = \frac{\pi \omega \rho_0}{4} g_{\parallel}^{\text{H}}(\omega) \quad (\text{E.32b})$$

$$\text{Im} \left\{ G_{zz}^{\text{H}}(\omega) \right\} = \frac{\pi \omega \rho_0}{8} g_{\perp,1}^{\text{H}}(\omega) \quad (\text{E.32c})$$

where  $g_{\perp,1}^{\text{H}}$ ,  $g_{\perp,2}^{\text{H}}$ , and  $g_{\parallel}^{\text{H}}$  given by Eq. (E.29). For the  $xy$  and  $yx$  component of the Green's function, however, we get

$$\text{Re} \left\{ G_{xy}^{\text{H}}(\omega) \right\} - \text{Re} \left\{ G_{yx}^{\text{H}}(\omega) \right\} = \frac{\pi \omega \rho_0}{4} g_{g,2}^{\text{H}}(\omega) \quad (\text{E.33})$$

with

$$g_{g,2}^{\text{H}}(\omega) = \frac{1}{\pi} \int_0^{2\pi} d\phi \left\{ \int_0^1 \frac{\kappa^2 d\kappa}{p} \left[ p \sin \phi \text{Im} \left\{ r_{ss} e^{2ik_0pd} \right\} + \frac{\cos \phi}{2} \text{Im} \left\{ (r_{ps} - r_{sp}) e^{2ik_0pd} \right\} \right] \right. \\ \left. + \int_1^{\infty} \frac{\kappa^2 d\kappa}{|p|} \left[ |p| \sin \phi \text{Im} \left\{ r_{ss} \right\} - \frac{\cos \phi}{2} \text{Re} \left\{ r_{sp} - r_{ps} \right\} \right] e^{-2k_0|p|d} \right\} \quad (\text{E.34})$$

and thus we have for the case when the YIG interface is the  $x - z$  plane,

$$\Gamma^{\text{H}}(\omega) = (\omega \rho_0 / 8) \left\{ \left[ g_{\perp,2}^{\text{H}}(\omega) + 2g_{\parallel}^{\text{H}}(\omega) + 2g_{g,2}^{\text{H}}(\omega) \right] \left[ \text{Im} \left\{ \alpha_{m,\perp}(\omega^-) \right\} - \text{Re} \left\{ \alpha_{m,g}(\omega^-) \right\} \right] \left[ n_1(\omega^-) - n_0(\omega) \right] \right. \\ \left. + g_{\perp,1}^{\text{H}}(\omega) \text{Im} \left\{ \alpha_{m,\parallel}(\omega) \right\} \left[ n_1(\omega) - n_0(\omega) \right] \right\} \quad (\text{E.35})$$

with  $g_{\perp,1}^{\text{H}}$ ,  $g_{\perp,2}^{\text{H}}$ , and  $g_{\parallel}^{\text{H}}$  given by Eq. (E.29) and  $g_{g,2}^{\text{H}}$  by Eq. (E.34). This is the same equation as Eq. (6.2).

### E.3 Local Density of States

Although the expressions found in the previous sections for the radiated power are not in general exactly proportional to the local density of states (LDOS), they are proportional to terms that are on the same order of magnitude as the LDOS. This is because the expression for LDOS is given by [168],

$$\rho(\mathbf{r}, \omega) = \frac{1}{\pi\omega} \text{Tr} [\epsilon_0 \text{Im} \{G^{\text{E}}(\mathbf{r}, \mathbf{r}, \omega)\} + \text{Im} \{G^{\text{H}}(\mathbf{r}, \mathbf{r}, \omega)\}] \quad (\text{E.36})$$

where the trace Tr operator indicates summation over the  $xx$ ,  $yy$ , and  $zz$  components of the electric and magnetic Green's functions.

Using the expressions of the previous section, it is easy to see that the LDOS at the location of the nanosphere is given by,

$$\rho(\omega) = (\rho_0/8) \left[ \epsilon_0 (g_{\perp,1}^{\text{E}} + g_{\perp,2}^{\text{E}} + 2g_{\parallel}^{\text{E}}) + g_{\perp,1}^{\text{H}} + g_{\perp,2}^{\text{H}} + 2g_{\parallel}^{\text{H}} \right] \quad (\text{E.37})$$

where the expressions for  $g_{\perp,1}^{\text{H}}$ ,  $g_{\perp,2}^{\text{H}}$ , and  $g_{\parallel}^{\text{H}}$  are given by Eq. (E.29) and the expression for the electric Green's functions are found from the magnetic ones by replacing  $s \rightarrow p$  and  $p \rightarrow s$  and dividing by  $\epsilon_0$ . As discussed before, the magnetic Green's functions are about 8 orders of magnitude larger than the electric ones at GHz frequencies and thus, similar to the radiated power, the density of states is dominated by the magnetic LDOS. This shows that the magnetic fields dominate the vacuum radiation, vacuum torque, and LDOS simultaneously.

### E.4 Magnetic Polarizability Tensor of YIG

A simple model can be used to describe YIG with the permeability tensor [171],

$$\bar{\bar{\mu}} = \begin{pmatrix} \mu_{\perp} & -\mu_g & 0 \\ \mu_g & \mu_{\perp} & 0 \\ 0 & 0 & \mu_{\parallel} \end{pmatrix} \quad (\text{E.38})$$

where

$$\mu_{\perp}(\omega) = \mu_0(1 + \chi_{\perp}) = \mu_0 \left\{ 1 + \frac{\omega_0 \omega_m (\omega_0^2 - \omega^2) + \omega_0 \omega_m \omega^2 \alpha^2 + i \{ \alpha \omega \omega_m [\omega_0^2 + \omega^2 (1 + \alpha^2)] \}}{[\omega_0^2 - \omega^2 (1 + \alpha^2)]^2 + 4\omega_0^2 \omega^2 \alpha^2} \right\} \quad (\text{E.39a})$$

$$\mu_g(\omega) = \mu_0 \chi_g = \mu_0 \frac{-2\omega_0 \omega_m \omega^2 \alpha + i \omega \omega_m [\omega_0^2 - \omega^2 (1 + \alpha^2)]}{[\omega_0^2 - \omega^2 (1 + \alpha^2)]^2 + 4\omega_0^2 \omega^2 \alpha^2} \quad (\text{E.39b})$$

$$\mu_{\parallel} = \mu_0 \quad (\text{E.39c})$$

and  $\omega_0 = \mu_0\gamma H_0$  is the Larmor precession frequency with  $\gamma$  being the gyromagnetic ratio and  $H_0$  the bias magnetic field (assumed to be along  $\hat{z}$  direction),  $\omega_m = \mu_0\gamma M_s$  with  $M_s$  being the saturation magnetization of the material, and  $\alpha$  is the damping factor, related to the width of the magnetic resonance through

$$\Delta H = \frac{2\alpha\omega}{\mu_0\gamma} \quad (\text{E.40})$$

When the magnetic field is reversed (along  $-\hat{z}$  direction), we can use the same results by doing the substitutions

$$\omega_0 \rightarrow -\omega_0, \quad \omega_m \rightarrow -\omega_m, \quad \alpha \rightarrow -\alpha. \quad (\text{E.41})$$

which gives

$$\mu_{\perp} \rightarrow \mu_{\perp}, \quad \mu_g \rightarrow -\mu_g. \quad (\text{E.42})$$

Using the method used in Ref. [176] for the polarizability tensor of a sphere with arbitrary anisotropy, we find for the polarizability tensor of YIG with the permeability tensor of Eq. (E.38),

$$\bar{\alpha}_m = 4\pi a^3 \begin{pmatrix} \frac{(\mu_{\perp} - \mu_0)(\mu_{\perp} + 2\mu_0) + \mu_g^2}{(\mu_{\perp} + 2\mu_0)(\mu_{\perp} + 2\mu_0) + \mu_g^2} & \frac{-3\mu_0\mu_g}{(\mu_{\perp} + 2\mu_0)(\mu_{\perp} + 2\mu_0) + \mu_g^2} & 0 \\ \frac{3\mu_0\mu_g}{(\mu_{\perp} + 2\mu_0)(\mu_{\perp} + 2\mu_0) + \mu_g^2} & \frac{(\mu_{\perp} - \mu_0)(\mu_{\perp} + 2\mu_0) + \mu_g^2}{(\mu_{\perp} + 2\mu_0)(\mu_{\perp} + 2\mu_0) + \mu_g^2} & 0 \\ 0 & 0 & \frac{\mu_{\parallel} - \mu_0}{\mu_z + 2\mu_0} \end{pmatrix}. \quad (\text{E.43})$$

Therefore the magnetic polarizability terms in Eqs. (E.31) and (E.35) are given by,

$$\alpha_{m,\perp}(\omega) = 4\pi a^3 \frac{(\mu_{\perp} - \mu_0)(\mu_{\perp} + 2\mu_0) + \mu_g^2}{(\mu_{\perp} + 2\mu_0)(\mu_{\perp} + 2\mu_0) + \mu_g^2} \quad (\text{E.44a})$$

$$\alpha_{m,g}(\omega) = 4\pi a^3 \frac{3\mu_0\mu_g}{(\mu_{\perp} + 2\mu_0)(\mu_{\perp} + 2\mu_0) + \mu_g^2} \quad (\text{E.44b})$$

where  $\mu_{\perp}$  and  $\mu_g$  are frequency dependent terms give by Eqs. (E.39).

It is important to note that in the derivation of the magnetic polarizability, magneto-static approximation has been assumed. This is similar to the electro-static approximation used for the derivation of the electric polarizability [192] where using the duality of electromagnetic theory the electric fields and electric dipoles have been replaced by the magnetic fields and magnetic dipoles. In this approximation, the fields inside the sphere are assumed to be constant.

One can apply the Mie theory to find the magnetic polarizability to the first order in the Mie scattering components. This, however, is mathematically challenging due to the

anisotropy of the magnetic material. For the purpose of our study, magneto-static assumption is enough to find the polarizability properties of YIG since the size of the sphere is much smaller compared to the wavelength and the polarizability is dominated by the magneto-static term.

For metals, however, higher order terms are important for finding the magnetic polarizability since the magneto-static terms are zero and only higher order terms due to electric dipole fluctuations give rise to the magnetic polarizability of metals [174]. In the next section we briefly introduce the application of Mie theory for finding the polarizability constant of a metallic particle such as aluminum.

## E.5 Non-Electrostatic Limit and Magnetic Polarizability due to Electric Fluctuations

In this section we present a brief derivation of the magnetic polarizability due to the electric dipole terms for metallic particles. If a sphere is placed in the direction of a plane wave polarized along  $\hat{x}$  direction and propagating along  $z$  direction

$$\mathbf{E}_i = E_0 e^{ik_0 r \cos \theta} \hat{x}, \quad (\text{E.45})$$

The scattered fields are give by [192],

$$\mathbf{E}_s = - \sum_{n=1}^{\infty} E_n \left( ia_n \mathbf{N}_{e1n}^{(1)} - b_n \mathbf{M}_{o1n}^{(1)} \right), \quad (\text{E.46})$$

$$\mathbf{H}_s = - \frac{k_0}{\omega \mu} \sum_{n=1}^{\infty} E_n \left( ib_n \mathbf{N}_{o1m}^{(1)} + a_n \mathbf{M}_{e1n}^{(1)} \right) \quad (\text{E.47})$$

where

$$\mathbf{M}_{emn} = \frac{-m}{\sin \theta} \sin m\phi P_n^m(\cos \theta) z_n(kr) \hat{\theta} - \cos m\phi \frac{dP_n^m(\cos \theta)}{d\theta} z_n(kr) \hat{\phi} \quad (\text{E.48a})$$

$$\mathbf{M}_{omn} = \frac{m}{\sin \theta} \cos m\phi P_n^m(\cos \theta) z_n(kr) \hat{\theta} - \sin m\phi \frac{dP_n^m(\cos \theta)}{d\theta} z_n(kr) \hat{\phi} \quad (\text{E.48b})$$

$$\begin{aligned} \mathbf{N}_{emn} = & \frac{z_n(kr)}{kr} \cos m\phi n(n+1) P_n^m(\cos \theta) \hat{r} + \cos m\phi \frac{dP_n^m(\cos \theta)}{d\theta} \frac{1}{kr} \frac{d}{d(kr)} [kr z_n(kr)] \hat{\theta} \\ & - m \sin m\phi \frac{P_n^m(\cos \theta)}{\sin \theta} \frac{1}{kr} \frac{d}{d(kr)} [kr z_n(kr)] \hat{\phi} \end{aligned} \quad (\text{E.48c})$$

$$\begin{aligned} \mathbf{N}_{omn} = & \frac{z_n(kr)}{kr} \sin m\phi n(n+1) P_n^m(\cos \theta) \hat{r} + \sin m\phi \frac{dP_n^m(\cos \theta)}{d\theta} \frac{1}{kr} \frac{d}{d(kr)} [kr z_n(kr)] \hat{\theta} \\ & + m \cos m\phi \frac{P_n^m(\cos \theta)}{\sin \theta} \frac{1}{kr} \frac{d}{d(kr)} [kr z_n(kr)] \hat{\phi}, \end{aligned} \quad (\text{E.48d})$$

the superscripts (1) for  $M$  and  $N$  indicate that the Bessel functions are the hankel function of the first kind  $h^{(1)}(kr)$ ,  $E_n = i^n E_0(2n+1)/n(n+1)$ , and  $a_n$  and  $b_n$  are the Mie scattering coefficients. On the other hand, the radiated fields due to an electric dipole are given by

$$\mathbf{E}_d = \frac{k_0^3}{4\pi\epsilon_m} \left\{ (\hat{\mathbf{r}} \times \mathbf{p}) \times \hat{\mathbf{r}} \frac{e^{ikr}}{kr} + [3\hat{\mathbf{r}}(\hat{\mathbf{r}} \cdot \mathbf{p}) - \mathbf{p}] \left( \frac{1}{(kr)^3} - \frac{i}{(kr)^2} \right) e^{ikr} \right\} \quad (\text{E.49a})$$

$$\mathbf{H}_d = \frac{ck_0^2}{4\pi} (\hat{\mathbf{r}} \times \mathbf{p}) \frac{e^{ikr}}{r} \left( 1 - \frac{1}{ikr} \right) \quad (\text{E.49b})$$

Using the facts that

$$P_1^1(\cos \theta) = -\sin \theta, \quad \frac{dP_1^1(\cos \theta)}{d\theta} = -\cos \theta \quad (\text{E.50})$$

$$h_1^{(1)}(kr) = -e^{ikr} \left( \frac{i}{(kr)^2} + \frac{1}{kr} \right), \quad \frac{1}{kr} \frac{d}{d(kr)} [kr h_1^{(1)}(kr)] = -e^{ikr} \left( -\frac{i}{(kr)^3} - \frac{1}{(kr)^2} + \frac{i}{kr} \right) \quad (\text{E.51})$$

The scattered fields to the first order of  $n$  become

$$\begin{aligned} \mathbf{E}_s = \frac{3}{2} E_0 \left\{ i a_1 \left[ e^{ikr} \left( \frac{1}{(kr)^3} - \frac{i}{(kr)^2} \right) 2 \cos \phi \sin \theta \hat{\mathbf{r}} - (\cos \phi \cos \theta \hat{\theta} - \sin \phi \hat{\phi}) e^{ikr} \left( \frac{1}{(kr)^3} - \frac{i}{(kr)^2} - \frac{1}{kr} \right) \right] \right. \\ \left. - b_1 \left[ (\cos \phi \hat{\theta} - \sin \phi \cos \theta \hat{\phi}) e^{ikr} \left( \frac{-1}{(kr)^2} + \frac{i}{kr} \right) \right] \right\} \quad (\text{E.52}) \end{aligned}$$

Assuming that the dipole is along  $x$  direction  $\mathbf{p} = p_0 \hat{x}$ , the dipole fields become

$$\begin{aligned} \mathbf{E}_d = \frac{p_0 k_0^3}{4\pi\epsilon_m} \left\{ (\cos \theta \cos \phi \hat{\theta} - \sin \phi \hat{\phi}) \frac{e^{ikr}}{kr} + (2\hat{\mathbf{r}} \sin \theta \cos \phi - \hat{\theta} \cos \theta \cos \phi + \hat{\phi} \sin \phi) \left( \frac{1}{(kr)^3} - \frac{i}{(kr)^2} \right) e^{ikr} \right\} \\ = \frac{p_0 k_0^3}{4\pi\epsilon_m} \left\{ 2\hat{\mathbf{r}} \sin \theta \cos \phi \left( \frac{1}{(kr)^3} - \frac{i}{(kr)^2} \right) e^{ikr} - (\hat{\theta} \cos \theta \cos \phi - \hat{\phi} \sin \phi) \left( \frac{1}{(kr)^3} - \frac{i}{(kr)^2} - \frac{1}{kr} \right) e^{ikr} \right\} \quad (\text{E.53}) \end{aligned}$$

In the low-frequency limit when  $kr = \frac{2\pi r}{\lambda} \ll 1$ , the scattered fields are dominated by terms of the order  $(kr)^{-3}$ . Thus, we can neglect the contribution from the  $M$  terms, or the  $b_1$  terms in Eq. (E.52). In this limit, the fields of the dipole and the scattered fields become equivalent, if we take

$$p_0 = \frac{6\pi\epsilon_m i a_1}{k_0^3} E_0, \quad (\text{E.54})$$

or in other words, the sphere takes the polarizability

$$\alpha_e = \frac{6\pi\epsilon_m c^3}{\omega^3} i a_1 \quad (\text{E.55})$$

where

$$a_n = \frac{\epsilon_1 j_n(x_1)[x_0 j_n(x_0)]' - \epsilon_0 j_n(x_0)[x_1 j_n(x_1)]'}{\epsilon_1 j_n(x_1)[x_0 h_n^{(1)}(x_0)]' - \epsilon_0 h_n^{(1)}(x_0)[x_1 j_n(x_1)]'} \quad (\text{E.56})$$

with  $x_0 = k_0 a$ ,  $x_1 = k_1 a$ , and  $k_1 = \omega \sqrt{\mu_1 \epsilon_1}$ , and  $\mu_1$  and  $\epsilon_1$  being properties of the sphere.

Now we look at the scattered magnetic fields. We have to the first order

$$\begin{aligned} \mathbf{H}_s = \frac{3}{2} \frac{k_0}{\omega \mu_0} E_0 \left\{ ib_1 \left[ 2\hat{r} \sin \phi \sin \theta \left( \frac{1}{(kr)^3} - \frac{i}{(kr)^2} \right) e^{ikr} - (\hat{\theta} \sin \phi \cos \theta + \hat{\phi} \cos \phi) \left( \frac{1}{(kr)^3} - \frac{i}{(kr)^2} - \frac{i}{kr} \right) e^{ikr} \right] \right. \\ \left. - a_n \left[ (\hat{\phi} \cos \theta \cos \phi + \hat{\theta} \sin \phi) \left( \frac{i}{(kr)^2} + \frac{1}{kr} \right) e^{ikr} \right] \right\} \end{aligned} \quad (\text{E.57})$$

Again we can ignore the second line or, in other words,  $a_n$  in this expression for low frequencies. Then, comparing this expression with the the magnetic fields of a magnetic dipole polarized along  $\hat{y}$  direction  $\mathbf{m} = m_0 \hat{y}$ ,

$$\mathbf{H}_m = \frac{m_0 k_0^3}{4\pi} \left\{ 2\hat{r} \sin \theta \sin \phi \left( \frac{1}{(kr)^3} - \frac{i}{(kr)^2} \right) e^{ikr} - (\hat{\theta} \cos \theta \sin \phi + \hat{\phi} \cos \phi) \left( \frac{1}{(kr)^3} - \frac{i}{(kr)^2} - \frac{1}{kr} \right) e^{ikr} \right\}, \quad (\text{E.58})$$

Taking  $H_0 = \frac{k_0}{\omega \mu_0} E_0$ , we find that the two are equivalent if we have

$$m_0 = \frac{6\pi i b_1}{k_0^3} H_0 \quad (\text{E.59})$$

or, if the sphere takes the magnetic polarizability

$$\alpha_m = \frac{6\pi c^3}{\omega^3} i b_1 \quad (\text{E.60})$$

where

$$b_n = \frac{\mu_1 j_n(x_1)[x_0 j_n(x_0)]' - \mu_0 j_n(x_0)[x_1 j_n(x_1)]'}{\mu_1 j_n(x_1)[x_0 h_n^{(1)}(x_0)]' - \mu_0 h_n^{(1)}(x_0)[x_1 j_n(x_1)]'} \quad (\text{E.61})$$

In the low-frequency limit, we have

$$\lim_{x \rightarrow 0} j_n(x) = \frac{2^n n!}{(2n+1)!} x^n \quad (\text{E.62})$$

and

$$\lim_{x \rightarrow 0} y_n(x) = -\frac{(2n)!}{2^n n!} \frac{1}{x^{n+1}} \quad (\text{E.63})$$

Therefore, we have in this limit  $j_1(x) \simeq x/3$ ,  $y_1(x) \simeq -1/x^2$ ,  $[x j_1(x)]' \simeq 2x/3$  and  $[x y_1(x)]' \simeq 1/x^2$  which gives

$$a_1 \simeq \frac{\epsilon_1 \frac{x_1}{3} \frac{2x_0}{3} - \epsilon_0 \frac{x_0}{3} \frac{2x_1}{3}}{\epsilon_1 \frac{x_1}{3} \left( \frac{2x_0}{3} + \frac{i}{x_0^2} \right) - \epsilon_0 \frac{2x_1}{3} \left( \frac{x_0}{3} - \frac{i}{x_0^2} \right)} \simeq \frac{2k_0^3 a^3}{3i} \frac{\epsilon_1 - \epsilon_0}{\epsilon_1 + 2\epsilon_0} \quad (\text{E.64a})$$

$$b_1 \simeq \frac{2k_0^3 a^3}{3i} \frac{\mu_1 - \mu_0}{\mu_1 + 2\mu_0}. \quad (\text{E.64b})$$

We thus get for the polarizabilities

$$\alpha_e \simeq 4\pi\epsilon_0 a^3 \frac{\epsilon_1 - \epsilon_0}{\epsilon_1 + 2\epsilon_0}, \quad \alpha_m \simeq 4\pi a^3 \frac{\mu_1 - \mu_0}{\mu_1 + 2\mu_0}, \quad (\text{E.65})$$

which are exactly equal to the results derived using the electro-static and magneto-static approximations method. For a non-magnetic material,  $b_1$  becomes

$$b_1 \simeq \frac{x_0^3}{45i} x_0^2 \left( \frac{\epsilon_1}{\epsilon_0} - 1 \right) \quad (\text{E.66})$$

which gives for the magnetic polarizability,

$$\alpha_m \simeq \frac{2\pi}{15} k_0^2 a^5 \left( \frac{\epsilon_1}{\epsilon_0} - 1 \right) = \frac{8\pi^3}{15} a^3 \left( \frac{a}{\lambda} \right)^2 \left( \frac{\epsilon_1}{\epsilon_0} - 1 \right). \quad (\text{E.67})$$

## E.6 Barnett Effect

In the simplest models of magnetic materials, electrons are assumed to be magnetic dipoles with the moments  $\mu_B$  spinning about the magnetization axis determined by the applied magnetic field  $H_0$  with the Larmor precession frequency  $\omega_0 = \mu_0 \gamma H_0$ , where  $\gamma$  is the gyromagnetic ratio of the material [171]. Barnett showed that the spontaneous magnetization of a material with the magnetic susceptibility of  $\chi$  is given by [177]

$$\mathbf{M}_{\text{rot}} = \chi \Omega / \gamma \quad (\text{E.68})$$

where  $\Omega$  is the rotation frequency of the magnetic material. This magnetization can be assumed to be caused by an applied magnetic field  $H_{\text{rot}}$  which is  $H_{\text{rot}} = \mathbf{M}_{\text{rot}} / \chi = \frac{\Omega}{\gamma \mu_0}$ . We thus get for the Larmor frequency due to rotation,

$$\omega_{0,\text{rot}} = \Omega \quad (\text{E.69})$$

Therefore, Larmor frequency of a spinning magnetic material is the same as the rotation frequency. We thus can write the total Larmor frequency of spinning YIG as

$$\omega_0 = \Omega + \mu_0 \gamma H_0 \quad (\text{E.70})$$

We use this expression in finding the permeability tensor of a spinning YIG.

## E.7 Non-local Model for Aluminum

Due to the fact that the sphere is spinning at a distance much smaller than the free space wavelength, the non-local effects can become important. To find the non-local Fresnel

reflection coefficients we use the results of Refs. [193] and [23]. In the semi-classical infinite barrier (SCIB) approximation, in which it is assumed that free electrons are reflected at the metal surface and Fermi-Dirac statistics are used, we get for the Fresnel reflection coefficients,

$$r_{12}^s = \frac{Z^s - \frac{4\pi}{cp}}{Z^s + \frac{4\pi}{cp}}, \quad r_{12}^p = \frac{4\pi p/c - Z^p}{4\pi p/c + Z^p} \quad (\text{E.71})$$

where  $p = \sqrt{1 - \kappa^2}$ , and

$$Z^s = \frac{8i}{c} \int_0^\infty dq \frac{1}{\epsilon_t(k, \omega) - (q^2 + \kappa^2)} \quad (\text{E.72a})$$

$$Z^p = \frac{8i}{c} \int_0^\infty dq \frac{1}{q^2 + \kappa^2} \left( \frac{q^2}{\epsilon_t(k, \omega) - (q^2 + \kappa^2)} + \frac{\kappa^2}{\epsilon_l(k, \omega)} \right) \quad (\text{E.72b})$$

with the longitudinal and transverse dielectric permittivities given by

$$\epsilon_l(k, \omega) = 1 + \frac{3\omega_p^2}{k^2 v_F^2} \frac{(\omega + i\Gamma) f_l(u)}{\omega + i\Gamma f_l(u)} \quad (\text{E.73a})$$

$$\epsilon_t(k, \omega) = 1 - \frac{\omega_p^2}{\omega(\omega + i\Gamma)} f_t(u) \quad (\text{E.73b})$$

where  $k^2 = (\omega/c)^2 (q^2 + \kappa^2)$ ,  $u = (\omega + i\Gamma)/(k v_F)$ , and

$$f_l(u) = 1 - \frac{1}{2} u \ln \frac{u+1}{u-1}, \quad f_t(u) = \frac{3}{2} u^2 - \frac{3}{2} u(u^2 - 1) \ln \frac{u+1}{u-1} \quad (\text{E.74})$$

These expressions give the non-local reflection coefficients at a metallic interface for the SCIB model. Note that  $r_{12}^s$  and  $r_{12}^p$  are the same as the  $r_{ss}$  and  $r_{pp}$  introduced in the previous section. The SCIB model is accurate as long as  $z = \frac{k}{2k_F} \sim 0$  where  $k_F = m v_F / \hbar$  with  $m$  being the free-electron mass. For example for Aluminum with  $v_F \simeq 2.03 \times 10^6$  m/s, we have  $k_F \simeq 1.754 \times 10^{10}$  while  $k = \omega/c \simeq 20$  which shows that for our case the SCIB model is quite accurate.

## E.8 Quantum Vacuum Torque

In this section we evaluate the torque exerted on the spinning sphere due to vacuum fluctuations. The torque on a magnetic dipole is given by

$$\mathbf{M} = \mathbf{m} \times \mathbf{H} \quad (\text{E.75})$$

Since we are interested in the torque along  $z$  direction, the rotation axis, we can write the torque as

$$\begin{aligned} M_z &= \hat{z} \cdot \langle \mathbf{m}^{\text{fl}} \times \mathbf{H}^{\text{ind}} + \mathbf{m}^{\text{ind}} \times \mathbf{H}^{\text{fl}} \rangle \\ &= \langle m_x^{\text{fl}} H_y^{\text{ind}} - m_y^{\text{fl}} H_x^{\text{ind}} + m_x^{\text{ind}} H_y^{\text{fl}} - m_y^{\text{ind}} H_x^{\text{fl}} \rangle \end{aligned} \quad (\text{E.76})$$

we get using the Fourier transformation,

$$M_z = \int \frac{d\omega d\omega'}{(2\pi)^2} e^{-i(\omega+\omega')t} \left[ \langle m_x^{\text{fl}}(\omega) H_y^{\text{ind}}(\omega') \rangle - \langle m_y^{\text{fl}}(\omega) H_x^{\text{ind}}(\omega') \rangle + \langle m_x^{\text{ind}}(\omega) H_y^{\text{fl}}(\omega') \rangle - \langle m_y^{\text{ind}}(\omega) H_x^{\text{fl}}(\omega') \rangle \right] \quad (\text{E.77})$$

Using a similar approach to the one used in Section E.1, we find after some algebra,

$$M_z = \frac{\hbar}{2\pi} \int_{-\infty}^{\infty} d\omega \left\{ \left( \text{Im} \{ G_{yy}^{\text{H}}(\omega) \} + \text{Im} \{ G_{xx}^{\text{H}}(\omega) \} + \text{Re} \{ G_{yx}^{\text{H}}(\omega) \} - \text{Re} \{ G_{xy}^{\text{H}}(\omega) \} \right) \times \right. \\ \left. \left[ \text{Im} \{ \alpha_{m,\perp}(\omega^+) \} + \text{Re} \{ \alpha_{m,g}(\omega^+) \} \right] [n_1(\omega^+) - n_0(\omega)] \right. \\ \left. - \left( \text{Im} \{ G_{yy}^{\text{H}}(\omega) \} + \text{Im} \{ G_{xx}^{\text{H}}(\omega) \} - \text{Re} \{ G_{yx}^{\text{H}}(\omega) \} + \text{Re} \{ G_{xy}^{\text{H}}(\omega) \} \right) \times \right. \\ \left. \left[ \text{Im} \{ \alpha_{m,\perp}(\omega^-) \} - \text{Re} \{ \alpha_{m,g}(\omega^-) \} \right] [n_1(\omega^-) - n_0(\omega)] \right\}, \quad (\text{E.78})$$

and can be written as

$$M_z = - \int_{-\infty}^{+\infty} d\omega \hbar \Gamma_M^{\text{H}}(\omega) \quad (\text{E.79})$$

where for an interface in the  $x - y$  plane  $\Gamma_M^{\text{H}}$  is given by

$$\Gamma_M^{\text{H}}(\omega) = (\omega \rho_0 / 8) [g_{\perp,1}^{\text{H}}(\omega) + g_{\perp,2}^{\text{H}}(\omega) + 2g_{g,1}^{\text{H}}(\omega)] [\text{Im} \{ \alpha_{m,\perp}(\omega^-) \} - \text{Re} \{ \alpha_{m,g}(\omega^-) \}] [n_1(\omega^-) - n_0(\omega)] \quad (\text{E.80})$$

which is the same expression for the radiated power minus the term related to the axis of rotation  $z$ . For an interface in the  $x - z$  plane, on the other hand,  $\Gamma_M^{\text{H}}$  we have

$$\Gamma_M^{\text{H}}(\omega) = (\omega \rho_0 / 8) [g_{\perp,2}^{\text{H}}(\omega) + 2g_{\parallel}^{\text{H}}(\omega) + 2g_{g,2}^{\text{H}}(\omega)] [\text{Im} \{ \alpha_{m,\perp}(\omega^-) \} - \text{Re} \{ \alpha_{m,g}(\omega^-) \}] [n_1(\omega^-) - n_0(\omega)]. \quad (\text{E.81})$$

This expression is the same as Eq. (6.2) with the difference that it does not have the last term involving the term  $n_1(\omega) - n_0(\omega)$ . Note that comparing to the expression for the vacuum radiation, vacuum torque has an extra minus sign in Eq. (E.79) indicating that this torque acts as friction rather than a driving force, as expected.

### E.8.1 Other components of torque

In the previous section we only derived the  $z$  components of the torque exerted on the nanosphere. The  $x$  and  $y$  components can be written as

$$M_x = \langle m_y^{\text{fl}} H_z^{\text{ind}} - m_z^{\text{fl}} H_y^{\text{ind}} + m_y^{\text{ind}} H_z^{\text{fl}} - m_z^{\text{ind}} H_y^{\text{fl}} \rangle \quad (\text{E.82a})$$

$$M_y = \langle m_z^{\text{fl}} H_x^{\text{ind}} - m_x^{\text{fl}} H_z^{\text{ind}} + m_z^{\text{ind}} H_x^{\text{fl}} - m_x^{\text{ind}} H_z^{\text{fl}} \rangle \quad (\text{E.82b})$$

Again, using the approaches used in the previous section and section E.1, incorporating the torque due to the electric field fluctuations of vacuum and the magnetic dipole fluctuations of the YIG sphere, we find for the  $x$  component of torque,

$$\begin{aligned}
M_x = & \frac{\hbar}{4\pi} \int_{-\infty}^{\infty} d\omega \left\{ [2n_1(\omega^-) + 1] [\text{Im}\{\alpha_{m,\perp}(\omega^-)\} - \text{Re}\{\alpha_{m,g}(\omega^-)\}] [2\text{Im}\{G_{zx}^H(\omega)\} + 2\text{Re}\{G_{zy}^H(\omega)\}] \right. \\
& - 4[n_1(\omega) + 1] \text{Im}\{\alpha_{m,\parallel}(\omega)\} \text{Re}\{G_{yz}^H(\omega)\} \\
& + [2n_0(\omega) + 1] \left\{ [\text{Re}\{\alpha_{m,\perp}(\omega^-)\} + \text{Im}\{\alpha_{m,g}(\omega^-)\}] (\text{Re}\{G_{xz}^H(\omega)\} - \text{Re}\{G_{zx}^H(\omega)\} + \text{Im}\{G_{yz}^H(\omega)\} + \text{Im}\{G_{zy}^H(\omega)\}) \right. \\
& \left. + [\text{Im}\{\alpha_{m,\perp}(\omega^-)\} - \text{Re}\{\alpha_{m,g}(\omega^-)\}] (-\text{Im}\{G_{xz}^H(\omega)\} - \text{Im}\{G_{zx}^H(\omega)\} + \text{Re}\{G_{yz}^H(\omega)\} - \text{Re}\{G_{zy}^H(\omega)\}) \right\} \\
& \left. + [n_0(\omega) + 1] \left\{ -2\text{Re}\{\alpha_{m,\parallel}(\omega)\} (\text{Im}\{G_{zy}^H(\omega)\} + \text{Im}\{G_{yz}^H(\omega)\}) + 2\text{Im}\{\alpha_{m,\parallel}(\omega)\} (-\text{Re}\{G_{yz}^H(\omega)\} + \text{Re}\{G_{zy}^H(\omega)\}) \right\} \right\} \quad (\text{E.83})
\end{aligned}$$

and for the  $y$  component,

$$\begin{aligned}
M_y = & \frac{\hbar}{4\pi} \int_{-\infty}^{\infty} d\omega \left\{ [2n_1(\omega^-) + 1] [\text{Im}\{\alpha_{m,\perp}(\omega^-)\} - \text{Re}\{\alpha_{m,g}(\omega^-)\}] [-2\text{Re}\{G_{zx}^H(\omega)\} + 2\text{Im}\{G_{zy}^H(\omega)\}] \right. \\
& \left. + 4[n_1(\omega) + 1] \text{Im}\{\alpha_{m,\parallel}(\omega)\} \text{Re}\{G_{xz}^H(\omega)\} \right\} \\
& - [2n_0(\omega) + 1] \left\{ [\text{Re}\{\alpha_{m,\perp}(\omega^-)\} + \text{Im}\{\alpha_{m,g}(\omega^-)\}] (\text{Im}\{G_{xz}^H(\omega)\} + \text{Im}\{G_{zx}^H(\omega)\} - \text{Re}\{G_{yz}^H(\omega)\} + \text{Re}\{G_{zy}^H(\omega)\}) \right. \\
& \left. + [\text{Im}\{\alpha_{m,\perp}(\omega^-)\} - \text{Re}\{\alpha_{m,g}(\omega^-)\}] (\text{Re}\{G_{xz}^H(\omega)\} - \text{Re}\{G_{zx}^H(\omega)\} + \text{Im}\{G_{yz}^H(\omega)\} + \text{Im}\{G_{zy}^H(\omega)\}) \right\} \\
& - [n_0(\omega) + 1] \left\{ -2\text{Re}\alpha_{m,\parallel}(\omega) (\text{Im}\{G_{zx}^H(\omega)\} + \text{Im}\{G_{xz}^H(\omega)\}) + 2\text{Im}\alpha_{m,\parallel}(\omega) (-\text{Re}\{G_{zx}^H(\omega)\} + \text{Re}\{G_{xz}^H(\omega)\}) \right\} \quad (\text{E.84})
\end{aligned}$$

In the case when the interface is in the  $x - y$  plane, we have

$$\begin{aligned}
\text{Re}\{G_{xz}^H(\omega)\} = & (\pi\omega\rho_0/8) \frac{1}{\pi} \int_0^{2\pi} d\phi \left\{ \int_0^1 \frac{\kappa^2 d\kappa}{p} \left( \text{Im}\{r_{ss}e^{2ik_0pd}\} p \cos\phi - \text{Im}\{r_{ps}e^{2ik_0pd}\} \sin\phi \right) \right. \\
& \left. + \int_1^\infty \frac{\kappa^2 d\kappa}{|p|} e^{-2k_0|p|d} \left( \text{Im}\{r_{ss}\} |p| \cos\phi + \text{Re}\{r_{ps}\} \sin\phi \right) \right\} \quad (\text{E.85a})
\end{aligned}$$

$$\begin{aligned}
\text{Re}\{G_{zx}^H(\omega)\} = & (\pi\omega\rho_0/8) \frac{1}{\pi} \int_0^{2\pi} d\phi \left\{ \int_0^1 \frac{\kappa^2 d\kappa}{p} \left( -\text{Im}\{r_{ss}e^{2ik_0pd}\} p \cos\phi - \text{Im}\{r_{sp}e^{2ik_0pd}\} \sin\phi \right) \right. \\
& \left. + \int_1^\infty \frac{\kappa^2 d\kappa}{|p|} e^{-2k_0|p|d} \left( -\text{Im}\{r_{ss}\} |p| \cos\phi + \text{Re}\{r_{sp}\} \sin\phi \right) \right\} \quad (\text{E.85b})
\end{aligned}$$

$$\begin{aligned}
\text{Im}\{G_{xz}^H(\omega)\} = & (\pi\omega\rho_0/8) \frac{1}{\pi} \int_0^{2\pi} d\phi \left\{ \int_0^1 \frac{\kappa^2 d\kappa}{p} \left( -\text{Re}\{r_{ss}e^{2ik_0pd}\} p \cos\phi + \text{Re}\{r_{ps}e^{2ik_0pd}\} \sin\phi \right) \right. \\
& \left. + \int_1^\infty \frac{\kappa^2 d\kappa}{|p|} e^{-2k_0|p|d} \left( -\text{Re}\{r_{ss}\} |p| \cos\phi + \text{Im}\{r_{ps}\} \sin\phi \right) \right\} \quad (\text{E.85c})
\end{aligned}$$

$$\begin{aligned} \text{Im} \{G_{zx}^H(\omega)\} &= (\pi\omega\rho_0/8) \frac{1}{\pi} \int_0^{2\pi} d\phi \left\{ \int_0^1 \frac{\kappa^2 d\kappa}{p} \left( \text{Re} \{r_{ss} e^{2ik_0pd}\} p \cos \phi + \text{Re} \{r_{sp} e^{2ik_0pd}\} \sin \phi \right) \right. \\ &\quad \left. + \int_1^\infty \frac{\kappa^2 d\kappa}{|p|} e^{-2k_0|p|d} \left( \text{Re} \{r_{ss}\} |p| \cos \phi + \text{Im} \{r_{sp}\} \sin \phi \right) \right\} \end{aligned} \quad (\text{E.85d})$$

and

$$\begin{aligned} \text{Re} \{G_{zy}^H(\omega)\} &= (\pi\omega\rho_0/8) \frac{1}{\pi} \int_0^{2\pi} d\phi \left\{ \int_0^1 \frac{\kappa^2 d\kappa}{p} \left( -\text{Im} \{r_{ss} e^{2ik_0pd}\} p \sin \phi + \text{Im} \{r_{sp} e^{2ik_0pd}\} \cos \phi \right) \right. \\ &\quad \left. + \int_1^\infty \frac{\kappa^2 d\kappa}{|p|} e^{-2k_0|p|d} \left( -\text{Im} \{r_{ss}\} |p| \sin \phi - \text{Re} \{r_{sp}\} \cos \phi \right) \right\} \end{aligned} \quad (\text{E.86a})$$

$$\begin{aligned} \text{Re} \{G_{yz}^H(\omega)\} &= (\pi\omega\rho_0/8) \frac{1}{\pi} \int_0^{2\pi} d\phi \left\{ \int_0^1 \frac{\kappa^2 d\kappa}{p} \left( \text{Im} \{r_{ss} e^{2ik_0pd}\} p \sin \phi + \text{Im} \{r_{ps} e^{2ik_0pd}\} \cos \phi \right) \right. \\ &\quad \left. + \int_1^\infty \frac{\kappa^2 d\kappa}{|p|} e^{-2k_0|p|d} \left( \text{Im} \{r_{ss}\} |p| \sin \phi - \text{Re} \{r_{ps}\} \cos \phi \right) \right\} \end{aligned} \quad (\text{E.86b})$$

$$\begin{aligned} \text{Im} \{G_{zy}^H(\omega)\} &= (\pi\omega\rho_0/8) \frac{1}{\pi} \int_0^{2\pi} d\phi \left\{ \int_0^1 \frac{\kappa^2 d\kappa}{p} \left( \text{Re} \{r_{ss} e^{2ik_0pd}\} p \sin \phi - \text{Re} \{r_{sp} e^{2ik_0pd}\} \cos \phi \right) \right. \\ &\quad \left. + \int_1^\infty \frac{\kappa^2 d\kappa}{|p|} e^{-2k_0|p|d} \left( \text{Re} \{r_{ss}\} |p| \sin \phi - \text{Im} \{r_{sp}\} \cos \phi \right) \right\} \end{aligned} \quad (\text{E.86c})$$

$$\begin{aligned} \text{Im} \{G_{yz}^H(\omega)\} &= (\pi\omega\rho_0/8) \frac{1}{\pi} \int_0^{2\pi} d\phi \left\{ \int_0^1 \frac{\kappa^2 d\kappa}{p} \left( -\text{Re} \{r_{ss} e^{2ik_0pd}\} p \sin \phi - \text{Re} \{r_{ps} e^{2ik_0pd}\} \cos \phi \right) \right. \\ &\quad \left. + \int_1^\infty \frac{\kappa^2 d\kappa}{|p|} e^{-2k_0|p|d} \left( -\text{Re} \{r_{ss}\} |p| \sin \phi - \text{Im} \{r_{ps}\} \cos \phi \right) \right\} \end{aligned} \quad (\text{E.86d})$$

And for the case when it is in the  $x - z$  plane

$$\begin{aligned} \text{Re} \{G_{xz}^H(\omega)\} &= (\pi\omega\rho_0/8) \frac{1}{\pi} \int_0^{2\pi} d\phi \left\{ \int_0^1 \frac{\kappa d\kappa}{2p} \left[ \sin 2\phi \text{Im} \{r_{pp} e^{2ik_0pd}\} + p^2 \sin 2\phi \text{Im} \{r_{ss} e^{2ik_0pd}\} \right. \right. \\ &\quad \left. \left. + 2p \text{Im} \{r_{ps} e^{2ik_0pd}\} \cos^2 \phi + 2p \text{Im} \{r_{sp} e^{2ik_0pd}\} \sin^2 \phi \right] \right. \\ &\quad \left. + \int_1^\infty \frac{\kappa d\kappa}{2|p|} \left[ -\sin 2\phi \left( 1 + \text{Re} \{r_{pp}\} e^{-2k_0|p|d} \right) - p^2 \sin 2\phi \text{Re} \{r_{ss}\} e^{-2k_0|p|d} \right. \right. \\ &\quad \left. \left. + 2 \text{Im} \{r_{ps}\} |p| e^{-2k_0|p|d} \cos^2 \phi + 2 \text{Im} \{r_{sp} e^{-2k_0|p|d}\} \sin^2 \phi \right] \right\} \end{aligned} \quad (\text{E.87a})$$

$$\begin{aligned}
\text{Re} \{G_{zx}^H(\omega)\} &= (\pi\omega\rho_0/8) \frac{1}{\pi} \int_0^{2\pi} d\phi \left\{ \int_0^1 \frac{\kappa d\kappa}{2p} \left[ \sin 2\phi \text{Im} \{r_{pp} e^{2ik_0pd}\} + p^2 \sin 2\phi \text{Im} \{r_{ss} e^{2ik_0pd}\} \right. \right. \\
&\quad \left. \left. - 2p \text{Im} \{r_{ps} e^{2ik_0pd}\} \sin^2 \phi - 2p \text{Im} \{r_{sp} e^{2ik_0pd}\} \cos^2 \phi \right] \right. \\
&\quad \left. + \int_1^\infty \frac{\kappa d\kappa}{2|p|} \left[ -\sin 2\phi \left(1 + \text{Re} \{r_{pp}\} e^{-2k_0|p|d}\right) - p^2 \sin 2\phi \text{Re} \{r_{ss}\} e^{-2k_0|p|d} \right. \right. \\
&\quad \left. \left. - 2 \text{Im} \{r_{ps}\} |p| e^{-2k_0|p|d} \sin^2 \phi - 2 \text{Im} \{r_{sp}\} |p| e^{-2k_0|p|d} \cos^2 \phi \right] \right\} \\
&\hspace{15em} \text{(E.87b)}
\end{aligned}$$

$$\begin{aligned}
\text{Im} \{G_{xz}^H(\omega)\} &= (\pi\omega\rho_0/8) \frac{1}{\pi} \int_0^{2\pi} d\phi \left\{ \int_0^1 \frac{\kappa d\kappa}{2p} \left[ -\sin 2\phi \left(1 + \text{Re} \{r_{pp} e^{2ik_0pd}\}\right) - p^2 \sin 2\phi \text{Re} \{r_{ss} e^{2ik_0pd}\} \right. \right. \\
&\quad \left. \left. - 2p \text{Re} \{r_{ps} e^{2ik_0pd}\} \cos^2 \phi - 2p \text{Re} \{r_{sp} e^{2ik_0pd}\} \sin^2 \phi \right] \right. \\
&\quad \left. + \int_1^\infty \frac{\kappa d\kappa}{2|p|} e^{-2k_0|p|d} \left[ -\sin 2\phi \text{Im} \{r_{pp}\} - p^2 \sin 2\phi \text{Im} \{r_{ss}\} \right. \right. \\
&\quad \left. \left. - 2 \text{Re} \{r_{ps}\} |p| \cos^2 \phi - 2 \text{Re} \{r_{sp}\} |p| \sin^2 \phi \right] \right\} \\
&\hspace{15em} \text{(E.87c)}
\end{aligned}$$

$$\begin{aligned}
\text{Im} \{G_{zx}^H(\omega)\} &= (\pi\omega\rho_0/8) \frac{1}{\pi} \int_0^{2\pi} d\phi \left\{ \int_0^1 \frac{\kappa d\kappa}{2p} \left[ -\sin 2\phi \left(1 + \text{Re} \{r_{pp} e^{2ik_0pd}\}\right) - p^2 \sin 2\phi \text{Re} \{r_{ss} e^{2ik_0pd}\} \right. \right. \\
&\quad \left. \left. + 2p \text{Re} \{r_{ps} e^{2ik_0pd}\} \sin^2 \phi + 2p \text{Re} \{r_{sp} e^{2ik_0pd}\} \cos^2 \phi \right] \right. \\
&\quad \left. + \int_1^\infty \frac{\kappa d\kappa}{2|p|} e^{-2k_0|p|d} \left[ -\sin 2\phi \text{Im} \{r_{pp}\} - p^2 \sin 2\phi \text{Im} \{r_{ss}\} \right. \right. \\
&\quad \left. \left. + 2 \text{Re} \{r_{ps}\} |p| \sin^2 \phi + 2 \text{Re} \{r_{sp}\} |p| \cos^2 \phi \right] \right\} \\
&\hspace{15em} \text{(E.87d)}
\end{aligned}$$

and the expressions for the real and imaginary parts of  $G_{zy}^H$  and  $G_{yz}^H$  are the same as the ones for  $G_{xz}^H$  and  $G_{zx}^H$ , respectively, for when the interface is in the  $x - y$  plane as given in Eq. (E.85). We can find the  $x$  and  $y$  components of torque by plugging these expressions into Eqs. (E.83) and (E.84) for the two cases when the interface is the  $x - y$  or  $x - z$  plane. We present the plots of these torques at the end of this section.

## E.8.2 Recoil torque

There is also another contribution to the torque from the case when the induced dipole moments on the YIG sphere, due to the vacuum electric field fluctuations, re-radiate. This causes a recoil torque on the sphere and can be written as

$$\mathbf{M}^{\text{rec}} = \langle \mathbf{m}^{\text{ind}} \times \mathbf{H}^{\text{sc}} \rangle \tag{E.88}$$

where  $\mathbf{H}^{\text{sc}}$  is the scattered fields from the dipole and are give by,

$$\mathbf{H}^{\text{sc}}(\mathbf{r}, \omega) = \bar{\mathbf{G}}^H(\mathbf{r}, \mathbf{r}', \omega) \cdot \mathbf{m}^{\text{ind}}(\mathbf{r}', \omega) \tag{E.89}$$

which shows that this term is of higher order contribution and is thus smaller compared to the torque derived in Eq. (E.79). Repeating a similar procedure used before and plugging in for all of the induced terms and writing them in terms of the fluctuations, we find after some algebra,

$$\begin{aligned}
M_z^{\text{rec}} = \frac{\hbar}{\pi} \int_{-\infty}^{\infty} d\omega [n_0(\omega) + 1] & \left\{ \text{Im}\{G_{xx}\} \left[ \text{Re}\{G_{yx}\} \alpha_{\perp\perp}^{\text{eff}} - \text{Re}\{G_{xy}\} \alpha_{gg}^{\text{eff}} + \text{Re}\{\alpha_{\perp g}\} \text{Re}\{G_{yy} - G_{xx}\} + \text{Im}\{\alpha_{\perp g}\} \text{Im}\{G_{yy} + G_{xx}\} \right] \right. \\
& + \text{Im}\{G_{yy}\} \left[ \text{Re}\{G_{yx}\} \alpha_{gg}^{\text{eff}} - \text{Re}\{G_{xy}\} \alpha_{\perp\perp}^{\text{eff}} + \text{Re}\{\alpha_{\perp g}\} \text{Re}\{G_{xx} - G_{yy}\} + \text{Im}\{\alpha_{\perp g}\} \text{Im}\{G_{yy} + G_{xx}\} \right] \\
& + \text{Re}\{G_{yx} - G_{xy}\} \left[ \text{Re}\{G_{yx} - G_{xy}\} \text{Im}\{\alpha_{\perp g}\} + \frac{1}{2} \text{Im}\{G_{yy} + G_{xx}\} (\alpha_{\perp\perp} + \alpha_{gg}) \right] \\
& + \text{Im}\{G_{yx} + G_{xy}\} \left[ -\text{Re}\{G_{yx} + G_{xy}\} \text{Re}\{\alpha_{\perp g}\} + \frac{1}{2} \text{Re}\{G_{xx} - G_{yy}\} (\alpha_{gg} - \alpha_{\perp\perp}) \right] \\
& \left. + \frac{1}{2} \text{Im}\{\alpha_{m,\parallel}^{\text{eff}*}\} \left[ (G_{xz} - G_{zx}^*) (G_{yz}^* \alpha_{m,\perp}^{\text{eff}} - G_{xz}^* \alpha_{m,g}^{\text{eff}}) - (G_{yz} - G_{zy}^*) (G_{yz}^* \alpha_{m,g}^{\text{eff}} + G_{xz}^* \alpha_{m,\perp}^{\text{eff}}) \right] \right\} \quad (\text{E.90})
\end{aligned}$$

where we have defined

$$\begin{aligned}
\alpha_{m,\perp\perp}^{\text{eff}}(\omega) &= \alpha_{m,\perp}^{\text{eff}}(\omega) \alpha_{m,\perp}^{\text{eff}}(-\omega) & \alpha_{m,gg}^{\text{eff}}(\omega) &= \alpha_{m,g}^{\text{eff}}(\omega) \alpha_{m,g}^{\text{eff}}(-\omega) \\
\alpha_{m,\perp g}^{\text{eff}}(\omega) &= \alpha_{m,\perp}^{\text{eff}}(\omega) \alpha_{m,g}^{\text{eff}}(-\omega) & \alpha_{m,g\perp}^{\text{eff}}(\omega) &= \alpha_{m,\perp}^{\text{eff}}(-\omega) \alpha_{m,g}^{\text{eff}}(\omega)
\end{aligned} \quad (\text{E.91})$$

and have used the facts that  $\alpha_{m,\perp\perp}^{\text{eff}}(\omega)$  and  $\alpha_{m,gg}^{\text{eff}}(\omega)$  are real, and  $\alpha_{m,\perp g}^{\text{eff}}(\omega) = \left[ \alpha_{m,g\perp}^{\text{eff}}(\omega) \right]^*$ .

Note that we have dropped the frequency dependence as well as the H superscript of the Green's function in Eq. (E.90) for simplicity. For the special case when the substrate material is isotropic, the non-diagonal elements of the Green's function become zero and we get

$$M_z^{\text{rec}} = \frac{\hbar}{\pi} \int_{-\infty}^{\infty} d\omega [n_0(\omega) + 1] \left\{ \text{Im}\{G_{xx} - G_{yy}\} \text{Re}\{G_{yy} - G_{xx}\} \text{Re}\{\alpha_{\perp g}\} + [\text{Im}\{G_{xx} + G_{yy}\}]^2 \text{Im}\{\alpha_{\perp g}\} \right\} \quad (\text{E.92})$$

Note that the expressions for the real and imaginary parts of  $G_{xz}$  and  $G_{yz}$  are given by Eqs. (E.85), (E.86), and (E.87) for the two possible interface directions while the imaginary parts of  $G_{xx}$  and  $G_{yy}$  are given by Eqs. (E.28a), (E.28b), (E.32a), and (E.32b). Also note that  $\text{Re}\{G_{yx}^{\text{H}}\}$  for when the interface is the  $x - y$  plane is the same as  $\text{Re}\{G_{xz}^{\text{H}}\}$  for when the interface is in the  $x - z$  plane given by Eq. (E.87). Also  $\text{Re}\{G_{yx}^{\text{H}}\}$  for when the interface is the  $x - z$  plane is the same as  $\text{Re}\{G_{zy}^{\text{H}}\}$  for when the interface is in the  $x - y$  plane given by Eq. (E.86). Thus, the only new term is  $\text{Re}\{G_{yy} - G_{xx}\}$  which is given by

$$\begin{aligned}
\text{Re}\{G_{yy}^{\text{H}}(\omega) - G_{xx}^{\text{H}}(\omega)\} &= (\pi\omega\rho_0/8) \frac{1}{\pi} \int_0^{2\pi} d\phi \left\{ \int_0^1 \frac{\kappa d\kappa}{p} \left[ -\cos 2\phi \text{Im}\{r_{pp} e^{2ik_0pd}\} - \cos 2\phi \text{Im}\{r_{ss} e^{2ik_0pd}\} \right] \right. \\
& + 2p \sin \phi \cos \phi \text{Im}\{(r_{ps} - r_{sp}) e^{2ik_0pd}\} \\
& + \int_1^\infty \frac{\kappa d\kappa}{|p|} \left[ \cos 2\phi \left( \kappa^2 + \text{Re}\{r_{pp}\} e^{-2k_0|p|d} \right) + p^2 \cos 2\phi \text{Re}\{r_{ss}\} e^{-2k_0|p|d} \right. \\
& \left. \left. + 2|p| \sin \phi \cos \phi \text{Im}\{r_{ps} - r_{sp}\} e^{-2k_0|p|d} \right] \right\} \quad (\text{E.93})
\end{aligned}$$

when the interface is the  $x - y$  plane, and

$$\begin{aligned}
\text{Re} \{ G_{yy}^H(\omega) - G_{xx}^H(\omega) \} = & (\pi\omega\rho_0/8) \frac{1}{\pi} \int_0^{2\pi} d\phi \left\{ \int_0^1 \frac{\kappa d\kappa}{p} \left[ \cos^2 \phi \text{Im} \{ r_{pp} e^{2ik_0pd} \} - (\kappa^2 + p^2 \sin^2 \phi) \text{Im} \{ r_{ss} e^{2ik_0pd} \} \right. \right. \\
& \left. \left. - p \sin \phi \cos \phi \text{Im} \{ (r_{ps} - r_{ps}) e^{2ik_0pd} \} \right] \right. \\
& \left. + \int_1^\infty \frac{\kappa d\kappa}{|p|} \left[ -\cos^2 \phi \left( 1 + \text{Re} \{ r_{pp} \} e^{-2k_0|p|d} \right) - p^2 \sin^2 \phi + \kappa^2 + (\kappa^2 + p^2 \sin^2 \phi) \text{Re} \{ r_{ss} \} e^{-2k_0|p|d} \right. \right. \\
& \left. \left. - |p| \sin \phi \cos \phi \text{Im} \{ r_{ps} - r_{sp} \} e^{-2k_0|p|d} \right] \right\}
\end{aligned} \tag{E.94}$$

when the interface is the  $x - z$  plane.

### E.8.3 Plots of torque terms

In this section we look at the torque expressions derived in previous sections for various bias magnetic fields applied to the YIG slab and for the two cases when the slab is the  $x - y$  and  $x - z$  planes.

Figure E.3 shows the plots of  $M_x$ ,  $M_y$ ,  $M_z$ , and  $M_{\text{rec}}$  derived in the previous sections for the magnetic and electric fluctuations. The expressions for the torques due to the electric fields and dipoles fluctuations are found by changing  $s$  to  $p$  and  $p$  to  $s$  in  $r_{ss}$ ,  $r_{pp}$ ,  $r_{sp}$ , and  $r_{ps}$ , in the expressions for the Green's functions. Moreover, magnetic polarizabilities are replaced by a simple isotropic electric polarizability, assuming a simple dielectric polarizability scalar for the YIG and Al interfaces. The results are for three directions of the bias magnetic field for the YIG interface labeled as  $x-$ ,  $y-$ , and  $z-$  bias. The meaning of these bias directions are demonstrated in Fig. E.2 when the YIG slab is the  $x - y$  and  $x - z$  planes.

It is interesting to note that in Figs. (E.3(a)), (E.3(e)), and (E.3(g)), the sphere can experience a large value of torque along  $x$  or  $y$  directions for the  $x-$  or  $y-$  biases. This means that in these cases, the sphere can rotate out of the rotation axis and start to precess. This will of course change the validity of the equations found for the quantum vacuum radiation and quantum vacuum torque along the  $z$  axis since it has been assumed that the sphere is always rotating around the  $z$  axis and it is also magnetized along that axis. This torque is still small enough compared to the driving torque of the trapping laser and it will still give enough time to make the observations. A more careful investigation of these components of torque are out of scope of this study and will be explored in future.

Figures E.3(i)-E.3(p) show the axial torque  $M_z$  as well as the recoil torque  $M_{\text{rec}}$  for all orientations of the bias magnetic field and YIG slab. As expected, the recoil torque is much smaller compared to  $M_z$  since it is a second order term.

Figure E.4 shows the results for  $M_z$  and  $M_{\text{rec}}$  for the case when Al interface is placed

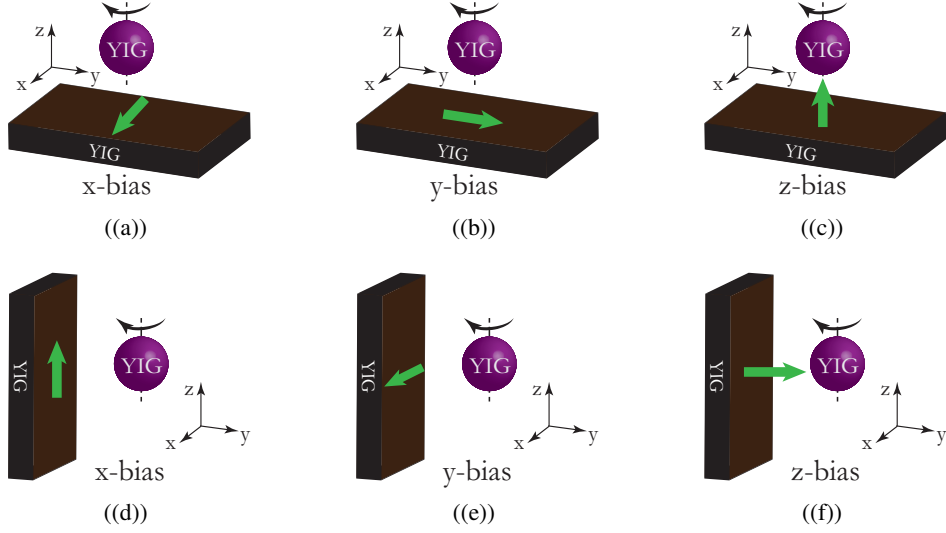


Figure E.2: Schematics of different bias directions for the YIG interface for the two cases of the interface being the  $x - y$  (top row) and  $x - z$  planes (bottom row). The green arrow shows the direction of the bias magnetic field applied to the slab of YIG.

in vicinity of the spinning sphere. Because Al is an isotropic material,  $M_x$  and  $M_y$  vanish for both orientations of the interface and thus are not included in the plots of the torques. Note that similar to the YIG interface results,  $M_{\text{rec}}$  is much smaller compared to the  $M_z$  for all cases of the Al interface. These results show that the recoil torque  $M_{\text{rec}}$  can be ignored in all studied cases.

## E.9 Experimental Analysis

In this section we present the analytical steps in finding the experimental predictions plots provided in section 6.4.

### E.9.1 Effect of drag torque due to imperfect vacuum

In the real system of spinning sphere, the environment is not purely vacuum. This causes an extra account of torque on the spinning sphere. The steady state spin of the sphere happens when the driving torque of the trap laser is equal to the drag and vacuum friction torques. In the case when there is no interface present, the only important counteracting torque is the drag torque given by

$$M_{\text{drag}} = \frac{2\pi\mu a^4}{1.497\lambda}\Omega \quad (\text{E.95})$$

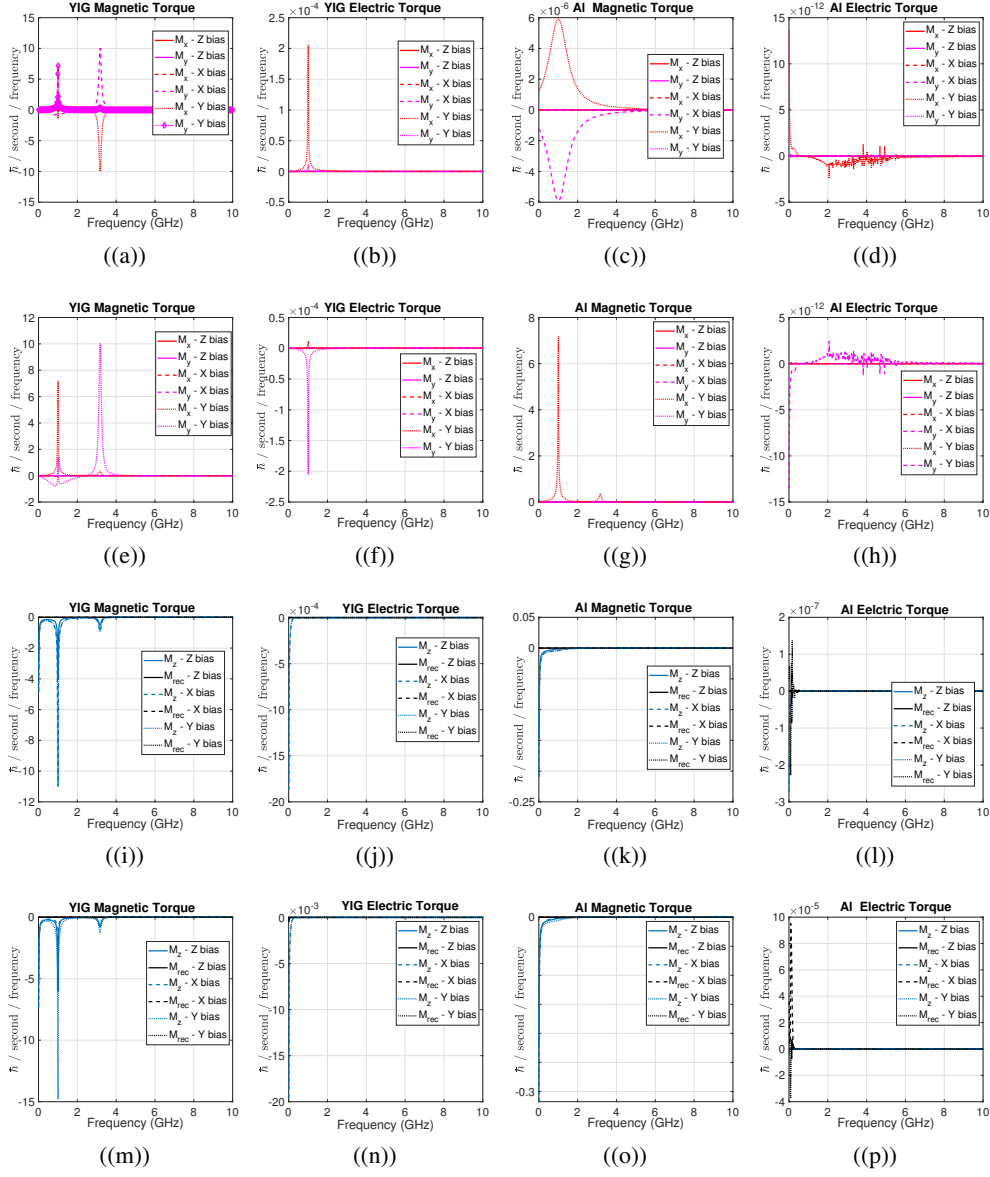


Figure E.3: Plots of  $M_x$  and  $M_y$  (first two rows) and  $M_z$  and  $M_{rec}$  (second two rows) in the vicinity of the YIG slab when the slab is the  $x - y$  plane (first and third rows), and when the slab is  $x - z$  plane (second and fourth rows). The plots show the results for various magnetic field directions. The meanings of  $x$ -,  $y$ -, and  $z$ -bias are demonstrated in Fig. E.2 for the two orientations of the interface.

where  $\mu$  is the viscosity of the gas the sphere is spinning in,  $\lambda$  is the mean free path of the gas molecules, and  $\Omega$  is the rotation frequency [194]. We further have for gases [195],

$$\lambda = \frac{\mu}{p_{\text{gas}}} \sqrt{\frac{\pi K_B T}{2m}} \quad (\text{E.96})$$

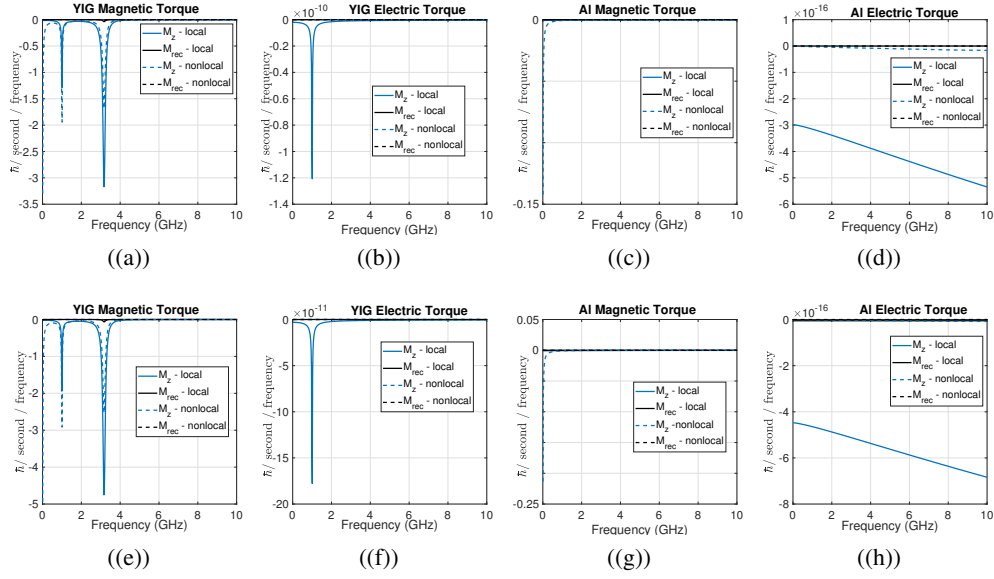


Figure E.4: Plots of  $M_z$  and  $M_{rec}$  in the vicinity of the YIG slab when the slab is the  $x - y$  plane (first row), and when the slab is  $x - z$  plane (second row). Note that due to isotropy of Al, the other components of torque including  $M_x$  and  $M_y$  vanish.

where  $p_{\text{gas}}$  and  $m$  are the pressure and the molecular mass of the gas, respectively. Thus, we get for the drag torque,

$$M_{\text{drag}} = \frac{2a^4 p_{\text{gas}}}{1.479} \sqrt{\frac{2\pi m}{k_B T}} \Omega \quad (\text{E.97})$$

For 1 GHz rotation of a sphere, the balance between the drag torque and the optical torque  $M_{\text{opt}}$  happens at about  $p_{\text{gas}} = 10^{-4}$  torr. Therefore we get, at room temperature and for a molecular mass of 28.966gram/mol,

$$\sqrt{\frac{2\pi m}{K_B T}} = 8.542 \times 10^{-3} \quad (\text{E.98})$$

and thus [8],

$$M_{\text{opt}} = 1.568 \times 10^{-21} \text{N} \cdot \text{m} \quad (\text{E.99})$$

we can use this torque to find the effect of quantum vacuum torque on the rotation speed of the sphere. We can see that for vacuum pressures of about  $10^{-4}$  torr there will be about 0.1% change in the speed of the nanoparticle which is detectible in the power spectral density (PSD) of the nanosphere [8].

## E.9.2 Effect of torque due to the trapping laser

When the trapping laser is linearly polarized, it can exert a negative torque on the spinning particle. The torque on the sphere due to the laser is given by [8],  $M_{\text{opt}} = \frac{1}{2} \text{Re}\{\mathbf{p}^* \times \mathbf{E}\}$ ,

where  $\mathbf{p}$  is the dipole moment of the sphere, given by  $\mathbf{p} = \bar{\alpha}^{\text{eff}} \cdot \mathbf{E}$ , with  $\bar{\alpha}^{\text{eff}}$  being the effective polarizability of the sphere as seen in the frame of the lab, and  $\mathbf{E}$  is the electric field from the laser. As shown in the first section, the polarizability tensor of the sphere, for the sphere spinning in the  $x - y$  plane is given by

$$\bar{\alpha}^{\text{eff}}(\omega) = \begin{pmatrix} \alpha_{\perp}^{\text{eff}}(\omega) & -\alpha_g^{\text{eff}}(\omega) & 0 \\ \alpha_g^{\text{eff}}(\omega) & \alpha_{\perp}^{\text{eff}}(\omega) & 0 \\ 0 & 0 & \alpha_{\parallel}^{\text{eff}}(\omega) \end{pmatrix} \quad (\text{E.100})$$

where

$$\alpha_{\perp}^{\text{eff}}(\omega) = \frac{1}{2} [\alpha(\omega^+) + \alpha(\omega^-)], \quad \alpha_g(\omega) = -\frac{i}{2} [\alpha(\omega^+) - \alpha(\omega^-)], \quad \alpha_{\parallel}(\omega) = \alpha(\omega). \quad (\text{E.101})$$

with  $\alpha(\omega)$  being the electric polarizability of YIG at the laser frequency. Note that here we have assumed that the polarizability of the YIG is scalar in the range of frequencies around 1550 nm. plugging these into the equation for the exerted torque, we find for the  $z$  component of the torque

$$\begin{aligned} M_{\text{opt}} &= \frac{1}{2} \text{Re} \{ \alpha_{\perp}^{\text{eff}*}(\omega) E_x^* E_y - \alpha_g^{\text{eff}*}(\omega) E_y^* E_x - \alpha_g^{\text{eff}*}(\omega) E_x^* E_x - \alpha_{\perp}^{\text{eff}*}(\omega) E_y^* E_x \} \\ &= \frac{1}{2} [\text{Im}\{\alpha_{\perp}^{\text{eff}}(\omega)\} \text{Im}\{\mathbf{E}^* \times \mathbf{E}\} - \text{Re}\{\alpha_g^{\text{eff}}(\omega)\} (|E_x|^2 + |E_y|^2)] \\ &= \frac{1}{2} [\text{Im}\{\alpha(\omega^+) + \alpha(\omega^-)\} \text{Im}\{\mathbf{E}^* \times \mathbf{E}\} - \text{Im}\{\alpha(\omega^+) - \alpha(\omega^-)\} (|E_x|^2 + |E_y|^2)] \end{aligned} \quad (\text{E.102})$$

The first term is proportional to the spin of the electromagnetic field and causes a positive torque on the particle. This is the term for the transferring of angular momentum from the laser to the particle. The second term is negative and thus causes a negative torque on the sphere. In the case when the laser is linearly polarized, this negative term is proportional to  $\text{Im}\{\alpha(\omega_0 + \Omega)\} - \text{Im}\{\alpha(\omega_0 - \Omega)\}$  where  $\omega_0 = 1.21 \times 10^{16}$  is the frequency of the laser, and  $\Omega = 6.28 \times 10^9$  is the rotation frequency. Since  $\Omega \ll \omega_0$ , we get  $\alpha(\omega^+) \simeq \alpha(\omega^-)$  and thus the second term is negligible. We can thus ignore the negative torque coming from the laser when the laser is linearly polarized.

### E.9.3 Effect of heating due to the shot noise

The particle can heat up due to the shot noise of the trapping laser. In this section we calculate the rate of change in the temperature of the particle and its change due to quantum vacuum radiation. The rate of change in the energy of the nanosphere due to the shot noise can be shown to be [178],

$$\dot{E}_{TR} = \frac{\hbar k I_0}{M c} \sigma \quad (\text{E.103})$$

where  $I_0$  is the power of the laser per unit area,  $M$  is the mass of the particle, and  $\sigma$  is the cross section of scattering where, for Rayleigh particles, is equal to  $\sigma = \left(\frac{8\pi}{3}\right) \left(\frac{\alpha k^2}{4\pi\epsilon}\right)^2$ , with  $\alpha$  being the polarizability of the particle and it is given for Rayleigh particles by  $\alpha = 4\pi\epsilon_0 R^3 \left(\frac{\epsilon-1}{\epsilon+2}\right)$ . The Rayleigh limit, for the range of wavelengths around visible and infrared, is valid for particle of radii smaller than 50nm. Since the radius of the particle in our case is 200 nm, this expression may not be valid. Mie scattering parameters should be used to evaluate the scattering cross section. Assuming the trapping laser wavelength of  $\lambda = 1550$  nm, the rate of energy change of YIG with  $n = 2.21$  [173], using the Mie theory, is closely equal to that of the diamond with  $n = 2.39$  in the Rayleigh limit [178]. Therefore, we get for the energy change rate in the sphere

$$\dot{E}_{TR} = \frac{2\hbar\omega_0}{\rho c^2 A} P_0 R^3 k^4 \left(\frac{n^2 - 1}{n^2 + 2}\right)^2 \quad (\text{E.104})$$

where  $A = \pi R_L^2$  is the area of the beam where the laser with the power  $P_0$  is focused on, and  $\rho$  is the mass density which for YIG is  $\rho = 5110\text{kg/m}^3$ . For a laser power of 500 mW focused on an area of radius  $0.7566\mu\text{m}$ , we find

$$\dot{T}_L = 15.45\text{K/s} \quad (\text{E.105})$$

This is a very small change of temperature compared to the time-scale of the rotation which is 1 ns. Therefore, the thermodynamic equilibrium condition for the FDT is still valid. This temperature change gets damped by the radiated power of the sphere due to the rotation. For a YIG sphere spinning at about  $0.5\mu\text{m}$  from the Aluminum interface, the rate of change due to quantum vacuum radiation at the equilibrium temperature  $T_0 = 300$  K is,

$$\dot{T}_R = -362.973\text{K/s} \quad (\text{E.106})$$

which is much larger than the temperature rise due to the shot noise of the laser and this shows that the sphere will cool down. Note that this energy heats up the aluminum instead. In this derivation we have not included the heating due to the noise in the aluminum or YIG interface. The value found in Eq. (E.106) is much smaller at lower temperatures.

## E.10 Solving for Fresnel Coefficients for an Arbitrarily Positioned YIG

In this section we present our method for solving the matrix Eqs. (E.22) and (E.23) for the wave propagation inside YIG material. For a material with  $\bar{\epsilon} = \epsilon\bar{\mathbf{I}}_3$ , and a general permeability tensor with the property  $\mu_{ij} = -\mu_{ji}$ , the determinant of coefficients in Eq. (E.22)

can be written as a quartic equation as

$$a (k'_z)^4 + c (k'_z)^2 + dk'_z + e = 0 \quad (\text{E.107})$$

with

$$a = \mu_{zz} \quad (\text{E.108a})$$

$$c = \mu_{zz}\kappa^2 + \mu_{xx}\kappa^2 \cos^2 \phi + \mu_{yy}\kappa^2 \sin^2 \phi - \mu_{zz}(\mu_{xx} + \mu_{yy}) - \mu_{yz}^2 - \mu_{zx}^2 \quad (\text{E.108b})$$

$$d = 2\mu_{xy}\kappa (\mu_{yz} \cos \phi + \mu_{zx} \sin \phi) \quad (\text{E.108c})$$

$$e = \kappa^4 (\mu_{xx} \cos^2 \phi + \mu_{yy} \sin^2 \phi) + \mu_{xx}\mu_{yy}\mu_{zz} - \mu_{xx}\mu_{yy}\kappa^2 - \mu_{zz}\kappa^2 (\mu_{xx} \cos^2 \phi + \mu_{yy} \sin^2 \phi) \\ + \mu_{xx}\mu_{yz}^2 + \mu_{yy}\mu_{zx}^2 + \mu_{zz}\mu_{xy}^2 - \mu_{xy}^2\kappa^2 - \kappa^2 (\mu_{zx} \cos \phi + \mu_{yz} \sin \phi)^2 \quad (\text{E.108d})$$

The solutions of this equation are written as

$$k'_z{}^{(1,2)} = -S \pm \frac{1}{2} \sqrt{-4S^2 - \frac{2c}{a} + \frac{d}{aS}} \quad (\text{E.109}) \\ k'_z{}^{(3,4)} = +S \pm \frac{1}{2} \sqrt{-4S^2 - \frac{2c}{a} - \frac{d}{aS}}$$

with

$$S = \frac{1}{2} \sqrt{-\frac{2c}{3a} + \frac{1}{3a} \left( Q + \frac{\Delta_0}{Q} \right)} \quad (\text{E.110a})$$

$$Q = \left( \frac{\Delta_1 + \sqrt{\Delta_1^2 - 4\Delta_0^3}}{2} \right)^{\frac{1}{3}} \quad (\text{E.110b})$$

$$\Delta_0 = c^2 + 12ae, \quad \Delta_1 = 2c^3 + 27ad^2 - 72ace \quad (\text{E.110c})$$

Once we get possible  $k'_z$ , we can use boundary conditions to find the reflection coefficients. There are four possible solutions for this equations. Two of these solutions are minus the other pair. Therefore, only the two solutions with positive imaginary part are acceptable. Calling these solutions  $k'_z{}^{(i)}$  with  $i = 1, 2$ , we have two sets of  $t_{ss}^{(i)}$ ,  $t_{sp}^{(i)}$ ,  $t_{ps}^{(i)}$ , and  $t_{pp}^{(i)}$ . Thus we get from Eq. (E.22)

$$\begin{aligned} & \epsilon E_x^t + k'_z{}^{(i)} \eta_0 H_y^t + \kappa \sin \phi \eta_0 H_z^t \\ = & \epsilon \left( E_{0s} t_{ss}^{(i)} \sin \phi + \frac{E_{0p} t_{pp}^{(i)} k'_z{}^{(i)} \cos \phi}{\sqrt{\kappa^2 + k'_z{}^{(i)2}} + \frac{E_{0s} t_{ps}^{(i)} k'_z{}^{(i)} \cos \phi}{\sqrt{\kappa^2 + k'_z{}^{(i)2}} + E_{0p} t_{sp}^{(i)} \sin \phi} \right) \\ & - k'_z{}^{(i)} \left[ -\mu_{xy}^{-1} \left( E_{0s} t_{ss}^{(i)} k'_z{}^{(i)} \cos \phi - \sqrt{\kappa^2 + k'_z{}^{(i)2}} E_{0p} t_{pp}^{(i)} \sin \phi - \sqrt{\kappa^2 + k'_z{}^{(i)2}} E_{0s} t_{ps}^{(i)} \sin \phi + E_{0p} t_{sp}^{(i)} k'_z{}^{(i)} \cos \phi \right) \right. \\ & + \mu_{yy}^{-1} \left( E_{0s} t_{ss}^{(i)} k'_z{}^{(i)} \sin \phi + \sqrt{\kappa^2 + k'_z{}^{(i)2}} E_{0p} t_{pp}^{(i)} \cos \phi + \sqrt{\kappa^2 + k'_z{}^{(i)2}} E_{0s} t_{ps}^{(i)} \cos \phi + E_{0p} t_{sp}^{(i)} k'_z{}^{(i)} \sin \phi \right) \\ & \left. + \mu_{yz}^{-1} \left( E_{0s} t_{ss}^{(i)} \kappa + E_{0s} t_{sp}^{(i)} \kappa \right) \right] \\ & - \kappa \sin \phi \left[ \mu_{xx}^{-1} \left( E_{0s} t_{ss}^{(i)} k'_z{}^{(i)} \cos \phi - \sqrt{\kappa^2 + k'_z{}^{(i)2}} E_{0p} t_{pp}^{(i)} \sin \phi - \sqrt{\kappa^2 + k'_z{}^{(i)2}} E_{0s} t_{ps}^{(i)} \sin \phi + E_{0p} t_{sp}^{(i)} k'_z{}^{(i)} \cos \phi \right) \right. \\ & \left. - \mu_{yz}^{-1} \left( E_{0s} t_{ss}^{(i)} k'_z{}^{(i)} \sin \phi + \sqrt{\kappa^2 + k'_z{}^{(i)2}} E_{0p} t_{pp}^{(i)} \cos \phi + \sqrt{\kappa^2 + k'_z{}^{(i)2}} E_{0s} t_{ps}^{(i)} \cos \phi + E_{0p} t_{sp}^{(i)} k'_z{}^{(i)} \sin \phi \right) \right. \\ & \left. + \mu_{zz}^{-1} \left( E_{0s} t_{ss}^{(i)} \kappa + E_{0s} t_{sp}^{(i)} \kappa \right) \right] = 0 \end{aligned} \quad (\text{E.111})$$

which gives

$$\begin{aligned}
& t_{ss}^{(i)} E_{0s} \left[ \epsilon \sin \phi + \left( k_z'^{(i)} \right)^2 \mu_{xy}^{-1} \cos \phi - \mu_{yy}^{-1} \left( k_z'^{(i)} \right)^2 \sin \phi - \mu_{yz}^{-1} \kappa k_z'^{(i)} - \mu_{zx}^{-1} \kappa k_z'^{(i)} \sin \phi \cos \phi + \mu_{yz}^{-1} \kappa k_z'^{(i)} \sin^2 \phi - \mu_{zz}^{-1} \kappa^2 \sin \phi \right] \\
& + t_{pp}^{(i)} E_{0p} \sqrt{\kappa^2 + k_z'^{(i)2}} \left[ \frac{\epsilon k_z'^{(i)} \cos \phi}{\left( \kappa^2 + k_z'^{(i)2} \right)} - \mu_{xy}^{-1} k_z'^{(i)} \sin \phi - \mu_{yy}^{-1} k_z'^{(i)} \cos \phi + \mu_{zx}^{-1} \kappa \sin^2 \phi + \mu_{yz}^{-1} \kappa \sin \phi \cos \phi \right] \\
& + t_{ps}^{(i)} E_{0s} \sqrt{\kappa^2 + k_z'^{(i)2}} \left[ \frac{\epsilon k_z'^{(i)} \cos \phi}{\left( \kappa^2 + k_z'^{(i)2} \right)} - \mu_{xy}^{-1} k_z'^{(i)} \sin \phi - \mu_{yy}^{-1} k_z'^{(i)} \cos \phi + \mu_{zx}^{-1} \kappa \sin^2 \phi + \mu_{yz}^{-1} \kappa \sin \phi \cos \phi \right] \\
& + t_{sp}^{(i)} E_{0p} \left[ \epsilon \sin \phi + \mu_{xy}^{-1} \left( k_z'^{(i)} \right)^2 \cos \phi - \mu_{yy}^{-1} \left( k_z'^{(i)} \right)^2 \sin \phi - \mu_{yz}^{-1} \kappa k_z'^{(i)} - \mu_{zx}^{-1} \kappa k_z'^{(i)} \sin \phi \cos \phi + \mu_{yz}^{-1} \kappa k_z'^{(i)} \sin^2 \phi - \mu_{zz}^{-1} \kappa^2 \sin \phi \right] = 0
\end{aligned} \tag{E.112}$$

Setting  $E_{0p} = 0$ , we find

$$A^{(i)} = \frac{t_{ps}^{(i)}}{t_{ss}^{(i)}} = - \frac{\epsilon \sin \phi + \left( k_z'^{(i)} \right)^2 \mu_{xy}^{-1} \cos \phi - \mu_{yy}^{-1} \left( k_z'^{(i)} \right)^2 \sin \phi - \mu_{yz}^{-1} \kappa k_z'^{(i)} - \mu_{zx}^{-1} \kappa k_z'^{(i)} \sin \phi \cos \phi + \mu_{yz}^{-1} \kappa k_z'^{(i)} \sin^2 \phi - \mu_{zz}^{-1} \kappa^2 \sin \phi}{\sqrt{\kappa^2 + k_z'^{(i)2}} \left[ \frac{\epsilon k_z'^{(i)} \cos \phi}{\left( \kappa^2 + k_z'^{(i)2} \right)} - \mu_{xy}^{-1} k_z'^{(i)} \sin \phi - \mu_{yy}^{-1} k_z'^{(i)} \cos \phi + \mu_{zx}^{-1} \kappa \sin^2 \phi + \mu_{yz}^{-1} \kappa \sin \phi \cos \phi \right]} \tag{E.113}$$

and setting  $E_{0s} = 0$ ,

$$B^{(i)} = \frac{t_{sp}^{(i)}}{t_{pp}^{(i)}} = \frac{1}{A^{(i)}} \tag{E.114}$$

We can also get  $A^{(i)}$  and  $B^{(i)}$  from a different component of Eq. (E.22) which should give the same result. For the  $y$  component, for instance, we get

$$\begin{aligned}
& \epsilon E_y^t - k_z'^{(i)} \eta_0 H_x^t - \kappa \cos \phi \eta_0 H_z^t = 0 \\
& = \epsilon \left( -E_{0s} t_{ss}^{(i)} \cos \phi + \frac{E_{0p} t_{pp}^{(i)} k_z'^{(i)} \sin \phi}{\sqrt{\kappa^2 + k_z'^{(i)2}}} + \frac{E_{0s} t_{ps}^{(i)} k_z'^{(i)} \sin \phi}{\sqrt{\kappa^2 + k_z'^{(i)2}}} - E_{0p} t_{sp}^{(i)} \cos \phi \right) \\
& + k_z'^{(i)} \left[ \mu_{xx}^{-1} \left( E_{0s} t_{ss}^{(i)} k_z'^{(i)} \cos \phi - \sqrt{\kappa^2 + k_z'^{(i)2}} E_{0p} t_{pp}^{(i)} \sin \phi - \sqrt{\kappa^2 + k_z'^{(i)2}} E_{0s} t_{ps}^{(i)} \sin \phi + E_{0p} t_{sp}^{(i)} k_z'^{(i)} \cos \phi \right) \right. \\
& + \mu_{xy}^{-1} \left( E_{0s} t_{ss}^{(i)} k_z'^{(i)} \sin \phi + \sqrt{\kappa^2 + k_z'^{(i)2}} E_{0p} t_{pp}^{(i)} \cos \phi + \sqrt{\kappa^2 + k_z'^{(i)2}} E_{0s} t_{ps}^{(i)} \cos \phi + E_{0p} t_{sp}^{(i)} k_z'^{(i)} \sin \phi \right) \\
& \left. - \mu_{zx}^{-1} \left( E_{0s} t_{ss}^{(i)} \kappa + E_{0s} t_{sp}^{(i)} \kappa \right) \right] \\
& + \kappa \cos \phi \left[ \mu_{zx}^{-1} \left( E_{0s} t_{ss}^{(i)} k_z'^{(i)} \cos \phi - \sqrt{\kappa^2 + k_z'^{(i)2}} E_{0p} t_{pp}^{(i)} \sin \phi - \sqrt{\kappa^2 + k_z'^{(i)2}} E_{0s} t_{ps}^{(i)} \sin \phi + E_{0p} t_{sp}^{(i)} k_z'^{(i)} \cos \phi \right) \right. \\
& \left. - \mu_{yz}^{-1} \left( E_{0s} t_{ss}^{(i)} k_z'^{(i)} \sin \phi + \sqrt{\kappa^2 + k_z'^{(i)2}} E_{0p} t_{pp}^{(i)} \cos \phi + \sqrt{\kappa^2 + k_z'^{(i)2}} E_{0s} t_{ps}^{(i)} \cos \phi + E_{0p} t_{sp}^{(i)} k_z'^{(i)} \sin \phi \right) \right. \\
& \left. + \mu_{zz}^{-1} \left( E_{0s} t_{ss}^{(i)} \kappa + E_{0s} t_{sp}^{(i)} \kappa \right) \right] = 0
\end{aligned} \tag{E.115}$$

which gives

$$\begin{aligned}
& t_{ss}^{(i)} E_{0s} \left[ -\epsilon \cos \phi + \left( k_z'^{(i)} \right)^2 \mu_{xx}^{-1} \cos \phi + \mu_{xy}^{-1} \left( k_z'^{(i)} \right)^2 \sin \phi - \mu_{zx}^{-1} \kappa k_z'^{(i)} + \mu_{zx}^{-1} \kappa k_z'^{(i)} \cos^2 \phi - \mu_{yz}^{-1} \kappa k_z'^{(i)} \sin \phi \cos \phi + \mu_{zz}^{-1} \kappa^2 \cos \phi \right] \\
& + t_{pp}^{(i)} E_{0p} \sqrt{\kappa^2 + k_z'^{(i)2}} \left[ \frac{\epsilon k_z'^{(i)} \sin \phi}{\left( \kappa^2 + k_z'^{(i)2} \right)} - \mu_{xx}^{-1} k_z'^{(i)} \sin \phi + \mu_{xy}^{-1} k_z'^{(i)} \cos \phi - \mu_{zx}^{-1} \kappa \sin \phi \cos \phi - \mu_{yz}^{-1} \kappa \cos^2 \phi \right] \\
& + t_{ps}^{(i)} E_{0s} \sqrt{\kappa^2 + k_z'^{(i)2}} \left[ \frac{\epsilon k_z'^{(i)} \sin \phi}{\left( \kappa^2 + k_z'^{(i)2} \right)} - \mu_{xx}^{-1} k_z'^{(i)} \sin \phi + \mu_{xy}^{-1} k_z'^{(i)} \cos \phi - \mu_{zx}^{-1} \kappa \sin \phi \cos \phi - \mu_{yz}^{-1} \kappa \cos^2 \phi \right] \\
& + t_{sp}^{(i)} E_{0p} \left[ -\epsilon \cos \phi + \mu_{xx}^{-1} \left( k_z'^{(i)} \right)^2 \cos \phi + \mu_{xy}^{-1} \left( k_z'^{(i)} \right)^2 \sin \phi - \mu_{zx}^{-1} \kappa k_z'^{(i)} + \mu_{zx}^{-1} \kappa k_z'^{(i)} \cos^2 \phi - \mu_{yz}^{-1} \kappa k_z'^{(i)} \sin \phi \cos \phi + \mu_{zz}^{-1} \kappa^2 \cos \phi \right] = 0
\end{aligned} \tag{E.116}$$

Therefore we find again,

$$A^{(i)} = \frac{t_{ps}^{(i)}}{t_{ss}^{(i)}} = - \frac{-\epsilon \cos \phi + \left( k_z'^{(i)} \right)^2 \mu_{xx}^{-1} \cos \phi + \mu_{xy}^{-1} \left( k_z'^{(i)} \right)^2 \sin \phi - \mu_{zx}^{-1} \kappa k_z'^{(i)} + \mu_{zx}^{-1} \kappa k_z'^{(i)} \cos^2 \phi - \mu_{yz}^{-1} \kappa k_z'^{(i)} \sin \phi \cos \phi + \mu_{zz}^{-1} \kappa^2 \cos \phi}{\sqrt{\kappa^2 + k_z'^{(i)2}} \left[ \frac{\epsilon k_z'^{(i)} \sin \phi}{\left( \kappa^2 + k_z'^{(i)2} \right)} - \mu_{xx}^{-1} k_z'^{(i)} \sin \phi + \mu_{xy}^{-1} k_z'^{(i)} \cos \phi - \mu_{zx}^{-1} \kappa \sin \phi \cos \phi - \mu_{yz}^{-1} \kappa \cos^2 \phi \right]} \tag{E.117}$$

$$B^{(i)} = \frac{t_{sp}^{(i)}}{t_{pp}^{(i)}} = \frac{1}{A^{(i)}} \tag{E.118}$$

which should be equal to the previous values for  $A$  and  $B$ . By comparing these two, we find the numerical error of the problem.

The boundary conditions for electric fields are

$$\begin{aligned}
\hat{x} : & E_{0s} \sin \phi (1 + r_{ss}) + E_{0p} k_z \cos \phi (1 - r_{pp}) - E_{0s} r_{ps} k_z \cos \phi + E_{0p} r_{sp} \sin \phi = \\
& \sum_{i=1}^2 \left[ E_{0s} t_{ss}^{(i)} \sin \phi + \frac{E_{0p} t_{pp}^{(i)} k_z'^{(i)} \cos \phi}{\sqrt{\kappa^2 + k_z'^{(i)2}}} + \frac{E_{0s} t_{ps}^{(i)} k_z'^{(i)} \cos \phi}{\sqrt{\kappa^2 + k_z'^{(i)2}}} + E_{0p} t_{sp}^{(i)} \sin \phi \right]
\end{aligned} \tag{E.119a}$$

$$\begin{aligned}
\hat{y} : & -E_{0s} \cos \phi (1 + r_{ss}) + E_{0p} k_z \sin \phi (1 + r_{pp}) - E_{0s} r_{ps} k_z \sin \phi - E_{0p} r_{sp} \cos \phi = \\
& \sum_{i=1}^2 \left[ -E_{0s} t_{ss}^{(i)} \cos \phi + \frac{E_{0p} t_{pp}^{(i)} k_z'^{(i)} \sin \phi}{\sqrt{\kappa^2 + k_z'^{(i)2}}} + \frac{E_{0s} t_{ps}^{(i)} k_z'^{(i)} \sin \phi}{\sqrt{\kappa^2 + k_z'^{(i)2}}} - E_{0p} t_{sp}^{(i)} \cos \phi \right]
\end{aligned} \tag{E.119b}$$

and

$$\begin{aligned}
\hat{x} : & E_{0s} k_z \cos \phi (1 - r_{ss}) - E_{0p} \sin \phi (1 + r_{pp}) - E_{0s} r_{ps} \sin \phi - E_{0p} r_{sp} k_z \cos \phi = \\
& \sum_{i=1}^2 \left\{ \mu_{xx}^{-1} \left[ E_{0s} t_{ss}^{(i)} k_z'^{(i)} \cos \phi - E_{0p} t_{pp}^{(i)} \sqrt{\kappa^2 + k_z'^{(i)2}} \sin \phi - E_{0s} t_{ps}^{(i)} \sqrt{\kappa^2 + k_z'^{(i)2}} \sin \phi + E_{0p} t_{sp}^{(i)} k_z'^{(i)} \cos \phi \right] \right. \\
& + \mu_{xy}^{-1} \left[ E_{0s} t_{ss}^{(i)} k_z'^{(i)} \sin \phi + E_{0p} t_{pp}^{(i)} \sqrt{\kappa^2 + k_z'^{(i)2}} \cos \phi + E_{0s} t_{ps}^{(i)} \sqrt{\kappa^2 + k_z'^{(i)2}} \cos \phi + E_{0p} t_{sp}^{(i)} k_z'^{(i)} \sin \phi \right] \\
& \left. + \mu_{xz}^{-1} \left[ E_{0s} t_{ss}^{(i)} \kappa + E_{0p} t_{sp}^{(i)} \kappa \right] \right\}
\end{aligned} \tag{E.120a}$$

$$\begin{aligned}
& \hat{y} : E_{0s}k_z \sin \phi(1 - r_{ss}) + E_{0p} \cos \phi(1 + r_{pp}) + E_{0s}r_{ps} \cos \phi - E_{0p}r_{sp}k_z \sin \phi = \\
& \sum_{i=1}^2 \left\{ \mu_{yx}^{-1} \left[ E_{0s}t_{ss}^{(i)}k_z^{(i)} \cos \phi - E_{0p}t_{pp}^{(i)}\sqrt{\kappa^2 + k_z'^{(i)2}} \sin \phi - E_{0s}t_{ps}^{(i)}\sqrt{\kappa^2 + k_z'^{(i)2}} \sin \phi + E_{0p}t_{sp}^{(i)}k_z^{(i)} \cos \phi \right] \right. \\
& \quad \left. + \mu_{yy}^{-1} \left[ E_{0s}t_{ss}^{(i)}k_z^{(i)} \sin \phi + E_{0p}t_{pp}^{(i)}\sqrt{\kappa^2 + k_z'^{(i)2}} \cos \phi + E_{0s}t_{ps}^{(i)}\sqrt{\kappa^2 + k_z'^{(i)2}} \cos \phi + E_{0p}t_{sp}^{(i)}k_z^{(i)} \sin \phi \right] \right. \\
& \quad \left. + \mu_{yz}^{-1} \left[ E_{0s}t_{ss}^{(i)}\kappa + E_{0p}t_{sp}^{(i)}\kappa \right] \right\}
\end{aligned} \tag{E.120b}$$

for the boundary condition of the magnetic field with  $\mu_{ij}^{-1}$  being the elements of the inverse of  $\bar{\mu}$  matrix assuming that it is invertible. We get from the electric field's boundary conditions

$$\begin{aligned}
& \sum_{i=1}^2 \left\{ E_{0s} \left[ \sin \phi \left( 1 + r_{ss} - t_{ss}^{(i)} \right) - \cos \phi \left( r_{ps}k_z + \frac{t_{ps}^{(i)}k_z^{(i)}}{\sqrt{\kappa^2 + k_z'^{(i)2}}} \right) \right] \right. \\
& \quad \left. + E_{0p} \left[ \cos \phi \left( k_z - r_{pp}k_z - \frac{t_{pp}^{(i)}k_z^{(i)}}{\sqrt{\kappa^2 + k_z'^{(i)2}}} \right) + \sin \phi \left( r_{sp} - t_{sp}^{(i)} \right) \right] \right\} = 0
\end{aligned} \tag{E.121a}$$

$$\begin{aligned}
& \sum_{i=1}^2 \left\{ E_{0s} \left[ \cos \phi \left( 1 + r_{ss} - t_{ss}^{(i)} \right) + \sin \phi \left( r_{ps}k_z + \frac{t_{ps}^{(i)}k_z^{(i)}}{\sqrt{\kappa^2 + k_z'^{(i)2}}} \right) \right] \right. \\
& \quad \left. + E_{0p} \left[ -\sin \phi \left( k_z - k_z r_{pp} - \frac{k_z^{(i)}t_{pp}^{(i)}}{\sqrt{\kappa^2 + k_z'^{(i)2}}} \right) + \cos \phi \left( r_{sp} - t_{sp}^{(i)} \right) \right] \right\} = 0
\end{aligned} \tag{E.121b}$$

Taking  $E_{0p} = 0$ , we get

$$1 + r_{ss} = \sum_{i=1}^2 t_{ss}^{(i)}, \quad k_z r_{ps} = - \sum_{i=1}^2 \frac{k_z^{(i)} t_{ps}^{(i)}}{\sqrt{\kappa^2 + k_z'^{(i)2}}} = - \sum_{i=1}^2 \frac{k_z^{(i)} A^{(i)} t_{ss}^{(i)}}{\sqrt{\kappa^2 + k_z'^{(i)2}}} \tag{E.122}$$

and taking  $E_{0s} = 0$ , we find

$$k_z(1 - r_{pp}) = \sum_{i=1}^2 \frac{t_{pp}^{(i)}k_z^{(i)}}{\sqrt{\kappa^2 + k_z'^{(i)2}}}, \quad r_{sp} = \sum_{i=1}^2 t_{sp}^{(i)} = \sum_{i=1}^2 t_{pp}^{(i)} B^{(i)}. \tag{E.123}$$

On the other hand, we get from the boundary conditions of the magnetic field

$$\begin{aligned}
& \sum_{i=1}^2 \left[ E_{0s} \left\{ \cos \phi \left[ (1 - r_{ss})k_z - t_{ss}^{(i)} k_z'^{(i)} \mu_{xx}^{-1} - \sqrt{\kappa^2 + k_z'^{(i)2}} t_{ps}^{(i)} \mu_{xy}^{-1} \right] \right. \right. \\
& \quad \left. \left. - \sin \phi \left[ r_{ps} - \sqrt{\kappa^2 + k_z'^{(i)2}} t_{ps}^{(i)} \mu_{xx}^{-1} + t_{ss}^{(i)} k_z'^{(i)} \mu_{xy}^{-1} \right] - t_{ss}^{(i)} \kappa \mu_{xz}^{-1} \right\} \right. \\
& \quad \left. + E_{0p} \left\{ - \sin \phi \left[ (1 + r_{pp}) - \sqrt{\kappa^2 + k_z'^{(i)2}} t_{pp}^{(i)} \mu_{xx}^{-1} + t_{sp}^{(i)} k_z'^{(i)} \mu_{xy}^{-1} \right] \right. \right. \\
& \quad \left. \left. - \cos \phi \left[ r_{sp} k_z + t_{sp}^{(i)} k_z'^{(i)} \mu_{xx}^{-1} + \sqrt{\kappa^2 + k_z'^{(i)2}} t_{pp}^{(i)} \mu_{xy}^{-1} \right] - t_{sp}^{(i)} \kappa \mu_{xz}^{-1} \right\} \right] = 0
\end{aligned} \tag{E.124a}$$

$$\begin{aligned}
& \sum_{i=1}^2 \left[ E_{0s} \left\{ \sin \phi \left[ k_z(1 - r_{ss}) + \sqrt{\kappa^2 + k_z'^{(i)2}} t_{ps}^{(i)} \mu_{yx}^{-1} - t_{ss}^{(i)} k_z'^{(i)} \mu_{yy}^{-1} \right] \right. \right. \\
& \quad \left. \left. + \cos \phi \left[ r_{ps} - t_{ss}^{(i)} k_z'^{(i)} \mu_{yx}^{-1} - \sqrt{\kappa^2 + k_z'^{(i)2}} t_{ps}^{(i)} \mu_{yy}^{-1} \right] - t_{ss}^{(i)} \kappa \mu_{yz}^{-1} \right\} \right. \\
& \quad \left. + E_{0p} \left\{ \cos \phi \left[ (1 + r_{pp}) - t_{sp}^{(i)} k_z'^{(i)} \mu_{yx}^{-1} - \sqrt{\kappa^2 + k_z'^{(i)2}} t_{pp}^{(i)} \mu_{yy}^{-1} \right] \right. \right. \\
& \quad \left. \left. - \sin \phi \left[ r_{sp} k_z - \sqrt{\kappa^2 + k_z'^{(i)2}} t_{pp}^{(i)} \mu_{yx}^{-1} + t_{sp}^{(i)} k_z'^{(i)} \mu_{yy}^{-1} \right] - t_{sp}^{(i)} \kappa \mu_{yz}^{-1} \right\} \right] = 0
\end{aligned} \tag{E.124b}$$

Setting  $E_{0p} = 0$ , we get

$$\begin{aligned}
& \sum_{i=1}^2 \left[ a_s^{(i)} t_{ss}^{(i)} + 2k_z \cos \phi \right] = 0 \\
& \sum_{i=1}^2 \left[ b_s^{(i)} t_{ss}^{(i)} + 2k_z \sin \phi \right] = 0
\end{aligned} \tag{E.125}$$

where

$$\begin{aligned}
a_s^{(i)} &= - \cos \phi \left[ k_z + \mu_{xx}^{-1} k_z'^{(i)} + \sqrt{\kappa^2 + k_z'^{(i)2}} A^{(i)} \mu_{xy}^{-1} \right] \\
& \quad - \sin \phi \left[ - \frac{k_z'^{(i)}}{k_z \sqrt{\kappa^2 + k_z'^{(i)2}}} A^{(i)} + k_z'^{(i)} \mu_{xy}^{-1} - \sqrt{\kappa^2 + k_z'^{(i)2}} \mu_{xx}^{-1} A^{(i)} \right] - \kappa \mu_{xz}^{-1}
\end{aligned} \tag{E.126}$$

$$\begin{aligned}
b_s^{(i)} &= - \sin \phi \left[ k_z + \sqrt{\kappa^2 + k_z'^{(i)2}} \mu_{xy}^{-1} A^{(i)} + \mu_{yy}^{-1} k_z'^{(i)} \right] \\
& \quad + \cos \phi \left[ - \frac{k_z'^{(i)}}{k_z \sqrt{\kappa^2 + k_z'^{(i)2}}} A^{(i)} + k_z'^{(i)} \mu_{xy}^{-1} - \sqrt{\kappa^2 + k_z'^{(i)2}} \mu_{yy}^{-1} A^{(i)} \right] - \kappa \mu_{yz}^{-1}
\end{aligned} \tag{E.127}$$

Also, setting  $E_{0s} = 0$ , we get

$$\begin{aligned} \sum_{i=1}^2 \left[ a_p^{(i)} t_{pp}^{(i)} - 2 \sin \phi \right] &= 0 \\ \sum_{i=1}^2 \left[ b_p^{(i)} t_{pp}^{(i)} + 2 \cos \phi \right] &= 0 \end{aligned} \quad (\text{E.128})$$

where

$$\begin{aligned} a_p^{(i)} &= -\sin \phi \left[ -\frac{k_z'^{(i)}}{k_z \sqrt{\kappa^2 + k_z'^{(i)2}} - \sqrt{\kappa^2 + k_z'^{(i)2}} \mu_{xx}^{-1} + \mu_{xy}^{-1} B^{(i)} k_z'^{(i)} \right] \\ &\quad - \cos \phi \left[ B^{(i)} k_z + B^{(i)} k_z'^{(i)} \mu_{xx}^{-1} + \sqrt{\kappa^2 + k_z'^{(i)2}} \mu_{xy}^{-1} \right] - B^{(i)} \kappa \mu_{xz}^{-1} \end{aligned} \quad (\text{E.129})$$

$$\begin{aligned} b_p^{(i)} &= \cos \phi \left[ -\frac{k_z'^{(i)}}{k_z \sqrt{\kappa^2 + k_z'^{(i)2}} + \mu_{xy}^{-1} k_z'^{(i)} B^{(i)} - \sqrt{\kappa^2 + k_z'^{(i)2}} \mu_{yy}^{-1} \right] \\ &\quad - \sin \phi \left[ B^{(i)} k_z + B^{(i)} k_z'^{(i)} \mu_{yy}^{-1} + \sqrt{\kappa^2 + k_z'^{(i)2}} \mu_{xy}^{-1} \right] - B^{(i)} \kappa \mu_{yz}^{-1} \end{aligned} \quad (\text{E.130})$$

Solving these equations we find  $t_{ss}^{(i)}$  and  $t_{pp}^{(i)}$  from which all the reflection coefficients can be found.